A STUDY ON THE SYNTHESIS AND STABILITY OF THE C_{60} FULLERENE/TETRACENE ADDUCT

Franco Cataldo[a]*, D. Aníbal García-Hernández[b] and Arturo Manchado[b,c]

Keywords: fullerene C_{60}; tetracene or naphthacene; Diels-Alder adduct; retro Diels-Alder; spectroscopy; thermal stability

A C_{60} fullerene/tetracene adduct was synthesized and studied by electronic absorption spectroscopy and FT-IR spectroscopy. Essentially the mono-adduct was obtained as suggested by the spectroscopic analysis and by the thermogravimetric analysis (TGA). The stability and the retro Diels-Alder reaction of the C_{60}/tetracene adduct was studied by TGA, differential thermogravimetric analysis (DTG) and by differential scanning calorimetry (DSC). It was found that the adduct is stable above 300°C and decomposes at 323-390 °C according to the DSC analysis. The decomposition involves the release of tetracene and the restoration of C_{60} in high yields. However, part of the C_{60} is lost as amorphous carbon in the retro Diels-Alder reaction.

* Corresponding Authors
E-Mail: franco.cataldo@fastwebnet.it
[a] Actinium Chemical Research srl, Via Casilina 1626A, 00133 Rome, Italy
[b] Instituto de Astrofisica de Canarias, Vía Lactea s/n, E-38205 La Laguna, Tenerife Spain; Departamento de Astrofisica, Universidad de La Laguna (ULL), E-38206 La Laguna, Tenerife, Spain
[c] Consejo Superior de Investigaciones Científicas, Madrid, Spain

Introduction

Fullerenes are able to form a series of interesting Diels-Alder adducts with polycyclic aromatic hydrocarbons (PAHs) and other dienes.[1-7] More in detail, C_{60} fullerene forms a [4+2] addition products with acenes.[1-8] One of the most studied reaction in this field regards the adduct formation between C_{60} and anthracene where the former acts as a dienophile while the PAH is the diene.[8] The property of fullerenes to form adducts has been exploited in the synthesis of quite complex supramolecular structures.[9,10] The Diels-Alder reaction applied on carbon materials is so versatile that it has been proposed as a tool for the synthesis of new carbon materials and surface functionalization.[11] The general interest on the fullerene/acene and then fullerene/PAHs adducts regards new molecules which may combine certain features of fullerenes with those of PAHs which show promising in molecular electronics or other materials science applications,[12] including also organic photovoltaics.[13]

Our interest on adducts between fullerenes and PAHs is linked to the search of such molecules in certain interstellar and circumstellar environments. Indeed, fullerenes were found mixed with PAHs in the circumstellar envelopes around low-mass evolved stars (the so-called planetary nebulae).[14] The current debate involves not only how and where fullerenes were formed but also their possible interaction with PAHs, forming adducts.[15-17] Thus, the present synthesis of the fullerene-tetracene adduct is a follow-up of our earlier study on the C_{60}-anthracene adduct.[16] We are using the infrared spectra of these adducts as references of searching evidence for the presence of such quite complex molecules in space.[16]

Experimental

Materials and equipment

C_{60} fullerene was 99+% pure grade and was obtained from MTR Ltd. (Cleveland, OH, USA). Tetracene and all solvents used were from Sigma-Aldrich (St. Louis, MO, USA).

The FT-IR spectra were recorded on the FT-IR spectrometer Nicolet 6700 from Thermo-Fischer in transmittance mode with samples embedded in KBr pellets. The electronic absorption spectra were recorded on a Shimadzu UV2450 spectrophotometer.

The thermogravimetric analysis (TGA) was performed on a Linseis apparatus model L81+DTA under nitrogen flow of 18 L h^{-1} under a heating rate of 10 °C min^{-1}. The differential scanning calorimetric analysis (DSC) was made on a Mettler DSC 1 Star System apparatus using conventional Al crucible with punched caps at a heating rate of 10°C/min under N_2 flow.

Synthesis of C_{60}-tetracene adduct 1:1 molar ratio

Tetracene (15 mg, $6.98x10^{-5}$ mol) was dissolved in 50 ml of a stock solution of C_{60} in toluene (C_{60} conc. in stock solution 1 mg mL^{-1}; thus, 55 mg C_{60} are $7.64x10^{-5}$ mol). The mixture was refluxed for 1h and then toluene was distilled under reduced pressure leaving a homogeneous and brown solid in quantitative yields.

When part of the reaction product (25 mg) is treated with 8 ml of n-hexane it shows a minimal solubility. The electronic absorption spectrum of the extract does not show any trace of unreacted tetracene but only a series of absorption bands at 209, 228, 255 and 326 nm which can be assigned to C_{60} or directly to the mono-adduct.

The reaction between tetracene and C_{60} was also followed spectrophotometrically using a C_{60} and tetracene concentration in toluene of $1.46x10^{-4}$ M each.

Synthesis of C_{60}-tetracene adduct 1:2 molar ratio

Tetracene (22 mg, $9.6x10^{-5}$ mol) was dissolved in 35 ml of a stock solution of C_{60} in toluene (C_{60} conc. in stock solution 1 mg mL^{-1}; thus, 35 mg C_{60} are $4.86x10^{-5}$ mol). The mixture was refluxed for 1h and then toluene was distilled under reduced pressure leaving a homogeneous and dark-brown solid in quantitative yields.

Part of the reaction product (20 mg) was treated with 5 ml of n-hexane. The soluble fraction was analyzed by electronic absorption spectroscopy and show a series of new absorption bands which can be attributed to the mono- and bis-adduct. The absorption bands were found at 209, 228, 255, 261, 272, 291, 310 and 325 nm. The insoluble residue after n-hexane extraction displays the same infrared spectrum of the starting product. Therefore, the nature of the soluble fraction is identical to the insoluble fraction and it can be assigned to the mono-adduct and, possibly, with a contribution also from the bis-adduct.

Results and Discussion

Spectrophotometric analysis of the reaction between C_{60} and tetracene

The kinetics of the reaction between anthracene and C_{60} and tetracene and C_{60} has been studied spectrophotometrically.[18] It was found that tetracene reacts much more readily with C_{60} than does anthracene. In fact at 40°C the kinetic rate constant k for the formation of the anthracene/C_{60} adduct was found at $7.8x10^{-4}$ $M^{-1}s^{-1}$ while at the same temperature k = 0.16 $M^{-1}s^{-1}$ was measured for the tetracene/C_{60} adduct. This behavior was theoretically predicted since the different reactivity's of anthracene and tetracene towards C_{60} correlate with the respective aromaticity loss upon cycloaddition.[19-21] The two mono-adducts display different behavior as regards the retro Diels-Alder reaction (dissociation back to the reagents), being negligible in the case of the tetracene adduct and important in the case of the anthracene mono-adduct.

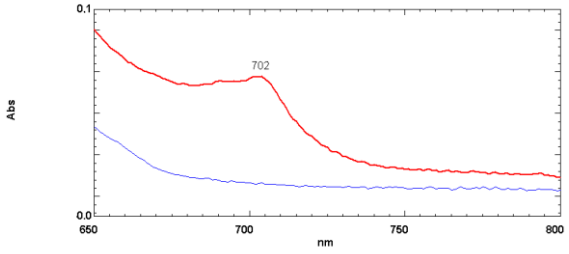

Figure 1. Electronic absorption spectra showing the adduct formation between C_{60} and tetracene (red line).

The Diels-Alder addition of acenes to C_{60} is an equilibrium reaction and in the case of anthracene addition it was necessary to use a stoichiometric excess to achieve the formation of the mono-adduct.[18] On the other hand, in the case of tetracene addition to C_{60} the mono-adduct was obtained even by working in a 1:1 molar ratio between the dienophile and the diene.[18]

The formation of the C_{60}/acene mono-adduct can be followed by the growth of the characteristic absorption band at 706 nm accompanied by a shoulder at 640 nm and the evidence of the mono-adduct formation is suggested by a series of isobiestic points in the electronic absorption spectrum which in the case of C_{60}/tetracene adduct are located at 409, 436, 586 and 612 nm. The eventual absence of isobestic points can be considered as an evidence of the formation of multiple adducts.[18] Fig. 1 shows the detail of the weak absorption band of the C_{60}/tetracene adduct synthesized by us. The absorption band occurs at 702 nm and is characterized by a relatively small molar extinction coefficient of only 350 L mol^{-1} cm^{-1}.

FT-IR spectroscopy on the C_{60}/tetracene adduct

The FT-IR spectrum of the C_{60}/tetracene adduct is fundamental for the search and potential identification of this adduct in space. In Figs. 2 and 3 are shown the FT-IR spectra of the C_{60}/tetracene adduct prepared in 1:2 and 1:1 molar ratio. In both spectra there are no significant differences, so that it can be assumed that prevalently a mono-adduct was obtained in both cases. It was also crucial the experiment of n-hexane extraction of the C_{60}/tetracene adduct resulting from the 1:2 molar ratio. The FT-IR spectrum of the insoluble part resulted identical to that of the whole sample before the n-hexane treatment. Furthermore, the solubilised fraction displayed an electronic absorption spectrum which appeared different from that of pure C_{60} and pure tetracene. Consequently, the spectrum could be attributed to the mono- and bis-adduct.

The main infrared feature of the C_{60}/tetracene adduct in the C-H stretching region (Fig. 2) is the presence of a series of absorption bands which are completely absent in pure C_{60} and which are found at 3042 cm^{-1} in the case of pure tetracene. The FT-IR spectrum of the C_{60}/tetracene adduct is characterized by two aromatic C-H stretching bands respectively at 3045 and 3021 cm^{-1} followed by a group of infrared bands at 2950, 2910 and 2848 cm^{-1} which are due to cycloaliphatic C-H stretching and are due just to the tetracene C-H groups attached to the fullerene cage.[22] A similar (but not identical) spectrum was observed in the case of the C_{60}/anthracene adduct.[8, 16]

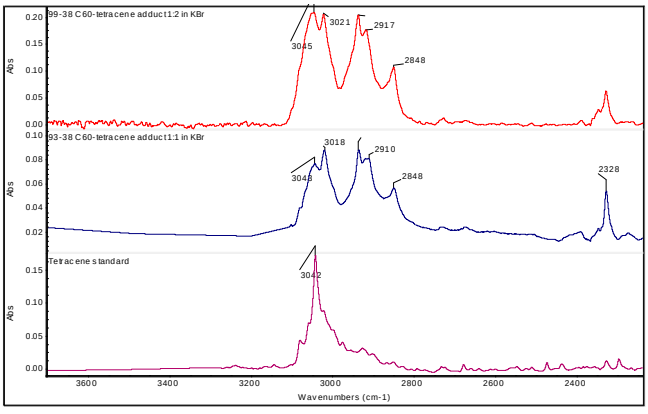

Figure 2. FT-IR spectrum in KBr in the C-H stretching region of C_{60}/tetracene adduct prepared from a 1:2 (top) and 1:1 (middle) molar ratio. The spectra at the bottom of the figure are due to pure tetracene standard.

 DOI: 10.17628/ecb.2014.3.740-744

Fig. 3 shows the spectra of the C_{60}/tetracene adduct in the mid-infrared spectral region in comparison to the spectra of pure C_{60} and pure tetracene. The new infrared bands attributable to the adduct are certainly those at 1673, 1490, 1480, and 1460 cm^{-1} and the other series at 804, 727, 699, 671, and 640 cm^{-1} which could be attributed to the C-H bending modes of the tetracene CH groups after the addition to C_{60}.[22] The C_{60} cage is still intact and displays the typical bands at 1426 and 526 cm^{-1}. The other two C_{60} infrared bands at 1180 and 574 cm^{-1} appear weaker or even absent in the spectrum of the C_{60}/tetracene adduct. Similarly, also some strong absorption bands of reference tetracene, for example those at 902 and 471 cm^{-1} appear very weak in the infrared spectrum of the adduct. Thus, the infrared spectrum of the adduct looks consistent with the known Diels-Alder structure.

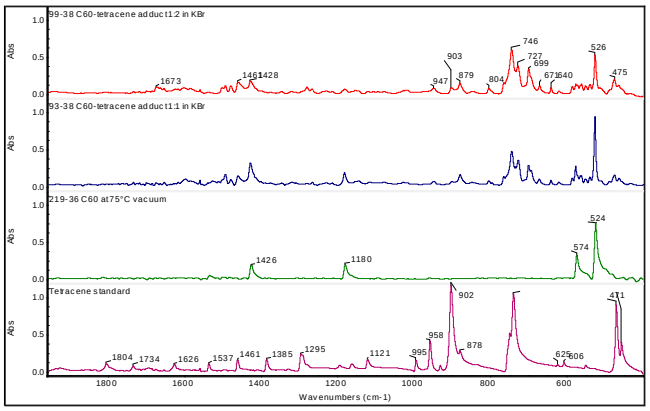

Figure 3. FT-IR spectrum in KBr in the mid infrared region of C_{60}/tetracene adduct prepared from a 1:2 (top) and 1:1 (second from top) molar ratio. The two spectra at the bottom of the figure are due to pure C_{60} and to tetracene standard, respectively.

Thermogravimetric analysis (TGA) of the C_{60}/tetracene adduct

The TGA of the C_{60}/tetracene adduct is useful not only to establish the stability of the adduct but especially also for the interpretation of the stoichiometry of the adduct. In Fig. 4 it is reported the TGA made on the C_{60}/tetracene adduct prepared from a molar ratio 1:1. It is evident that the adduct decomposition occurs above 300 °C (see next section for a deeper discussion) and then a large plateau is reached up to 650 °C. The decomposition of the adduct implies the vaporization of the tetracene leaving C_{60}, which is much less volatile as residue. Surprisingly, the weight loss observed at the plateau above 300 °C is only -15.4 % which once corrected for the weight loss at 300°C (-4.0 %) becomes -11.4 %. This value is much less than the weight loss theoretically expected for the retro Diels-Alder reaction of C_{60}/tetracene 1:1 adduct. In fact, the theoretical weight loss due to tetracene vaporization should be 24.05 %. Since we have evidence that the reaction between C_{60} and tetracene was practically complete, as suggested by the n-hexane extraction experiment, it is reasonable to think that the thermal decomposition of the C_{60}/tetracene adduct does not yields quantitatively the reactants, at least above 300 °C but in part produces a crosslinked carbon soot. This is clearly confirmed by the TGA of Fig. 4 where it is possible to observe that above 900°C under N_2, about 50 % of the starting adduct was not vaporized as C_{60} but remained as non-volatile carbon black. Instead, we know that pure C_{60} is completely volatile above 750 °C.[23]

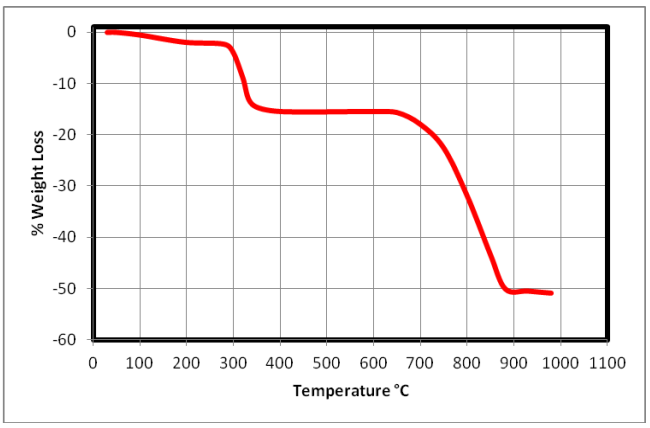

Figure 4. Thermogravimetric analysis of the C_{60}/tetracene adduct prepared from a 1:1 molar ratio

The TGA of the C_{60}/tetracene adduct prepared from a 1:2 molar ratio is shown in Fig. 5. The adduct decomposition occurs again above 300 °C but this time the plateau weight loss is -31.0 % which corrected by the weight loss measured at 300 °C (-7.6 %) it gives -23.4 % in good agreement with the theoretical value of -24.0 % for the mono-adduct. However, as said in the previous case, the decomposition of the C_{60}/tetracene adduct is not a smooth reaction in the TGA. In fact, also Fig. 5 shows that a carbonaceous residue remained in the crucible above 900 °C under N_2. The residual amount is about 34 % by weight of the starting sample.

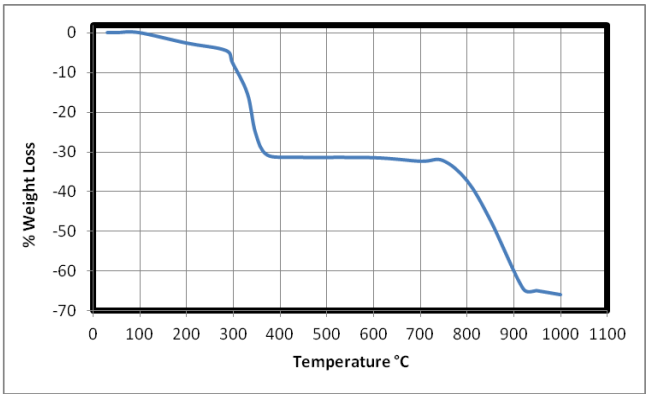

Figure 5. Thermogravimetric analysis of the C_{60}/tetracene adduct prepared from a 1:2 molar ratio

Study of the decomposition reaction of the C_{60}/tetracene adduct

The C_{60}/tetracene adduct prepared from a 1:2 molar ratio was heated in a DSC crucible at a heating rate of 10°C/min under N_2 flow. One sample was heated to 350°C and then cooled under N_2 and then analyzed by FT-IR, while another sample was heated to 630°C and then cooled to room temperature under N_2 and analyzed by FT-IR as well. The FT-IR spectra are shown in Fig. 6.

The infrared spectra of Fig. 6 show that when heated at 350°C the C_{60}/tetracene adduct is just at an incipient decomposition stage as suggested by the presence of the C-

H stretching bands at 3045 and 3021 cm^{-1} followed by a group of infrared bands at 2950, 2910, and 2848 cm^{-1} which are typical of the adduct.

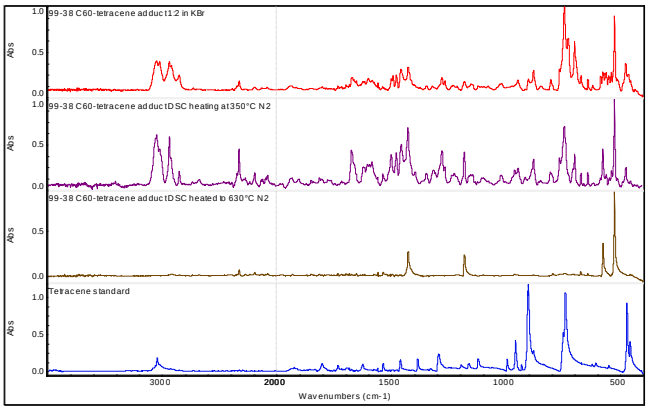

Figure 6. FT-IR spectrum in KBr of C_{60}/tetracene adduct prepared from a 1:2 (top); after heating at 350°C under N_2 (second from top); after heating at 630°C under N_2 (third from top); The spectrum at the bottom of the figure is due to pure tetracene standard.

Fig. 6 shows also that at 630 °C the adduct is completely decomposed and the tetracene was completely vaporized leaving a residue of C_{60}. Based on these spectral data it can be affirmed that the decomposition of the C_{60}/tetracene adduct is complete with the restoration of the reagents. Tetracene is vaporized while C_{60} remains in the crucible since its vaporization occurs above 750 °C as it can be observed also in the TGA of Fig. 4 and 5.[23]

The TGA of Fig. 5 shows that at above 900 °C the total weight loss after C_{60} vaporization corresponds to –66 %. The amount of C_{60} formed by the retro Diels-Alder and vaporized corresponds to 31-66 = 35 % of the starting adduct. This implies that about 35/75.95= 46 % of the C_{60} formed from the retro Diels-Alder was vaporized while the remaining 54% was transformed into a non-volatile carbon black. This behaviour is typical for all fullerene adducts including also the C_{60}/anthracene adduct which however is not able to give back so large amounts of C_{60} as in the case of the tetracene adduct discussed here.[8]

For a further insight into the decomposition reaction of the C_{60}/tetracene adduct in Fig. 7 is reported the DSC trace of the sample heated up to 630 °C under N_2. Two endothermic transitions are observed. The first one is observed at 323 °C with an onset at 315°C and an enthalpy of 10.2 J g^{-1} (9.7 kJ mol^{-1}) while the second transition is more energetic with an enthalpy of 37.7 J g^{-1} (35.7 kJ mol^{-1}) with peak at 390°C and onset at 378 °C. The tetracene melting point occurs at 375°C, thus in the middle of the two DSC transitions. The sublimation enthalpy of tetracene is reported at 126 kJ mol^{-1}.[24]

The exact assignments of these two endothermic transitions remain uncertain although it is possible to assume that the first transition is associated to the initial breakdown of the adduct while the second with the vaporization of tetracene resulting from the retro Diels-Alder.

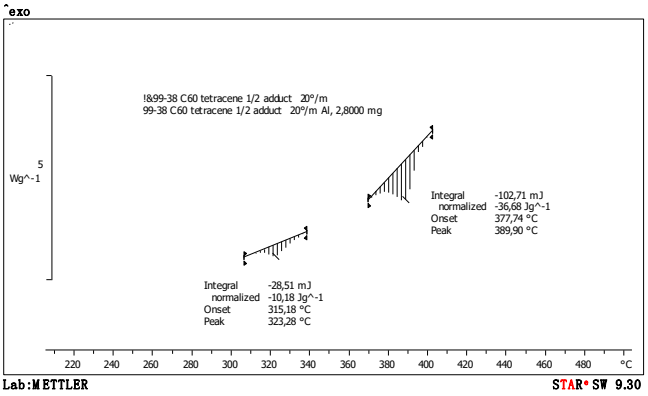

Figure 7. DSC trace of the C_{60}/tetracene adduct prepared from a 1:2 molar ratio. Two endothermal transitions can be distinguished at 323°C and 390°C.

It is interesting in any case to compare the DSC results with the DTG data obtained from the first derivative of the TGA curve of Fig. 4 and Fig. 5. Both the C_{60}/tetracene adducts prepared from 1:1 molar ratio and 1:2 molar ratio show in the DTG of Fig. 8 two transitions connected with the weight loss and hence to the decomposition episodes of the adduct. The first transition occurs at 336 °C followed by another transition at higher temperature: 369 °C. Thus, there is a parallelism in the double endothermic transitions observed both with DSC and with DTG irrespective of the C_{60}/tetracene molar ratio used confirming the idea that first it occurs the adduct breakdown and then the vaporization of the products.

The last annotation here regards the enthalpy of the Diels –Alder reactions. All the spontaneous Diels-Alder reactions are exothermal reactions in the formation of the adduct and endothermal ractions in the retro reactions.[25] For example, the acene dimerization involving anthracene dimerization is reported to be and exothermal reaction with release of -22.6 kJ mol^{-1}.[25] Of course, the retro reaction is instead endothermal and at least 22.6 kJ mol^{-1} plus the activation energy should be administered to decompose the adduct. Consequently, since the decomposition of the C_{60}/tetracene adduct requires the administration of 45.4 kJ mol^{-1} plus the activation energy, the reaction enthalpy for the formation of the adduct is exothermal and should be of the order of -45.4 kJ mol^{-1}.

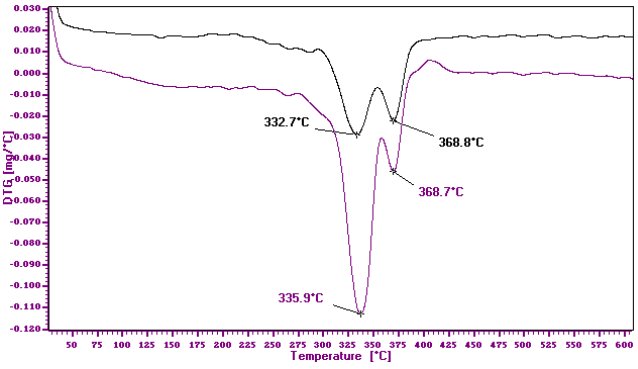

Figure 8. DTG of the C_{60}/tetracene adduct prepared from 1:1 molar ratio (upper trace) and 1:2 molar ratio (lower trace). Two transitions at about 335 °C and 369 °C were detected.

 DOI: 10.17628/ecb.2014.3.740-744

The interpretation of the DSC data is complicated by the fact that the decomposition of the adduct and the vaporization of tetracene may occur also at the same time and this hinders the separation of the reaction enthalpy from the vaporization enthalpy.

Conclusions

In toluene solution C_{60} and tetracene react swiftly to produce mainly a mono-adduct, which is stable above 300 °C and decompose at 323- 390 °C according to the DSC analysis. The decomposition temperature of the C_{60}/tetracene adduct is considerably higher than that of the C_{60}/anthracene adduct studied previously and that decomposes between 225-260°C.[8]

The thermal decomposition of the C_{60}/tetracene adduct causes the release of tetracene and the recovery of the starting C_{60} in relatively high yields. However, about 50 % of the C_{60} employed as reactant is lost as amorphous carbon in the retro Diels Alder reaction.

The C_{60}/tetracene adduct can be easily recognized through the electronic absorption spectroscopy by the development of the absorption band at 702 nm, which, however, is characterized by a low molar extinction coefficient. More useful is the FT-IR spectroscopy which show clear evidence of the formation of the C_{60}/tetracene adduct, especially in the C-H stretching region due to aromatic and cycloaliphatic chemical structure, completely in line with the C_{60}/tetracene adduct structure.

References

[1]Kaur, I.,Glen P. Miller, G.P., *New J. Chem.*, **2008**, *32*, 459.

[2]Athans, A.J., Briggs, J.B., Jia, W., Miller, G.P., *J. Mater. Chem.*, **2007**, *17*, 2636.

[3]Briggs, J.B. and Miller, G.P. *Compt. Rend. Chimie*, **2006**, *9*, 916.

[4]Hirsch, A. and Brettreich, M. "*Fullerenes. Chemistry and Reactions"*, Wiley-VCH: Weinhem, **2005**.

[5]Yurovskaya, M. A. and Trushkov, I. V., *Russian Chem. Bull. Int. Ed*., **2002**, *51*, 367.

[6]Taylor, R. "*Lecture Notes on Fullerene Chemistry. A Handbook for Chemists"*, Imperial College Press: London, **1999.**

[7]Sliva, W., *Fullerenes Nanot. Carbon Nanostruct*., 1995, *3*, 243.

[8]Cataldo, F., Garcia-Hernandez, D. A., Manchado, A., *Fullerenes, Nanoubes, Carbon Nanostruct.*, **2014**, *22*, 565.

[9]Ray, D., Belin, C., Hui, F., Fabre, B., Hapiot, P., Bassani, D., *Chem. Commun.*, **2011**, *47*, 2547.

[10]Wei, L., Wu, Y., Wang, L., Fu, H., Yao, J., *J. Phys. Chem. C*, **2011**, *115*, 21629.

[11]Zydziak, N., Yameen, B, Barner-Kowollik, C., *Polym. Chem.*, **2013**, *4*, 4072.

[12]Martin, N. M., Luzan, S. M., and Talyzin, A. V., *Chem. Phys*., **2010,** *368*, 49.

[13]Yan, S., Srinivas, S., Chih-Wei, C., Douglas, S., Yang, Y., *Appl. Phys. Lett.*, **2007**, *90*, 103501.

[14]García-Hernández, D. A., Manchado, A., García-Lario, P., Stanghellini, L., Villaver, E., Shaw, R. A., Szczerba, R., Perea-Calderón, J. V., *Astrophys. J. Lett.*, **2010**, 724, L39.

[15]García-Hernández, D. A., Iglesias-Groth, S., Acosta-Pulido, J. A., Manchado, A., García-Lario, P., Stanghellini, L., Villaver, E., Shaw, R. A. and Cataldo, F., *Astrophys. J. Lett*., **2011**, *737*, L30.

[16]Garcia-Hernandez, D. A., Cataldo, F., Manchado, A., *Monthly Not. Roy. Astron. Soc*., **2013**, *434*, 415.

[17]Dunk, P.W., Adjizian, J.J., Kaiser, N.K., Quinn, J.P., Blakney, G.T., Ewels, C.P., Marshall, A.G., Kroto, H.W. *Proc. Nat. Acad. Sci. USA*, **2013**, *110*, 18081.

[18]Sarova, G.H., Berberan-Santos, M.N., *Chem. Phys. Lett.*, 2004, *397*, 402.

[19]Manoharan, M., De Proft, F., Geerlings, P., *J. Org. Chem.*, **2000**, *65*, 6132.

[20]Schleyer, P.V.R., Manoharan, M., Jiao, H., Stahl, F., *Org. Lett.*, **2001**, *3*, 3643.

[21] Cheng, M. F., Li, W. K., *Chem. Phys. Lett.*, **2003**, *368*, 630.

[22] Komatsu, K., *Topics Curr. Chem.*, **2005**, *254*, 185.

[23] Cataldo, F., *Fullerenes, Nanotubes, Carbon Nanostruct*., **2002**, *10*, 293.

[24]Chickos, J. S., Acree, W. E., *J. Phys. Chem. Ref. Data*, **2002**, *31*, 537.

[25]Zade, S. S., Zamoshchik, N., Reddy, A. R., Fridman-Marueli, G., Sheberla, D., Bendikov, M., *J. Am. Chem. Soc.*, **2011**, *133*, 10803.

Received: 28.05.2014.
Accepted: 30.06.2014.

PYRIDAZINE AND ITS RELATED COMPOUNDS: PART 30.[1] SYNTHESIS AND APPLICATION OF SOME MONOAZO DISPERSE DYES DERIVED FROM PYRIDAZIN-3(2*H*)-ONE

Ali Deeb,[a*] Mamdoh El-Hossami[b] and Ahmed Awad[c]

Keywords: 5,6-diphenyl-2,3-dihydro-3-oxopyridazine-4-carbohydrazide; disperse dyes; dyeing; fixation; fastness.

A series of monoazo disperse dyes based on 5,6-diphenyl-2,3-dihydro-3-oxopyridazine-4-carbohydrazide was prepared by reacting with azobenzeneacetylacetone, ethyl azobenzeneacetoacetate, and azobenzenemalononitrile derivatives. The dyeing performance of these dyes was assessed on polyester fabrics. The dyes were found to give yellow to brown color shades on dyeing with good depth levelness on fabrics. The dye bath exhaustion, fixation and fastness properties of the dye were also determined.

* Corresponding Authors
E-Mail: dralideeb@hotmail.com
[a] Department of Chemistry, Faculty of Science, Zagazig University, Zagazig, Egypt
[b] Printing, Dyeing and Finishing Department, Faculty of Applied Arts, Helwan University, Egypt.
[c] Aromatic and Medicinal Plants Department, Desert Research Center, Elmatariya, Cairo, Egypt.; Department of Chemistry, Faculty of Science, Jazan University, Jizan 2097, Saudi Arabia.

Introduction

Many pyridazine ring systems are of considerable importance because of their biological and pharmacological properties.[2] On the other hand some pyrazole derivatives are very important class of heterocycles due to their biological and pharmacological activities.[3] Also, they are used as key starting material for the synthesis of commercial aryl/hetarylazopyrazole dyes.[4] All these properties aroused our interest in synthesizing new heterocyclic compounds including the pyridazine and pyrazole moieties which is a continuation of our previous work.[5,6]

The present investigation deals with the synthesis of 4-[(4-arylazo-3,5-dimethylpyrazol-1-yl)carbonyl]-5,6-diphenylpyridazin-3(2*H*)-one, 4-[(4-arylazo-4,5-dihydro-3-methyl-5-oxopyrazol-1-yl)carbonyl]-5,6-diphenylpyridazin-3(2*H*)-one, and 4-[(4-arylazo-3,5-diaminopyrazol-1-yl)carbonyl]-5,6-diphenylpyridazin-3(2*H*)-one derivatives and an evaluation of their properties on polyester fabrics.

Results and discussion

The starting material 5,6-diphenyl-2,3-dihydro-3-oxopyridazine-4-carbohydrazide **2** was prepared as reported[6] from 4-carbethoxy-5,6-diphenyl-3(2*H*)-pyridazinone **1** by refluxing with hydrazine hydrate in 1-butanol (Scheme 1).[7,8]

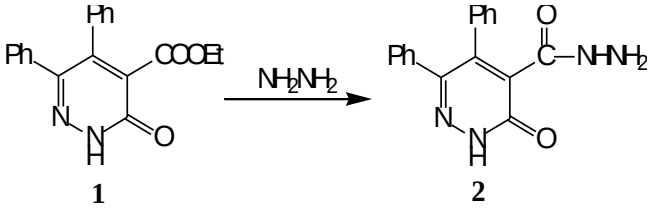

Scheme 1

Arylamine derivatives **3** were diazotized using sodium nitrite in hydrochloric acid, the temperature was maintained below 5°C in an ice-bath. The diazotized products **4** were then coupled with active methylene compounds such as acetylacetone **5a**, ethyl acetoacetate **5b**, and malononitrile **5c** in sodium acetate buffered solution to give the azobenzeneacetylacetone **7a-h**, ethyl azobenzene-acetoacetate **7a-h**, and azobenzenemalononitrile **8a-h** derivatives in good yields (Scheme 2). Spectral data for such compounds indicate them to have a hydrazone configuration, characterization and spectral data for compounds **6a-h**, **7a-h**, and **8a-h** were described in the previous work.[9]

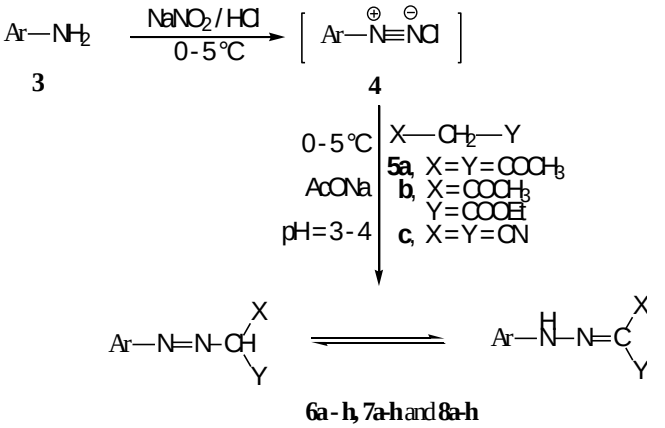

Scheme 2. Compounds **6,7** and **8**: **a** (Ar = Ph); **b** (Ar = 2-MeC$_6$H$_4$); **c** (Ar = 4-MeC$_6$H$_4$); **d** (Ar = 2-MeOC$_6$H$_4$); **e** (Ar = 4-MeOC$_6$H$_4$); **f** (Ar = 2-ClC$_6$H$_4$); **g** (Ar = 3-ClC$_6$H$_4$); **h** (Ar = 4-NO$_2$C$_6$H$_4$); **6a-h** (X,Y = COCH$_3$); **7a-h** (X=COCH$_3$, Y = COOEt); **8a-h** (X,Y= CN).

 DOI: 10.17628/ecb.2014.3.745-751

Compound **2** when reacted with azobenzeneacetylacetone derivatives **6a-h** in absolute ethanol at reflux temperature yielded 4-[(4-arylazo-3,5-dimethylpyrazol-1-yl)carbonyl]-5,6-diphenylpyridazin-3(2*H*)-one derivatives **9a-h**. The reaction proceeds in two stages, viz, the initially formed hydroxypyrazoline subsequently loses water.[10] Compound **2**, when reacted with the ethyl azobenzeneacetoacetate derivatives **7a-h** in a similar manner yielded 4-[(4-arylazo-4,5-dihydro-3-methyl-5-oxopyrazol-1-yl)carbonyl]-5,6-diphenylpyridazin-3(2*H*)-one derivatives **10a-h**.

In addition 3,5-diaminopyrazole derivatives **11a-h** were prepared by treatment of compound **2** with azobenzenemalononitrile **8a-h** in a similar manner gave the corresponding 4-[(4-arylazo-3,5-diaminopyrazol-1-yl)carbonyl]-5,6-diphenylpyridazin-3(2*H*)-one derivatives **11a-h**.

The structures of the prepared compounds were supported by their spectroscopic and elemental analysis and these data are shown in Experimental part.

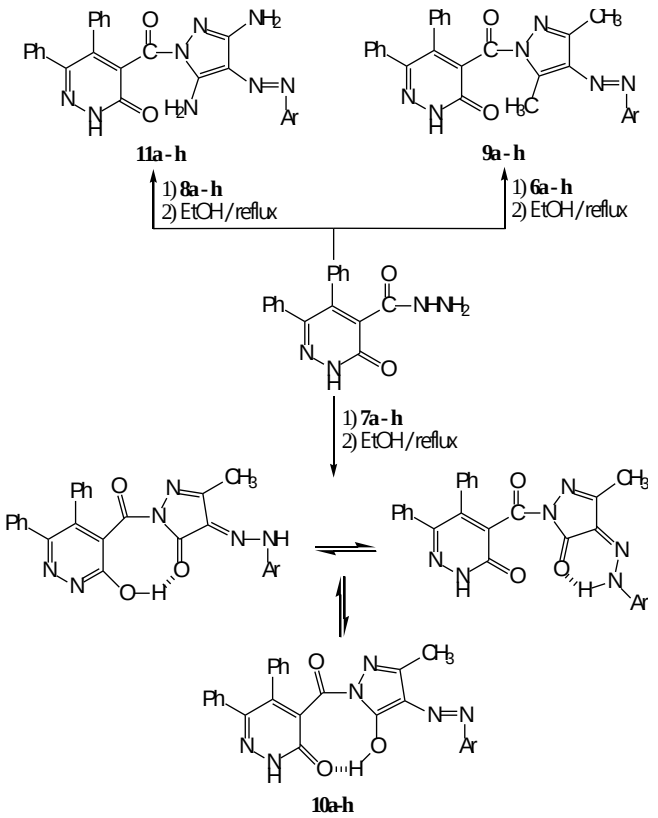

Scheme 3. Compounds **9**, **10** and **11**: **a** (Ar=Ph); **b** (Ar=2-MeC_6H_4); **c** (Ar=4-MeC_6H_4); **d** (Ar=2-$MeOC_6H_4$); **e** (Ar=4-$MeOC_6H_4$); **f** (Ar=2-ClC_6H_4); **g** (Ar=3-ClC_6H_4); **h** (Ar=4-$NO_2C_6H_5$).

Dyeing of polyester fabrics and dyeing properties

Color measurement

The effect of the nature of different substituents on dyeing behavior, color hue, and depth was investigated. This investigation depends on some spectral data of the dyed materials. The most commonly used function *f*(R) is that developed theoretically by Kubelka and Munk. In their theory, the optical properties of a sample were described by two values: *K* is the measure of the light absorption, and *S* is a measure of the light scattering. On textiles, *K* is determined primarily by the dyestuffs and *S* only by the substrate. From the wavelength, Kubelka and Munk calculate Eq. (1) for the reflectance *R* of thick, opaque samples with the constants of *K* and *S*:

$$\frac{K}{S}=\frac{(1-R)^2}{2R} \qquad (1)$$

In this equation *R* is used as a ratio, e.g., 32 % reflectance as 0.32. The *K*/*S* value at λ max was taken as a measure of color depth.

On the other hand, the psychometric coordinates (*L**, *a**, *b**) for each dyed sample were obtained to illustrate the color hues, where *L** is the lightness, ranging from 0 to 100 (0 for black and 100 for white); *a** is the red-green axis, (+) for red, zero for grey, and (-) for green; and *b** is the yellow-blue axis, (+) for yellow, zero for gray, and (-) for blue.

The parent dyestuff in each group is taken as the standard in color difference calculation (Δ*L**, Δ*C**, Δ*H** and Δ*E**). The results are measured using CIE-LAB techniques and given in Table 1, Where Δ*L** is the lightness difference, Δ*C** the chroma difference, Δ*H** the hue difference and Δ*E** the total color difference. A negative sign of Δ*L** indicates that the dyed fiber becomes darker than the standard, but a positive sign indicates that the dyed fiber indicates that the dyed fiber becomes duller than the standard, but a positive sign indicates that the dyed fiber becomes brighter than the standard. A negative sign of Δ*H** indicates that the color directed to red color, while a positive sign indicates that the color directed to yellowish. The values of *K*/*S* of compounds **9, 10,** and **11** vary from 1.2 to 14. The introduction of different groups in dyes **9, 10,** and **11** increases the strength of *K*/*S* values and deepens the color compared with the corresponding parent dye **9a, 10a, 11a** (Table 1).

The values of K/S for 3,5-diaminopyrazol dyes **11** derived from azobenzenemalononitrile derivatives **8a-h** with acid hydrazide **2** were greater than the corresponding 3,5-dimethyl pyrazole dyes **9** derived from azobenzeneacetylacetone derivatives **6a-h** with the same acid hydrazide **2** on dyed polyester fibers except **11b** and **11f**. This bathochromic shift is attributed to the stronger electron-releasing of the amino group with respect to the methyl group at the 3-, 5-position of the pyrazole ring, thus enhancing electron delocalization in the dye molecule and consequently increases the vibrational energy of the dye molecule which in turn increases the color strength (K/S) values of the dyed fibers and directed the color toward reddish and yellowish directions on the red-green and yellow-blue axis respectively.

Assessment of color fastness

Most influences that can affect fastness are light, washing, heat, perspiration, and atmospheric pollution. Conditions of such tests are chosen to correspond closely to treatments

 DOI: 10.17628/ecb.2014.3.745-751

Table 1. Optical measurements of compounds **9ah**, **10a-h** and **11a-h**.

K/S	ΔH^*	ΔC^*	ΔL^*	ΔE^*	L^*	h^*	C^*	b^*	a^*	Dyes
1.2	00.00	00.00	00.00	00.00	87.94	86.20	31.44	31.37	2.08	9a
14	-0.992	-7.795	1.468	7.994	80.71	82.17	98.82	97.90	13.47	9b
2	-32.598	6.208	-13.929	35.989	74.01	29.64	37.64	18.62	32.72	9c
2	-1.324	66.800	-4.819	66.986	83.12	84.84	98.24	97.84	8.84	9d
4	6.908	15.356	1.114	16.875	89.05	96.54	46.79	46.49	-5.33	9e
2.5	-10.541	11.937	-16.656	23.044	71.28	69.79	43.37	40.70	14.98	9f
1.2	5.073	13.029	1.332	14.045	89.27	93.98	44.46	44.36	-3.09	9g
3.9	-0.233	0.569	0.435	0.753	88.37	85.78	32.00	31.92	2.35	9h
2.3	00.00	00.00	00.00	00.00	90.12	99.28	49.62	48.97	-8.00	10a
3.9	-4.441	-5.759	-0.826	7.319	89.30	93.82	43.86	43.76	-2.93	10b
1.2	-6.170	-17.701	-1.326	18.792	88.34	85.41	32.18	32.08	2.58	10c
2.3	-26.592	-21.576	-25.796	42.873	64.32	57.52	28.04	23.66	15.06	10d
3.8	-20.970	49.045	-9.418	54.165	80.70	82.04	98.66	79.72	13.66	10e
2.8	-1.261	9.235	-0.590	9.339	89.53	97.94	58.85	58.29	-8.13	10f
2.1	-11.116	-20.758	-1.459	23.597	88.66	82.39	28.86	28.61	3.82	10g
11.5	-5.496	23.734	-3.493	24.611	86.63	94.06	73.35	73.17	-5.19	10h
2.8	00.00	00.00	00.00	00.00	73.14	73.70	80.29	77.06	22.53	11a
11	-22.255	-51.299	-35.455	66.211	37.68	47.03	28.99	21.21	19.76	11b
7.1	-1.595	-3.591	2.613	4.719	75.75	72.54	76.70	73.16	23.02	11c
11.3	-10.633	-4.272	-7.119	13.491	66.02	65.90	76.02	69.39	31.05	11d
11.1	-10.915	-4.240	-5.384	12.888	67.75	65.69	76.05	69.31	31.31	11e
1.8	-15.139	-30.456	4.624	34.324	77.76	59.95	49.83	43.14	24.95	11f
1.8	18.869	-38.392	15.430	45.475	88.57	92.42	41.90	41.86	-1.77	11g
7.4	-37.413	-23.059	-21.259	48.820	51.88	41.66	52.23	38.04	42.76	11h

a^*, red/green axis**;** b^*, yellow/blue axis; C^*, color brightness; h^*, hue value; L^*, lightness of the color, ΔE^*, total color difference, ΔL^*, lightness difference, ΔC^*, color difference, ΔH^*, hue difference.

Table 2. Fastness properties of compounds **9ah**, **10a-h** and **11a-h**.

Light (40 h)	Sublimation 180 ° C	Rubbing		Acidic Perspiration	Washing	Dyes
		wet	dry			
5-6	4	4	4	4	4	**10e**
5	4	4	3-4	3-4	4-5	**10f**
4-5	4	4	4	4	4	**10g**
4-5	4	4	4	4	4-5	**10h**
5-6	4	3-4	3-4	4	4	**11a**
4	4	3-4	3-4	4	4	**11b**
4-5	4	3-4	3-4	4	4	**11c**
6	4-5	4	3-4	4	4-5	**11d**
4-5	4-5	3-4	3-4	4-5	4	**11e**
5-6	4-5	4	3-4	4-5	4-5	**11f**
4	4	4	3-4	4	4	**11g**
5	4	3-4	3-4	4	4	**11h**
5-6	4	4	4	3-4	4-5	**9a**
4-5	4	4	4	4	4	**9b**
5-6	4	4	4	3-4	4	**9c**
6	4	3-4	4	4	4	**9d**
4-5	4	4	4	4	4--5	**9e**
4	4	4	3-4	4-5	4	**9f**
5-6	4	4	4	4	4	**9g**
4-5	4	4	3-4	4-5	4-5	**9h**
5-6	4	4	3-4	3-4	4-5	**10a**
5-6	4-5	4-5	4	4-5	4-5	**10b**
5-6	4	4	4	4	4-5	**10c**
5-6	4-5	4-5	4-5	4-5	4	**10d**

employed in manufacture and ordinary use conditions.[11] Results are given after usual matching of tested samples against standard reference (the grey scale).[11] The results revealed that these dyes have good fastness properties (Table 2).

Experimental

All melting points were determined on a Gallenkamp electric melting point apparatus. Thin-layer chromatography (TLC) analysis was carried out on silica gel 60 F254 precoated aluminum sheets. Infrared spectra were recorded on FTIR 5300 Spectrometer and Perking Elmer Spectrum RXIFT-IR System, using the potassium bromide wafer technique. ^{1}H-NMR spectra were recorded on Varian Gemini 200 MHz spectrometer using the indicated solvents and tetramethylsilane (TMS) as an internal reference. Electron impact mass spectra were obtained at 70 eV using a GCMS–qp1000 EX Shimadzo spectrometer. Elemental analysis (C, H, N) were carried out at the micro-analytical Center of Cairo University, Giza, Egypt.

The elemental analyses were found to agree favorably with the calculated values. The dyeing assessment fastness tests, and color measurements were carried out at Misr Company for Spinning and Weaving, El-Mahala El-Kobra, Egypt. The syntheses of carbohydrazide **2**,[6-8] and azobenzene compounds **6a-h**, **7a-h**, and **8a-h**[9] were conducted according to known procedures.

Synthesis of 4-[(4-arylazo-3,5-dimethylpyrazol-1-yl)carbonyl]-5,6-diphenylpyridazin-3(2*H*)-one 9, 10 and 11.

General procedure: A mixture of 5,6-diphenyl-2,3-dihydro-3-oxopyridazine-4-carbohydrazide **2** (0.50 g, 1.6 mmole) and the azobenzeneacetylacetone derivatives **6a-h** (1.6 mmole) was refluxed in ethanol (20 mL) for 6 hours. The reaction mixture was cooled to room temperature and the separated solid was filtered off, washed with diluted ethanol (10 mL), dried and recrystallized from ethanol.

4-[(4-Phenylazo-3,5-dimethylpyrazol-1-yl)carbonyl]-5,6-diphenylpyridazin-3(2*H*)-one (9a, $C_{28}H_{22}N_6O_2$).

Yellow crystals in 77 % yield; mp 282 – 283 °C; IR: 3445.1 and 3193.5 (NH), 3059.3 ($CH_{arom.}$), 2927.3 ($CH_{aliph.}$), 1734.1 and 1652 (C=O groups), 1583.2 (C=N) and 1495.4 (C=C) cm^{-1}; Ms (m/z): 476 [M^+ + 2, 5%], 475 [M^+ + 1, 16.6%], 474 [M^+, 11.3%], 397 [M^+ - C_6H_5, 13.4%], 275 [M^+ - substituted pyrazole ring, 31.9 %, ion A], 247 [ion A - CO, 6.9 %], 199 [M^+ - diphenyloxopyridazinone, 86.2 % ion B], 122 [ion B - C_6H_5, 100 %] and 77 [$(C_6H_5)^+$, 35.6 %]; ^{1}H-NMR ($CDCl_3$): δ 12.09 (s, 1H, NH), δ 7.82 - 7.04 (m, 15H, aromatic protons), 2.84 (s, 3H, CH_3-5) and 2.46 (s, 3H, CH_3-3).

4-[(4-(2-Methyphenylazo)-3,5-dimethylpyrazol-1 yl)carbonyl]-5,6-diphenylpyridazin-3(2*H*)-one (9b, $C_{29}H_{24}N_6O_2$).

Yellow, crystals in 75 % yield; mp 260 – 261 °C; IR: 3435.7, 3193.7 and 3134.3 (NH), 3058 ($CH_{arom.}$), 2923.1 ($CH_{aliph.}$), 1727.6 and 1646.4 (C=O groups), 1587.8 (C=N) and 1503 (C=C) cm^{-1}; ^{1}H-NMR ($CDCl_3$): δ 11.5 (s, 1H, NH), 7.7 (d, 4H, aryl protons), 7.30 -7.00 (m, 10H, 2 ph), 2.82 (s, 3H, ortho CH_3), 2.40 (s, 6H, CH_3-3 and CH_3-5); UV (DMF): λ_{max} (log ε); 266.1 (4.2).

4-[(4-(4-Methyphenylazo)-3,5-dimethylpyrazol-1-yl)carbonyl]-5,6-diphenylpyridazin-3(2*H*)-one (9c, $C_{29}H_{24}N_6O_2$).

Yellow crystals in 81 % yield; mp. 251 – 252 °C; IR: 3436.8, 3193.9 and 3134.6 (NH), 3058 ($CH_{arom.}$), 2922.4 ($CH_{aliph.}$), 1727.6 and 1646.4 (C=O groups), 1589.1 (C=N) and 1503.6 (C=C) cm^{-1}; Ms (m/z): 489 [M^+ + 1, 24.4%], 488 [M^+, 13.8%], 275 [M^+ - substituted pyrazole ring, 29.3%, ion A], 274 [ion A - H, 56.1], 213 [M^+ - substituted pyridazinone, 100 %, ion B], 122 [ion B - MeC_6H_4, 97.6 %], 91 [$(CH_2C_6H_5)^+$, 28.5 %] and 77 [$(C_6H_5)^+$, 47.2 %].

4-[(4-(2-Methoxyphenylazo)-3,5-dimethylpyrazol-1-yl)carbonyl]- 5,6-diphenylpyridazin-3(2*H*)-one (9d, $C_{29}H_{24}N_6O_3$).

Yellow crystals in 85 % yield; mp 249 - 250 °C; IR: 3450, 3297 and 3194.3 (NH), 3059.1 ($CH_{arom.}$), 2938.9 ($CH_{aliph.}$), 2874.9 (OCH_3), 1738.1 and 1648.4 (C=O groups), 1598.5 (C=N) and 1547 (C=C) cm^{-1}; UV (DMF): λ_{max} (log ε); 266.2 (3.7).

4-[(4-(4-Methoxyphenylazo)-3,5-dimethylpyrazol-1-yl)carbonyl]-5,6-diphenylpyridazin-3(2*H*)-one (9e, $C_{29}H_{24}N_6O_3$).

Yellow crystals in 92 % yield; mp 265–266 °C; IR: 3432.4, 3307.4 and 3196.8 (NH), 3061.1 (CH_{arom}), 2927.4 ($CH_{aliph.}$), 2836.8 (OCH_3), 1727.6 and 1653 (C=O groups), 1600.8 (C=N) and 1501.6 (C=C) cm^{-1}; Ms (m/z): 506 [M^+ + 1, 22.1 %], 505 [M^+, 48.8 %], 476 [M^+ - OMe, 7.2 %], 275 [M^+ - substituted pyrazole ring, 47.8 %, ion A], 247 [ion A - CO, 7.2 %], 229 [M^+ - substituted pyridazinone, 73.7%, ion B], 123 [ion B - $MeOC_6H_4$, 100 %, ion C], 107 [$(CH_2OC_6H_4)^+$, 17 %], 95 [ion C – N_2, 30.7 %] and 77 [$(C_6H_5)^+$, 53.3 %].

4-[(4-(2-Chlorophenylazo)-3,5-dimethylpyrazol-1-yl)carbonyl]-5,6-diphenylpyridazin-3(2*H*)-one (9f, $C_{28}H_{21}ClN_6O_2$).

Yellow crystals in 90 % yield; mp 279 – 280 °C; IR: 3425.4, 3298 and 3195 (NH), 3060.8 ($CH_{arom.}$), 2927 (CH_{aliph}), 1723.4 and 1645.1 (C=O groups), 1586.9 (C=N), 1538.1 (C=C) and 758.4 (Cl-C) cm^{-1}; Ms (m/z): 509 [M^+, 4 %], 474 [M^+ - Cl, 24.9 %], 354 [M^+ - $2C_6H_5$, 11 %], 275 [M^+ - substituted pyrazole ring, 43.9%, ion A], 247 [ion A - CO, 13.3 %], 233 [M^+ - substituted pyridazinone, 50.9 %, ion B], 123 [ion B - ClC_6H_5, 100 %], 111 [$(ClC_6H_4)^+$, 62.4 %] and 77 [$(C_6H_5)^+$, 63 %].

4-[(4-(3-Chlorophenylazo)-3,5-dimethylpyrazol-1-yl)carbonyl]-5,6-diphenylpyridazin-3(2*H*)-one (9g, $C_{28}H_{21}ClN_6O_2$).

Yellow crystalsin 84 % yield; mp 271 – 272 °C; IR: 3426.7, 3299 and 3196 (NH), 3061.4 ($CH_{arom.}$), 2928.3 ($CH_{aliph.}$), 1724 and 1645.5 (C=O groups), 1587.4 (C=N), 1538.2 (C=C) and 758.2 (Cl-C) cm^{-1}; UV (DMF): λ_{max} (log ε); 267.9 (5.2).

4-[(4-(4-Nitrophenylazo)-3,5-dimethylpyrazol-1-yl)carbonyl]-5,6-diphenylpyridazin-3(2*H*)-one (9h, $C_{28}H_{21}N_7O_4$).

Yellow crystals in 94 % yield; mp 264 - 265 °C; IR: 3443.2 and 3198.4 (NH), 3061.8 ($CH_{arom.}$), 2885.2 ($CH_{aliph.}$), 1732.5 and 1653.6 (C=O groups), 1578.1 (C=N) and 1525.7 and 1341.3 (NO_2 group) cm^{-1}; UV (DMF): λ_{max} (log ε); 267.4 (3.7).

Synthesis of 4-[(4-arylazo-4,5-dihydro-3-methyl-5-oxopyrazol-1-yl)carbonyl]-5,6-diphenylpyridazin-3(2*H*)-one derivatives 10a-h.

General procedure: A mixture of 5,6-diphenyl-2,3-dihydro-3-oxopyridazine-4-carbohydrazide **2** (0.50 g, 1.6 mmole) and the ethyl azobenzeneacetoacetate derivatives **7a-h** (1.6 mmole) was refluxed in ethanol (20 mL) for 6 hours. The reaction mixture was cooled to room temperature and the separated solid was filtered off, washed with diluted ethanol (10 mL), dried and recrystallized from ethanol.

4-[(4-Phenylazo-4,5-dihydro-3-methyl-5-oxopyrazol-1-yl)carbonyl]-5,6-diphenylpyridazin-3(2*H*)-one (10a, $C_{27}H_{20}N_6O_3$).

Yellow crystals in 77 % yield; mp 297 – 298 °C; IR: 3422.4, 3301.6 and 3173.2 (NH), 3057.1 ($CH_{arom.}$), 2930.1 ($CH_{aliph.}$), 1723.4, 1702.5 and 1657.7 (C=O groups), 1598.4 (C=N) and 1545.1 (C=C) cm^{-1}; Ms (m/z): 476 [M^+, 14.1 %], 371 [M^+ - $N{=}NC_6H_5$, 0.3 %, ion A], 275 [ion A - substituted pyrazolone, 100 %, ion B], 247 [ion B - CO, 3.8 %], 299 [M^+ - substituted pyridazinone, 0.9 %, ion C] and 201 [ion C - CO, 0.3 %]; UV (DMF): λ_{max} (log ε); 266.7 (4.1).

4-[(4-(2-Methylphenylazo-4,5-dihydro-3-methyl-5-oxopyrazol-1-yl)carbonyl]-5,6-diphenylpyridazin-3(2*H*)-one (10b, $C_{28}H_{22}N_6O_3$).

Yellow crystals in 75 % yield; mp > 300 °C; IR: 3446.8, 3289.8 and 3179.7 (NH), 3061.6 ($CH_{arom.}$), 2922.7 and 2855.7 ($CH_{aliph.}$), 1713.4, 1690.7 and 1655.7 (C=O groups), 1599.6 (C=N) and 1542.1 (C=C) cm^{-1}; Ms (m/z): 490 [M^+, 75.4 %], 275 [M^+ - substituted pyrazolone, 100 %], 91 [$(CH_2C_6H_5)^+$, 17.9 %] and 77 [$(C_6H_5)^+$, 17.9 %].

4-[(4-(4-Methylphenylazo-4,5-dihydro-3-methyl-5-oxopyrazol-1-yl)carbonyl]-5,6-diphenylpyridazin-3(2*H*)-one (10c, $C_{28}H_{22}N_6O_3$).

Yellow crystals in 81 % yield; mp 283 – 284 °C; IR: 3396.7, 3291.2 and 3179.6 (NH), 3061.9 ($CH_{arom.}$), 2921 and 2856.3 ($CH_{aliph.}$), 1713.7, 1690.9 and 1655.6 (C=O groups), 1600.2 (C=N) and 1541.8 (C=C) cm^{-1}.

4-[(4-(2-Methoxyphenylazo-4,5-dihydro-3-methyl-5-oxopyrazol-1-yl)carbonyl]-5,6-diphenylpyridazin-3(2*H*)-one (10d, $C_{28}H_{22}N_6O_4$).

Yellow crystals in 75 % yield; mp 289 - 290 °C; IR: 3425.3 and 3291 (NH), 3067 ($CH_{arom.}$), 2923.7 ($CH_{aliph.}$), 2852.9 (OCH_3), 1708.6 and 1669.8 (C=O groups), 1604.3 (C=N) and 1541.2 (C=C) cm^{-1}; UV (DMF): λ_{max} (log ε); 266.2 (3.5).

4-[(4-(4-Methoxyphenylazo-4,5-dihydro-3-methyl-5-oxopyrazol-1-yl)carbonyl]-5,6-diphenylpyridazin-3(2*H*)-one (10e, $C_{28}H_{22}N_6O_4$).

Yellow crystals in 78 % yield; mp 281 – 282 °C; IR: 3448.1 and 3193.3 (NH), 3061.3 ($CH_{arom.}$), 2872.2 (OCH_3), 1738.8 and 1648.6 (C=O groups), 1600.3 (C=N) and 1544.4 (C=C) cm^{-1}.

4-[(4-(2-Chlorophenylazo-4,5-dihydro-3-methyl-5-oxopyrazol-1-yl)carbonyl]-5,6-diphenylpyridazin-3(2*H*)-one (10f, $C_{27}H_{19}ClN_6O_3$).

Yellow crystals in 90 % yield; mp 271 – 272 °C; IR: 3416.3 and 3190.1 (NH), 3059.6 ($CH_{arom.}$), 1720, 1685.1 and 1655.4 (C=O groups), 1590.4 (C=N), 1548.8 (C=C) and 751.4 (Cl-C) cm^{-1}; MS (m/z): 511 [M^+, 30.3 %], 275 [M^+ - substituted pyrazolone ring, 100%], 111[$(ClC_6H_4)^+$, 6.4%] and 77 [$(C_6H_5)^+$, 17.5 %].

4-[(4-(3-Chlorophenylazo-4,5-dihydro-3-methyl-5-oxopyrazol-1-yl)carbonyl]-5,6-diphenylpyridazin-3(2*H*)-one (10g, $C_{27}H_{19}ClN_6O_3$).

Yellow crystals in 84 % yield; mp 274 – 276 °C; IR: 3420.8 and 3191.9 (NH), 3060.8 ($CH_{arom.}$), 1720.6, 1685.5 and 1656.3 (C=O groups), 1590.6 (C=N), 1549.7 (C=C) and 751.2 (Cl-C) cm^{-1}; UV (DMF): λ_{max} (log ε); 266.2 (3.5).

4-[(4-(4-Nitrophenylazo-4,5-dihydro-3-methyl-5-oxopyrazol-1-yl)carbonyl]-5,6-diphenylpyridazin-3(2*H*)-one (10h, $C_{27}H_{19}N_7O_5$).

Yellow crystals in 94 % yield; mp > 300 °C; IR: 3414.4 and 3262.3 (NH), 3064.7($CH_{arom.}$), 3027 ($CH_{aliph.}$), 1642.4, 1686 and 1712.3 (C=O groups), 1596.9 (C=N) and 1554 (C=C) 1506.4 and 1332.4 (NO_2) cm^{-1}; Ms (m/z): 398 [M^+ - $NO_2C_6H_4$, 20.2 %], 275 [M^+ - substituted pyrazolone ring, 4.9 %, ion A], 247 [ion A - CO, 3.7 %], 122 [$(NO_2C_6H_4)^+$, 8.2 %] and 77 [$(C_6H_5)^+$, 100 %]; UV (DMF): λ_{max} (log ε); 265.3 (4.1).

Synthesis of 4-[(4-arylazo-3,5-diaminopyrazol-1-yl)carbonyl]-5,6-diphenylpyridazin-3(2*H*)-one derivatives 11a-h.

General procedure: A mixture of 5,6-diphenyl-2,3-dihydro-3-oxopyridazine-4-carbohydrazide **2** (0.50 g, 1.6 mmole) and azobenzenemalononitrile derivatives **8a-h**

(1.6 mmole) was refluxed in ethanol (20 mL) for 6 hours. The reaction mixture was cooled to room temperature and the separated solid was filtered off, washed with diluted ethanol (10 mL), dried and recrystallized from ethanol.

4-[(4-Phenylazo-3,5-diaminopyrazol-1-yl)carbonyl]-5,6-diphenylpyridazin-3(2*H*)-one (11a, $C_{26}H_{20}N_8O_2$).

Yellow crystals in 76 % yield; mp > 300 °C; IR: 3488.8, 3404.1, 3371.6, 3259.1 and 3115.1(NH and NH_2), 1651.8 (C=O) and 1603.6 (C=N) cm^{-1}.

4-[(4-(2-Methylphenylazo)-3,5-diaminopyrazol-1-yl)carbonyl]-5,6-diphenylpyridazin-3(2*H*)-one (11b, $C_{27}H_{22}N_8O_2$).

Yellow crystals in 82 % yield; mp>300 °C;IR: 3440.1 and 3225.3 (NH and NH_2), 2926.7 ($CH_{aliph.}$) and 1600.3 (C=N) cm^{-1}.

4-[(4-(4-Methylphenylazo)-3,5-diaminopyrazol-1-yl)carbonyl]-5,6-diphenylpyridazin-3(2*H*)-one (11c, $C_{27}H_{22}N_8O_2$).

Yellow crystals in 75 % yield; mp >300 °C; IR: 3467.2, 3395.8, 3274.9 and 3127.4 (NH and NH_2), 2916.9 and 2855.4 ($CH_{aliph.}$) and 1609.2 (C=N) cm^{-1}.

4-[(4-(2-Methoxyphenylazo)-3,5-diaminopyrazol-1-yl)carbonyl]-5,6-diphenylpyridazin-3(2*H*)-one (11d, $C_{27}H_{22}N_8O_3$).

Yellow crystals in 91 % yield; mp >300 °C; IR: 3456.3, 3408.7, 3258.5 and 3118.8 (NH and NH_2), 2960 ($CH_{aliph.}$), 2833.2 (OCH_3) and 1597.7 (C=N) cm^{-1}; ^{1}H-NMR (DMSO): δ 9.22 (s, 1H, NH), 7.98 - 6.82 (m, 14H, 3Ph), 3.8 (s, 2H, NH_2-3), 3.4 (s, 2H, NH_2-5) and 3.3 (s, 3H, OCH_3).

4-[(4-(4-Methoxyphenylazo)-3,5-diaminopyrazol-1-yl)carbonyl]-5,6-diphenylpyridazin-3(2*H*)-one (11e, $C_{27}H_{22}N_8O_3$).

Yellow crystals in 85 % yield; mp >300 °C; IR: 3456.7, 3410, 3259.4 and 3120.7 (NH and NH_2), 2960.6 ($CH_{aliph.}$), 2833.6 (OCH_3) and 1597.7 (C=N) cm^{-1}; Ms (m/z): 275 [M^+ - substituted pyrazole ring, 13.1 %], 230 [M^+ - substituted pyridazinone , 2.1 %, ion A], 135 [ion A – diaminopyrazole, 10.6 %] and 107 [$(CH_2OC_6H_4)^+$, 74.6 %].

4-[(4-(2-Chlorophenylazo)-3,5-diaminopyrazol-1-yl)-carbonyl]-5,6-diphenylpyridazin-3(2*H*)-one (11f, $C_{26}H_{19}ClN_8O_2$).

Yellow crystals in 79% yield; mp >300°C; IR: 3466.5, 3389.7, 3271.5 and 3141.3 (NH and NH_2), 2926.4 ($CH_{aliph.}$), 1610.6 (C=N) and 751.5 (Cl-C) cm^{-1}; Ms (m/z): 509 [M^+ - 2, 7.6%], 275 [M^+ - substituted pyrazole, 69.2%], 236 [M^+ - substituted pyridazinone, 21.1%, ion A], 139 [ion A - diaminopyrazole, 10.6%, ion B], 123 [ion A - C_6H_4Cl, 100%, ion C], 111[ion B - N_2, 61.6%] and 95 [ion C - N_2, 25%].

4-[(4-(3-Chlorophenylazo)-3,5-diaminopyrazol-1-yl)carbonyl]-5,6-diphenylpyridazin-3(2*H*)-one (11g, $C_{26}H_{19}ClN_8O_2$).

Yellow crystals in 85% yield; mp 279 - 280°C; IR: 3370.7 and 3244.8 (NH and NH_2), 3050.6 ($CH_{arom.}$), 2925.7 ($CH_{aliph.}$), 1603.1 (C=N) and 766.4 (Cl-C) cm^{-1}; Ms (m/z): 236 [M^+ - substituted pyridazinone, 3.97%, ion A], 139 [ion A - diaminopyrazole, 6.53%, ion B], 123 [ion A - C_6H_4Cl, 9.96%, ion C], 111[ion B - N_2, 34.95%] and 95 [ion C - N_2, 11.10%].

4-[(4-(4-Nitrophenylazo)-3,5-diaminopyrazol-1-yl)carbonyl]-5,6-diphenylpyridazin-3(2*H*)-one (11h, $C_{26}H_{19}N_9O_4$).

Red crystals in 88% yield; mp >300 °C; IR: 3449.8 (NH and NH_2), 2924.7 ($CH_{aliph.}$), and 1609 (C=N) cm^{-1}; Ms (m/z): 275 [M^+ - substituted pyrazole ring, 11.2%], 122 [$(NO_2C_6H_4)^+$, 34.95%].

Dyeing procedure

The required amount of dye (2% shade) was dissolved in DMF and added dropwise with stirring to a solution of Dekol-N (2 g/dm^3), an anionic dispersing agent of BASF, then the dye was precipitated in a fine dispersion ready for use in dyeing.

Dyeing of polyester at 130°C under pressure using Levegal PT (carrier of Buyer)

The dye bath (1:20 liquor ratio), containing 5g/dm^3Levegal PT (Bayer) as carrier, 4% ammonium sulfate, and acetic acid at pH 5.5, was brought to 60°C, the polyester fabric was entered and run for 15 min. The fine dispersion of the dye (2%) was added, and the temperature was raised to boiling within 45 min, dyeing was continued at boiling temperature for about 1 h, and then the dyed material was rinsed and soaped with 2% nonionic detergent to improve rubbing and wet fastness.

Assessment of color fastness (Table 2)

Fastness to washing, perspiration, light, and sublimation was tested according to the reported methods.[11]

Color assessment

Table 1 reports the color parameters of the dyed fabrics assessed by tristimuluscolorimetry. The color parameters of the dyed fabrics were determined using a SPECTRO multichannel photodetector (model MCPD1110A), equipped with a D65 source and barium sulfate as a standard blank. The values of the chromaticity coordinates, luminance factor, and the position of the color in the CIE-LAB color solid are reported.

Conclusions

A set of 24 disperse dyes **9, 10, and 11** were synthesized by reaction of 5,6-diphenyl-2,3-dihydro-3-oxopyridazine-4-carbohydrazide **2** with arylazoacetylacetone, ethyl arylazoacetoacetate and arylazomalononitrile derivatives.

 DOI: 10.17628/ecb.2014.3.745-751

All of them were investigated for their dyeing characteristics on polyester. They give bright intense hues from yellow to pale brown on polyester fabrics, due to the variations in polarity.The dyed fabrics exhibit very good to excellent (4-5) washing, perspiration, sublimation and good (4) rubbing fastness properties (Table 2). The remarkable degree of levelness and brightness after washings is indicative of good penetration and the excellent affinity of these dyes for the fabric due to the accumulation of polar groups. This in combination with the ease of preparation makes them particularly valuable.

References

[1]Part 29, El-Azony K.M., Ei-Mohty A.A., Deeb A. and Khater S.I., *Radiochim. Acta* **2010**, *98*, 1-7.

[2]Witherington, J., Bordas, V., Haigh, D., Hickey, D.M.B., Ife, R.J., Rawlings, A.D., Slingsby, B.P., Smith, D.G., Ward, R.W., *Bioorg. Med. Chem. Lett.*, **2003,** *13*, 1581-1584.

[3]Beswick, P., Bingham, S., Bountra, C., Brown, T., Browning, K., Campbell, I., Chessell, I., Clayton, N., Collins, S., Corfield, J., *Bioorg. Med. Chem. Lett.*, **2004**, *14*, 5445-5448.

[4]Ho, Y.W.,*Dyes and Pigments*, **2005**, *64*, 223.

[5]Deeb, A., Kotb, M., *Heterocycles*, **2004**, *63*, 1143-1151.

[6]Deeb, A., Saad, H., *Heterocycles*, **2003**, *60*, 1873.

[7]Schmidt, P., Druey, J., *Helv. Chim. Acta*, **1954a**,*37*, 134.

[8]Schmidt, P., Druey, J., *Helv. Chim. Acta*, **1954b**, *37*, 1467.

[9]Shawali, A.S., Abdel Galil, F.M., *Tetrahedron*, **1971**, *27*, 4305.

[10]Singh, S.P., Kumar, *Heterocycles*, **1990**, *31*, 855.

[11]Society of Dyes and Colorists Standard methods for the determination of color fastness of textiles and leather,5th edn. Society of Dyes and Colorists, Bradford **1990**.

Received: 25.05.2014.
Accepted: 30.06.2014.

ADSORPTION CHARACTERISTICS OF VICTORIA BLUE ON LOW COST NATURAL SAND AND ITS REMOVAL FROM AQUEOUS MEDIA

Arun Kant[a] and Monika Datta[b]*

Keywords: Victoria blue; natural sand, adsorption isotherm and kinetics.

Triarylmethane dyes have been identified as one of the toxic dyes. The presence of triarylmethane dyes in water act as pollutant and cause hazardous effect on natural resources, aquatic life as well as to human being. Triarylmethane dyes are extensively used for wool, silk, cotton, leather and paper industries. In the present work, natural sand has been utilised as an adsorbent for developing methodology for the removal of these dyes, which does not easily biodegrades in aqueous medium. The adsorption efficiency of natural sand was tested by using Victoria Blue (VB) as model dye. The adsorpion behaviour as a function of the pH of the aqueous dye solution, the contact time, initial concentration of the dye and the amount of adsorbent was studied. All studies were performed at room temperature (298 K). It was observed that under optimized conditions, 91 % of VB can be removed from aqueous media. The adsorption data was fitted well by the Langmuir and Freundlich adsorption isotherm; pseudo-second-order and intraparticle diffusion models were also applied.

*Corresponding Author
E-mail: monikadatta_chem@yahoo.co.in
[a] Department of Chemistry, University of Delhi, Delhi-110007, India. Eail: arun107941@gmail.com
[b] Department of Chemistry, University of Delhi, Delhi-10007, India

INTRODUCTION

The use of dyes in different industries (textile, paper and pulp, tannery, Kraft bleaching industries etc.) introduces a wide variety of organic pollutants into natural water resources, resulting in colored industrial effluents containing high concentration of organic chemicals.[1] The presence of dyes block sunlight, which is essential for many photo-initiated chemical reactions that are necessary for aquatic life.[2-3] Worldwide More than 10,000 textile dyes are commercially available and their annual production is ~7×10^5 metric tons.[4] About 2% of the annual dye production is discharged in the effluent from manufacturing units.[5] In textile industry, 10% of dyes are lost during textile coloration process.[6] Color is one of the most obvious indicators of water pollution, and discharge of highly colored synthetic dyes in the effluent can be damaging to the receiving water bodies.[7]

Due to the low biodegradability of triarylmethane dyes, conventional biological wastewater treatment systems are not very effective. These methods include physicochemical flocculation with Fe(II)/$Ca(OH)_2$, membrane filtration, electrokinetic coagulation, electrochemical destruction, ion exchange, precipitation, ozonation, adsorption etc. However, apart from being costly, these technologies are not very effective for the removal of color.[3] Amongst the numerous techniques available, adsorption is the procedure of choice due to its sludge free clean operation and capability to completely remove different types of coloring materials, even from dilute solutions.[8-9] Of all the available adsorbents, activated carbon has been most widely used for the removal of pollutants from wastewater.[10-11] However, regeneration of the saturated carbon is expensive and is the main reason for the low economic efficiency in its application.

The objective of the work presented in this paper is to examine the adsorption characteristics of a non-biodegradable cationic dye from aqueous solution onto natural sand, which is porous crystalline solid. The structure of sand is given in Figure 1.[12]

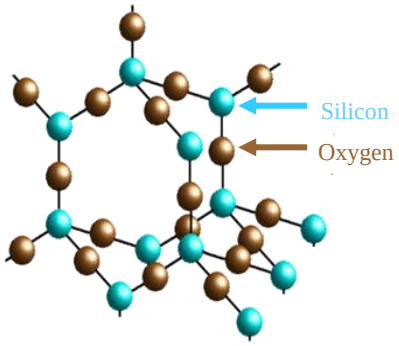

Figure 1. Structure of sand

EXPERIMENTAL

Materials

The sand sample was collected from Chandra Prabha Wildlife Sanctuary, Varanasi, UP, India. After removing stones and other bigger particles the sand was ground and sieved through a 230 mesh sieve.

The dye chosen for such study was the non-biodegradable Victoria Blue (Fig. 2), a basic blue 26 with the C.I. 44045 molecular weight 506.1 and molecular formula $C_{33}H_{32}ClN_3$ was procured from Thomas Baker Chemical Limited Mumbai.

A class of triarylmethane dye and extensively used for dyeing wool, silk and cotton.[15] It is also used for staining in microscopic work.[16] This dye is known to cause strong coloration and toxicity in the waste water and

can produce irritation to eyes and respiratory system.[17] It may even promote tumour growth in some species of fish.[18] Fe and Cu sulphates, analytical grade were procured from Qualigens fine chemicals, Mumbai.

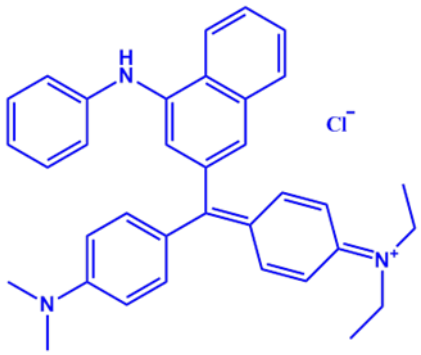

Figure 2. Molecular structure of Victoria blue

Instruments

Electronic absorption spectra were recorded on a Jena Analytik Specord 250 spectrophotometer, X-ray diffraction patterns were recorded on a Philips X' Pert-PRO PMRD (D8 Discover Bruker AXS)system using Cu Kα radiation (n = 1Å), FT-IR spectra were recorded using a Perkin-Elmer FT-IR (BXFTIR). TEM images were recorded using TECNAI G2T30 FEI Instrument operated with an accelerating voltage of 300 KV.

Effect of pH on the absorption behaviour of Victoria blue in aqueous media

The aqueous VB solution though the λ_{max} values remain same (617 nm) but the absolute value of absorbance appears to be ifluenced by the pH of the dye solution.

At higher pH (> 9), color of the dye solution was found to change from blue to wine red and at low pH (< 1), color of the dye solution changed to sky blue.

In case of pH 9 a very broad absorption band with λmax at 555nm was observed. Maximum absorbance was observed between pH 3 to 5 therefore, quantitative estimation of the dye was performed at pH 5, pH of each solution was adjsted using an Elico India – Li120 pH meter with a combined pH electrode. pH meter was calibrated/standardized[17] before every measurement.

Employing the batch extraction method, the adsorption behavior of VB onto natural sand was investigated as a function of (1) the pH of the aqueous dye solution, (2) the contact time of batch extraction method, (3) the initial concentration of the dye solution, and (4) adsorption as a function of metal ions.

Bach experiments were performed using 50 mg of natural sand sample and 25 ml of dye solution at room temperature.Each batch experiment, the supernatant was separated by centrifugation at 8000 rpm for 15 minute using a REMI R24 centrifuge machine. The concentration of the dye in supernatant was estimated spectrophotometrically (Jena Analytik Specord 250 spectrophotometer).

The concentration of unadsorbed dye was determined from the corresponding Beer–Lambert plot. The percentage of the adsorbed VB (φ) onto the natural sand was calculated by using Eqn. (1).

$$\varphi = 100\frac{C_i - C_e}{C_i} \qquad (1)$$

where

C_i is the initial concentration (ppm) of the dye solution and

C_e is the concentration of the dye (ppm) in the supernatant at the equilibrium stage.

The amount of dye adsorbed, q_e (mg g^{-1}), was calculated via the mass-balance relationship shown in equation (2).

$$q_e = \frac{(C_i - C_e)V}{m} \qquad (2)$$

where

V is the volume of the dye solution (ml) and

m is the mass of adsorbent employed (mg).

RESULTS AND DISCUSSION

Adsorption as a function of the pH of the dye solution

In the adsorption process pH of the dye solution plays an important role, particularly on adsorption capacity. This pH study was performed with 25 ml of 20 ppm dye solution. The uptake of VB onto natural sand sample at pH 7 and 7.5 exhibited 79.5 % and 79 % uptake respectively which decreased up to 74.5 at pH8. However, the percent uptake was much less at pH 2 showing only 58.5 % uptakes (Figure 3). Adsorption of VB at pH < 7 is low, may be because of the fact that the negative charge on sand tends to get saturated by protons[18-19] in acidic media as making H^+ ions compete effectively with cationic dye causing a decrease in the adsorption of dye on the surface of the sand.

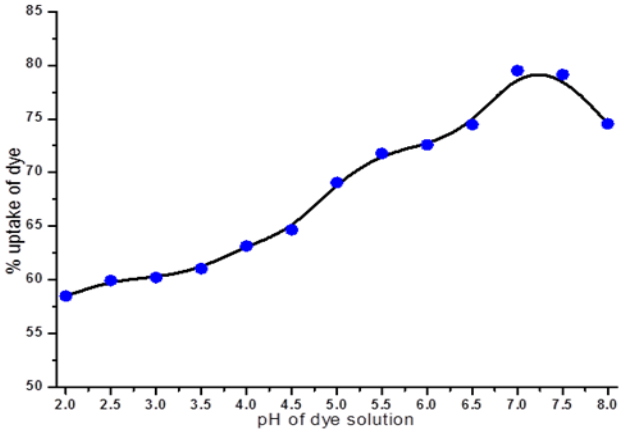

Figure 3. Effect of pH on the percentage uptake of VB by sand.

Every batch experiment was perform at pH 7 but after centrifugation the pH of supernatent was adjusted at pH 5, because maximum absorbance value of dye was observe at pH 5.

Adsorption as a function of contact time

81 % of the VB is extracted within 90 minutes at pH 7. This study was performed with 25 ml of 20 ppm dye solution. The maximum uptake was 91 % (Fig. 4) which was attained within 270 minutes and it remained constant up to 300 minutes.

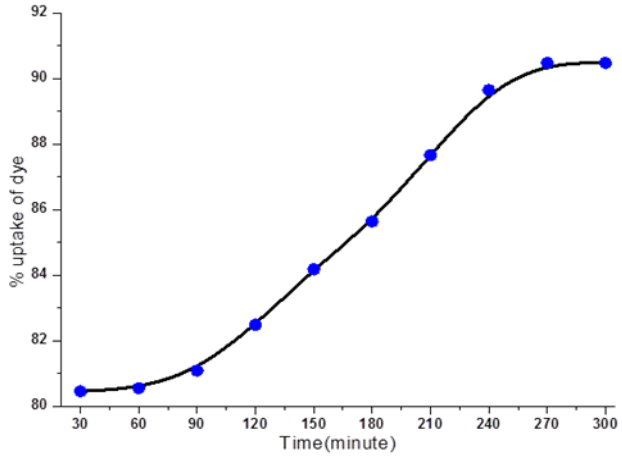

Figure 4. Effect of contact time on the percentage uptake of VB by sand

Adsorption as a function of initial concentration of the dye

Percentage uptake of VB on natural sand was found to decrease gradually at higher concentration. However, the uptake of dye (mg g^{-1}) with increasing concentration of dye (Fig. 5).

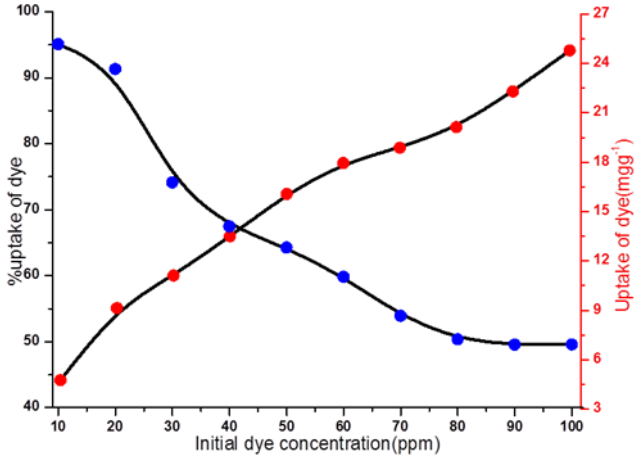

Figure 5. Effect of the initial dye concentration on the percentage uptake of VB by sand.

The percentage uptake of dye and efficiency of sand in mg g^{-1} sand is given in Table 1.

Table 1. Adsorption of VB as a function of initial dye concentration

Adsorbent	Variation in concentration of VB			Amount of VB adsorbed on sand	
	S. No.	ppm	(µg)	%	mg g^{-1}
50 mg	01	10	(250)	95.07	4.75
	02	20	(500)	91.30	9.13
	03	30	(750)	74.12	11.12
	04	40	(1000)	67.46	13.49
	05	50	(1250)	64.26	16.07
	06	60	(1500)	59.80	17.94
	07	70	(1750)	53.91	18.87
	08	80	(2000)	50.33	20.13
	09	90	(2250)	49.55	22.29
	10	100	(2500)	49.57	24.79

Adsorption as a function of metal ions concentration

The percent uptake of dye without metal ion was found 91 %. In the presence of Cu^{2+} and Fe^{2+} the percent uptake of dye on sand decreases with increase in cocentration of metal ions in solution (Fig. 6).

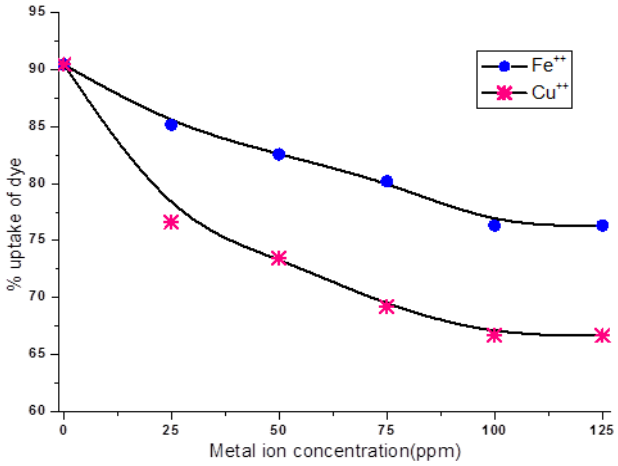

Figure 6. Effect of Fe^{2+} and Cu^{2+}ions on the percentage uptake of VB.

This is in agreement with the previous study mentioned in the literature (In the presence of trace metal ions i.e. Cd^{2+}, Mn^{2+}, Pb^{2+}, Fe^{2+}, Zn^{2+} and Ni^{2+} the adsorption capacity of dyes onto the sand surface decreases[20] because of the preferential adsorption of these metal ions onto the active sight of the sand).

Freundlich adsorption isotherm

This is commonly used to describe the adsorption characteristics of the heterogeneous surface.[21] These data often fit the empirical equation (3) proposed by Freundlich:

$$q_e = K_f C_e^{1/n} \quad (3)$$

where

K_f = Freundlich isotherm constant (mg g^{-1}),

n = adsorption intensity,

C_e=the equilibrium concentration of adsorbate (mg L^{-1}),

q_e = the amount of metal adsorbed per gram of the adsorbent at equilibrium (mg g^{-1}).

Linearizing equation 3, gives Eqn. (4):

$$\log q_e = \log K_f + \frac{1}{n}\log C_e \qquad (4)$$

The plot of logq_e versus log C_e was linear (Fig. 8), with a slope equal to 1/n and an intercept equal to logK_f. The correlation coefficient, R^2, and the values of q_{max} and K_L for sand is showed in Table 2.

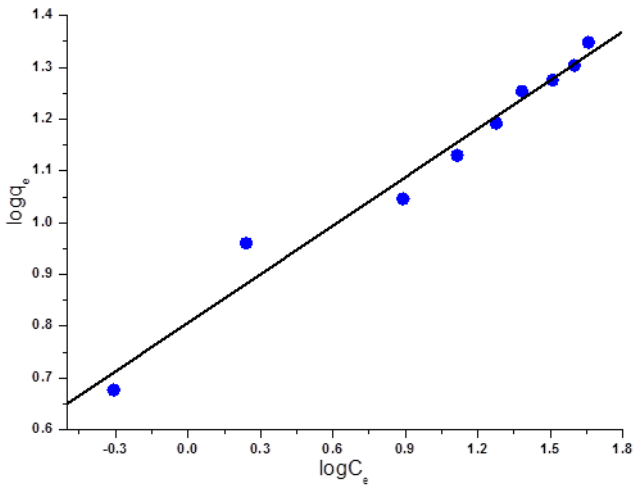

Figure 7. Freundlich adsorption isotherm

The constant K_f is an approximate indicator of adsorption capacity, while 1/n is a function of the strength of adsorption in the adsorption process.[22] If n=1 then the partition between the two phases is independent of the concentration. If a value of 1/n is below one it indicates a normal adsorption. On the other hand, 1/n being above one indicates cooperative adsorption.[23]

This expression reduces to a linear adsorption isotherm when 1/n = 1. If n lies between 1 to 10, this indicates a favorable adsorption process.[24] From the parameters obtained as in table 2, a value of 1/n = 0.3127 while n=3.198 indicates that the adsorption of VB onto the sand is favorable.

Langmuir adsorption isotherm

This describes quantitatively the formation of a monolayer adsorbate on the outer surface of the adsorbent, and after that no further adsorption takes place. Thereby, the Langmuir represents the equilibrium distribution of VB ions between the solid and liquid phases.[25] The Langmuir isotherm is valid for monolayer adsorption onto a surface containing a finite number of identical sites.

The model assumes uniform energies of adsorption onto the surface and no transmigration of the adsorbate in the plane of the surface.

Based upon these assumptions, the Langmuir isotherm equation may be expressed in a linearized form as shown in equation (5):

$$\frac{C_e}{q_e} = \frac{1}{q_{max}K_L} + \frac{C_e}{q_{max}} \qquad (5)$$

where

q_{max} is the monolayer capacity of the adsorbent (mg g^{-1})

and K_L is the Langmuir adsorption constant (dm^3 mg^{-1}).

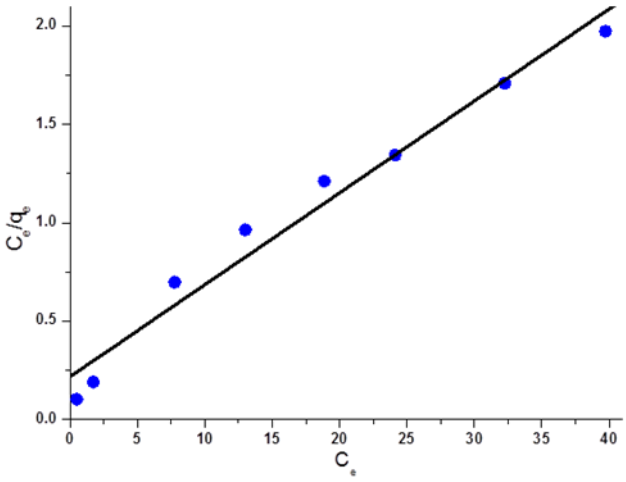

Figure 8. Langmuir adsorption isotherm

The plot of C_e/q_e versus C_e was linear (Fig. 8), with a slope equal to $1/q_{max}$ and an intercept equal to $1/(q_{max}K_L)$.The correlation coefficient, R^2, and the values of q_{max} and K_L for sand sample studied are listed in Table 2.

The R^2 value of 0.988 for sand sample indicates that the adsorption of VB onto sand sample is well fitted by the Langmuir isotherm.

Table 2. Freundlich constants for the adsorption of VB onto the sand sample.

Adsorbent	Freundlich isotherm constants			
	1/*n*	*n*	K_f (mg g^{-1})	R^2
Sand	0.313	3.198	6.408	0.971

Table 3. Langmuir constants for the adsorption of VB onto the sand sample.

Adsorbent	Langmuir isotherm constants		
	q_{max} (mg g^{-1})	K_L (dm^3mg^{-1})	R^2
Sand	2.371	2.719	0.988

The essential characteristics of the Langmuir equation can be expressed in terms of a dimensionless constant which is called equilibrium parameter defined as:

$$R_L = \frac{1}{1+K_L C_i} \quad (6)$$

where

K_L is the Langmuir constant was found, which is used to determine the enthalpy of adsorption, and

C_i is the highest initial dye concentration employed.

The value of R_L was found 0.00368 it indicates whether the type of isotherm observed is unfavorable (R_L>1), linear (R_L=1) or favorable (R_L<1).[26] The R_L values are listed in Table 3 along with the other Langmuir constants. For all the adsorption studies of Victoria blue dye onto sand, the R_L values were in the range $0<R_L<1$, indicating that the adsorption process was favourable.

Adsorption kinetics

Several kinetic models are available to understand the behavior of the adsorbent and also to examine the controlling mechanism of the adsorption process and to test the experimental data. In the present investigation, the adsorption data were analyzed using three kinetic models, the pseudo-first-order, pseudo-second-order kinetic and the intraparticle diffusion models.

The pseudo-first-order model was presented by Lagergren.[27] The Lagergren's first-order reaction model is expressed in linear form as Eqn. (7):

$$\log(q_e - q_t) = \log q_e - \frac{K_1}{2.303} t \quad (7)$$

where

q_e and q_t are the amounts of VB dye (mg g^{-1}) adsorbed on the sand at equilibrium, and at time t, respectively and

K_1 is the rate constant (min^{-1}) of the pseudo-first-order adsorption process.

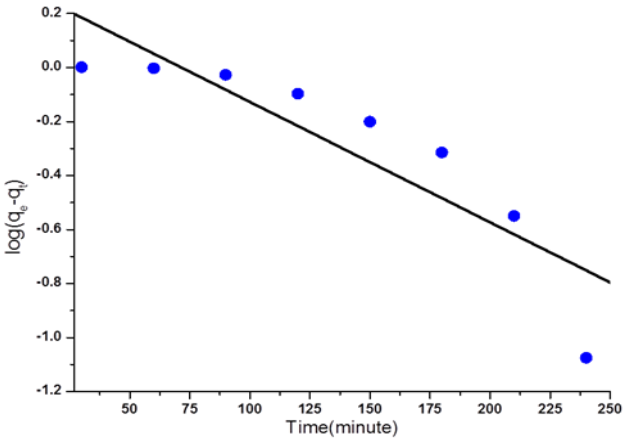

Figure 9. Pseudo-first-order kinetic model for the adsorption of VB onto sand sample.

The plot of $\log(q_e - q_t)$ versus t would be linear with a slope of $-K_1/2.303$ and an intercept of $\log q_e$ (Fig. 9).

The adsorption data was also analysed in terms of pseudo-second-order mechanism, described by Ho and McKay.[28] The linear form of the Eqn. (8) as follows:

$$\frac{t}{q_t} = \frac{1}{K_2 q_e^2} + \frac{1}{q_e} t \quad (8)$$

where K_2 is the rate constant of pseudo-second-order adsorption (g mg^{-1} min^{-1}), $K_2 q_e^2$ is the initial rate of adsorption (mg g^{-1} min^{-1}). The plot of t/q_t against t of Eqn. (8) should give a linear relationship with a slope of $1/q_e$ and an intercept of $1/K_2 q_e^2$(Fig. 11).

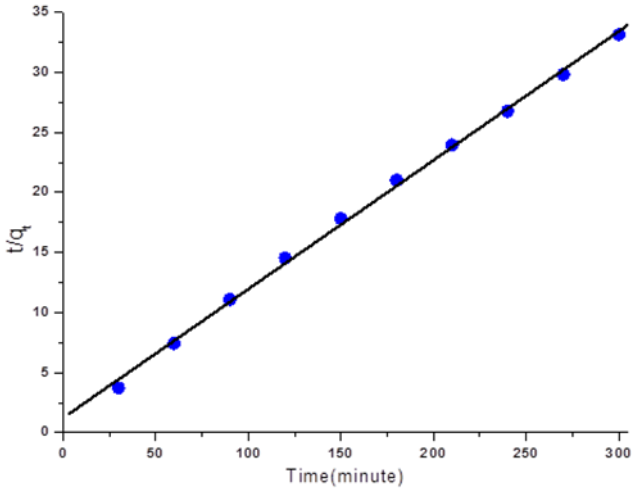

Figure 10. Pseudo-second-order kinetic model for the adsorption of VB onto sand sample.

The plot of q_t against $t^{1/2}$ of Equation (9) should give a linear relationship with a slope of K_d and an intercept of C (Fig. 10).where q_t is the amount of dye adsorbed (mg g^{-1}) at time t, K_d (mg g^{-1} min$^{0.5}$) is the rate constant for intraparticle diffusion.

The intraparticle diffusion plots for the effect of temperature on the adsorption of VB onto sand sample. In adsorption systems where there is the possibility of intraparticle diffusion being the rate-limiting step, the intraparticle diffusion approach described by Weber and Morris is used.[29]

$$q_t = K_d t^{1/2} + C \quad (9)$$

The R^2 value was 0.9998 for sand indicates that the adsorption of VB onto these adsorbents was well fitted by the intraparticle diffusion (Table 4c). The K_d for sand is 0.13423 and intercept of C is 7.8099 was calculated by using Eqn. 9.

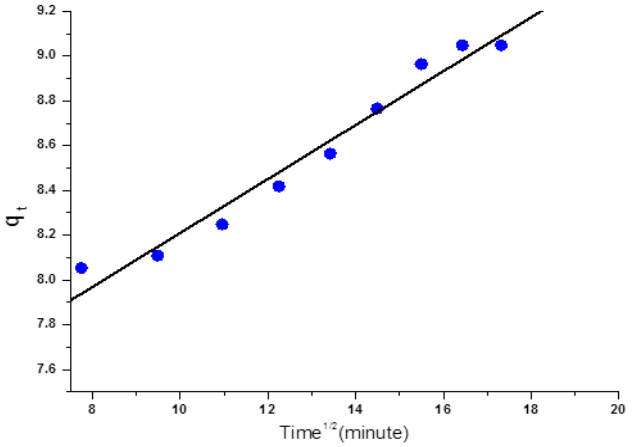

Figure 11. Intraparticle Diffusion model for the adsorption of VB onto sand sample.

Table 4a. Parameters of the fitted kinetic of Pseudo-first-order mode for thesand.

Adsorbent	Pseudo-first-order model		
	K_1 (min^{-1})	q_e (mg g^{-1})	R^2
Sand	0.010364	2.084	0.7781

Table 4b. Parameters of the fitted kinetic of Pseudo-second-order model for the sand.

Adsorbent	Pseudo-second-order model		
	K_2 [g mg^{-1} min^{-1}]	q_e (mg g^{-1})	R^2
Sand	0.00939	9.3197	0.9982

Table 4c. Parameters of the fitted kinetic of Intraparticle diffusion model for the sand

Adsorbent	Intraparticle diffusion		
	K_d	C	R^2
Sand	0.13423	7.8099	0.9998

Table 4a, 4b and 4c represents the equilibrium sorption capacity (q_e), the correlation coefficient, R^2, and the rate constants for the pseudo-first-order (K_1) and pseudo-second-order (K_2) models. The data demonstrate good compliance with pseudo-second-order rate law rather than the pseudo-first-order rate law. This shows that the pseudo-second-order kinetic model show a better explanation of the kinetic adsorption data obtained in the present study. This was probably true in the present case sand is negatively in nature which attracts the positively charged dye charged. This would allow electrostatic interaction between the positively VB dye and the sand surface.

XRD analysis

Before recording XRD patterns sand sample was kept it in double distilled water for 24 hours and was washed with double distilled water followed by centrifugation at ~ 8000 rpm for 10 minutes. The supernatent was rejected and the residue was dried in the oven at 100 ºC, for 24 h. XRD pattern of the sand sample shows sharp peaks indicating its crystalline nature as the presence of silica as its constitutents.

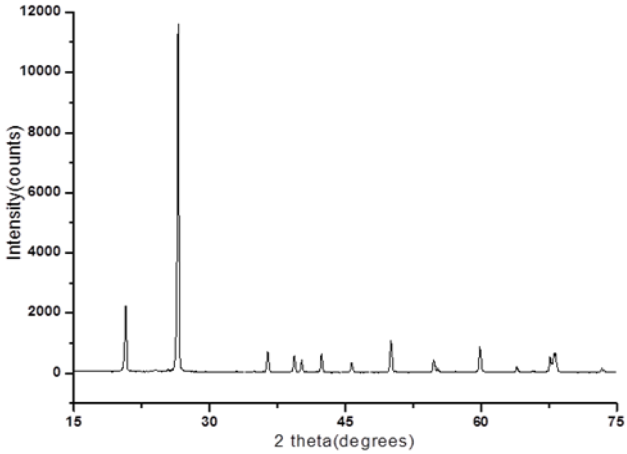

Figure 12a. XRD patterns of sand

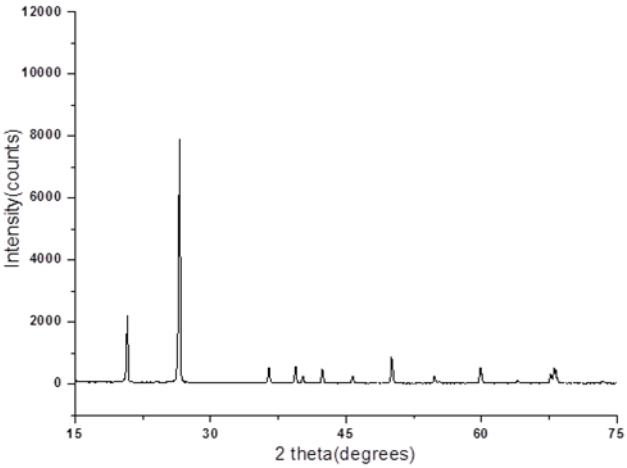

Figure 12b. XRD patterns of VB adsorbed sand

In the XRD analysis of sand sample and VB adsorbed sand sample (Figs. 12a and 12b), a slightly different in intensity (counts) curves. This is because of the dye adsorb on sand surface and made a layer around the sand surface.

FT-IR spectroscopic studies

FT-IR spectra of sand, washed sand, VB adsorbed sand and VB was recorded over the 500–4000 cm^{-1} wavenumber region and represented it in two parts (Figs. 13a and 13b). In the FT-IR spectrum of VB, secondary amines (Ar_2NH) show only a single weak band in the 3300-3000 cm^{-1} region, since they have only one N–H bond. Tertiary amines (Ar_3N) do not show any band in this region since they do not have N–H bond and the bands in the region 3100 – 3040 cm^{-1} exhibit aromatic C-H stretching vibrations. The C–N stretching frequency[30] appears at 1289 cm^{-1} due to the aromatic nature of the VB dye. While the C–C stretching band of the aromatic ring was observed at 1584 cm^{-1}. There is no any substantial difference in the FTIR spectrum of natural sand and washed sand. The absorption band at 1105 cm^{-1} indicate silicon sulfide (Si–S stretching), the one at 1010 cm^{-1}correspond to Si–O, 1049 cm^{-1}has been assigned to Si–O stretching peak[31], The characteristics IR absorption band in both case sand and VB adsorbed sand the presence of 3442 cm^{-1}, 1584 cm^{-1} and1289 cm^{-1} indicates VB dye adsorbed on the sand surface.

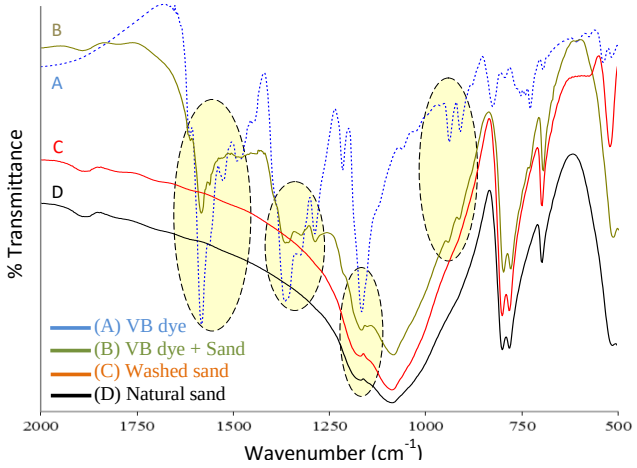

Figure 13a. FT-IR spectra of VB + sand (B), VB (A), washed sand (C) and sand (D).

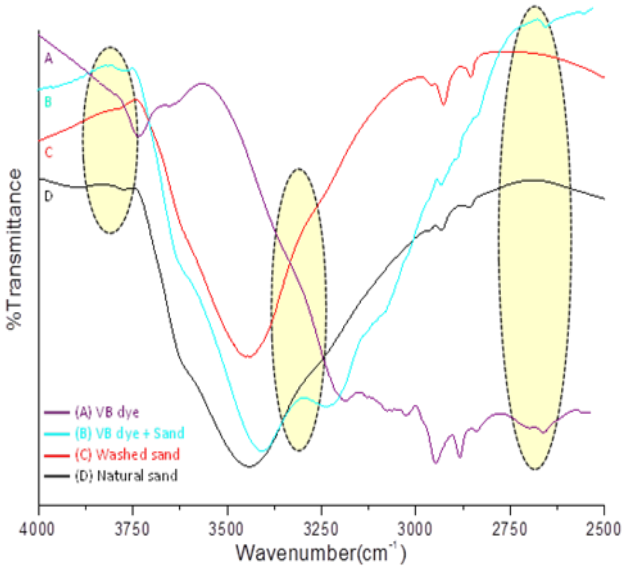

Figure 13b. FT-IR spectra of VB (A), VB + sand (B), washed sand (C) and sand (D).

Transmission electron microscopic studies

The samples were prepared by depositing the aqueous suspensions of the sand samples on a carbon film attached to a 400 mesh Cu grid.

The high resolution transmission electron microscopic images of sand sample (Fig. 14) show the layerand pellets like structure and particles of 100 nm in size (A) which is vanished due to deposition of VB around the sand surfaces and change into rough granular smoke like structure and particles of 100 nm in size (C).

The diffraction pattern of sand (B) shows white granular spotted circling in a continuous way of the TEM image; it indicates sand is crystalline in nature.

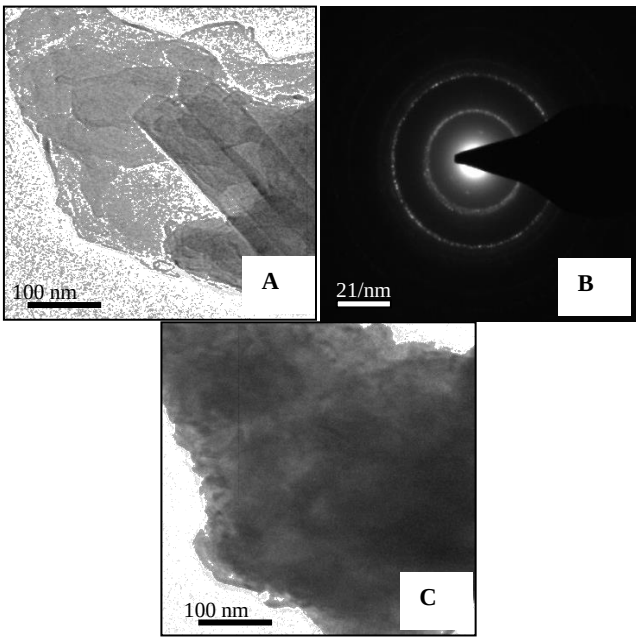

Figure 14. TEM images of sand (A), diffraction pattern of TEM image of the sand (B) TEM image of VB adsorbed sand (C).

The adsorption mechanism

The mechanism of adsorptive removal of VB dye by sand sampl is shown in Fig. 15. The sand molecule composed of oxygen atoms carries a partial negative charge while Victoria Blue dye beaing cationic in nature carries a partial positive charge on nitrogen atom. Thus there occure an electrostatic interaction[32] between the negatively charged sand and positively charged charged dye.

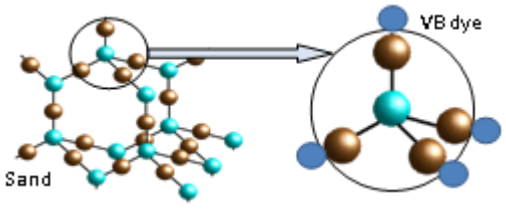

Figure 15. Electrostatic interaction between sand surface and VB dye

CONCLUSION

Sand has negatively charged surface and imparts electrostatic attraction towards cationic dye. Maximum 91% of Victoria Blue dye was removed. For the present sand sample, which was collected fromChandra Prabha Wildlife Sanctuary, Varanasi, UP, India, the active component was related to tridymite, cristobalite, a negatively charged mineral that imparts electrostatic attraction towards cationic dye. The adsorption data for VB investigated in this work fitted well to Langmuir adsorption isotherm equation and pseudo-second-order kinetic model.

The present study indicates that natural sand sample is a good low cost adsorbent moreover which can be used for the removal of VB dye from aqueous solution. Beautifully colored dye adsorbed sand thus recovered may be further used as a colorant in various application.

ACKNOWLEDGEMENTS

The authors are grateful to the Head of the Department of Chemistry and the Director of the University Science Instrumentation Centre (USIC) of the University of Delhi for providing the necessary laboratory facilities and thanks to CSIR for providing Junior Research Fellowship.

REFERENCES

[1] Muhammad, A. R., Shehadeh,I., Ahmed, A. and Ahmed Al-Zamly, *Engineering and Technology*, **2009**, *9*, 7-26.

[2] Robinson, T., McMullan, G., Marchant, R. and Nigam, P., *Biores. Technol*. **2001**, *77*, 247–255.

[3] Banat, I. M., Nigam, P. and Marchant, R., *Biores.Tech*., **1996**, *58*, 217–227.

[4] McMullan, G., Meehan, C., Conneely, A., Kirby, N., Robinson, T., Nigam, P., Banat, I. M., *Appl. Microbiol. Biotechnol*. **2001**, *56*, 81- 87.

[5] Easton, J. R., Cooper P., *Society of dyers and colourists*, **1995**, 9-21.

[6] Pearce, C. I., Lioyd, J.R. and Guthrie, J. T., *A review, Dyes Pigments*, **2003**, *58*, 179-196.

[7] Nigam, P., Banat, I., Singh, D. and Marchant, R., *Process Biochem*, **1996**, *31*, 435–442.

[8] Jain, A. K., Gupta, V. K., Bhatnagar, A. and Suhas, *J. Hazard Mater*, **2003**, *101*, 31–42.

[9] HO, K. Y., McKay, G. and Yeung, K. L., *Langmuir*, **2003**, *19*, 3019-3024.

[10] Ramakrishna, K. R., and Viraraghavan, T., *Waste Management*, **1997**, *17(8)*, 483-488.

[11]Babel, S. and Kurniawan, T. A., *Journal Hazard Mater*, **2003**, *97*, *(1-3)*, 219-243.

[12]http://www.green-planet-solar-energy.com/silicon-element-facts.html

[13] Ayed, L., Chaieb, K., Cheref, A. and Bakhrouf, A., *Desalination*, **2010**, *260*, 137-146.

[14] Kowaltowski, A. J., Turin, J., Indig, G. L. and Vercesi, A. E., *J. Bioenerg Biomembr*, **1999**, *6*, 581-590.

[15] Schulte, E. and Wittekind, D., *Histochemistry*, **1988**, *88*, 427-433.

[16]Cho, B. P., Yang, T., Blankenship, L. R., Moody, J. D., Churchwell, M., Beland, F. A. and Culp, S., *J. Chem. Res. Toxicol*., **2003**, *3*, 285-294.

[17] Delory, G. E. And King, E. J., *Biochem J*., **1945**, 39, 245.

[18]Canan, V., Vlasoula, B., Mahmut, K., Numan, B., Ilker, O., Panagiotis, L., Gerasimos, L. and Siddik, I., *Journal of Hazardous Materials*, **2009**, *170*, 27-34.

[19]Chih-Huang Weng and Yi-Fong Pan., *Journal of Hazardous Materials*, **2007**, *144*, 355–362.

[20] Khan, M. N. and Uzma, Z., *Journal of Hazardous Materials*, **2006**, *133*, 269-275.

[21] Hutson, N. D. and Yang, R. T., *J. Colloid Interf Sci*., **2000**, 189.

[22]Voudrias, E., Fytianos, F. and Bozani, E., *The Int. J*. **2002**, *4(1)*, 75-83.

[23]S. Mohan and Karthikeyan, *J., Environ. Pollut*., **1997**, *97*, 183-187.

[24]Goldberg, S., *Soil Science Society of America, Chemical Processes in Soils. SSSA Book Series*, no. 8.**2005**.

[25]Vermeulan, T. H., Vermeulan, K. R., and Hall, L. C., *Ind. Eng. Chem.* **1966**, *5*, 212–223.

[26] Koswojo, R., Utomo, R. P., Y.-H. Ju, Ayucitra, A., Soetaredjo, F. E., Sunarso, J. and Ismadji, S., *Applied Clay Science*, **2010**, *48*, 81-86.

[27] Lagergren, S., *Handlingar*, **1898**, *24 (4)*, 1–39.

[28] Ho, Y. S., and McKay, G., *J. Environ. Sci. Health Part A-Toxic/Hazard. Subst. Environ. Eng*. **1999**, *34*, 1179–1204.

[29] Weber, W. J. and Morris, J. C., *Eng. Div. proceed. Am. Soc. Civil. Eng*. **1963**, *89*, 31–60.

[30] Satheesh, B. S., Mohandass, C., Vijay Raj, A. S., Rajasabapathy, R. and Mohan, A. D., *Water Air Soil Pollut*., **2013**, *224(4)*, 1500-1522.

[31] Kaur, M. and Datta, M., *Adsorption Science & Technology*, **2011**, *29 (3)*, 301-318.

[32] Ajmal, M., Rao, R. A. K., Ahmad, R., Ahmad, J. and Rao, L. A. K., *Journal of Hazardous Materials*, **2001**, *87*, 127–137.

Received: 03.04.2014.
Accepted: 30.06.2014.

ASSESSMENT AND EXAMINATION OF MINERAL ELEMENTS IN APRICOT (*PRUNUS ARMENIACA* L.) CULTIVARS: A SPECIAL ATTENTION TO SELENIUM AND OTHER ESSENTIAL ELEMENTS

Anita Gergely[a], Nóra Papp[a], Éva Stefanovits-Bányai[a], Attila Hegedűs[b*], Mária Rábai[c] and Klára Szentmihályi[c]

Keywords: mineral elements, apricots, inductively coupled plasma optical emission spectrometry.

The climatic conditions of some regions of Hungary provide great opportunity for apricot cultivation. A majority of apricot fruit is harvested in the northern part of the country. The most important traditional cultivars include 'Gönci magyar kajszi', 'Ceglédi óriás' and 'Bergeron'. The element content of six different apricot cultivars ('Goldrich', 'Ceglédi óriás', 'Aurora', 'Gönci Magyar kajszi', 'Magyar kajszi C.235' and 'Orange Red') was examined in this study. The total element content was measured by Inductively Coupled Plasma Optical Emission Spectrometry (ICP-OES). Selenium content was determined by polarography. From geographical point of view there is a wide variation in the selenium content of fruits. Apricot cultivars show great variations in element contents. It was determined that apricot contains a low quantity from most elements and daily requirements may not be covered by consumption of 300 g fresh apricot. Although they might be good sources of some essential elements. On the basis of RDA and DRI each examined apricot cultivar proved to be a good source of potassium; 'Gönci Magyar kajszi' and 'Ceglédi óriás' for manganese, 'Aurora' for manganese, potassium and copper. 'Aurora' fruits contain the most appreciable element concentrations (Ca, Fe, K, Mg, Na and S). An excellent content of potassium (ranged from 2127 to 4175 mg kg^{-1} fresh weight) was observed in fruits of all tested cultivars. Although non-essential elements such as B and Al were also present in multiple DRI quantities in samples.

* Corresponding Authors
Fax: +36-1-482-6343
E-Mail: hegedus.attila@uni-corvinus.hu
[a] Corvinus University of Budapest, Department of Applied Chemistry, H-1118 Budapest, POBox 53, Hungary
[b] Corvinus University of Budapest, Department of Genetics and Plant Breeding, H-1118 Budapest, POBox 53, Hungary
[c] Institute of Materials and Environmental Chemistry, Research Centre for Natural Sciences of the HAS, H-1119 Budapest, POBox 286, Hungary

Introduction

A sum of 3 900 828 Mt apricot (*Prunus armeniaca* L.) fruit production was noticed all over the world in 2011.[1] In Hungary alone, it was 24 766 t in 2011, although this value was reduced to only 10 800 t in 2012[2]. Most apricot varieties are harvested in the region of Northern Hungary.[3] Because of large cultivation and production of apricot, Gönc city has a special attention in northern region of the country.[4] In Hungary, 'Gönci magyar kajszi' cultivar was produced in the 20 % of orchards and it was followed by 'Ceglédi óriás' and 'Bergeron' each with 11 % share respectively in 2012.[5]

Like other fruits apricot has a beneficial effect on human health and constitutes a rich source of minerals including potassium, iron, zinc, magnesium, manganese and selenium. Iron is a trace element and it has an important role as a core ion in haemoglobin while zinc is reported as a coenzyme for over 200 enzymes involved in body immunity systems.[6] Magnesium has an important role in the nervous system stability, muscle contraction and as an activator of alkaline phosphatase.[7] Manganese is a component of arginase and superoxide dismutase and plays a role as co-factor of certain enzymes.[7] Selenium has an important role as a part of glutathione peroxidase, which was the first described seleno`enzyme, which has also been identified as a cellular antioxidant.[8,9] Because of the increased applications of fertilizers and other chemicals the heavy metal pollution may cause problems in the human body. However, according to previous reports hazardous element (As, Cd, Hg, Pb) contents of nine apricot cultivars in Hungary were found to be lower than in apricots of other countries, and hence the daily intake of fresh and dry apricot may not cause serious health problems.[10]

Apricot is rich in polyphenols, carotenoids and vitamins, such as vitamin C.[8, 11] Half of the carotenoids (about 50 % of total available carotenoids) is β-carotene, which is followed by β-cryptoxanthin and γ-carotene.[12, 13] It is well known fact that the protective effects of natural antioxidants in fruits and vegetables are associated with vitamins, phenolics and carotenoids.[14]

Apricot is one of the most widely processed fruits in Hungary too. End users and consumers can have the benefit of the fresh fruit in a short period of the year with various forms of processed apricot like canned, frozen, jam, dried, juice or puree.[15] Almost the half of the world's total dried apricots is produced in Turkey. These fruits are pre-treated with SO_2 and then sun-dried to have moisture content of 23-28 %.[15] Apricot kernel is used in the production of cosmetics, oil, activated carbon, benzaldehyde and aroma perfume.[16]

The main aim of the present research article was to evaluate and assessment of the element content, especially the selenium content, which is one of the least studied elements, in fruits of six apricot cultivars.

Materials and methods

Fruits of six different apricot (*Prunus armeniaca* L.) cultivars ('Goldrich', 'Ceglédi óriás', 'Aurora', 'Gönci Magyar kajszi', 'Magyar kajszi C.235' and 'Orange Red') were collected in the germplasm collection of Department of Genetics and Plant Breeding, Corvinus University of Budapest.

Each apricot fruit (peel and flesh together) was lyophilized (ScanVac lyophilizer, Denmark). The freeze-dried fruit samples (0.5 g) were digested in a mixture of 5 mL HNO_3 (65 %) and 2 mL H_2O_2 (30 %) in Thermoreactor (VELP-ECO 6). The digested samples were diluted with double-distilled water to 25 mL. Element concentrations (Al, B, Ba, Ca, Cu, Fe, K, Li, Mg, Mn, Na, P, S, Si, Sr, Ti and Zn) in apricot fruit samples were determined by inductively coupled plasma optical emission spectrometry (ICP-OES). Type of instrument is Spectro Genesis ICP-OES (Kleve, Germany).[17,18] In the study, lyophilized samples were used and each quantity was expressed in fresh weight.

Selenium measurement was carried out with polarographic method (MDE 150 polarograph) using lyophilized fruite samples (0.5 g) which were digested in a mixture of 3 mL HNO_3 (65 %), 3 mL HCl (37%) and 2 mL H_2O_2 (30 %) and diluted with bidistilled water to 10 mL.[19]

Statistical analysis

In order to determine the statistical analysis, the SPSS 13.0 (SPSS Inc., Chicago, USA) program was used. In each case the evaluation was preceded by normality and homogenity tests. One way analysis of variance (ANOVA) was used for identifying the deviation within groups for equal variances or Welch test was used for unequal variances. The significance level was determined at 5 %.

Results

The element concentration in fresh fruit of six apricot cultivars are shown in Table 1. The concentrations of As, Co, Cd, Cr, Mo, Ni, Sn, Pb and V were under the detection limit; therefore, these elements are not shown in the table. Potassium was the most abundant mineral in apricot. In our study, the range of potassium content varied between 2127 ('Orange Red') and 4175 mg kg^{-1} ('Aurora'), further, it is followed by phosphorus, calcium and magnesium. 'Aurora' has the highest content of Ca (187.10 mg kg^{-1}) and Mg (160.74 mg kg^{-1}), which was approximately the double of the content found to be in 'Gönci Magyar kajszi' and 'Ceglédi óriás'. The content of Fe and Zn varied from 1.95-3.40 and 0.72-2.12 mg kg^{-1}. The concentrations of these two essential elements were the highest in 'Aurora' (3.40 and 2.12 mg kg^{-1}). The concentration of Mg and Mn varied from 88.79 to 160.74 and from 0.77 to 1.44 mg kg^{-1} in fresh weight, respectively. 'Gönci Magyar kajszi' had the highest content of manganese.

Fruits of the six apricot cultivars contained a low amount of selenium ranging from 0.003 to 0.005 mg kg^{-1} fresh weight. The highest content of selenium was measured in 'Orange Red', 'Ceglédi óriás' and 'Magyar kajszi C.235'. According to previous studies on different Turkish apricot cultivars, selenium content ranged between 0.1 and 0.2 mg kg^{-1} in fresh weight so this fruit can be considered as a rich source of selenium.[8] Although in our study the selenium content of six cultivars remained below the range compared to Turkish apricots. This may be explained by the general poor selenium content of the Carpathian basin soils.[20]

According to these results significant variations were observed among all tested cultivars except in the cases of boron and iron. It is also to be mentioned here that the lowest iron content was found in 'Gönci Magyar kajszi'. In respect of boron and iron contents the cultivars were similar.

Discussion

Fruits of the 'Aurora' apricot cultivar had the highest average element content. Even than by consuming 300 g apricot per day (this amount is equivalent to about seven pieces of medium-sized apricot), the daily requirement will not be covered for some metal ions. Although apricot can be a good source of some elements, which reach at least 15 % of the Recommended Dietary Allowances (RDA) or Dietary Reference Intake (DRI).[21, 22]

Based on the RDA values and taking into consideration consumption of 300 g apricot, 'Goldrich', 'Orange Red', 'Gönci Magyar kajszi', 'Aurora', 'Ceglédi óriás' and 'Magyar kajszi C.235' may be considered as good sources (33.1 %, 32 %, 43.1 %, 62.6 %, 43.7 % and 36.0 % of the daily need) of potassium (RDA value: 2000 mg day^{-1}/ adult of 70 kg). Our study shows that 'Gönci Magyar kajszi', 'Aurora' and 'Ceglédi óriás' apricot cultivars also seem to be good sources (21.6 %, 20.1 % and 18.0 % of the daily need) of manganese (RDA value: 2 mg day^{-1}/ adult of 70 kg). It should be also mentioned that 'Aurora' contains sufficient quantities of copper (31.8 % of the daily need, RDA value: 1 mg day^{-1}).

The intake of non-essential elements is relatively low, although aluminium intake in case of 'Aurora' and 'Magyar kajszi C.235', which contains 38.5-50.9 % and 28.4-37.6 % of DRI (DRI value between: 3.1-4.1 mg day^{-1}/adult of 70 kg), is relatively high but it has to be mentioned that other cultivars may also accumulate high quantity of aluminium. 'Gönci Magyar kajszi', which contains the least aluminium, is also abundant in aspect of this non-essential element (17.6-23.2 % of the daily need). Boron contents in fruits of each apricot cultivar may result in the consumption of multiple amounts of the recommended intake. In the case of 'Aurora' containing the least boron, the intake is 204.4 % (DRI value: 0.96 mg day^{-1}/adult of 70 kg). According to previous reports the major minerals of the apricot fruit are Al, Ca, Fe, K, Mg, Na and P and in the present study we determined that K and P were the most abundant minerals in apricot. The content of minerals was found to vary widely depending on the different cultivars of apricot.[23]

During the examination and assessment we found significant variations among the element contents of six apricot cultivars; however, in case of elements like boron and iron there were no significant variation between the cultivars under examination.

Table 1. Element concentrations (mg kg $^{-1}$ fresh weight ± standard deviation, *n*=3) in fruits of apricot cultivars (**n*=1).

	Goldrich	Orange Red	Gönci Magyar kajszi	Aurora	Ceglédi óriás	M. kajszi C.235	ANOVA (*P*<0,05)
Al	3.70±0.47	3.60±0.22	2.40±0.41	5.26±0.08	2.63±0.46	3.88±0.52	< 0.001
B	7.36±1.71	7.74±1.28	7.11±1.19	6.54±0.51	6.63±0.24	8.13±1.47	0.689
Ba	0.11±0.01	0.09±0.01	0.09±0.01	0.14±0.01	0.09±0.01	0.12±0.01	< 0.001
Ca	164.11±5.69	108.22±0.26	81.70±0.79	187.10±2.26	92.71±6.50	116.36±1.71	< 0.001
Cu	0.42±0.01	0.65±0.03	0.75±0.02	1.06±0.04	0.40±0.02	0.28±0.02	< 0.001
Fe	3.06±0.37	2.73±0.29	1.95±0.2	3.40±0.63	2.92±0.47	2.85±0.14	0.064
K	2205±22	2127±56	2871±22	4175±50	2910±88	2400±17	< 0.001
Li	0.004±0.001	0.010±0.002	0.007±0.002	0.01±0.002	0.002±0.002	0.003±0.001	0.008
Mg	104.80±17.91	98.10±16.30	88.79±6.03	160.74±13.13	92.84±14.36	100.60±15.92	< 0.001
Mn	0.77±0.06	0.75±0.03	1.44±0.01	1.34±0.02	1.12±0.05	0.98±0.01	< 0.001
Na	4.85±0.87	5.27±0.85	8.25±1.16	10.21±1.04	6.66±0.9	5.35±0.20	< 0.001
P	277.8±22.3	278.1±22.4	251.9±18.8	296.7±22.2	317.0±25.0	260.0±20.7	< 0.001
S	64.91±0.86	52.94±1.76	64.51±0.93	92.07±1.71	72.14±1.15	51.84±0.26	< 0.001
Se*	0.004	0.005	0.003	0.004	0.005	0.005	
Si	19.60±1.54	18.38±1.59	17.35±1.00	16.87±1.97	24.35±0.60	14.62±1.55	0.003
Sr	0.66±0.03	0.50±0.01	0.37±0.01	1.10±0.02	0.39±0.03	0.46±0.01	< 0.001
Ti	0.07±0.01	0.15±0.01	0.13±0.02	0.17±0.01	0.07±0.01	0.08±0.01	< 0.001
Zn	1.29±0.02	0.90±0.09	1.25±0.06	2.12±0.06	1.01±0.09	0.72±0.08	< 0.001

Results of the present investigation show that each apricot cultivar contains significant quantity of potassium, which is followed by phosphorus, calcium and magnesium. It may also be significant that apricot may prove to be a good source of manganese too. Among the major cultivars 'Aurora' has the greatest mineral content. Our study indicates that fruits of the six apricot cultivars contain a low amount of selenium.

Acknowledgements

This work was financed by the OTKA K84290 grant. Attila Hegedűs is grateful for receiving a János Bolyai Scholarship, Hungarian Academy of Sciences.

References

[1] FAOSTAT (Food and Agriculture Organization of the United Nations), **2013**, Production (crops data). http://faostat3.fao.org/faostat gateway/go/to/download/Q/QC/E

[2] Központi Statisztikai Hivatal. **2013**, 4.1.17. A szőlő és fontosabb gyümölcsfajok összes termése (1990-). http://www.ksh.hu/docs/hun/xstadat/xstadat_eves/i_omn009.html

[3] Központi Statisztikai Hivatal. **2013**, 6.4.1.17. Gyümölcstermelés (2000-).http://www.ksh.hu/docs/hun/xstadat/xstadateves/i_omn025.html

[4] Szalay L., **2009**, *Agrofórum,* **2009. szeptember. 9**., 66.

[5] Központi Statisztikai Hivatal, 2013d. Alma-, körte-, kajszi-, őszibarack ültetvények adatai, **2012**, Előzetes adatok. http://www.ksh.hu/docs/hun/xftp/stattukor/almault12.pdf

[6] Manzoor, M., Anwar, F., Mahmood, Z., Rashid, U., Ashraf, M., *Molecules*, **2012,** *17*, 6491-6506.

[7] Tolerable upper intake levels for vitamins and minerals. European Food Safety Authority, Scientific Committee on Food,Scientific Panel on Dietetic Products, *Nutrition and Allergies*, Parma, **2006**.

[8] Munzuroglu, O., Karatas, F., Geckil, H., *Food Chem*., **2003**, 83, 205–212.

[9] Mézes M., Balogh K., **2006**, *International Symposium on Trace Elements in the Food Chain*, 2006. május 25-27., 9-14.

[10] Davarynejad, G. H., Vatandoost, S., Soltész, M., Nyéki, J., Szabó, Z., Nagy, P., *Int. J. Hort. Sci.,* **2010,** *16(4)*, 61–65.

[11] Hacıseferogulları, H., Gezer, I., Özcan, M. M., MuratAsma, B., *J. Food Eng.,* **2007,** *79*, 364–373.

[12] Németh S., Szalay L., Ficzek G., Stéger-Máté M., Sándor G., Végvári G., Tóth M., *Acta Aliment. Hung.,* **2011**, *40*, 109-119.

[13] Erdogan-Orhan, I., Kartal, M., *Food Res. Int.*, **2011,** *44*, 1238-1243.

[14] Thaipong, K., Boonprakob, U., Crosby, K., Cisneros-Zevallos, L., Byrne, H. D., *J. Food Comp. Anal.*, **2006**, *19*, 669-675.

[15] Hui,Y.H., **2006**, *Handbook of Fruits and Fruit Processing* , 1st ed., Blackwell Publishing, Oxford, 279-291.

[16] Yıldız, F., **1994**, *J. Standard*, *Apricot*, Special Issue, 67–69.

[17] Skesters, A., Kleiner, D., Blázovics, A., May, Z., Kurucz, D., Silova, A., Szentmihályi, K., *Eur. Chem. Bull.*, **2014**, *3(1)*, 98-101.

[18] Szentmihályi, K., Then, M., *Acta Aliment. Hung*., **2000**, *29*, 43-49.

[19] May Z., Ladó K., Taba G., Csedő K., Fekete T., Bíró E., Szentmihályi K., **2005**, *Proc. 12th Symp. Anal. Environ. Problems*. Ed. Galbács Z., Szeged, 430-433.

[20] Kovács B., Széles É., Simon L., Győri Z., **2008**, *Szeléntartalom vizsgálata tartamkísérletben*. Talajtani vándorgyűlés. Nyíregyháza, 275-280.

[21] Országos Élelmezés- és Táplálkozástudományi Intézet (OÉTI), RDA értékek, http://www.oeti.hu/?m1id=6&m2id=128&m3id=19#pbtm

[22] *Dietary Reference Intakes for vitamin A, vitamin K, arsenic, boron, chromium, copper, iodine, iron, manganese, molybdenum, nickel, silicon, vanadium, and zinc*. Food and Nutritional Board, Institute of medicine. Academic Press, Boston, **2002**.

[23] Hacıseferogulları, H., Gezer, I., Musa Özcan, M., MuratAsma, B., *J. Food Eng.*, **2007,** *79*, 364-373.

Received: 24.06.2014.
Accepted: 30.06.2014.

CONTRIBUTION OF WEAK INTERMOLECULAR INTERACTIONS IN 3-ACETYL COUMARIN DERIVATIVES

Ahsan Elahi and Rajni Kant*

Keywords: Coumarins; PIXEL; hydrogen bonding; intermolecular interactions; lattice energy.

Analysis of the nature of intermolecular interactions is of utmost importance in the field of crystal engineering to facilitate the design of new materials with desirable properties. A better understanding of these interactions and their influence on the crystal packing can be obtained by evaluating the energetics associated with these interactions. In this regard, we have identified from the literature a series of 3-acetyl coumarin derivatives and calculated the lattice energy of these crystal structures by using PIXELC module in Coulomb London Pauli (CLP) package. The lattice energy of all the compouds have been partitioned into corresponding coulombic, polarization, dispersion and repulsion contributions. The important packing motifs have been extracted from the crystal packing for a complete understanding of the nature of intermolecular interactions with quantitative inputs from an evaluation of the interaction energy calculated from Pixel. It is found that most stabilizing molecular pair in most of the structures involve bifurcated C-H…O hydrogen bonding. The weak interactions like C-H…O, π…π and C-H…X (Cl or Br) also play an important role in the stabilization of the crystal packing.

Corresponding Authors
Fax: +91 191 243 2051
E-Mail: rkvk.paper11@gmail.com
[a] Department of Physics& Electronics, University of Jammu , Jammu Tawi -180 006, India.

Introduction

In nature, benzopyran analogues are widespread, and many of them have interesting biological and physical properties.[1] Coumarin derivatives have diverse biological properties, such as enzyme inhibition, hypotoxicity, carcinogenicity, anticoagulant or antibiotic action.[2,3] 3-Acetylcoumarin and its derivatives have been reported to be effective antimicrobial[4] and anticancer agents.[5]

3-Acetylcoumarin exists in two polymorphic forms i.e. form A (Triclinic) and form B (Monoclinic) and evaluation of lattice energy suggest that form A is thermodynamically more stable.[6] Calculation of the lattice energy not only offers a possible way for polymorph prediction but may also help understand the supramolecular chemistry and self-assembly during the nucleation and crystal growth processes and also help to predict the melting and solubility behaviour of the compounds. In view of the immense biological importance of coumarins, we have identified from the literature a series of 3-Acetylcoumarin derivatives and calculated theoretically their lattice energies.

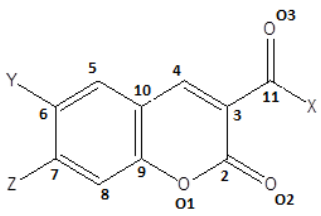

Figure 1. Coumarine moiety and the numbering scheme used.

The Crystallographic Information File (CIF) for each compound was obtained. through the CSD licensed access. All important molecular motifs which provide maximum stabilization to the crystal structure were extracted and the nature and energy of these pairs was determined using PIXEL.[7] A representative illustration of the coumarin moiety indicating the atomic numbering scheme used for the present work is shown in Fig.1. The chemical name, molecular code, position of the substituent(s) and precise crystallographic data for each compound is presented in Table 1a and 1b, respectively.

Table 1a. List of compounds and the position of substituent(s)

Chemical name	Substituent		
	X	Y	Z
3-Acetyl-6-bromocoumarin (M-1)[8]	Me	Br	-
3-Acetyl-6-chlorocoumarin (M-2)[9]	Me	Cl	-
3-Acetyl-6-methoxycoumarin (M-3)[10]	Me	OMe	-
3-Acetyl-7-methoxycoumarin (M-4)[11]	Me	-	OMe
3-Acetyl-7-(diethylamino) coumarin (M-5)[12]	Me	-	NEt_2
3-(Bromoacetyl)coumarin (M-6)[13]	CH_2Br	-	-
3-Dibromoacetylcoumarin (M-7)[14]	$CHBr_2$	-	-

Theoretical calculations

The lattice energies of all the compounds were calculated by PIXELC module in Couloumb-London-Pauli (CLP) computer program package (version 13.2.2012).[7] The total lattice energy is partitioned into its coulombic, polarization, dispersion and repulsion contributions (Table 2). All the stabilizing molecular pairs involved in crystal packing were selected from the mlc output file, which is generated after

Table 1b. Precise crystal data for 3-acetylcoumarin derivatives

Data	M-1	M-2	M-3	M-4	M-5	M-6	M-7
Formula	$C_{11}H_7BrO_3$	$C_{11}H_7ClO_3$	$C_{12}H_{10}O_4$	$C_{12}H_{10}O_4$	$C_{15}H_{17}NO_3$	$C_{11}H_7BrO_3$	$C_{11}H_6Br_2O_3$
MW	267.08	222.62	218.20	218.20	259.30	267.08	345.98
Crystal system	Triclinic	Triclinic	Triclinic	Triclinic	Monoclinic	Monoclinic	Triclinic
Space group	P1-	P1-	P1-	P1-	C2/c	$P2_1/c$	P1-
a(Å)	4.029(1)	3.988(2)	5.424(1)	7.1501(6)	17.269 (2)	5.2932 (1)	7.1998 (17)
b(Å)	11.125(2)	11.010(7)	8.409(2)	8.0640(8)	7.5203(8)	18.4568(5)	8.969 (2)
c(Å)	11.775(1)	11.156(7)	11.579(2)	9.6850(10)	22.0868(10)	9.7473 (3)	9.722 (2)
α(°)	97.339(9)	97.078(9)	104.58(2)	80.247(13)	90	90	69.094 (5)
β(°)	99.948(9)	90.238(10)	99.29(1)	69.517(10)	108.524 (7)	98.768 (1)	85.974 (6)
γ(°)	90.040(10)	100.049(10)	90.97(2)	72.896(11)	90	90	71.177 (4)
Z	2	2	2	2	8	4	2
R	0.067	0.032	0.063	0.043	0.051	0.024	0.029

Table 2. Lattice energy from CLP (in kcal mol^{-1})

Molecule	E_{Cou}	E_{Pol}	E_{Disp}	E_{Rep}	E_{Tot}
M-1	-10.038	-2.915	-27.127	16.58	-23.49
M-2	-11.16	-3.608	-29.397	18.59	-25.57
M-3	-13.33	-4.636	-28.68	19.455	-27.17
M-4	-12.523	-4.636	-30.162	23.08	-24.306
M-5	-11.59	-4.58	-32.36	20.76	-27.74
M-6	-15.439	-4.78	-33.34	26.26	-27.29
M-7	-13.05	-4.18	-31.97	22.75	-26.48

PIXEL energy calculations and were analysed with their interaction energies. The symmetry operator and centroid–centroid distance along with coulombic, polarization, dispersion, repulsion and total interaction energies between the molecular pairs are presented in Table 3. The molecular pairs are arranged in decreasing order of their stabilization energies. The PIXEL method has been preferred for the quantification of intermolecular interactions, primarily because of the following reasons:

It is computationally less demanding.[7]

It allows partitioning of total interaction energy into corresponding coulombic, polarization, dispersion, and repulsion contribution which facilitates a better understanding of the nature of intermolecular interactions contributing towards the crystal packing.[15,16]

The energies obtained from PIXEL calculation are generally comparable with high level quantum mechanical calculations.[17, 18]

Results and Discussion

3-Acetyl-6-bromocoumarin (M-1)

Molecular pairs of M-1 (I-VIII) extracted from crystal structure along with their respective interaction energies are shown in Fig. 2. The most stabilized molecular pair in M-1 shows the presence of bifurcated acceptor C-H…O hydrogen bonding (involving O3 with H4 and H5) forming dimers related by centre of symmetry with an interaction energy of -7.98 kcal mol^{-1} (Fig. 2, motif I) and the interaction is mainly coulombic in nature (Table 3). The next most stabilized pair involves C=O…C=O interaction where C=O bond in one molecules points towards the carbonyl carbon of the second molecule. Along with these interactions Motif II also involves C-H…O (H12b with O2) and molecular stacking (C-C stacking) and hence resulting in a total interaction energy of -6.71 kcal mol^{-1} (Fig.2, motif II).

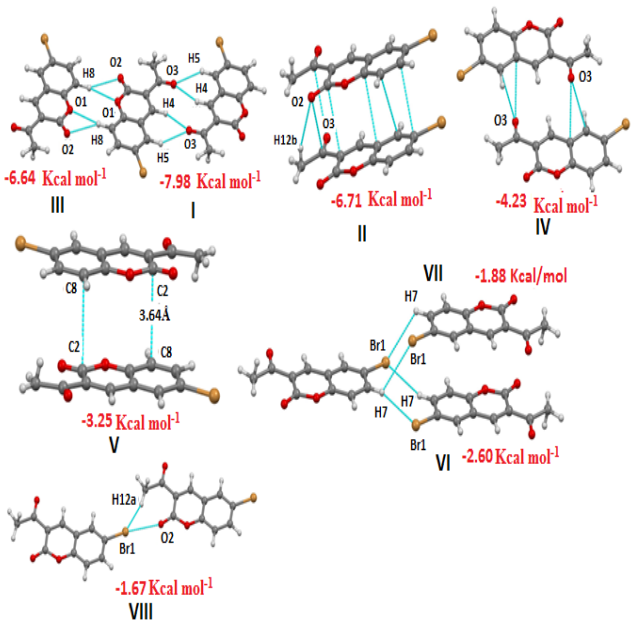

Figure 2. Molecular pairs (I-VIII in Table 3) along with their interaction energies calculated with PIXEL (values in red) in M-1.

Table 3 PIXEL interaction energies (I.E.) (kcal mol^{-1}) between molecular pairs related by a symmetry operation and the associated intermolecular interactions in the crystal

Motif	Centroid distance, Å	E_{Coul}	E_{Pol}	E_{Disp}	E_{Rep}	E_{Tot}	Symmetry	Important interactions
M-1								
I	7.393	-6.57	-1.792	-4.49	4.87	-7.98	2-x,1-y,1-z	C4-H4…O3, C5-H5…O3
II	4.029	-2.25	-0.93	-10.85	7.28	-6.71	1+x,y,z	Molecular stacking, C2=O2…C11=O3, C11=O3…C2=O2, C12-H12b…O2
III	7.817	-4.51	-1.009	-3.39	2.34	-6.64	-x,-y,1-z	C8-H8…O2, C8-H8…O1
IV	6.407	-0.23	-0.764	-6.26	3.05	-4.23	1-x,1-y,1-z	C11=O3… π (C5,C10)
V	6.504	-0.215	-0.47	-3.89	1.34	-3.25	1-x,-y,1-z	Molecular stacking
VI	9.495	-1.21	-0.525	-2.86	2.03	-2.60	-x,-y,-z	C7-H7…Br1
VII	9.368	-0.47	-0.167	-2.56	1.31	-1.88	1-x,-y,-z	C7-H7…Br1
VIII	11.775	-1.003	-0.31	-1.84	1.48	-1.67	x,y,-1+z	C12-H12a…Br1, C2=O2… Br1-C6
M-2								
I	6.958	-7.4	-2.03	-4.94	5.92	-8.5	2-x,1-y,1-z	C4-H4…O3, C5-H5…O3
II	3.988	-2.7	-1.26	-11.7	7.98	-7.71	1+x,y,z	Molecular stacking, C2=O2…C11=O3, C11=O3…C2=O2, C12-H12b…O2
III	7.095	-5.16	-1.29	-3.8	3.34	-6.93	-x,1-y,-z	C8-H8…O2, C8-H8…O1
IV	5.799	-0.38	-0.62	-5.80	2.29	-4.5	1-x,1-y,1-z	C11=O3… π (C5,C10)
V	10.316	-1.4	-0.74	-3.29	2.07	-3.41	-x,-y,-z	C7-H7…Cl1
VI	5.804	-0.11	-0.52	-4.23	1.57	-3.05	1-x,1-y,-z	Molecular stacking
VII	10.252	-0.86	-0.26	-2.79	1.22	-2.7	1-x,-y,-z	C7-H7…Cl1
VIII	11.010	-.549	-0.31	-2.05	1.55	-1.36	x,-1+y,z	C12-H12c…Cl1, C2=O2… Cl1-C6
M-3								
I	6.666	-8.79	-3.08	-6.78	9.13	-9.53	3-x,1-y,2-z	C4-H4…O3, C5-H5…O3
II	7.203	-4.85	-1.29	-3.7	3.06	-6.78	1-x,-y,2-z	C8-H8…O2, C8-H8…O1
III	4.186	-1.57	-1.24	-9.79	5.9	-6.69	2-x,1-y,2-z	Molecular stacking, H12b…H13a
IV	4.638	-1.457	-1.457	-8.46	4.75	-6.36	2-x,-y,2-z	Molecular stacking, C12-H12a…π
V	5.424	-1.5	-0.81	-6.23	3.01	-5.59	1+x,y,z	Molecular stacking, C=O…C=O
VI	10.483	-1.86	-0.693	-3.22	2.58	-3.2	1-x,-y,1-z	C7-H7…O4
VII	9.990	-1.05	-0.33	-3.17	1.649	-2.93	2-x,-y,1-z	C13-H13c…O4
VIII	11.579	-2.24	-0.74	-1.95	2.5	-2.41	x,y,1+z	C13-H13b…O2
M-4								
I	3.568	-5.87	-1.57	-14.96	12.14	-10.27	2-x,2-y,1-z	Cg1…Cg2
II	3.600	-3.8	-1.43	-13.00	8.65	-9.6	1-x,2-y,1-z	Cg1…Cg1, C12-H12c…O4, C12-H12c…C7
III	7.585	-4.94	-1.6	-5.11	3.8	-7.83	1-x,3-y,1-z	C13-H13b…O2, C13-H13c…O1
IV	8.019	-6.62	-2.1	-4.3	6.02	-7.002	2-x,1-y,1-z	C4-H4…O3, C5-H5…O3
V	12.293	-2.03	-0.57	-2.36	2.36	-2.605	1-x,3-y,2-z	C13-H13b…O4
VI	9.206	-1.72	-0.64	-2.07	1.88	-2.557	2-x,2-y,-z	C12-H12b…O2
VII	9.685	-0.93	-0.62	-2.53	2.1	-1.98	x,y,-1+z	C6-H6…O2
M-5								
I	4.556	-4.06	-1.36	-13.67	7.95	-11.16	1-x,-y,1-z	Cg2…Cg2, C13-H13a… π
II	5.504	-3.36	-1.3	-12.06	8.197	-8.58	1/2-x,1/2-y,1-z	Cg1…Cg1, C12-H12c…Cg2
III	7.262	-2.39	-1.19	-6.64	4.01	-6.19	1/2-x,-1/2-y, 1-z	C12-H12b…O1, C2=O2…C2=O2
IV	9.418	-4.397	-1.625	-3.82	4.39	-5.42	1/2+x,1/2+y,z	C6-H6…O2, C13-H13a…O2
V	11.878	-2.55	-0.788	-1.88	1.935	-3.29	1/2+x, 1/2-y,1/2+z	C14-H14b…O3, C15-H15b…O3

 DOI: 10.17628/ecb.2014.3.763-769

M-6								
I	5.918	-10.3	-3.035	-7.48	9.89	-10.94	2-x,1-y,1-z	C4-H4…O3, C5-H5…O3,C5-H5…Br1
II	5.029	-1.69	-1.195	-9.82	5.4	-7.289	1-x,1-y,1-z	Molecular stacking
III	5.293	-2.48	-1.21	-8.05	5.73	-6.02	-1+x,y,z	C-12-H12b…Br1, C11=O3…π(C2), Molecular stacking
IV	10.008	-2.98	-1.05	-3.967	4.01	-3.99	1-x,-0.5+y,1.5-z	C6-H6…O2, H6…H12a
V	6.894	-2.65	-0.74	-3.75	3.39	-3.75	x, 1.5-y,-0.5+z	C12-H12a…Br1
VI	9.491	-0.93	-0.454	-5.73	3.77	-3.34	1-x,1-y,2-z	Molecular stacking
M-7								
I	4.952	-4.68	-1.55	-8.84	4.73	-10.34	-x,1-y,-z	C11=O3…C4, C11=O3…O3=C11 C4-H4…Br1
II	6.940	-5.8	-2.39	-15.36	13.5	-10.01	-x,-y,-z	Cg1…Cg2
III	8.230	-3.8	-1.4	-11.5	8.24	-8.5	1-x,-y,-z	Cg1…Cg2, C7-H7…Br1
IV	5.837	-2.51	-1.09	-4.18	3.34	-4.42	-x,-y,1-z	C12-H12…O2
V	9.519	-2.41	-0.95	-3.17	2.61	-3.94	1+x,-1+y,z	C8-H8…O3, C8-H8…Br2
VI	9.722	-2.15	-0.526	-2.79	1.72	-3.75	x,y,1+z	C5-H5…Br1

Cg1- centre of gravity of pyrone ring (O1-C2-C3-C4-C10-C9) Cg2- centre of gravity of benzene ring(C5-C6-C7-C8-C9-C10)

The combined nature of these interactions is mainly dispersive in nature (Table 3). The third most stabilized interacting pair involves bifurcated donor C-H…O (H8 with O1 and O2) hydrogen bonding generating dimers across the centre of symmetry with an interaction energy of -6.64 kcal mol^{-1} (Fig.2, motif III). Additional stabilization to the structure comes from motif IV and V, motif IV involves C=O… π (O3 with C5 and C10) whereas motif V shows molecular stacking involving C2 of Cg1(where Cg1 represents centre of gravity of pyrone ring) and C8 of Cg2 (where Cg2 represents centre of gravity of benzene ring) with C…C distance of 3.64Å.

The interaction energy for IV and V are -4.23 and -3.25 kcal mol^{-1} respectively. Motif VI and VII involves the presence of weak C-H…Br interaction (involving H7 and Br1) forming dimers related by inversion centre having an interaction energies of -2.60 and -1.88 kcal mol^{-1} respectively and are mainly dispersive in nature (Table 3). The least stabilized molecular pair VIII involves C-H…Br (H12a with Br1) and C=O…Br-C (O2 and Br1) having an interaction energy of -1.67 kcal mol^{-1}.

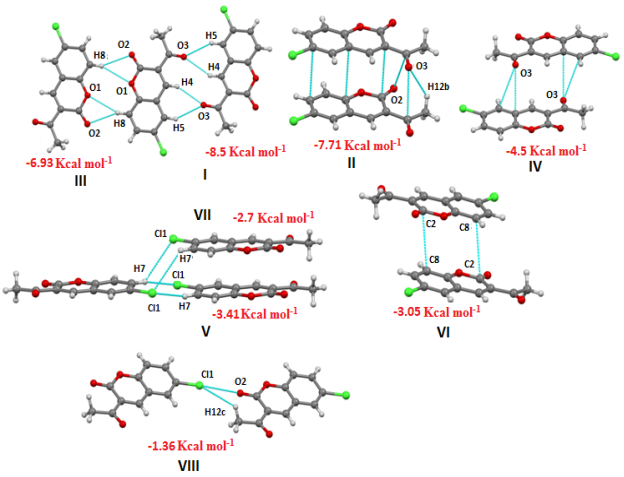

Figure 3. Molecular pairs (I-VIII in Table 3) along with their interaction energies calculated with PIXEL (values in red) in M-2.

3-Acetyl-6-chlorocoumarin (M-2)

Molecular pairs (I-VIII) extracted from M-2 along with their respective interaction energies are shown in Fig. 3. The packing features of M-2 were almost identical to those observed for M-1 and results in the generation of similar packing motifs. The energies of two bifurcated C-H…O hydrogen bonded pairs (Fig. 3, motif I and III) of M-2 were similar to those observed in M-1(Table 3). The only difference between M-1 and M-2 is the presence of different halogen atom (Cl in place of Br). An important striking feature is that an interaction in which Br is involved in M-1 is replaced by the similar interaction with Cl in M-2. The molecular pairs in which Cl1 is involved are motifs V, VII and VIII with their stabilization energies being -3.41 , -2.7 and -1.36 kcal mol^{-1} and are dispersive in nature.

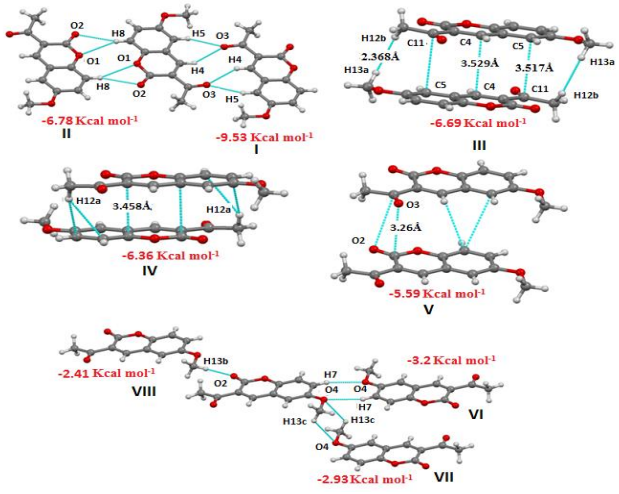

Figure 4. Molecular pairs (I-VIII in Table 3) along with their interaction energies calculated with PIXEL (values in red) in M-3.

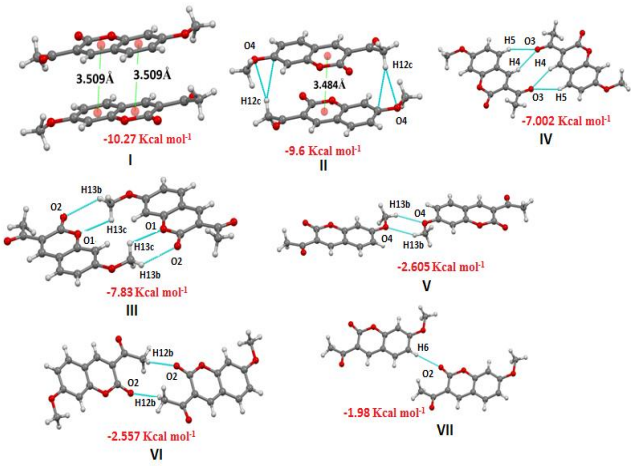

Figure 5. Molecular pairs (I-VII in Table 3) along with their interaction energies calculated with PIXEL (values in red) in M-4.

3-Acetyl-6-methoxy-coumarin (M-3)

The extracted molecular pairs of M-3 (I –VIII) are shown in Fig. 4. In M-3, halogen atom present at position 6 in case of M-1 and M-2 is replaced by the methoxy group. The major stabilizing motifs are identical whereas due to the presence of methoxy group, least stabilizing motifs involve weak C-H…O interaction in place of C-H…X (Br, Cl) interactions. The two most stabilized molecular pairs (I and II) in M-3 (identical to motifs I and III of M-1 and M-2) shows the presence of bifurcated C-H…O interaction form dimers (Fig. 4, motif I and II) having energies of -9.53 and -6.78 kcal mol^{-1} respectively. The major contribution to the stabilization of the pair comes from coulombic component (Table 3). The next two most stabilized molecular pairs (III and IV) involve C-C molecular stacking, along with this interaction motif III also involves C-H…H-C (involving H12b and H13a) with H…H distance being 2.368Å (Fig. 4, motif III) whereas motif IV also involves C-H… π interaction involving H12a with C7 and C8 of Cg2 ring (Fig. 4, motif IV) resulting in a total interaction energy of -6.69 and -6.36 kcal mol^{-1} respectively. Motif V involves C=O…C=O and C-C molecular stacking identical to motif II of M-1 and M-2 with an interaction energy of -5.59 kcal mol^{-1}. The remaining three least stabilized interacting pairs shows the presence of C-H…O interaction with motif VI(involving O4 and H7) and motif VII(involving O4 and H13c) forming dimers. The total interaction energy of the three pairs (VI, VII, VIII) being -3.2, -2.93 and -2.41 kcal mol^{-1} respectively.

3-Acetyl-7-methoxy-coumarin (M-4)

Molecular pairs of M-4 (I-VIII) extracted from crystal structure along with their respective interaction energies are shown in Fig. 5. The two most stabilized motifs (I and II) show the presence of π… π interaction, a packing feature which is not observed in M-1, M-2 and M-3. Motif I involves double ring stacking (Cg1…Cg2) with an interaction energy of -10.27 kcal mol^{-1} (Fig. 5, motif I). Motif II along with a stacking interaction (Cg1…Cg1) also shows the presence of C-H…O (H12c and O4) and C-H… π (H12c and C7 of Cg2) resulting in a total stabilization energy of kcal mol^{-1} (Fig. 5, motif II). In both the motifs I and II molecules are arranged in antiparallel arrangement and major contribution to the stabilization comes from dispersion component (Table 3). Additional stabilization to the structure comes from motif III which shows the presence of C-H…O interaction (involving H13b with O2 and H13c with O1) forming dimers generating rings that can be described as having graph set R_2^2 (6) (Fig. 5, motif III). The stabilization energy of this pair being -7.83 kcal mol^{-1}. Motif IV of this compound involving bifurcated C-H…O is found to be similar to the most stabilized motif I in M-1, M-2 and M-3 and contributing -7.002 kcal mol^{-1} (Fig. 5, motif IV) towards the stabilization. The last three interacting pairs show the presence of C-H…O interaction with motif V and motif VI forming dimers generating rings that can be described as having graph sets R_2^2 (6) to O4 (Fig.5, motif V) and R_2^2 (12) to O2 (Fig.5, motif VI). The stabilization energies of the three pairs (V, VI and VII) being -2.605, -2.557 and -1.98 kcal mol^{-1} respectively.

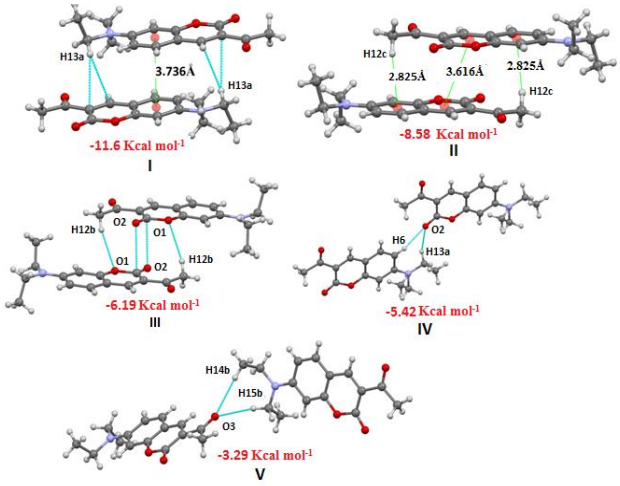

Figure 6. Molecular pairs (I-V in Table 3) along with their interaction energies calculated with PIXEL (values in red) in M-5.

3-Acetyl-7-(diethylamino)coumarin (M-5)

The extracted molecular pairs of M-5 (I –V) are shown in Fig. 6. The maximum stabilization to the structure comes from π…π interaction which is exhibited by motif I and II. Motif I involves Cg2…Cg2 interaction (Cg2-Cg2 distance being 3.736Å) along with C-H…π (involving H13a with C3 and C4 of Cg1) whereas motif II involves Cg1…Cg1 interaction (Cg1-Cg1 distance being 3.616Å) along with C-H…π (H12a with Cg2) generating dimers with stabilization energy of -11.6 kcal mol^{-1} (Fig. 6, motif I) and -8.58 kcal mol^{-1} (Fig. 6,Motif II) respectively. The combined nature of these interactions is mainly dispersive in nature (Table 3). The third stabilized pair shows the presence of C=O…C=O in which oxygen atom O2 of pyrone ring of one molecule interacts with carbonyl carbon C2 of pyrone ring of second molecule (Fig. 6, motif III). Along with this interaction motif III also involves C-H…O (involving H12b with O1) interaction and hence form dimer with an interaction energy of -6.19 kcal mol^{-1}. The last two stabilized pairs IV and V which also provide significant stabilization to the structure shows the presence of bifurcated acceptor C-H…O interaction with stabilization energy of -5.42 kcal mol^{-1} and -3.29 kcal mol^{-1} respectively.

 DOI: 10.17628/ecb.2014.3.763-769

3-(Bromoacetyl)coumarin (M-6)

Molecular pairs of M-6 (I-VI) extracted from crystal structure along with their respective interaction energies are shown in Fig. 7. The most stabilized motif I in this structure is similar to the most stabilized motif I as found in M-1, M-2 and M-3. However along with bifurcated C-H…O, it also involves C-H…Br (H5 with Br1) resulting in a stabilization energy of -10.94 kcal mol^{-1} (Fig. 7, motif I) with major contribution from coulombic component (-10.3 kcal mol^{-1}) which is almost equal to total interaction energy of the pair (Table 3). The second stabilized pair involves C…C molecular stacking with a stabilization energy of -7.289 kcal mol^{-1}. The third most stabilized interacting motif show the presence of C=O…π in which oxygen atom O3 of acetyl group interacts with C2 of Cg1 ring with O3-C2 distance being 3.095Å (Fig. 7, motif III) which is less than the sum of vander waal radii of two atoms. Motif III along with these interactions also involve C-H…Br (H12b with Br1) and stacking interaction (involving C4 of Cg1 and C8 of Cg2) with C…C distance being 3.401Å and hence resulting in a stabilization energy of -6.02 kcal mol^{-1} (Fig. 7, motif III). Motif IV is stabilized by the presence of C-H…O (H6 with O2) and C-H…H-C (involving H6 and H12a) with H…H distance of 2.372Å and having an interaction energy of -3.99 kcal mol^{-1}. Additional stabilization to the structure comes from motif V (C-H…Br) and VI (molecular stacking) with an interaction energy of -3.75 and -3.34 kcal mol^{-1} respectively.

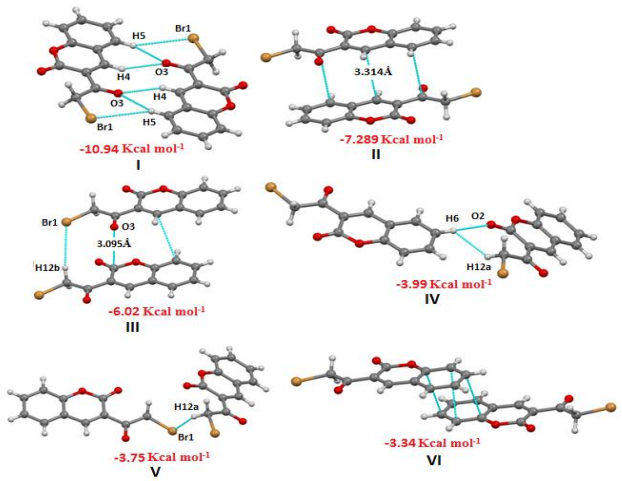

Figure 6. Molecular pairs (I-VI in Table 3) along with their interaction energies calculated with PIXEL (values in red) in M-6.

3-Dibromoacetylcoumarin (M-7)

The extracted molecular pairs (I –VI) of M-7 are shown in Fig. 8 along with their stabilization energies. The maximum stabilization to the structure comes from the interaction of oxygen atom O3 of acetyl group of one molecule with the carbon atom C4 of Cg1 ring (O3-C4 distance being 3.272Å) and oxygen atom O3 of acetyl group of second molecule (O3-O3 distance being 3.199Å). Motif I also shows the presence of weak C-H…Br (involving H4 and Br1) resulting in a total interaction energy of -10.34 kcal mol^{-1} (Fig. 8, motif I) with major contribution from dispersion component which is almost double the coulombic component (Table 3). The second and third stabilized motifs (II and III) involves double ring stacking with Cg1…Cg2 distance being 3.567Å and 3.642Å respectively and the molecules are arranged in antiparallel manner. Motif III along with π…π also involves a weak C-H…Br (involving H7 and Br1) interaction. The stabilization energy of the two pairs being -10.01 and -8.5 kcal mol^{-1} and are mainly dispersive in nature (Table 3). Motif IV providing additional stabilization to the structure (energy being -4.42 kcal mol^{-1}) shows the presence of dimeric C-H…O interaction (involving H12 and O2) forming ring that can be described as having graph set R_2^2 (12) (Fig. 8, motif IV) . Motif V is stabilized by the presence of another C-H…O interaction (H8 with O3) along with C-H…Br (H8 with Br2) with an interaction energy of -3.92 kcal mol^{-1}. The least stabilized molecular pair VI involves C-H…Br (involving H5 with Br1) having an interaction energy of -3.75 kcal mol^{-1}.

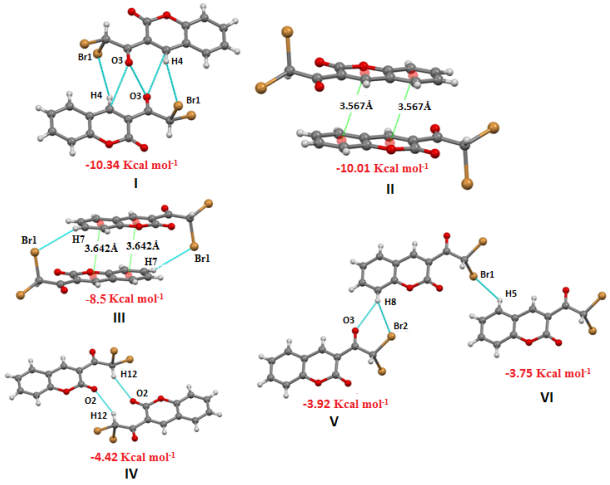

Figure 7. Molecular pairs (I-VI in Table 3) along with their interaction energies calculated with PIXEL (values in red) in M-7.

A careful analysis of some key supramolecular motifs obtained in these compounds leads to the following relevant observations:

The maximum stabilization to the crystal structure in most of these compounds comes from the motifs interacting via bifurcated C-H…O interaction with energy in the range -6 to -11 kcal mol^{-1}, with a major contribution to the stabilization being coulombic in origin. Hence this motif can be considered as the basic building unit observed in these structures.

The interaction energies of the motifs involving π…π interactions were observed to be in range -8.5 to -11.5 kcal mol^{-1} whereas the energy of the motifs involving molecular stacking and C-H…O lies in the range -3 to -7 kcal mol^{-1} and -2 to -5 kcal mol^{-1} respectively.

The energy of the molecular pairs involving hydrogen bonds with halogens (Cl or Br) lies in the range -1 to -4 kcal mol^{-1}and are mainly dispersive in nature. This observation is in agreement with the values reported in case of a similar study made by Panini and Chopra.[19]

The total interaction energy (lattice energy) appears to be the same for all the investigated compounds, the energy range being -23 to -28 kcal mol^{-1}.

Conclusions

An analysis of the energetics of the neighbouring molecular pairs in 3-acetylcoumarin derivatives shows the presence of different intermolecular interactions participating in the crystal packing. In addition to the significance of coulombic nature of bifurcated C-H…O hydrogen bonds, the stabilizing role of π…π, stacking and C-H…X(Br or Cl) interactions has been realized in these structures. Short intermolecular C-H…X (Br or Cl) occurs in the crystal structure and makes only a minor contribution to the cohesive energy of the crystal but they play an important role in crystal packing. It is of interest to extend this evaluation of energies of molecular pairs in other coumarin derivatives which will enable us to have better understanding of weak intermolecular interactions.

References

[1]Adeeleke, B. B., Weir, D., Depew, M. C., Wan, J. K. S., *Can J Chem.*, **1984**, *62*, 117-120.

[2]Rosskopt, F., Kraus, J., Franz, G., *Pharmazie*, **1992**, *47*, 139-142.

[3]Hirsh, J., Dalen, J. E., Anderson, D. R., Poller, L., Bussey, H., Ansell, J., Deykin, D., *CHEST*, **2001**, 119, 8S-21S.

[4]Ishii, Y., *J Agric. Chem.Soc. Jpn*, **1952**, *26*, 510-513.[5]Huang, X.L., Xu, S. P., Fu, Z. D., An, B., *Acta Pharm. Sinica*, **1996**, 31, 421–436.

[6]Munshi, P., Guru Row, T. N., *Crystal Growth and Design*, **2006**, *6(3)*,708-718.

[7]Gavezzotti, A., *New J. Chem.*, **2011**, *35*, 1360-1368.

[8]Kokila, M. K., Puttaraja, M., Kulkarni, M. V., Shivaprakash, N. C., *Acta Cryst C*, **1996**, *52*, 2078-2081.

[9]Deepak, C., Venugopal, K. N., Jayashree, B. S., Guru Row, T.N., *Acta Cryst E*, **2006**, *62*, o2310- o2312.

[10]Stancho, S., Anita, P., Pascal, R., Georgi, A., Ilia, M., *Anal. Sci.*, **2008**, *24*, x183-x184.

[11]Hong, M. H., Cheng, R. L., Yong, Z., De-Chun, Z., *Acta Cryst E*, **2005**, *61*, o1864- o1866.

[12]Christopher, G. H., Charles, S. M., *Acta Cryst E*, **2006**, *62*, o2072–o2074.

[13]Hazel, A. S., Judith A. K. H., *Acta Cryst E*, **2007**, *63*, o3895.

[14]Deepak, C., Venugopala, K. N., Rao, G. K., Guru Row, T. N., *Acta Cryst E*, **2007**, *63*, o2826.

[15]Dunitz, J. D., Gavezzotti, A., *Cryst. Growth Des.*, **2012**, *12*, 5873-5877.

[16]Dunitz, J. D., Gavezzotti, A., *Cryst. Growth Des.*, **2005**, *5*, 2180-2189.

[17]Maschio, L., Civalleri, B., Ugliengo, P., Gavezzotti, A., *J. Phys. Chem. A.*, **2011**, *115*, 11179-11186.

[18]Dunitz, J. D., Gavezzotti, A., *Chem. Soc. Rev.*, **2005**, *38*, 2622-2633.

[19]Panini, P., Deepak, C., *Cryst Eng Comm.*, **2013**, *15*, 3711-3733.

Received: 06.06.2014.
Accepted: 07.07.2014.

IN VITRO CYTOTOXICITY AND GENOTOXICITY EVALUATION OF NEWLY SYNTHESIZED STEROIDAL THIAZOLES

Shamsuzzaman[a]*, Ayaz Mahmood Dar [a]# and Manzoor Ahmad Gatoo [b]§

Keywords: Thiazole; 5α-iodocholestan-6-one; MTT assay; pBR322; Comet assay.

A preparation of new series of 2'-hydrazinocholest-6-eno[4,5-d]thiazoles **4-6** from 5α-cholestan-6-ones **1-3** are herein reported. After characterization by IR, ^{1}H NMR, ^{13}C NMR, MS and analytical data, the synthesized compounds **4-6** were tested for anticancer activity *in vitro* against the human cancer cell lines A549, HepG2, HeLa, SW480 and HL-60 by MTT assay during which compounds **4-6** showed significant anticancer behaviour. The gel electrophoresis pattern demonstrated that the compound **4** alone or in presence of Cu(II) causes the nicking of super coiled pBR322. Further the compound **4** is also able to generate reactive oxygen species (hydroxyl radical) in a dose dependent manner, which correlates its ability to cause DNA breakage in cancer cells. The genotoxicity of the compounds was studied by comet assay involving potential apoptotic degradation of DNA and was analyzed by agarose gel electrophoresis and visualized by ethidium bromide staining.

Corresponding Authors
E-Mail: shamsuzzaman9@gmail.com*, ayazchem09@gmail.com,# manzbio@gmail.com §
[a] Department of Chemistry Aligarh Muslim University Aligarh 202002, India
[b] Department of Biochemistry Jawaharlal Nehru Medical College Aligarh Muslim University, Aligarh 202002, India

Introduction

Steroids have always attracted considerable attention because of being a fundamental class of biologically signalling molecules. In addition to their profound physiological and clinical importance[1], they have the potential to be developed as drugs for the treatment of a large number of diseases including cardiovascular, autoimmune, brain tumours, breast cancer, prostate cancer and osteoarthritis.[2-4] Most of the steroid based pharmaceuticals are semi-synthetic compounds prepared by connecting a special functionality to the core structure of a steroid.[5] Most important of such functionalities are the heterocyclic systems because of their potent receptor binding properties. The advantage of employing hydrophobic steroid units is their ability to interact with cell membranes and thus pave the way for biological activity of such hybrid molecules.[4]

Thiazoles and their derivatives have attracted continuing interest over the years because of their varied biological activities. They have been used for the treatment of allergies,[6] hypertension,[7] inflammation,[8] schizophrenia,[9] bacterial infections,[10] HIV infections,[11] hypnotics[12] and more recently for the treatment of pain,[13] as fibrinogen receptor antagonists with antithrombotic activity[14] and as new inhibitors of bacterial DNA gyrase B.[15] The substituted thiazoles have number of other characteristic pharmacological features such as relative stability and ease of starting materials built in biocidal unit, enhanced lipid solubility with hydrophilicity and easy metabolism of compounds.[16]

DNA cleaving agents have attracted extensive attention in the field of molecular biology due to their potential applications.[17] Under uncatalyzed physiological conditions, the phosphodiester bonds of DNA are extremely stable and the half life of DNA hydrolysis is estimated to be around 200 million years.[18] Some of the metal complexes have been widely investigated as efficient cleaving agents of nucleic acids[19] but the serious issues over their lability and toxicity restricted the practical usage of these compounds in pharmacy.[20] To overcome these limitations, Gobel and co-workers[21] put forward the concept of 'metal free cleaving agents' which are being applied to active phosphodiesters like 'nucleic acid mimic' and RNA. In view of the pharmacological importance of thiazoles, our aim here is to synthesize the new steroid derivatives with a substituted thiazole ring attached at ring B of tertracyclic core and to study the *in vitro* anticancer activity.

Experimental

Materials and instruments

All the reagents and solvents were obtained from best known commercial sources and were freshly distilled. Melting points were determined on a Kofler apparatus and are uncorrected. The IR spectra were recorded on KBr pellets with Pye Unicam SP3-100 spectrophotometer and values are given in cm^{-1}. ^{1}H and ^{13}C NMR spectra were run in $CDCl_3$ on a JEOL Eclipse (400 MHz) instrument with TMS as internal standard and values are given in ppm (δ). Mass spectra were recorded on a JEOL SX 102/DA-6000 Mass spectrometer. Thin layer chromatography (TLC) plates were coated with silica gel G and exposed to iodine vapours to check the progress of reaction. Sodium sulphate (anhydrous) was used as a drying agent. Super coiled pBR322 DNA was purchased from GeNei (India) and used for the agarose gel experiment without further purification. Double-stranded calf thymus DNA, purchased from Sigma, was dissolved in a 0.1M Tris-buffer.

General procedure for the synthesis of steroidal thiazoles (4-6)

To a solution of steroidal ketones **1-3** (1 mmol) in absolute ethanol (15 mL) was added thiosemicarbazide (1 mmol) and iodine (2 mmol) in the same solvent (25 mL) and the reaction mixture was refluxed for about 13-17 h. The progress of the reaction was monitored by TLC. After completion of reaction, the excess solvent was removed to three fourths of the original volume under reduced pressure. The reaction mixture was cooled to room temperature, diluted with $Na_2S_2O_7$ solution and subsequently with water. The mixture was taken in ether, washed with water and dried over anhydrous Na_2SO_4. Evaporation of solvents and recrystallization from methanol afforded respective products **4-6**.

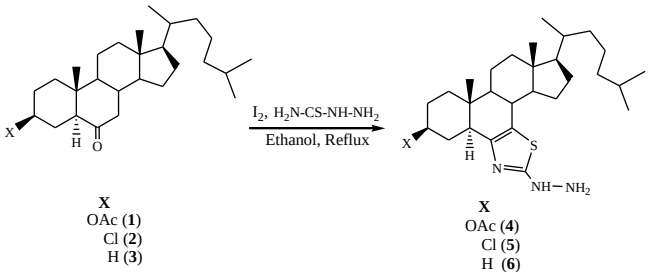

X
OAc (**1**)
Cl (**2**)
H (**3**)

X
OAc (**4**)
Cl (**5**)
H (**6**)

Scheme 1. Showing the synthesis of fused steroidal thiazoles

3β-Acetoxy-2'-hydrazinocholest-6-eno[4, 5-d]thiazole (4)

Yield 82 %, m.p.163-164 °C, IR (KBr, cm^{-1}): 3395, 3310 (NH, NH_2), 1730 (OAc), 1625 (C=C), 1555 (C=N), 1320 (C-N), 645 (C-S). ^{1}H NMR (400 MHz, $CDCl_3$): δ 6.8 (brs, 2H, N*H*$_2$, exchangeable with D_2O), 4.7 (m, 1H, C_3α-*H*, *W½* =15 Hz), 4.4 (s, 1H, N*H*, exchangeable with D_2O), 2.7 (dd, 1H, C_5α-*H*, *J* =15 Hz, 5 Hz), 2.03 (s, 3H, OCOC*H*$_3$), 1.18 (s, 3H, C_{10}-C*H*$_3$), 0.70 (s, 3H, C_{13}-C*H*$_3$), 0.97 & 0.83 (other methyl protons). ^{13}C NMR (100 MHz, $CDCl_3$): δ 171.2 (O*C*OCH$_3$), 163 (*C*=N), 132 (C_6), 120 (C_7), 70.2 (C_3), 46 (C_{14}), 44 (C_{13}), 42 (C_4), 39 (C_{10}), 35 (C_5), 26 (C_{19}), 24 (C_{11}), 22 (C_{18}), 20 (C_{15}), 17 (C_{16}). Anal. Calcd for $C_{30}H_{49}N_3O_2S$: C, 69.84, H, 9.39, N, 8.11 % found: C, 69.90, H, 9.51, N, 8.15 %. ESI MS: *m/z* 515 [$M^{+\cdot}$].

3β-Chloro-2'-hydrazinocholest-6-eno [4, 5-d] thiazole (5)

Yield 76 %, m.p.143-144 °C, IR (KBr, cm^{-1}): 3370, 3320 (NH, NH_2), 1622 (C=C), 1560 (C=N), 1323 (C-N), 745 (C-Cl), 635 (C-S). ^{1}H NMR (400 MHz, $CDCl_3$): δ 6.63 (brs, 2H, N*H*$_2$, exchangeable with D_2O), 4.45 (s, 1H, N*H*, exchangeable with D_2O), 3.9 (m, 1H, C_3α-*H*, *W½* = 17 Hz), 2.8 (dd, 1H, C_5α-*H*, *J* =17.05 Hz, 5.3 Hz), 1.18 (s, 3H, C_{10}-C*H*$_3$), 0.70 (s, 3H, C_{13}-C*H*$_3$), 0.97 & 0.83 (other methyl protons). ^{13}C NMR (100 MHz, $CDCl_3$): δ 162 (*C*=N), 134 (C_6), 120 (C_7), 57.7 (C_3), 46 (C_{14}), 45 (C_{13}), 42.6 (C_4), 39 (C_{10}), 35 (C_5), 26 (C_{19}), 24 (C_{11}), 22 (C_{18}), 20 (C_{15}), 17 (C_{16}). Anal. Calcd for $C_{28}H_{46}ClN_3S$: C, 68.37, H, 9.29, N, 8.49 % found: C, 68.43, H, 9.36, N, 8.54%. ESI MS: *m/z* 491/489 [$M^{+\cdot}$].

2'-Hydrazinocholest-6-eno[4, 5-d]thiazole (6)

Yield 73 %, m.p.129-130 °C, IR (KBr, cm^{-1}): 3376, 3328 (NH, NH_2), 1617 (C=C), 1557 (C=N), 1328 (C-N), 634 (C-S). ^{1}H NMR (400 MHz, $CDCl_3$): δ 6.2 (brs, 2H, N*H*$_2$, exchangeable with D_2O), 3.8 (s, 1H, N*H*, exchangeable with D_2O), 2.74 (dd, 1H, C_5α-*H*, *J* =16.9 Hz, 5.5 Hz), 1.18 (s, 3H, C_{10}-C*H*$_3$), 0.70 (s, 3H, C_{13}-C*H*$_3$), 0.97 & 0.83 (other methyl protons). ^{13}C NMR (100 MHz, $CDCl_3$): δ 163 (*C*=N), 130 (C_6), 120 (C_7), 46 (C_{14}), 42.2 (C_4), 39 (C_{10}), 35 (C_5), 26 (C_{19}), 24 (C_{11}), 22 (C_{18}), 20 (C_{15}), 17 (C_{16}). Anal. Calcd for $C_{28}H_{47}N_3S$: C, 73.47, H, 10.19, N, 9.13 % found: C, 73.52, H, 10.28, N, 9.19%. ESI MS: *m/z* 457 [$M^{+\cdot}$].

***In vitro* anticancer activity (MTT assay)**

Cell culture and conditions: Human cancer cell lines SW480 (colon adenocarcinoma cells)/ATCC (CCL-228), HeLa (cervical cancer cells)/ATCC (CCL-2), A549 (lung carcinoma cells)/ATCC (CCL-185), HepG2 (hepatic carcinoma cells)/ATCC (CRL-8065) and HL-60 (Leukaemia cells)/ATCC (CCL-240) were taken for the study. SW480, A549, HL-60 and HepG2 cells were grown in RPMI 1640 supplemented with 10 % foetal bovine serum (FBS), 10U penicillin and 100 µg mL^{-1} streptomycin at 37 °C with 5 % CO_2 in a humidified atmosphere. HeLa cells were grown in Dulbecco's modified Eagle's medium (DMEM) supplanted with FCS and antibiotics as described above for RPMI 1640. Fresh medium was given every second day and on the day before the experiments were done. Cells were passaged at preconfluent densities, using a solution containing 0.05 % trypsin and 0.5 mM EDTA.

Cell viability assay (MTT): The anticancer activity *in vitro* was measured using the MTT assay. The assay was carried out according to known protocol.[22,23] Exponentially growing cells were harvested and plated in 96-well plates at a concentration of 1×10^4 cells/well. After 24 h incubation at 37 °C under a humidified 5 % CO_2 to allow cell attachment, the cells in the wells were respectively treated with target compounds and Cisplatin at various concentrations for 48 h. The concentration of DMSO was always kept below 1.25 %, which was found to be non-toxic to the cells. A solution of 3-(4,5-dimethylthiazo1-2-y1)-2,5-diphenyltetrazolium bromide (MTT), was prepared at 5 mg mL^{-1} in phosphate buffered saline (PBS; 1.5 mM KH_2PO_4, 6.5 mM Na_2HPO_4, 137 mM NaCl, 2.7 mM KCl; pH 7.4). 20 µl of this solution was added to each well. After incubation for 4 h at 37 °C in a humidified incubator with 5 % CO_2, the medium/MTT mixtures were removed, and the formazan crystals formed by the mitochondrial dehydrogenase activity of vital cells were dissolved in 100 µl of DMSO per well. The absorbance of the wells was read with a microplate reader at 570 nm. Effects of the drug cell viability were calculated using cell treated with DMSO as control.

Data analysis: Cell survival was calculated using the formula: Survival (%) = [(absorbance of treated cells - absorbance of culture medium)/(absorbance of untreated cells - absorbance of culture medium)]×100.[24,25] The experiment was done in triplicate and the inhibitory concentration (*IC*) values were calculated from a dose response curve.

 DOI: 10.17628/ecb.2014.3.770-775

IC_{50} is the concentration in 'μM' required for 50 % inhibition of cell growth as compared to that of cisplatin as the values is shown in Table 1. IC_{50} values were determined from the linear portion of the curve by calculating the concentration of agent that reduced absorbance in treated cells, compared to control cells, by 50 %. Evaluation is based on mean values from three independent experiments, each comprising at least six microcultures per concentration level.

Treatment of supercoiled plasmid pBR322 DNA with compound 4

To investigate the mechanism of anticancer activity by studying the effect of compound **4** on supercoiled plasmid pBR322 DNA, an experiment was done in which the reaction mixture containing 10 mM Tris HCl (pH 7.5), 0.5 μg of pBR322 plasmid DNA, 100 μM copper, varying with concentrations of compound **4** was taken. Incubation at room temperature was performed for specified time periods. After incubation, 10 μL of a solution containing 40 mM EDTA, 0.05 % Bromophenol blue tracking dye and 50 % glycerol was added and the solution was subjected to electrophoresis in submarine 1 % agarose gel. The gel was stained with ethidium bromide (0.5 mg mL^{-1}), viewed and photographed on a transilluminator.

Detection of hydroxyl radicals ($^{\cdot}OH$)

The detection of hydroxyl radicals was investigated by the method studied by Quinlan and Gutteridge.[26] The reaction mixture (0.5 mL) containing Tris HCl (10 mM, pH 7.5), Calf thymus DNA (200 μg), increasing concentrations of compound **4** (12.5 μM, 25 μM, 50 μM, 75 μM, 100 μM, 200 μM, 400 μM, 600 μM), Cu(II) (100 μM) and volume is made up to 1mL by distilled water and incubated for 60 minutes at 37 ºC. Reaction is stopped using 0.5 ml of TCA (28 %) and 0.5 mL of 1% TBA is added and boiled for 15 minutes and cooled to room temperature. The intensity was read at 532 nm.

Molecular docking

The rigid molecular docking studies were performed using HEX 6.1 software.[27] The initial structure of the steroidal thiazoles was generated by Discovery Studio 3.5. The molecules of compound were optimized for use in the following docking study. The crystal structure of the B-DNA dodecamer d(CGCAAATTTCGC)2 (PDB ID: 1BNA) were downloaded from the protein data bank. All calculations were carried out on an Intel CORE i5, 2.6 GHz based machine running MS Windows 7 as the operating system. Visualization of the docked pose have been done using PyMol molecular graphics program.[28]

Comet assay

To assess the genotoxic effect of the steroidal thiazoles (**4-6**), comet assay[29] was performed in SW480 cells. SW480 (1×10^6) cells were treated with three different concentrations, 20 μg mL^{-1} of steroidal thiazoles (**4-6**) and cisplatin (20 μg mL^{-1}) for 24 h. The cells were then washed and 200 μL of cell suspension in low melting agarose (LMA) was layered on to the labelled slides precoated with Agarose (1.5 %). The slides were placed on ice for 10 min and submerged in lysis buffer (2.5 % NaCl, 100 mM EDTA, 10 mM Tris, 10 % DMSO and 1 % Triton X-100) at pH 10 at 4 °C for more than 1 h. The slides were then equilibrated in alkaline buffer (30 mM NaOH, 1 mM EDTA) at pH 13 at 4 °C, electrophoresed at 0.86 V cm^{-1} at 4 °C, neutralized, washed and dried. At the time of image capturing, the slides were stained with ethidium bromide (ETBr, 150 μL 1X) and cover slips were placed over them. For visualization of DNA-damage, ETBr stained slides were observed under 209 objectives of a fluorescent microscope (Olympus BX-51, Japan). The images of 50-100 randomly selected cells were captured per slide using a CCD camera.

Results and discussion

Chemistry

3*β*-Acetoxy-5*α*-cholestan-6-one **1**, 3*β*-chloro-5*α*-cholestan-6-one **2** and 5*α*-cholestan-6-one **3** were prepared according to the literature procedure.[30-32] Steroidal thiazoles 4-6 were conventionally prepared in one pot synthesis by reacting steroidal ketones **1-3** with iodine and thiosemicarbazide in absolute ethanol (Scheme 1). The key intermediates, α-haloketones are important precursors for the synthesis of a variety of heterocyclic compounds. Literature reveals about the synthesis of thiazoles via a Hantzsch protocol which also makes the reaction of α-haloketones with thiosemicarbazide mechanistically analogous.[33,34] The important feature of this reaction is the formation of α-haloketone intermediate which may be obtained separately by the treatment of ketones with halogens. The advantage of this synthesis is to evade the α-haloketones as a starting material. In spite of this modification, the method still remains cumbersome (13-17 h reflux).

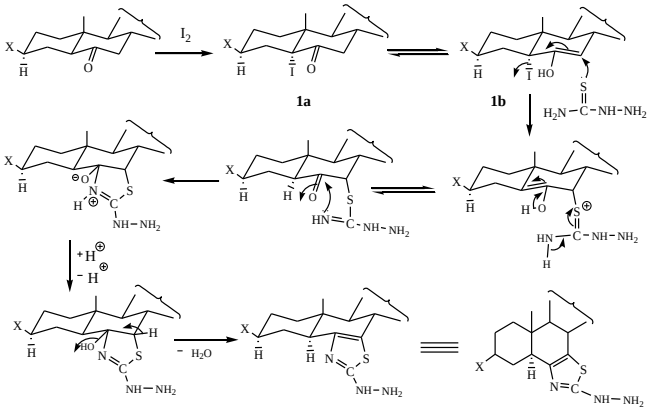

Scheme 2. Allylic displacement of iodine by the attack of sulphur atom of reagent

The formation of products **4-6** can be explained by considering that during the reaction the α-iodoketone 1a formed *in situ* undergoes allylic displacement of iodine via enolization and the subsequent attack of sulphur

 DOI: 10.17628/ecb.2014.3.770-775

Table 1. Showing the IC_{50} values of compounds **4-6** against human cancer cell lines

Compound	IC_{50}, µmol L^{-1}				
	SW480	**A549**	**HepG2**	**HeLa**	**HL-60**
4	13.04±0.6	11.32±0.2	9.71±1.1	13.17±0.4	14.71±0.3
5	21.66±0.4	15.44±1.3	>50	11.74±0.7	26.27±0.5
6	14.03±0.2	13.22±0.7	17.37±1.5	16.62±0.4	>50
Cisplatin	3.52±0.3	10.51 ±0.2	9.8±0.9	9.43±0.5	7.8±1.5

of thiosemicarbazide followed by cyclization leads to the formation of products **4-6** as shown in Scheme 2. An enol tautomeric form **1b** might be the driving force to accelerate the reaction towards product formation.[35]

In vitro anticancer activity

The growth inhibitory effect of compounds **4-6** towards the human cancer cells was measured by MTT [3-(4,5-Dimethylthiazol-2-yl)-2,5-diphenyltetrazolium bromide] assay. The conversion of the soluble yellowish MTT to the insoluble purple formazan by active mitochondrial lactate dehydrogenase of living cells has been used to develop an assay system for measurement of cell proliferation.[22,23] The results are expressed as IC_{50} values (Table 1) which indicate that compounds **4-6** showed different levels of anticancer activities. The compound **4** showed minimum IC_{50}= 9.71±1.1 (HepG2), 11.32±0.2 (A549), 13.04±0.6 (SW480) and 13.17±0.4 µmol L^{-1} (HeLa). While compound **5** showed minimum IC_{50}=11.74±0.7 (HeLa) and 15.44±1.3 µmol L^{-1} (A549). The minimum inhibitions shown by compound **6** were 13.22±0.7 (A549), 14.03±0.2 (SW480) and 16.62 ±0.4 µmol L^{-1} (HeLa).

From these results it is clear that the IC_{50} for compound **4** against A549 cell line is 11.32 ± 0.2 which is very close to the IC_{50} of cisplatin (10.51 ± 0.2) against the same cell line. IC_{50} for compound **5** against HeLa cell line is 11.74 ± 0.7 which is also close to the IC_{50} of cisplatin (9.43 ± 0.5) against the same cell line. Similarly IC_{50} for compound **4** against HepG2 is 9.71 ± 1.1 which is also near to the IC_{50} of cisplatin (9.6 ± 0.3) against the same cell line. It can be concluded that Compound **4** and **5** are showing potential anticancer activity against A549, HepG2, HeLa cell lines by showing IC_{50} close to that of standard drug, Cisplatin thus can be considered as potential cytotoxic agents. The graphical representation of IC_{50} values in MTT assay is shown in Fig. 1.

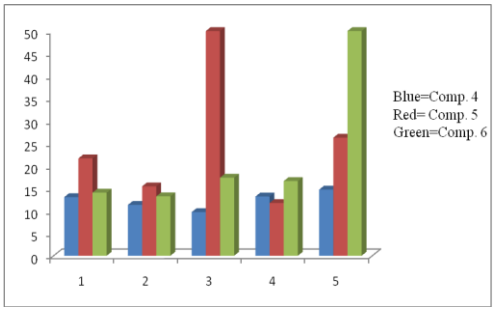

Figure 1. Graphical representation of IC_{50} values shown by compound **4-6** against SW480, A549, HepG2, HeLa and HL-60 by MTT assay

Treatment of supercoiled plasmid pBR322 DNA with compound 4 and detection of hydroxyl radicals (OH)

Anticancer activity mechanism was also confirmed by studying the treatment of supercoiled plasmid pBR322 DNA with different concentrations of compound **4** and 100 µM copper. Our nucleolytic experiments suggest that cell death may be due to cleavage or fragmentation of DNA of these cancer cells and that the active species responsible for this are ROS (hydroxyl radical) which resulted from the *in vitro* reaction of different concentrations of compound **4** with copper in presence of thiobarbituric acid. We observe from gel electrophoresis that after adding copper (100 µM) the concentration of radicals increase which in presence of different concentrations of compound **4** show the nicking of plasmid pBR322 DNA from its supercoiled form (form I) to open circular form (form II). Fig. 2 reveals that in lane 6, 7 and 8, the nicking is quite obvious by the disappearance of form I and appearance of form II and with the increase in concentration of compound **4** (lane 8) the band intensity (form II) became maximum, depicting the more pronounced cleavage at high concentration.

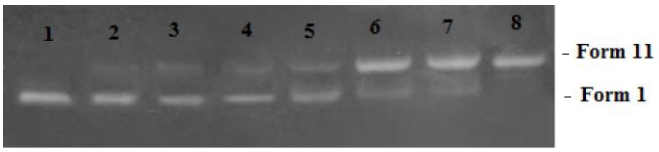

Figure 2. Fragmentation pattern of supercoiled plasmid pBR322, Lane 1 contains DNA only, lane 2 contains DNA and copper, lane 3, 4 and 5 contain DNA and compound **4** (100, 200 and 300 µM respectively) and lane 7, 8 and 9 contain DNA and compound **4** (100, 200, 300 µM respectively) plus 100 µM copper added to it.

In the DNA cleavage reactions mediated by various antioxidants in the presence of Cu(II), it has been established that Cu(II) is reduced to Cu(I) by the antioxidants and that Cu(I) is an essential intermediate in the DNA cleavage reactions.[36,37] It is also generally understood that DNA cleavage by various antioxidants and Cu(II) is the result of the generation of hydroxyl radicals. As mentioned in literature also, Cu(II) is reduced to Cu(I) and the re-oxidation of Cu(I) to Cu(II) by molecular oxygen gives rise to superoxide anion which in turn leads to the formation of H_2O_2.[38] Presumably Cu(I) is oxidized to Cu(II) by H_2O_2 in a Fenton type reaction giving rise to hydroxyl radicals. To determine the hydroxyl radical production and the role of copper ions in DNA cleavage, an experiment was performed where progressively increasing concentrations of compound **4** and cisplatin (12.5-600 µM) were tested on thiobarbituric acid induced DNA breakage (Fig. 3) and from these results we may conclude that the DNA cleavage by thiobarbituric acid involves endogenous copper ions and also that Cu(I) is an intermediate in the pathway that leads to DNA cleavage.

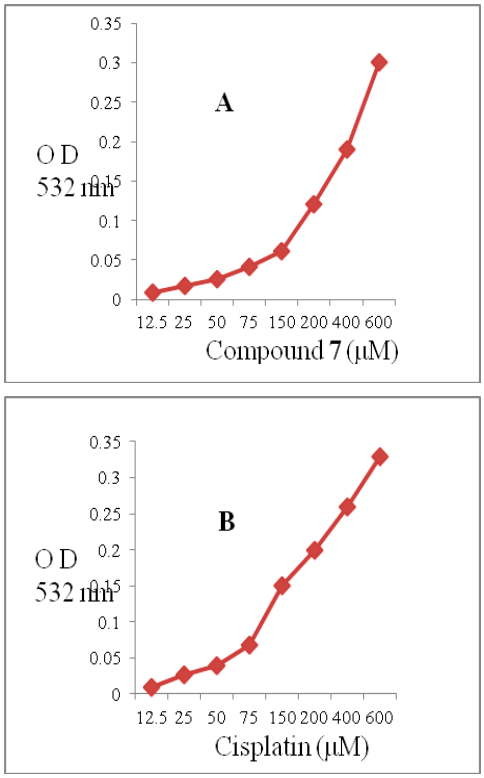

Figure 3. Showing comparative determination of hydroxyl radical production by compund **4** (A) and cisplatin (B) by the assay of thiobarbituric acid

The compound **4**–Cu(II) (Fig. 3A) and cisplatin–Cu(II) (Fig. 3B) are shown to generate the hydroxyl radicals that react with CT DNA, result in strand breaks. The assay is based on the fact that degredation of DNA by hydroxyl radical results in the release of TBA reactive material, which forms a coloured adduct readable at 532 nm.[39] Increasing concentrations of compound **4** or Cisplatin in presence of Cu(II) showed a corresponding increase in the generation of hydroxyl radicals. However, the generation of hydroxyl radical being more in case of cisplatin as shown in Fig. 3B. The results in Fig. 3 confirmed the relatively higher rate of formation of hydroxyl radicals and correlated with the rate of DNA degredation by the compound **4** as well as cisplatin.

Comet assay

In the comet assay, the images of SW480 cells treated with compounds (**4-6**) showed the formation of comets. Compound **4** presented maximum apoptotic DNA damage followed by compound **6** and **5**, which is in accordance with its maximum cytotoxicity as seen in MTT assay. None of the steroidal thiazoles exhibited apoptotic DNA damage to the extent of Cisplatin. The quantified increase in DNA damage suggested that all three thiazole derivatives induced dose dependent fragmentation of chromosomal DNA leading to apoptosis. The images of comet assay for control, cells treated with Cisplatin (20 μg mL^{-1}), **4** (20 μg mL^{-1}), **5** (20 μg mL^{-1}), and **6** (20 μg mL^{-1}) are shown in Fig. 4. Slides were analyzed for parameter like tail length (TL), using image analyzer CASP software version 1.2.2. The results of the assay for tail length are shown in graph given in Fig. 4.

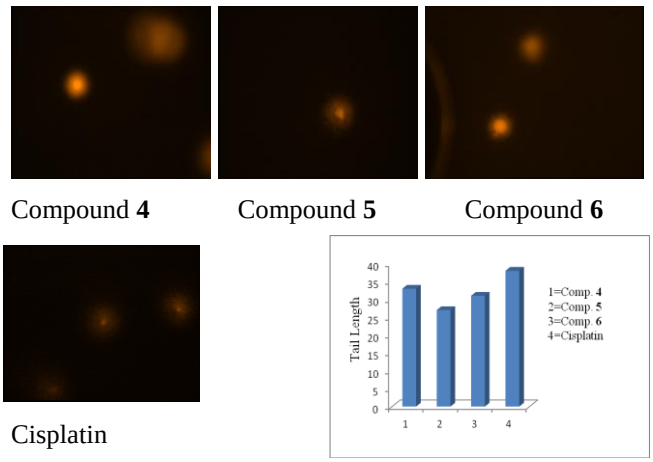

Figure 4. Detection of DNA damage in SW480 cells. Treated cells (24 h) were layered over agarose gel, lysed, electrophoresed in alkaline buffer and stained with propidium iodide. Control cells were treated with DMSO alone. The DNA fragmentation resulting in a comet-like appearance in cells treated with cisplatin and compounds **4-6**.

Molecular docking studies with DNA

In our experiment, molecular docking studies of steroidal thiazoles with DNA duplex of sequence d(CGCGAATTCGCG)$_2$ dodecamer (PDB ID: 1BNA) were performed in order to predict the chosen binding site along with preferred orientation of the molecules inside the DNA groove. The resulted docked model (Fig. 5) depicted that all the three compounds recognized minor groove interaction leading to van der Waals and hydrophobic interaction with DNA functional groups which stabilizes the groove and leads to the stablity of the complex. The compound **4** showed electrostatic interaction in the form of hydrogen bonding with NH of 7th Thiamine at a distance of 2.88 Å by the acetate group at 3β-position of steroidal molecule. The compound **5** showed the groove fit behaviour and arranged in a perpendicular manner with respect to the minor groove walls of the DNA helix while as compound **6** showed electrostatic interaction in the form of hydrogen bonding with NH of 11th Thiamine at a distance of 3.21 Å. The resulting relative binding energies of docked steroidal thiazole (**4-6**)–DNA complexes were found to be -308, -319 and -314 kJ mol^{-1}, respectively depicting the decrease in the energy after forming complexes with DNA.

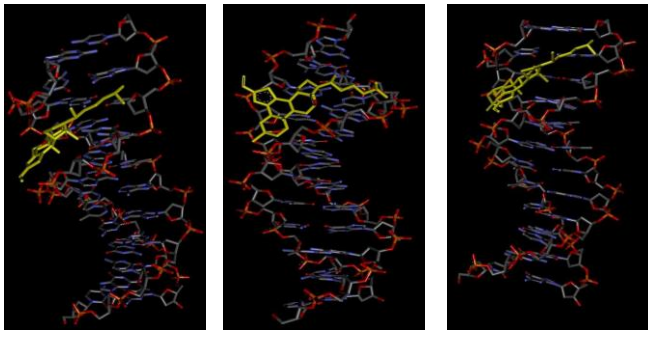

Figure 5. Cartoon representation of DNA molecules with the bound compounds. The steroidal thiazole derivatives are shown as yellow colour. Figure (a), (b), and (c) shows minimum energy poses of DNA–Steroidal thiazole (**4-6**) complexes, respectively.

Conclusion

In summary, we have developed a facile and convenient approach for the preparation of new steroidal thiazole derivatives in one-pot synthesis. All the newly synthesized compounds were evaluated for the anticancer activity *in vitro* against five cancer cell lines. The preliminary results showed that compounds **4-6** were found active during anticancer as well as genotoxic screening but compounds **4** and **6** were found to be potential anticancer agents. These compounds were also found to catalyze the oxidative degradation of isolated DNA either alone or in the presence of transition metal ions such as copper. However, in presence of copper the oxidative cleavage was enhanced. As mentioned earlier cancer cells being rich in transition metal ion like copper[40] we conclude that compound **4** in presence of endogenous copper may give rise to hydroxyl radical this may lead to the oxidative DNA cleavage in cancerous cells. Hence this protocol provides a convenient strategy to annelate steroid nucleus with widespread bioactive thiazoles there by extending the categories of heterosteroids. This strategy may also provide valuable information for the further design and development of more active anticancer agents through various modifications and derivatizations.

Acknowledgement

Authors thank the Chairman, Department of Chemistry, AMU Aligarh, for providing basic research facilities and Department of Biochemistry, JNMC, AMU for biological study of the compounds.

References

[1]Dauvious, S., Parker, M. G., *Steroid hormone action*, IRL Press Oxford, **1993**, 161-185

[2]Dubey, R. K., Oparil, S., Imthurn B., Jackson, E. K., *Cardiovasc. Res.*, **2002**, *53*, 688-708

[3]Latham, K. A., Zamora, A., Drought, H., Subramanian, S., Matejuk, A., Offner H., Rosloniec, E. F., *J. Immunol.*, **2003**, *171*, 5820-5827

[4]Moudgil, V. K., *Steroid receptors in health and disease*, New York/London: Plenum Press, **1987**.

[5]Gower D. B., Makin, H. L. J., "*Biochemistry of steroid hormones*," Oxford/ London/Edinburgh: Blackwell Scientific Publications. 1984, 122

[6]Hargrave, K. D., Hess F. K., Oliver, J. T., *J. Med. Chem.*, **1983**, *26*, 1158-1163

[7]Bondock, S., Khalifa W., Fadda, A. A., *Eur. J. Med. Chem*., **2007,** *42*, 948-954

[8]Sharma, P. K., Sawnhney, S. N., Gupta, A., Singh G. B., Bani, S. *Indian J. Chem*., **1998**, *37B*, 376-381

[9]Jaen, J. C., Wise, L. D., Caprathe, B. W., Tecle, H., Bergmeier, S., Humblet, C. C., Heffner, T. G., Meltzner L. T., Pugsley, T. A., *J. Med. Chem.*, **1990**, *33*, 311-317

[10]Tsuji, K., Ishikawa, H., *Bioorg. Med. Chem. Lett.*, **1994**, *4*, 1601-1606

[11]Bell, F. W., Cantrell, A. S., Hogberg, M., Jaskunas, S. R., Johansson, N. G., Jordon, C. L., Kinnick, M. D., Zhou, X. X., *J. Med. Chem.*, **1995**, *38*, 4929-4936

[12]Ergenc, N., Capan, G., Günay, N. S., Ozkirimli, S., Güngör, M., Ozbey S., Kendi, E., *Arch. Pharm. Pharm. Med. Chem.*, 1999, *332*, 343-347

[13]Carter, J. S., Kramer, S., Talley, J. J., Penning, T., Collins, P., Graneto, M. J., Seibert, K., Koboldt, C., Masferrer J., Zweifel, B., *Bioorg. Med. Chem. Lett.*, **1999**, *9*, 1171-1174

[14]Badorc, A., Bordes, M. F., De Cointet, P., Savi, P., Bernat, A., Lale, A., Petitou, M., Maffrand, J. P., Herbert, J. M., *J. Med. Chem.*, **1997,***40*, 3393-3401

[15]Rudolph, J., Theis, H., Hanke, R., Endermann, R., Johannsen L., Geschke, F. U., *J. Med. Chem.*, **2001**, *44*, 619-626.

[16]Pattan, S. R., Dighe1, N. S., Nirmal, S. A., Merekar, A. N., Laware, R. B., Shinde, H. V., Musmade, D. S., *Asian J. Research Chem*., **2009**, *2*, 196-201.

[17]Burger, R. M., *Chem. Rev*., **1998**, *98*, 1153-1169.

[18]Westheimer, F. H., *Science*, **1987**, *235*, 1173-1178

[19]Jin, Y., Cowan, J. A., *J. Am. Chem. Soc*., **2005**, *127*, 8408–8415.

[20]Smith, J., Ariga, K., Anslyn, E. V., *J. Am. Chem. Soc*., **1993**, *115*, 362-364

[21]Scheffer, U., Strick, A., Ludwig, V., Peter, S., Kalden, E., Gobel, M. W., *J. Am. Chem. Soc*., **2005**, *127*, 2211-2217

[22]Slater, T. F., Sawyer, B. Strauli, U., *Biochim. Biophys. Acta*., **1963**, *77*, 383-393,

[23]Mosmann, T., *J. Immunol. Methods*, **1983**, *65*, 55-63

[24]Saxena, H. O., Faridi, U., Kumar, J. K., Luqman, S., Darokar, M. P., Shanker, K., Chanotiya, C. S., Gupta M. M., Negi, A. S., *Steroids*, **2007**, *72*, 892-900.

[25]Woerdenbag, H. J., Moskal, T. A., Pras, N., Malingre, T. M., El-Feraly F. S., Kampinga, H. H., *J. Nat. Prod.*, **1993**, *56*, 849-856

[26]Quinlan, G. J., Gutteridge, *Biochem. Pharmacol.*, **1987**, 36, 3629-3633.

[27]Mustard, D., Ritchie, D. W., PROTEINS: *Struct. Funct. Bioinf*., **2005**, *60*, 269-274.

[28]Delano, W. L., The PyMOL Molecular Graphics System, DeLano Scientific, San Carlos, CA, USA, **2002**.

[29]Singh, N. P., *Mut. Res*., **2000**, *455*, 111-127.

[30]Constantine, E., Anagnostopoulos, Fieser, L. F., *J. Am. Chem. Soc*., **1954**, *76*, 532-536

[31]Backer, R. H., Squire, E. N., *J. Am. Chem. Soc*., **1948**, *70*, 1487-1490

[32]Rajnikant, Gupta, V. K., Firoz, J., Shafiullah, Gupta, R., *Cryst. Reports*, **2000**, *45*, 785-788

[33]Hantzsch, A., Weber, J. H., *Ber. Deutsch. Chem. Ges.*, **1887**, *20*, 3118-3132

[34]Rudolph, J., *Tetrahedron*, **2000**, *56*, 3161-3165

[35]Yang-i Lin, C. M., Seifert S. M., Kang J. P., Lang, S. A., *J. Heterocycl. Chem*., **1979**, *16*, 1377-1383

[36]Shamsi, F. A., Husain S., Hadi, S. M., *J. Biochemical Toxicol.*, **1996**, *11*, 67-71

[37]Ahmad, M. S., Fazal, F., Rahman, A., Hadi S. M., Parish, J. H., *Carcinogenesis*, **1992**, *13*, 605-608

[38]Badwey J. A., Kaenovsky, M. L., *Annual Rev. Biochem.*, **1980**, *49*, 695-726,

[39]Gupte A. Mumper, R. J., *Cancer Treat. Rev.*, **2009**, *35*, 32-46,

[40]Halliwell B., Gutteridge, J. M. C., *FEBS Lett.*, **1992**, *307*, 108-112

Received: 02.06.2014.
Accepted: 07.07.2014.

PHYSICO-CHEMICAL ASSESSMENT OF POLLUTION IN THE CALEDON RIVER AROUND MASERU CITY, LESOTHO

Emmanuel B. Tanor,[a] Sidwell Ts'enoli[a] and Mosotho J. George[a]

Keywords: water pollution, physico-chemical properties, principal component analysis, Caledon River, Maseru.

Water quality around the cities is a global concern owing to the impact of the population density and industrial activities. Assessment of the Caledon River (Mohokare), which flows along the periphery Maseru City, was carried out using a number of physico-chemical properties. The data obtained shed considerable light to the effect of the textile industry on the water quality. There was generally much higher increase in most parameters up to 900% at sampling site where textile effluents joins the river water (Tikoe-Thetsanae) compared to 'Maliemere (a sampling site upstream of the city). There was however a slight decrease in other parameters (dissolved oxygen, pH) while other parameters (silicates, nitrates and phosphates) did not seem to change or follow any particular pattern. Principal component analysis indicated conductivity, turbidity and total dissolved solids as the most prominent variants accounting for major difference in the PC1 in agreement with the comparison of relative amounts as a percentage of the 'Maliemere sampling site. The major contributor along the PC2 was found to be the silicates. However, only the concentrations of phosphates were above the maximum contaminant level (0.74 compared to 0.1 mg L^{-1} respectively) at all sampling points. Hence it is concluded that the water quality assessment shows a detrimental impact on the quality of the water.

Corresponding Authors
Tel: +266 5221 3502/3
Fax: +26 2234 0000
E-Mail: eb.tanor@nul.ls (E.B.Tanor); jm.george@nul.ls (M. J. George)
[a] Department of Chemistry and Chemical Technology, National University of Lesotho, P.O. Roma 180, Lesotho. Southern Africa.

Introduction

In recognition of the importance of the valuation of water resources to the country, the Government of Lesotho established the Division of Hydrological Survey under the Ministry of Public Works in the 1970's which later metamorphosed to Department of Water Affairs under the Ministry of Natural Resources. This Department is responsible for the integration of water resources management through water quality and quantity monitoring, updating and maintaining the water resources database as well as liaising with the international organisations in which Lesotho is a member while being guided by the Water Act of 2008.[1,2]

Lesotho is highly endowed with fresh water resources leading to the sale of the water to the Republic of South Africa through a multi-billion project called Lesotho Highlands Water Project earning closer to 25 % of its export and 5 % of the GDP.[3] This has led to a saying that water is Lesotho's white gold.[4,5] Despite this, access to clean water is still a challenge in the cities in Lesotho, such as Maseru, the situation which has led to the dependence of the city on Mohokare (Caledon) river for the municipal water supply owing to the lack of infrastructure to collect relatively cleaner water from the mountains. This however, is about to become history in that a multi-billion project to catch water at one rural area called Metolong and channel it to supply the Maseru City and neighbouring towns through the support of United States Millennium Challenge Corporation with between US$ 362- 400 million in cash injection.[6,7]

Trans-boundary river pollution is one of the critical issues between neighbouring countries especially for those countries with upstream/downstream configuration. This is the situation between Lesotho and its sole neighbour South Africa. Lesotho lies upstream and its rivers converge to Caledon, Makhaleng and Orange Rivers that flow into South Africa. Despite the generally clean water from the mountains, there are concerns about the quality of water in rivers that traverse through the highly dense and industrialised areas such as Maseru with some textile industries owned by Chinese companies due to the AGOA agreement that allows Lesotho and other African countries to export textile products to American markets without paying any 'tariff barriers'.[8] Since the introduction of AGOA in 2001, exports from Lesotho to the US have increased considerably, and Lesotho has become one of the largest exporters of apparel in Africa to the American market.[9]

In recognition of importance of clean water, there are arguments that by 2025, the World could face wars about water and not oil.[10] Cookley reported the first war over water in 1967 between Israel and its Arab neighbours Syria and Egypt after the latter tried to divert the River Jordan.[11] Gleick and Heberger argue that the conflicts over water resources are continuing despite the studies into prevention of such.[12] Gizelis and Wooden argue that most studies have focused on proving or disproving a direct deterministic relationship between scarcity of resources and conflict.[13] Katz on the other hand argues that the prediction of war over water is an over exaggeration of those seeking incentives for conserving water hence questioned the merits of such arguments.[14] Whatever the case, there seems to be some contention that warrants a study of trans-boundary water especially in the upstream/downstream setting to maintain peace and harmony between neighbouring countries.

There are many parameters that are used in river pollution monitoring such as using fresh water algae.[15,16] Other techniques especially at trace quantitative level require

highly sophisticated and expensive analytical instrumentation such as spectrometers. The price and level of investment depends on the level of the pollutant being considered. Some attributes are considered of primary while others are of secondary importance. The primary drinking water standards regulate organic and inorganic chemicals, microbial pathogens, and radioactive elements that may affect the safety of drinking water. These standards set limits - the maximum contaminant level (MCL) - on the highest concentrations of certain chemicals allowed in the drinking water supplied by a public water system. The most prominent agencies for setting these standards is United States Environmental Protection Agency (US-EPA)[17] and the World Health Organisation (WHO).[18]

Water quality analysis and monitoring usually generate a large volume of data. Multi-variate statistics is therefore used extensively in high volumes of data to reduce the data multiplicity to identify only a few parameters that are responsible for the variations within the system,[19] while preserving the relationships in the original data.[20] Due to its robustness multi-variate statistics has been reported in a number of areas ranging from medical diagnostics,[21] plant pathology,[22] engineered structures[23] to environmental monitoring.[24]

This study presents the analysis of a number of physico-chemical properties of the Caledon (Mohokare) River water which is an important source of potable water for the city of Maseru. The river flows along the periphery of the city and forms the national border with the Republic of South Africa. The study assesses the perceived impact of the indiscriminate discharge of domestic waste and industrial wastewater at various stages of treatment and uncontrolled inflows of urban surface run-offs on the quality of this river water. The data generated was analysed using conventional statistics and principal component analysis to identify the major contributors to the pollution from these multiple of the parameters.

Experimental

Sample collection and handling

The five sampling sites were selected at strategic locations with reference to key industries and human activities, which are potential sources of surface water pollution. The other deciding factor for selecting the sampling locations was the ease of accessibility of the sites. The sampling points from upstream to downstream as per the designation by the Department of Water Affairs are 'Maliemere, Seapoint, LEC, Ratjomose and Tikoe-Thetsane. The satellite image in Figure 1 shows the sampling sites designated with flags with the river flowing from top right corner to the bottom left corner of the picture. The sampling points are designated with small flags.

The collection, handling and preservation of samples were consistent with standard principles.[25,26] Some of the parameters, conductivity, dissolved oxygen, pH, temperature and turbidity were measured in the field at the sampling points to reflect the true values.

Figure 1. The Caledon River in Maseru showing the sampling points

Samples were collected on the same day at all sampling points to avoid possible momentary fluctuations in some of the target parameters as a result of surface run-off from rain or any other discharges into the river from the communities.

Determination of the selected physico-chemical parameters

Most of the analysis followed the New South Wales guidelines for sampling and analysis of water pollutants.[27] The field measurements were made using the Mettler-Toledo GmbH MX 300 multi-meter (Giessen, Germany) equipped with the temperature, pH, Dissolved Oxygen and Conductivity probes. The other parameters were determined in the laboratory by spectrophotometric methods using HACH DR/2400 Spectrophotometer (Düsseldorf, Germany), which has prescribed programmes and reagents/kits for each parameter. A 25-mL volume of each of the samples was used for the determination of each parameter using a set of specified reagents and programme for each parameter.[28] Total nitrogen was determined according to the US-EPA Method 1688.[29]

Data analysis

Other than a normal comparison of the data using normal replicates (n=3) for individual parameters, the data was subjected to the principal component analysis using the SIMCA P 13.0 Software (Umetrics, Umea Sweden).

Results and discussions

Determination of physical parameters

The quantities of the physical parameters determined were as presented in Table 1.

A clear comparison of the changes in the abundance of these parameters downstream was plotted relative to 'Maliemere sampling site and presented in Figure 2.

Table 1. Some physical parameters determined at different sampling sites

Sampling site Parameter	'Maliemere	Seapoint	L.E.C	Ratjomose	Tikoe-Thetsane
pH	7.34	7.77	7.54	8.20	7.95
Temperature, °C	20.5	19.6	18.4	20.8	21.2
Conductivity, µS cm^{-1}	257	286	355	367	458
Total dissolved solids, mg L^{-1}	88	90	123	126	157
Total suspended solids, mg L^{-1}	10	16	47	54	65
Turbidity, NTU	12	17	38	46	78
Dissolved oxygen, mg L^{-1}	0.95	0.87	0.72	0.84	0.69

Table 2. Chemical parameters determined at different sampling sites

Sampling site Parameter	'Maliemere	Seapoint	L.E.C	Ratjomose	Tikoe-Thetsane
NH_3, mg L^{-1}	0.30	0.29	0.34	0.38	0.32
Cl_2, mg L^{-1}	0.02	0.04	0.15	0.14	0.19
Total chlorine, mg L^{-1}	0.05	0.07	0.19	0.20	0.25
SiO_4^{4-}, mg L^{-1}	18.7	30.6	20.5	37.7	40.5
SO_4^{2-}, mg L^{-1}	14	17	12	15	13
Fe, mg L^{-1}	0.08	0.12	0.16	0.24	0.31
Total Fe, mg L^{-1}	0.17	0.25	0.31	0.42	0.50
Mn, mg L^{-1}	0.2	0.4	0.7	0.5	0.3
PO_4^{3-}, mg L^{-1}	0.57	0.64	0.71	0.68	0.74
NO_3^-, mg L^{-1}	1.7	1.6	1.3	1.6	1.4
NO_2^-, mg L^{-1}	0.003	0.005	0.004	0.003	0.007
Total Kjeldahl nitrogen, mg L^{-1}	35	23	19	29	21

An inspection of Figure 2 clearly shows that most parameters were increasing from Maliemere to Tikoe-Thetsane with suspended solids and turbidity increased to higher 600 % in Tikoe-Thetsane relative to 'Maliemere. Temperature is the only parameter that did not seem to change between the sampling sites ranging between 18.4 °C and 21.2 °C. Water temperature is important in water quality because it affects the rates of biological and chemical processes in the water as well as influencing the volume of dissolved oxygen in the water. Dissolved oxygen on the other hand seemed to decrease (1.5 to 0.65 mg L^{-1}) albeit not considerably as compared to other parameters such as suspended solids. The drop in dissolved oxygen can however not be totally be attributable to the noted temperature increase although this is a known fact the higher the temperature the less the dissolved oxygen, since the decrease in oxygen content is more marked than the increase in temperature. Dissolved oxygen is one of the most important water quality parameters for freshwaters, because aquatic organisms cannot survive without oxygen. Generally, dissolved oxygen levels lower than 5.0 mg L^{-1} are stressful to aquatic organisms.[30] Thus this indicates that this river is not habitable to most aquatic life.

The pH values fall within a narrow range of 8.20 to 7.15 units indicating neutral to slightly alkaline conditions for all the five sampling points. The highest pH values were measured at the Ratjomotse sampling point with the mean pH of 8.20 units. However the variation is not significant. The conductivity values fall within a wide range from 252 µS cm^{-1} ('Maliemere) to 490 µS cm^{-1} (Tikoe-Thetsane). Freshwater sources usually have a low conductivity and there is no set standard for the conductivity of water. Despite the lack of standards and the effects of the surrounding environment and local geology on conductivity, there are approximate values for freshwater sources in the range of 600 – 2000 µS cm^{-1}.[31]

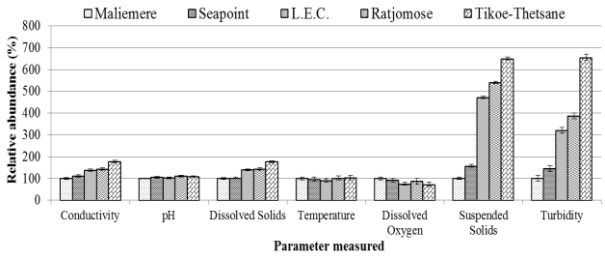

Figure 2. The abundances of the physical parameters relative to 'Maliemere sampling site

Total dissolved solids (TDS) give a general indication of the level of dissolved solids in the stream or lake that are smaller than 2 microns.[32] This includes all of the disassociated electrolytes that make up salinity concentrations, as well as other compounds such as dissolved organic matter. A high concentration of dissolved ions is not necessarily an indication of pollution of the stream. It is normal for streams to dissolve and accumulate fairly high concentrations of ions from the minerals in the rocks and soils over which they flow.

Table 3. Comparison of Maximum Contaminant Levels of Some Domestic Water Quality Parameters with the values obtained in the study

Parameter	*RSA (1996)	§ USA (2009)	#WHO (2008)	Obtained values from Caledon River Samples	
				Minimum	Maximum
pH value	6.0 – 9.0	6.5 – 8.5	6.5 – 8.5	7.34	8.20
TDS, mg L^{-1}	450	500	-	257	458
Turbidity, NTU	10	2	-	12	87
NO_2^- nitrogen, mg L^{-1}	-	0.1	0.5	0.003	0.007
NO_3^- nitrogen, mg L^{-1}	-	10.0	50	1.3	1.7
NH_3 nitrogen, mg L^{-1}	1.0	0.1	0.5	0.32	0.38
Phosphates (PO_4^{3-}), mg L^{-1}		0.1		0.57	0.74
Sulfate (SO_4^{2-}), mg L^{-1}	200	250	250	12	17
Total chlorine, mg L^{-1}	-	4.0	-	0.02	0.19
Iron, mg L^{-1}	0.1	0.3	0.2	0.17	0.50
Manganese, mg L^{-1}	0.05	0.05	0.05	0.2	0.7

Sources: #WHO, 2008; §US-EPA, 2009; * South African Quality Standards – Domestic use, 1996

A variety of human activities may contribute to elevated levels of TDS in river water. A few examples are fertilizers and urban runoffs during storm and wastewater and septic system effluents can add a variety of ions to a stream.[33] Dissolved solids are also important to aquatic life by keeping cell density balanced.[34] However, depending upon the ionic properties, excessive TDS can produce toxic effects on fish and fish eggs.[31]

The TDS values increase downstream from 'Maliemere to Tikoe-Thetsane sampling points. The values ranged between 75.85 and 185.20 mg L^{-1} 156.70 to 88.50 mg L^{-1} mean values respectively (See Table 1). The DO levels decrease downstream as the river flows along the industrial area where different industrial and domestic wastewaters, urban run-offs, storm waters and other discharges are discharged into it, which increase the amount of nutrients, i.e. phosphorus, nitrogen as ammonia, nitrate, and nitrite and organics. This can result in the increased growth of algae and flora and fauna that together use up oxygen, thus reducing the DO. The presence of oxidisable species and increased salinity further reduces DO as observed downstream.[35]

Total suspended solids (TSS) concentrations and turbidity both indicate the amount of solids suspended in the water, whether minerals or organic. While TSS measures the actual weight of solids per unit volume of water, turbidity measures the amount of light scattered from a water sample as the result of the suspended particles. High values for TSS and turbidity decreases light penetration and productivity and increases water temperature because suspended particles absorbs more heat. This will in turn decrease DO as warm water dissolves less oxygen.

The mean TSS values ranged from a maximum of 65 mg L^{-1} at the lowest downstream sampling point at Tikoe-Thetsane to a minimum of 10 mg L^{-1} at the uppermost upstream sampling point at 'Maliemere. The corresponding turbidity values are 78 NTU and 12 NTU respectively. TSS combined with storm water discharges play a crucial role in wet-weather pollution in urban areas and TSS during rain events can have toxic effects of aquatic organisms, because major potential toxic substances, such as heavy metals, organic matter can be absorbed onto TSS that would latter settle down into the sediments.[36]

Interestingly, there was a significant correlation between the conductivity and total dissolved solids (R^2 = 0.9839) as well as with the total suspended solids (R^2 = 0.9451) indicating the cause-effect relationship between these parameters.

Determination of Chemical Parameters

Chemical properties are those elements that can come from the chemical weathering of the rocks or washed into the river water from other activities. The chemical parameters analysed are as in Table 2. A graphical representation of the amounts at different sampling sites relative to 'Maliemere is shown in Figure 3.

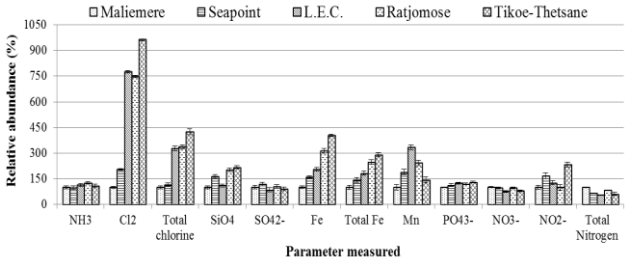

Figure 3. Some relative amounts of chemical parameters downstream of the river

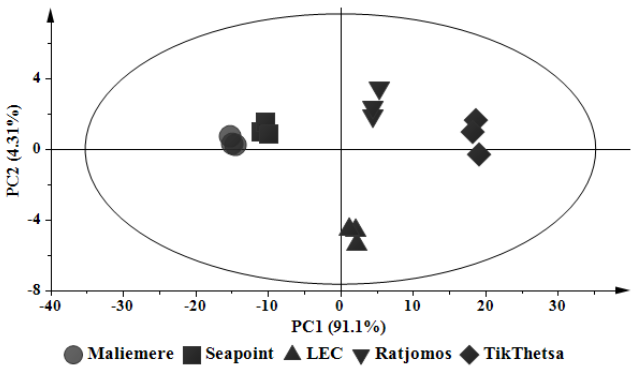

Figure 4. PCA scores plot: the scores plot (PC1 vs PC2) showing sample clustering.

Elements such as phosphorus and nitrogen are important plant nutrients. However excessive amounts in water can cause eutrophication which upsets the ecosystem through the reduction of light penetration capacity thus affecting other aquatic flora and fauna. Nitrates and phosphates levels vary within a narrow range 1.30 to 1.70 mg L^{-1} for nitrates and 0.57 to 0.74 mg L^{-1} for phosphates. The highest levels for nitrates were recorded at the 'Maliemere sampling point with a mean of 1.74 mg L^{-1}. This could be attributable to the surface run-off from fertilizers coming from the fields across the river in the South African side. The recommended levels for nitrates and nitrites to sustain the aquatic life and human consumption are 10 mg L^{-1} and 1.0 mg L^{-1} respectively. Typical levels of phosphorous in natural waters 0.02 mg L^{-1}.[37]

A guideline limit for phosphorus is 0.1 mg L^{-1} for surface waters. However, the range for the mean of total Kjeldahl nitrogen is 19-35 mg L^{-1}, which is much higher than the sum of nitrates, nitrites and ammonia indicating that there could be another significant source of nitrogen besides these three forms.

The levels of most parameters studied were within the maximum contaminant levels (MCL) as shown in Table 3. The value for phosphates was found to be more than 5 times the MCL values, at all the sampling sites including 'Maliemere which is has limited human activity. The decreasing amounts downstream could be attributable to dilution as other water streams and/or discharges join the river. Chlorine seemed to be the most dominant chemical species whose variation was about 10 times that in 'Maliemere. This could be attributable to the use and disposal of the chlorinated water in the munipality as well as bleaching processes in the textile industries.

The samples from the Tikoe-Thetsane point have the highest concentrations for the all the parameters investigated and a sharp increase in the concentrations was observed between Ratjomose and Tiko-Thetsane sampling points. This could be due the fact that the effluent from the wastewater treatment plant, which receives and treats the effluent from all the industries (mostly partially treated or totally untreated) in the Thetsane industrial area, is discharged into the river upstream to this sampling point.

Principal Component Analysis for potential markers for major differences

Examination of data in Tables 1 and 2, in comparison with Figure 2 and 3 creates some confusion as to which of the components account for the major pollution and that can be used as markers in this respect. Hence a principal component analysis of the complete raw data was used to determine the relationship between the sampling points. A five-component model, explaining 99.6 % of the variance (with the accuracy of prediction of 95.4 %), was computed.

The resulting scores and loadings plots are presented in Figures 4 and 5. A scores plot was constructed from PC1 and PC2 [R^2X (cum) of 0.954, Q^2 (cum) of 0.875 and 95 % confidence] and explains 95.4 % of the variation, and shows a differential clustering of the samples (sampling sites).

Clearly each of the sites seems to form its own cluster differentially from the rest with 'Maliemere and Seapoint sites closer to one another that the other sites. This makes sense in that 'Maliemere site comes prior to the city area and the Seapoint area is just on the northern tip of the city where not much effluent from the populated area is discharged. This suggests that the two sites are more similar (in the detected/measured variables) in comparison to the rest of the sites. The perpetual increase along PC1 demonstrates the continual increase of the contribution of the component as the river traverses the sampling sites. Interestingly, the LEC site seems to drift away from the rest of the sites and seems to be different in the PC2. However, it is still in line with the rest of the sites on the PC1. There are few industries around this side so the difference could be brought by the nature of the chemicals discharged into the river.

To understand more the underlying variables responsible of the clustering and the deviations observed on scores plot, a loadings plot was computed as shown in Figure 5.

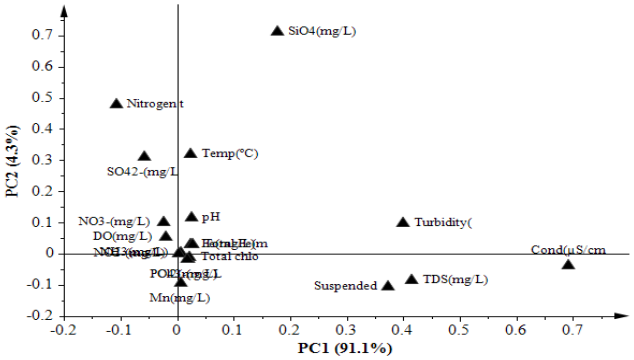

Figure 5. PCA loadings plot showing variables responsible clustering on the scores plot

From the loadings plot in Figure 5, it could be seen that variables that contribute significantly to the clustering are SiO_4^{4-} content and conductivity. The other variables that contributed to the shift of the LEC site from the rest of the sampling sites were nitrogen, temperature and sulphates; while those along the PC1 axis are those that generally change as the river flows downstream. The clustering along the PC1 was expected given that as the river traverses along the city, there are a number of areas that possible could lead to some increased level of pollution. What was surprising was the expression of variability in PC2.

A close inspection of the components drifting along the PC2 (those responsible for L.E.C. site deviation), namely, SiO_4^{4-}, SO_4^{2-}, temperature and Nitrogen, it was observed that these components break the trend of increasing levels of the other analytes from 'Maliemere down to Tikoe-Thetsane site as shown in Figure 4. The values did not conform to any trend as opposed to those values along the PC1 axis. It is however difficult to attribute the observed deviation along the PC2 to anything, except noting that there are some textile factories around that area as shown in Figure 4. Soluble silica in natural waters is usually not ionized, but present as the orthosilicic acid H_4SiO_4 or $Si(OH)_4$. The chemical transformation of silica in freshwaters is complex and it is influenced by the biological activity aquatic organisms such as diatoms. There is also an important relationship between silicon and the major nutrients, phosphorus in particular.[38]

Figure 6. The sampling point L.E.C and factories within close distance to the river

As can be seen from the map, the factories lie up-stream (towards the right with flow towards the left) of the L.E.C. sampling site marked with a flag since their discharge goes in the north direction. Some key parameters responsible for the PC2 variation were identified and their trends are presented in Figure 5. Only four of these, SiO_4^{4-}, nitrogen, temperature and SO_4^{2-} that can be picked from the loadings plot in Figure 3, are presented for the ease of scaling.

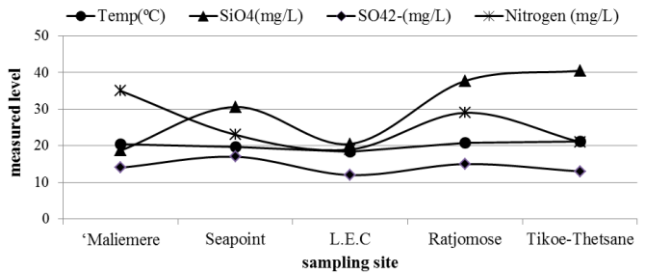

Figure 7. Some parameters responsible for the deviation in PC2 of the scores plot

On the other hand Figure 6 represents some of the parameters responsible for the shift of the different sampling sites along the PC1; notably conductivity, turbidity, total dissolved solids (TDS) and total suspended materials (denoted as 'suspended' in the loadings plot – Figure 6).

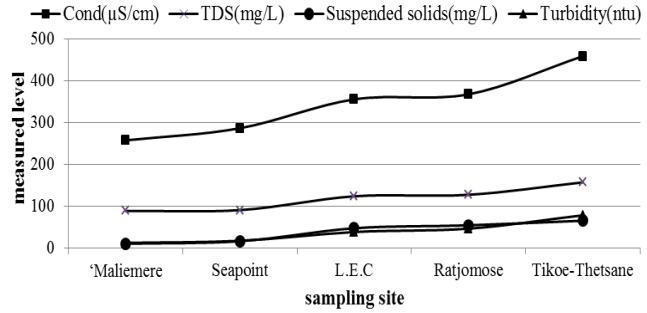

Figure 8. A chart showing some of the parameters responsible for the trend along PC1

Notably there was a significant jump for all the values from the LEC sampling site onwards. And there are not the only parameters that showed this dramatic jump, others as well, although they could not be included in Figure 8 due to their significantly lower numerical levels to fit on this scale (See Tables 1 and 2).

Conclusion

The water quality assessment of the Caledon River along Maseru City was carried out and principal component analysis was used to identify major role players in the observed trends. The levels of all most of the samples determined showed the expected increasing trend from 'Maliemere as shown on the PCA analysis. However, L.E.C. site shows some interesting break in the trends. Since the levels of most of the parameters assessed in this study peak up considerably around the factories, their respective levels could be attributed to the factory waste. Thus one of the ways in which to identify the responsible sources would be to identify the nature of waste from the factories, a very difficult task given the hostility of the factory owners and the relaxed regulation and law enforcement framework in the country. Other insignificant levels of chemicals such as phosphates and nitrates whose levels do not generally increase downstream could be attributable to the agricultural activities taking place across the border in the South African side of the river. In the follow-up study, the other elements responsible for general parameters such as high levels of conductivity as well as those responsible for the L.E.C. sampling site will be covered.

Acknowledgements

The authors would like to acknowledge Ms. N. Toae and Mr. N. Letsapo from the Department of Water Affairs where this work was carried out. Mr. F. Tugizimana is also acknowledged for the principal component analysis.

References

[1]Lesotho Government Gazette Extraordinary, 2008, LIII (88) retrieved from http://portal.unesco.org/en/ev.php-URL_ID=47373&URL_DO=DO_TOPIC&URL_SECTION=201.html.

[2]Lesotho Government, *Environment Act 2008*, retrieved on 01 June from http://www.osall.org.za/docs/2011/03/Lesotho-Environment-Act-10-of-2008.pdf.

[3]Mashinini, V., *AISA Policy Brief*, 2010, *22*, retrieved on 01 June 2014 from www.ai.org.za/wp-content/uploads/downloads/2011/11/No-22.

[4]World Report, *White gold powers economic cooperation*, retrieved on 01 June 2014 from http://www.worldreport-ind.com/lesotho/natural.htm.

[5]Tafirenyika, M., *Africa Renewal*, **2011**, retri. 20 May 2014 from http://www.un.org/africarenewal/magazine/december-2011/lesotho's-economy-catches-flu.

[6]Food, Agriculture and Natural Resources Policy Analysis Network (FARNPAN) **2006**, retri. on 01 June 2014 from http://www.fanrpan.org/documents/d00107/Lesotho_Program_MCC_July2006.pdf.

[7]Millennium Challenge Corporation, retrieved on 01 June 2014 from https://www.mcc.gov/pages/press/story/story-working-together-to-bring-water-to-lesotho.

[8]Central Bank of Lesotho, *CBL Economic Review*, 2011, *No. 131* retrieved from www.centralbank.org.ls/publications.

[9]Pullanikatil, D., *Afr. Technol. Policy Stud. Working Paper Ser.*, **2007**, *48*, 1-23.

[10]Morissette, J. J. and Borer, D.A., *Parameters*, **2004**, 86-101.

[11]Cooley, J.K., *Foreign Policy*, **1984**, *54*, 3-26.

[12]Gleick, P.H. and Heberger, M., *Water Conflict Chronol., The World's Water*, **2011**, 175-214.

[13]Gizelis, T.–I. and Wooden, A. E., *Polit. Geogr.*, **2010**, *29*, 444-453.

[14]Katz, D., *Global Environ.l Polit.*, **2011**, *11(1)*, 12-35.

[15]Ramakrishnan, N., *Proc. 3rd Int. Conf. Environ. Health, Chennai, India*, Chennai, **2003**, 374-385.

[16]Omar, W.M.W., *Tropic. Life Sci. Res.*, **2010**, *21(2)*, 51-67

[17]US-EPA, *Water Monitoring and Assessment*, **2012**, Retri. on 21 May 14 from water.epa.gov/type/rsi/monitoring.vms55.cfm

[18]World Health Organisation, *Guidelines for drinking-water quality - 4th ed*. Geneva, Switzerland, **2011**.

[19]Cao, X., Song, J. and Zhang, C., *Phys. Procedia*, **2011**, *24*, 1573-1581.

[20]Ouyang, Y., *Water Res.*, **2005**, *39*, 2621-2635.

[21]Lv, W. and Yang, T., *Clin. Biochem.*, **2012**, *45*, 127-133.

[22]Madala, N.E., Piater, L.A. Steenkamp, P.A. and Dubery, I.A., *Springer Plus*, **2014**, *3*, 254-264.

[23]Santos, J.P., Crémona, C., Orcesi, A.D. and Silveira, P., *Eng. Struct.*, **2013**, *56*, 273-285.

[24]Astela, A., Tsakovski, S., Barbieri, P. and Simeonov, V., *Water Res.*, **2007**, *41*, 4566-4578.

[25]U.S.EPA, *Field Sampling Guidance Document # 1225*, Rev. 1, 9/99 Region 9 Laboratory, Richmond, California.

[26]*Red River Basin Water Quality Monitoring Volunteer Manual*, **2012**, retrieved June 12 from http://www.iwinst.org/wp-content/uploads/2012/04/water_quality_manual_part1.pdf.

[27]*Department of Environment and Conservation*, New South Wales Environmental Protection Agency, **2004**.

[28]HACH Manual Change Notice, *DR/2400 Instrument Manual*, *59400-18*, 1st Edition, 7/02.

[29]Gomez-Taylor, M., *US-EPA Method 1688*, *EPA-821-R-01-007*, **2001**.

[30]Ivashchenko, A., Potential Urban Impacts on water quality of the Red River of the North, *MSc Thesis*, North Dakota State University of Agriculture and Applied Science, North Dakota, USA, **2009**.

[31]Boehrer, B. and Schultze, M., *Rev. Geophys.*, **2008**, *46*, 1-27.

[32]Kerr, S.J., *Southern Region Science & Technology Transfer Unit Technical Report TR-008*, Ontario Ministry of Natural Resources, Ontario, Canada, **1995**.

[33]Hayashi, M., *Environmental Monitoring and Assessment.* Netherlands. Kluwer Academic Publishers. **2004**.

[34]Miller, R. L., Bradford, W.L. and Peters, N.E., *U.S. Geol. Survey Water-Supply Paper* 2311, 1988.

[35]Wetzel, R.G., *Limnology*, 3rd edition. Academic Press, London, UK. 2001.

[36]Rossi, L., Fankhauser, R. and Chèvre, N., *Water Sci. Technol.*, **2006**, *54(6/7)*, 355-362.

[37]Osmond, D.L., Line, D.E., Gale, J.A., Gannon, R.W., Knott, C.B., Bartenhagen, K.A., Turner, M.H., Coffey, S.W., Spooner, J., Wells, J., Walker, J.C., Hargrove, L.L., Foster, M.A., Robillard, P.D. and Lehning, D.W.. *WATERSHEDSS: Water, Soil and Hydro-Environmental Decision Support System*, **1995**.

[38]Conley, D.J., Stalnacke, P., Pitkanen, H. and Wilander, A., *Limnol. Oceanog.*, **2000**, *45*, 1850-1853.

Received: 03.07.2014.
Accepted: 16.07.2014.

NEW COMPLEXONE DERIVATIVES OF 8-HYDROXY-QUINOLINE AND THEIRS APPLICATION IN UO_2^{2+} EXTRACTION

Fatiha Zaoui,[a] Didier Villemin,[b] Nathalie Bar[b] and Mohamed Amine Didi[a]*

Keywords: Multicomponent Mannich reactions; microwave irradiation; 7-(alkylaminomethyl)quinolin-8-ol type complexones; uranyl-ion extraction; 7-(dioctylaminomethyl)quinolin-8-ol.

New complexone derivatives of 8-hydroxyquinoline (quinolinol) were synthesized by the Mannich reaction from secondary and primary amines. Our syntheses were carried out either at room temperature, at reflux or under microwave irradiation, in good yields. The use of the 7-(dioctylamino) methyl) quinolin-8-ol (3f) as new extractant for the uptake and removal of UO_2^{2+} was investigated. Conditions for an effective sorption were optimized. The total sorption capacity was 102 ($mg.g^{-1}$) under optimum experimental conditions.

Corresponding Authors
Tel: +213552639237
Fax: +21343213198
E-Mail: madidi13@yahoo.fr; ma_didi@mail.univ-tlemcen.dz

[a] Laboratoire des Technologies de Séparation et de Purification, Département de chimie, Faculté des Sciences, Université de Tlemcen, BP119, Algeria
[b] Ecole Nationale Supérieure des Ingénieurs de CAEN & Centre de Recherche, Université de Normandie, LCMT, UMR CNRS 6507, Labex EMC3, Labex SynOrg, F-14050, Caen, France.

Introduction

Complexones according to Schwarzenbach definition are small chelating agents able to form chelate with metal ions.[1,2] One of the most well known examples of complexone is ethylenediaminetetraacetic acid (EDTA).[3] It was used for the chelation of metallic ions in analytical chemistry and as antioxidative compound. More generally, complexones present many applications in analytical chemistry and are also used in prevention of action of metallic ions as stabilising, anti-oxidative product.

8-Hydroxyquinoline **(1)** (8-HQ or quinolinol) is a non-specific ligand chelating a large variety of metal ions.[4,5] 8-Hydroxyquinoline is able to chelate essential metallic ions for metabolism of bacteria and fungi, so 8-HQ derivatives are used as antibacterial and antifungal. 8-HQ complexes of Zn or Mn can be also used for such applications.[6]

Polymer containing 8-HQ group have been described as chelating polymers.[7] Generally these polymers were obtained by a Beckland reaction of 8-HQ with formaldehyde. Such chelating polymer derivatives can be used in hydrometallurgy for the extraction of metals, such as iron, copper, nickel and uranium.[8]

Recently, metal complexes of 8-hydroxyquinolines were used in supramolecular chemistry as luminescent or fluorescent solids.[9] We are interested in the synthesis of new chelating molecules possessing 8-hydroxyquinoline group for the metal extraction[8] and as precursor of new luminescent complexes.[10,11]

As application, we suggested applying the compound **3f** as an extracting agent for the uptake and removal of the uranyl ion, using liquid-liquid extraction.

Experimental

All commercial reagents were purchased from Agfa or Aldrich, and were used as received without further purification. Reaction times were monitored by TLC until no starting material remained. TLC was performed using Silica gel 60 F_{254} precoated aluminium sheets. ^1H and ^{13}C NMR spectra are recorded on a Bruker AC 400 spectrometers. Mass spectra were recorded on a QTOF Micro (Waters) spectrometer with electrospray ionization (ESI, positive mode), lockspray orthophosphoric acid, infusion introduction at 10 µL min^{-1}, a source temperature of 80°C and desolvation temperature of 120°C. Molecular modelisation and energy minimisations were performed with MP3 using Spartan Software. Microwave irradiations were performed at 2450 MHz with a Synthewave 402 oven (Prolabo). Analytik Jena SPECORD 210 Double Beam UV-VIS was used for spectra recording and absorbance measurements. Spectra were recorded in the range from 400 to 800 nm with 0.2 nm resolution in 10 mm quartz cells. Data were processed with WinLab software.

pH measurements for all solutions were taken on a potentiometer Consort C831, with combined glass electrode, that was calibrated with pH 4.00, 7.00 and 10.00 buffer standards.

7-(morpholinomethyl)quinolin-8-ol (3a, $C_{14}H_{16}N_2O_2$)

Morpholine (1.8 mL, 20 mmol) and aqueous solution of formaldehyde (37 %, 2.7 mL) were added to 8-hydroxyquinoline (2.90 g, 20 mmol) dissolved in 35 mL of

ethanol. The resulting mixture was stirred overnight (12 h) at room temperature (20 °C). After evaporation under vacuum, an orange viscous liquid was obtained. Yield: 4.73 g (97 %); mp=66 °C (ethanol-water) (lit: mp=66 °C);[14] ^{1}H NMR (400 MHz, $CDCl_3$): δ = 2.67 (m, 4H, NCH_2CH$_2$), 3.76 (m, 4H, CH_2O), 3.88 (s, 2H, NCH_2), 7.27 (s, 2H, H^5 and H^6), 7.38 (dd, 1H, J=4.2 Hz and J=8.4 Hz, H^3), 8.07 (dd, 1H, J=1.2 Hz and J=8.4 Hz, H^4), 8.85 (dd, 1H, J=1.2 Hz and J=4.2 Hz, H^2) ppm; ^{13}C NMR ($CDCl_3$, 100.6 MHz) δ= 152.8, 149.0, 148.7, 139.2, 135.8, 128.5, 128.1, 121.4, 117.7, 67.0, 60.1, 53.3 ppm. The NMR spectra were identical to the litterature.[14]

7-(thiomorpholinomethyl)quinolin- 8-ol (3b, $C_{14}H_{16}N_2OS$)

Thiomorpholine (2.08 mL, 20 mmol) and aqueous solution of formaldehyde (37 %, 1.2 mL) was added to 8-hydroxyquinoline (2.90 g, 20 mmol) dissolved in 35 mL of EtOH. The resulting mixture was stirred 12 h at room temperature. After evaporation under vacuum, a yellow viscous liquid was obtained 5.14 g (99 %). ^{1}H NMR (400 MHz, $CDCl_3$): δ = 2.82-2.83 (m, 4H,SCH_2CH$_2$), 2.94-2.95 (m, 4H, NCH_2CH$_2$), 3.95 (s, 2H, NCH_2Ar), 7.31 (s, 2H, H^5 and H^6), 7.39 (dd, 1H, J=4.2 Hz and J=8.4 Hz, H^3), 8.11 (dd, 1H, J=1.6 Hz and J=8.4 Hz, H^4), 8.88 (d, 1H, J=1.6 Hz and J=4.2 Hz, H^2) ppm ; ^{13}C NMR ($CDCl_3$, 100.6 MHz) δ= 152.7, 148.9, 139.1, 135.7, 128.4, 127.9, 121.4, 117.7, 117.6, 60.8, 54.7, 28.1 ppm; IR (neat): ν= 3354, 2921, 2791, 1503, 1454, 1365, 1283 cm^{-1}; MS (m/z) %: 261 (70 M+H), 158(100); ESI-HRMS calcd for $C_{14}H_{17}N_2OS$ 261.1062, found 261.1069.

7,7'-(piperazine-1,4-diylbis(methylene))diquinolin-8-ol (3c, $C_{24}H_{24}N_4O_2$)

Piperazine (0.86 g, 10 mmol) and aqueous solution of formaldehyde (37 %, 2.7 mL) were added to 8-hydroxyquinoline (2.90 g, 20 mmol) dissolved in 35 mL of EtOH. The resulting mixture was stirred overnight (12 h) at room temperature (20 °C). A yellow precipitate was observed; after filtration, it was washed with diethyl ether (25 mL) to give the product namely **(3c)** as a yellow solid, 2.48 g (62 %). m.p: 204 °C. ^{1}H NMR (400 MHz, DMSO-d_6): δ = 2.50 (s, 2×4H, NCH_2(CH$_2$N)), 3.75 (s, 2×2H, ArCH_2N), 7.36 (d, 2×H, J= 8.4 Hz, H^6), 7.47 (d, 2×H, J=8.4 Hz, H^5), 7.50 (dd, 2×H, J=4.4 Hz, and J=8.4 Hz, H^3), 8.28 (dd, 2×H, J=1.6 Hz and J=8.4 Hz, H^4), 8.82 (dd, 2×H, J=1.6 Hz and J=4.4 Hz, H^2) ppm; ^{13}C NMR (DMSO-d_6, 100.6 MHz) δ= 151.4, 148.1, 138.2, 135.9, 128.8, 127.6, 121.4, 119.6, 116.9, 56.5, 52.6 ppm ; IR (neat): ν= 2947, 1504, 1464, 1376 cm^{-1}; MS m/z (%): 401 (40, M+H), 244 (30), 158 (100); ESI-HRMS calcd for $C_{24}H_{25}N_4O_2$ 401.1978, found 401.1989.

7,7'-(ethane-1,2-diylbis(methylazanediyl))bis(methylene)diquinolin-8-ol (3d, $C_{24}H_{26}N_4O_2$)

N,N'-dimethylethylenediamine (0.53 mL, 5 mmol) and aqueous solution of formaldehyde (37 %, 1 mL) was added to 8-hydroxyquinoline (1.45 g, 10 mmol) dissolved in 20 mL of EtOH. The resulting mixture was stirred and heated at 50 °C for 5 hours. After cooling and evaporation under vacuum, a brown viscous liquid was obtained, which crystallizes at room temperature, 1.68 g (84 %). Mp= 60 °C (ethanol); ^{1}H NMR (400 MHz, $CDCl_3$): δ = 2.36 (s, 2×3H, NCH_3), 2.77 (s, 2×2H, NCH_2CH$_2$), 3.86 (s, 2×2H, ArCH_2N), 7.21 (d, 2H, J=8.4 Hz, H^6), 7.29 (d, 2×H, J=8.4 Hz, H^5), 7.36 (dd, 2×H, J=4.2 Hz and J=8.4 Hz, H^3), 8.07 (dd, 2H, J=1.6 Hz and J=8.4 Hz, H^4), 8.84 (dd, 2H, J=2.5 Hz and J=4.2 Hz, H^2) ppm; ^{13}C NMR ($CDCl_3$, 100.6 MHz) δ= 152.7, 148.8, 139.2, 135.8, 128.4, 128.3, 121.4, 118.9, 117.5, 58.6, 54.5, 42.4 ppm ; IR (neat): ν= 2924, 1501, 1457, 1371, 1271 cm^{-1}; SM: (m/z) %: 403 (80 M+H), 246 (100), 158 (60); ESI-HRMS calcd for $C_{24}H_{27}N_4O_2$ 403.2134, found 403.2125.

7-((dicyclohexylamino)methyl)quinolin-8-ol) (3e, $C_{22}H_{30}N_2O$)

Dicyclohexylamine (3.98 mL, 20 mmol) and aqueous solution of formaldehyde (37 %, 1.7 mL) was added to 8-hydroxyquinoline (2.90 g, 20 mmol) dissolved in 17 mL of EtOH. The resulting mixture was stirred at 70 °C for 2 hours. After evaporation under vacuum and extraction with diethyl ether (25 mL), a brown viscous liquid is obtained 3.90 g (58 %). ^{1}H NMR (400 MHz, $CDCl_3$): δ = 1.01-1.96 (m, 20 H, 2x(CH_2)$_5$), 2.74-2.81 (m, 2×H, NCH), 4.13 (s, 2H, ArCH_2N), 7.13 (d, 1H, J=8.4 Hz, H^6), 7.19 (d, 1H, J=8.4 Hz, H^5), 7.33 (dd, 1H, J= 4.4 Hz and J=8.0 Hz, H^3), 8.04 (dd, 1H, J=1.6 Hz and J= 8.0 Hz, H^4), 8.86 (dd, 1H, J=1.6 Hz and J=4.4 Hz, H^2) ppm; ^{13}C NMR ($CDCl_3$, 100.6 MHz) δ= 154.8, 149.0, 139.8, 135.6, 128.3, 126.9, 121.0, 119.5, 116.8, 58.2, 49.9, 30.6, 26.2, 26.1 ppm ; IR (neat): ν= 3342, 2924, 2850, 1505, 1379, 1278 cm^{-1}; SM (m/z) %: 339 (100 M+H), 182 (40), 158 (10); ESI-HRMS calcd for $C_{22}H_{31}N_2O$ 339.2436, found 339.2433.

7-((dioctylamino)methyl)quinolin-8-ol (3f, $C_{26}H_{42}N_2O$)

Dioctylamine (4,82 g, 20 mmol), and aqueous solution of formaldehyde (37 %, 1.7 mL) were added to 8-hydroxyquinoline (2.90 g, 20 mmol) dissolved in 40 mL of EtOH. 1.3 mL of hydrochloric acid (37%) was added to the mixture. The mixture was heated at 60°C for 6 hours under stirring. After cooling, a precipitate was observed. After filtration and washing with diethyl ether (25 mL), a yellow solid was obtained 4.61 g (58 %). m.p: 252 °C. ^{1}H NMR (400 MHz, $CDCl_3$): δ = 0.75-0.90 (m, 2×3H, CH_3), 1.10-1.40 (m, 2x10H, (CH_2)$_5$CH$_3$), 1.86-1.90 (m, 2x2H, NCH$_2$CH_2), 2.87-2.89 (m, 2x2H, NCH_2), 4.48 (s, 2H, NCH_2Ar$_{o\ or\ p}$), 4.56 (s, 2H, NCH_2Ar$_{o\ or\ p}$), 7.10-7.60 (m, 2x3H, $ArH_{o,p}$), 8.02-8.18 (m, 2xH, $ArH_{o,p}$), 8.66-8.80 (m, 2xH, $HAr_{o,p}$) ppm; ^{13}C NMR ($CDCl_3$, 100.6 MHz) δ= 149.6, 149.3, 139.3, 135.9, 128.0, 126.0, 121.2, 118.7, 118.0, 54.8, 50.5, 31.7, 30.5, 29.8, 28.0, , 27.1, 22.5, 14.0 ppm; IR (cm^{-1}): 3359, 2923, 1504, 1464, 1374; SM (m/z): 399 (30 M+H), 242 (100), 158 (30); ESI-HRMS calcd for $C_{26}H_{43}N_2O$ 399.3375, found 399.336. Ratio 60/40.

7-(octylamino) methyl)quinolin-8-ol (3g, $C_{18}H_{26}N_2O$)

N-octylamine (1.65 mL, 10 mmol) and aqueous solution of formaldehyde (37 %, 1.7 mL) was added to 8-hydroxyquinoline (1.45 g, 10 mmol) dissolved in 25 mL of EtOH. The resulting mixture was refluxed for 1 hour. After evaporation under vacuum, a yellow viscous liquid was obtained 2.80 g (98 %). ^{1}H NMR (400 MHz, $CDCl_3$): δ =

0.84-0.87 (m, 3H, C*H*$_3$), 1.17-1.24 (m, 5×2H, (C*H*$_2$)$_5$CH$_3$), 1.57-1.63 (m, 2H, NCH$_2$C*H*$_2$), 2.80-2.83 (m, 2H, NC*H*$_2$CH$_2$), 4.15 (s, 2H, ArC*H*$_2$N), 7.14 (d, 1H, J=8.4 Hz, *H*^{6}), 7.31 (d, 1H, J=8.4 Hz, *H*^{5}), 7.38 (dd, 1H, J=4.2 Hz and J=8.4 Hz, *H*^{3}), 8.07 (dd, 1H, J=1.6 Hz and J=8.4 Hz, *H*^{4}) 8.89 (dd, 1H, J=1.6 Hz and J=4.2 Hz, *H*^{2}) ppm; ^{13}C NMR ($CDCl_3$,100.6 MHz) δ= 149.6, 149.3, 139.3, 135.8, 128.0, 126.1, 121.1, 118.7, 118.1, 51.7, 50.5, 31.7, 29.4, 29.2, 28.1, 27.1, 22.5, 14.0 ppm; IR (neat): ν=3370, 2923, 2852, 1501, 1463, 1371 cm^{-1}; SM (m/z) %: 287 (45 M+H), 158 (100); ESI-HRMS calcd for $C_{18}H_{27}N_2O$ 287.2123, found 287.2135.

Results and Discussion

8-Hydroxyquinoline is a phenol able to react in a reaction of Mannich.[12] The reaction of 8-HQ was described with different aldehydes (Betti reaction[13]) and some amines.

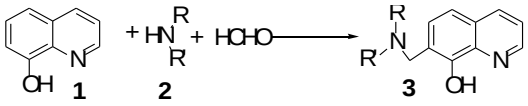

Scheme 1: Synthesis of 8-hydroxyquinoline derivatives **(3)** from secondary amines by Mannich reaction

In our work, we have studied the reaction of formaldehyde and different amines in order to obtain molecules with one or two 8-HQ units for the coordination of metal ion. The reaction of morpholine with formaldehyde and 8-hydroxyquinoline was already described and was used as a basis of our work.[14]

First, we have been interested in using new 8-HQ derivatives as ligand of metals in complexes formation. We have synthesized ligands with a second site of coordination in the molecule (oxygene with morpholine, sulfur with thiomorpholine) or with two HQ units with diamines. The reaction with thiomorpholine introduced a sulfur atom, a soft site of coordination on the ligand according to R.G. Pearson.[15,16] With diamine such as piperazine **(2c)** a compound **(3c)** with two 8-HQ units**,** is obtained. The N,N'-1,2-dimethylenediamine **(2d)** is not so reactive so the reaction required heating. By comparison by molecular modelisation, the compound **(3d)** obtained with N,N'-1,2-dimethylenediamine is more flexible than the preceding one with piperazine.

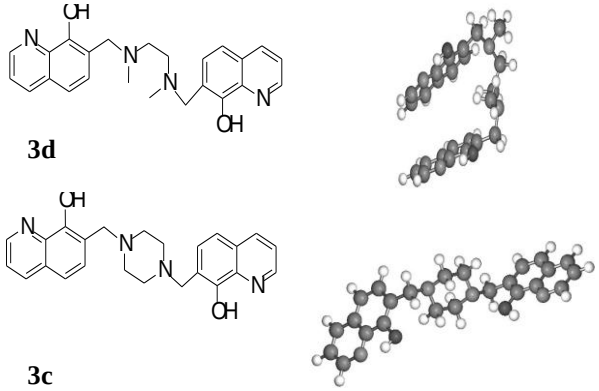

Scheme 2. Molecular representation of (3c) and (3d).

In a second approach, we were interested in the synthesis of a lipophilic molecule with 8-HQ ligand, such molecule can be used as metal extractant in liquid-liquid extraction process. In this aim, we have used bicyclohexylamine, bisoctylamine and monooctylamine as starting amines.

Table 1. New complexone derivatives of 8-hydroxyquinoline obtained under Mannich conditions.

Amine, 2	Product (3)	Conditions	Yield (%)
2a 	**3a** 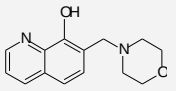	12 h, 20 °C	97
2b 	**3b** 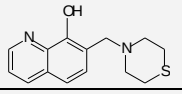	12 h, 20 °C	99
2c 	**3c** 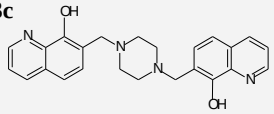	12 h, 20 °C	62
2d 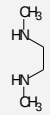	**3d** 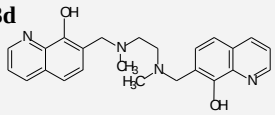	5 h, 50 °C	84
2e 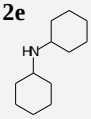	**3e** 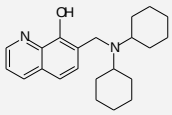	2 h, 70 °C	58
2f 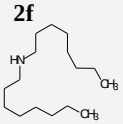	**3f** 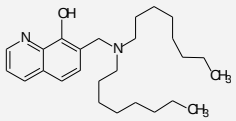	6 h, 60 °C	58
2g 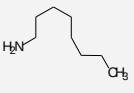	**3g** 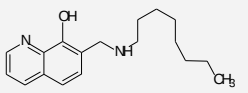	1 h, 78 °C	98

Under microwave irradiation (10min, 300W) the yield obtained were similar to those obtained under classical conditions. In all the products synthesized by the Mannich reaction, the addition of amine was at the position 7 of 8-hydroxyquinoline. However, in the case of dioctylamine **(2f)**, two products (substituted in 5 or 7 position) were obtained in a mixture.

We can propose two probable mechanisms: the first involved the attack of the iminium (A) by 8-hydroxyquinoline and the second one the reaction of benzyl cation (B) with amine in this Mannich reaction.

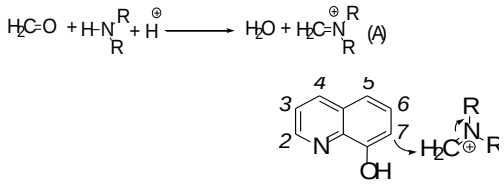

Scheme 3: Mechanism (A).

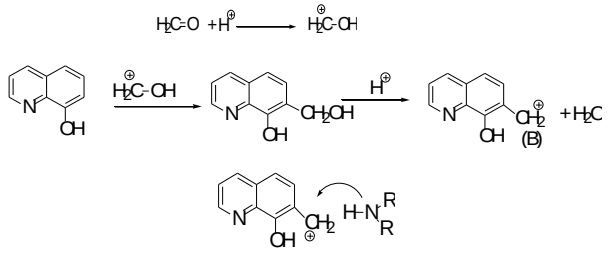

Scheme 4. Mechanism (B)

The new compound **(3f)** was used in the liquid-liquid extraction of uranyl ion: **3f** which is soluble in ethyl acetate, was taken as the organic solvent throughout this study. Equal volumes of organic and aqueous phases (5 mL) were agitated for 30 minutes (enough for equilibrium) at 22 °C under the desired experimental conditions. The two phases were then separated by decantation and assayed by taking known aliquots from the aqueous phases. The concentration of UO_2^{2+} in the sample was determined by Arsenazo(III) visible spectrophotometric analysis at 650 nm,[17] and that in the organic phase was obtained by subtracting the aqueous concentration from the total initial aqueous concentration of UO_2^{2+}.

Effect of molar ratio Q

The extraction experiment results are discussed in term of the extraction yield (Y) defined as follows:

$$Y(\%) = 100\frac{(m_i - m_f)}{m_i} \quad (1)$$

where

m_i = initial mass of UO_2^{2+} in aqueous phase and

m_f = mass of UO_2^{2+} after extraction.

The variable Q is the ratio of the number of moles of ligand in organic phase to the number of moles of metal in aqueous phase before extraction; $Q = n_{ligand}/n_{metal}$.

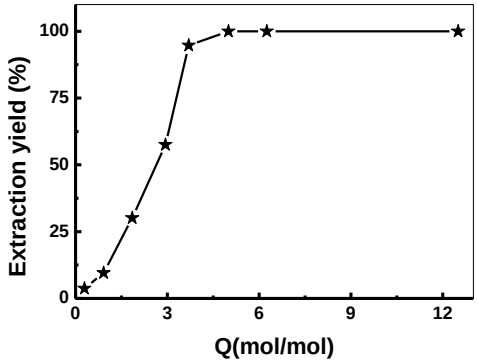

Figure 1. Extraction yield of UO_2^{2+} by **3f** as a function of Q. V_{org} =5.0 mL, [Ex]=1.0 mmol L^{-1}, V_{aq} =5 mL, pH^i = 0.6, t = 30 min, T =22 °C.

The extraction results of uranyl ion as a function of Q, are reported in Fig.1. We observe that the best performance is achieved for Q equal to 5.0. For the extraction of one mole of UO_2^{2+} in aqueous phase, 5.0 mol of extractant in organic phase are required, under the operating conditions listed above.

Effect of initial concentration of UO_2^{2+}

Figure 2 shows that the extraction yield of UO_2^{2+} extracted by the **3f** increased from 0.0 % to 100.0 % with an increase in the initial concentration from 0.00 (mol.L^{-1}) to 16.2 ppm, and thereafter remains constant at 41.59 ppm. At initial concentrations, higher than 41.59 ppm, the extraction yield decreases. With increasing concentrations, the ratio of the available sorption sites of ligand to the initial number of moles of metal ions becomes lower, and hence, the extent of metal removal depends on the initial concentration.

The extraction results of uranyl ions as a function of Q are reported in Fig. 2.

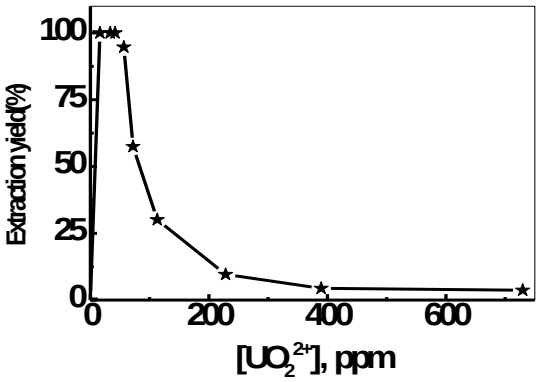

Figure 2. UO_2^{2+}extraction yield versus initial molar UO_2^{2+}concentration. V_{org} = 5.0 mL, [Ex.] = 1.0 mmol L^{-1}, V_{aq} =5.0 mL, pH_i =0.65, t=30 min, T=22 °C

The curve in Figure 2 shows that the extraction is quantitative for dilute solutions of UO_2^{2+}.

Effect of initial pH

The effect of the initial pH on the extraction yield of UO_2^{2+} was studied in the pH range of 0.65 to 1.67 (see Figure 3). The extraction yield (99.4 %) was found to be higher at pH = 1.13. The extractant is suitable for chelate formation with UO_2^{2+} ions, as it has a nitogen atom and an OH group. As the complex formation is strongly pH dependent, careful adjustment of proper pH was necessary.[13] The extraction results of UO_2^{2+} ion as a function of pH are reported in Figure 3.

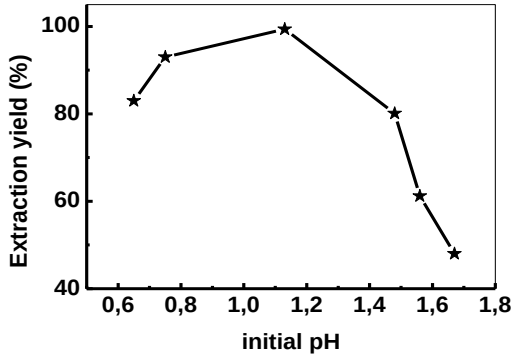

Figure 3. pH effect on the extraction of UO_2^{2+} V_{org} = 5.0 ml, [Ex] = 1.0 mmol L^{-1}, V_{aq} = 5 mL, $[UO_2^{2+}]_{initial}$ = 60 ppm, t = 30 min, T = 22 °C

The negative effect of pH increase on the extraction yield can be attributed to the formation, in aqueous phase, of hydroxide species like $UO_2(OH)_2$ and $(UO_2)_6(OH)_{12}$, larger and more stable than UO_2^{2+} and $UO_2(OH)^+$ majority in the more acidic medium.

In conclusion, the Mannich reaction of 8-hydroxyquinoline, formaldehyde and amines allowed a rapid, convenient and easy synthesis of new ligands and new extractants.

The 7-(dioctylaminomethyl)quinolin-8-ol obtained has exhibited high efficiency for the uptake and removal of uranyl ion from water and the recovery was quantitative (≈100 %).

Acknowledgements

The authors thank Mr Rémy Legay and Mr Baptiste Rigaud for NMR spectra and Mrs Karine Jarsalé for HRMS analysis.

References

[1]Schwarzenbach, G., *Analyst*, **1955**, *80*, 713 and references cited

[2]Schwarzenbach, G., *Helv. Chim Acta*, **1952**, *35*, 2344.

[3]Hart, R. J., Ethylenediaminetetraacetic Acid and Related Chelating Agents in: *Ullmann's Encyclopedia of Industrial Chemistry*, Wiley-VCH, Weinheim, **2005**.

[4]Hollingshead, R. G. W., *Oxine and its Derivatives*, Vol. 1-4, Butterworth, London, **1954**.

[5]Phillips, J. P., *Chem. Rev.*, **1956**, *56*, 271.

[6]Shen, A. Y., Wu, S. N., Chiu, C. T., *J. Pharm. Pharmacol.*, **1999**, *51*, 543.

[7]Degeiso, R. C., Donaruma, L. G., Tomic, E. A., *J. Appl. Polym. Sci.*, **1965**, *9*, 411.

[8]Gloe, K., Stephan, H., Krüger, T., Möckel, A., Woller, N., Subklew, G., Schwuger, M. J., Neumann, R., Weber, E., *Progr. Coll. Polym. Sci*., **1996**, *101*, 145.

[9]Sarmiento, L. E., Rodriguez, M., Echevarria, L., Lubes, V., *J. Sol. Chem.*, **2010**, *39*, 1484.

[10]Zhigang, Y., Bingxi, W., Guihua, C., Mingjian, Z., *J. Mater. Sci.*, **2011**, *46*, 2397.

[11]Albrecht, M., Fiege, M., Osetska, O., *Coord. Chem. Rev*., **2008,** *252*, 812.

[12]Blicke, F. F., *The Mannich reaction, in Organic Reactions*, **1947**, vol. 1., Chap 10., 303., John Wiley, Chichester:

[13]Phillips, J. P., Barall, E., *J. Org. Chem*., **1956**, *21*, 692 and references cited.

[14]Albrecht, M., Blau, O., *Synthesis*, **1997**, *28*, 213.

[15]Pearson, R. G., *J. Chem. Educ.*, **1968**, *45*, 581.

[16]Pearson, R. G., *J. Chem. Educ*., **1968**, *45*, 643.

[17]Bouhoun-Ali, M., Badjah Hadj Ahmed, A. Y., Attou, M., Elias, A., Didi, M. A., *Solvent Extr. Ion Exch*., **2012**, *30*(5), 469.

Received: 02.07.2014.
Accepted: 16.07.2014.

ETHYL GALLATE AND PYROGALLOL FROM *ACALYPHA WILKESIANA VAR. LACE-ACALYPHA* (MUELL &ARG.)

Olawale H. Oladimeji,[a]* Ephraim U. Tom[a] and Emmanuel E. Attih[a]

Keywords: Polyphenols; ethyl gallate; pyrogallol; bacteriostatic; *A. wilkesiana var. lace-acalypha*.

Acalypha wilkesiana var. lace-acalypha (Muell & Arg.) is a cultivated ornamental plant used in folkloric medicine for the treatment of fever, bacterial, skin fungal infections, wounds, tumors, inflammations and gastro-intestinal troubles. Silica gel column chromatography of the butanol fraction gave two polyphenolic compounds, designated as compounds **1** [m.p. 148-150 ^{0}C; R_f 0.67; $[n]^{20}_D$ 1.4118] and **2** [m.p. 130-132 ^{0}C; R_f 0.46; $[n]^{20}_D$ 1.4079]. The structures of **1** and **2** have been established to be ethyl 3, 4, 5-trihydroxybenzoate (ethyl gallate) and 1, 2, 3-benzenetriol (pyrogallol or fouramine brown) respectively using the ^{1}H NMR, ^{13}C NMR, MS and IR spectral techniques. Both polyphenols were strongly bacteriostatic against against *B. subtilis*, *S. aureus*, *E. coli*, *Ps. aeriginosa* and *S. typhi.* Furthermore, **2** was more suppressive of the bacterial strains than **1**. However, neither gave any anticandidal activity. The crude extract and butanol fraction demonstrated comparatively weaker antimicrobial activities than the two isolated compounds. The results of the antimicrobial screening have lent scientific credence to the traditional uses of the plant**.**

Corresponding Author
Tel: +2347038916740
E-Mail: wale430@yahoo.co.uk
[a] Department of Pharmaceutical and Medicinal Chemistry, Faculty of Pharmacy, University of Uyo, Uyo, Nigeria.

INTRODUCTION

The genus, *Acalypha*, comprises of about 570 species[1] which are used in African, South American and Asian traditional medicine. *Acalypha wilkesiana var. lace-acalypha* (Muell & Arg.) is used in the treatment of fever, bacterial, skin fungal infections,[2-5] wounds, tumors, inflammations and gastro-intestinal disorders.[6] Extracts of this plant have demonstrated both hypotensive and hypoglycaemic activities.[7] The antiproliferative (antitumor) potential of this plant had been carried out on human lung carcinoma and fibroblast.[8] A pilot study carried out on six *Acalypha* species (including *lace-acalypha*) demonstrated that the antimicrobial activity was most pronounced in the butanol fractions of the species.[9] Hence, two tannins; corilagin and gerannin were obtained from butanol fractions of *A. wilkesiana var. red-acalypha* and *A. hispida.*[10] This present study was carried out with the aim of isolating chemical constituents in *A. wilkesiana var. lace-acalypha* and subsequently classifying compounds obtained therefrom as chemotaxonomic markers for this species and variety in particular and the genus, *Acalypha* in general.

MATERIAL AND METHODS

Collection of plant

The fresh leaves of *A. wilkesiana var. lace-acalypha* were collected around the month of February, 2013 from a privately cultivated orchard at Nwaniba, Akwa Ibom State, Nigeria. The plant was identified by O. Etefia of the Department of Pharmacognosy and Natural Medicine, University of Uyo, Nigeria. The authentication by comparison was done with herbarium samples of the Forestry Research Institute of Nigeria (FRIN) and the National Institute of Horticulture (NIHORT), Nigeria. A voucher specimen of the plant (No H113) was deposited in the Herbarium Unit of the Faculty of Pharmacy. Immediately after collection, the plant was dried in an oven (Gallenkamp, England) at 40 ^{0}C for 48 h and the resultant dried material powdered on an electric mill (Uniscope, England).

Bulk extraction and isolation

The dried powder (1.4 kg) was exhaustively extracted with 50 % EtOH (5x5 L) at room temperature (27± 2 ^{0}C) for 72 h. The resultant crude extract was filtered, concentrated *in vacuo* on a rotary evaporator (R205D, Shensung BS & T, China), weighed and stored in a desiccator prior to further use. 125 g of the extract was partitioned using H_2O:BuOH (7 x 500 mL). The obtained butanol fraction was evaporated to dryness to give a solid residue from which the two polyphenols were isolated. The butanol fraction (10 g) was chromatographed on a silica gel 254 column (Pyrex, USA; 10 g pre-swollen in 100 % toluene; 3 g concentration zone + 7 g separation zone; 17.5 x 4 cm) and eluted with a gradient of 20 % acetone:toluene (100 mL), 30 % acetone:toluene (100 mL), 40 % acetone:toluene (100 mL), 50 % acetone:toluene (100 mL) and 60 % acetone:toluene (100 mL). Fractions of 10 mL each were collected, monitored on silica plates in acetone:toluene:H_2O (10:20:1) using $FeCl_3$/CH_3OH and vanillin-H_2SO_4 as spray reagents. Hence, fractions with similar TLC characteristics (R_f values, reaction with $FeCl_3$ reagent or vanillin-H_2SO_4 spray) were bulked and four semi-pure residues coded 5A, 5B, 5C and 5D were obtained.

Sample 5B (1.8 g, dirty green) was purified on a much shorter silica gel 254 column (10 x 2 cm) successively with 100 % toluene (130 mL) and 20 % acetone:toluene (50 mL) resulting in ethyl 3, 4, 5-trihydroxybenzoate (ethyl gallate) **1** (amorphous white solid; R_f (0.67); 165 mg). Likewise, 5C (2.4 g, greenish brown substance) was also cleaned on a short silica gel 254 column using 30 % acetone:toluene (210 mL) which furnished 1,2,3-benzenetriol (pyrogallol or fouramine brown) **2** (light brown crystals; R_f (0.46); 243 mg).

Efforts to equally purify 5A and 5D were abortive. Hence, they were not procesed any further in this study. The melting points of the two compounds were determined using the melting point apparatus (Electrothermal, England) while the refractive indices were obtained using WAY-15 Abbe refractometer (England).

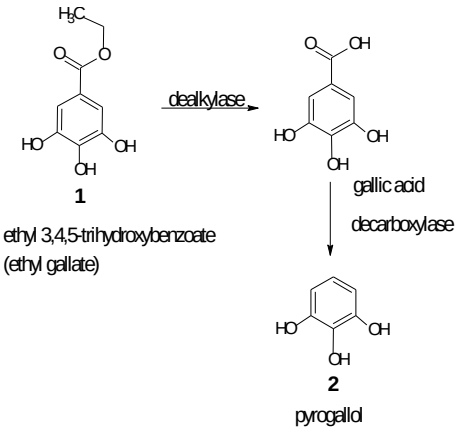

Antimicrobial tests

The micro-organisms used in this study, namely; *Bacillus subtilis* (NCTC 8853), *Staphylococcus aureus* (NCTC 6872), *Escherichia coli* (NCTC 10764), *Pseudomonas aeriginosa* (ATCC 2654), *Samonella typhi* (NCTC 5438) and *Candida albicans* (NCYC 436) were clinically isolated from specimens of diarrheal stool, abscesses, necrotizing fascitis, osteomyelitis, urine, wounds and vaginal swabs obtained from the Medical Laboratory, University of Uyo Health Centre, Uyo. The clinical isolates were collected in sterile bottles, identified and typed by convectional biochemical tests[11-12] and then refrigerated at -5 ^{0}C at the Microbiology and Parasitology Unit, Faculty of Pharmacy prior to use. The hole-in-plate agar diffusion method was used observing standard procedure with Nutrient Agar and Sabouraud Dextrose Agar (Oxoid, England) for the bacteria and fungus respectively. The inoculum of each micro-organism was introduced into each petri-dish (Pyrex, England). Cylindrical plugs were removed from the agar plates by means of a sterile cork borer (Pyrex, England) to produce wells with diameter of approximately 5 mm.

The wells were equidistant from each other and the edge of the plate.[13-14] Concentrations of 20 mg mL^{-1}of crude extract, 10 mg mL^{-1} of butanol fraction, 2 mg mL^{-1} of **1** and **2** were introduced into the wells. Also, different concentrations of 10 µg mL^{-1} streptomycin (Fidson Chemicals, Nigeria), 1 mg mL^{-1} of nystatin (Gemini Drugs, Nigeria) and 100 % methanol were introduced into separate wells as positive and negative controls respectively.[9-10,15-16]

The experiments were carried out in triplicates. The plates were left at room temperature for 2 h to allow for diffusion. The plates were then incubated at 37± 2 ^{0}C for 24 h. Zones of inhibition were measured in millimetre (mm).

RESULTS AND DISCUSSION

Spectroscopic data: The data were obtained thus: ES$^+$-MS on Kratos MS 80, IR on Shimadzu FTIR 8400S, ^{1}H and ^{13}C NMR on Bruker AC 250 operating 300 MHz for proton and 75 MHz for carbon-13 using CD_3OD as solvent and TMS as internal standard.

Compound **1:** $C_9H_{10}O_5$; amorphous white solid; m.p. 148-150 ^{0}C; R_f 0.67; $[n]^{20}_D$ 1.4118; MS [ES$^+$-MS] m/z (relative intensity): 198 $[M]^+$ (48.45 %), 183 $[M\text{-}CH_3]^+$ (5.24 %), 170 $[M\text{-}(CH_2)_2]^+$ (32.67 %), 154 [M- OC=O]$^+$ (20.49 %), 153 $[M\text{-}OC_2H_5]^+$ (100.00 %) (base peak), 125 $[M\text{-}(CH_2)_2$ -3OH +2H]$^+$ (26.27 %), 79 [M- 3OH-74+ 6H]$^+$ (15.27 %) and 51[M-198+3OH] 12.87 %; IR [FTIR] cm^{-1}: 773 (finger print), 1648 (Ar CH=CH), 1720 (-C=O) and 3647 (Ar-OH); ^{1}H NMR δ (ppm): 1.12, 1.41, 6.15, 7.45, 7.54 and 7.66 ; ^{13}C NMR δ (ppm): 19.45 (methyl- C), 34.42 (methylene-C), 100.45, 105.23 (hydroxylated-C), 123.32 (Ar- C) and 161.84 (ester -C).

Compound **2:** $C_6H_6O_3$; light brown crystals; m.p. (130-132 ^{0}C); R_f 0.46; $[n]^{20}_D$ 1.4079; MS [ES$^+$-MS] m/z (relative intensity): 126 $[M]^+$ (100.0 %), 108 $[M\text{-}OH_2]^+$ (62.82 %), 97 [M-2OH +5]$^+$ (31.67 %), 80 [M- 3OH +5]$^+$ (52.77 %), 68 [M-3OH-7]$^+$ (14.84 %) and 52 [M-75+3OH+1]$^+$ (21.53 %); IR [FTIR] cm^{-1}: 1641 (Ar CH=CH) and 3528 (Ar-OH); ^{1}H NMR δ (ppm): 6.45, 7.65 and 7.84; ^{13}C NMR δ (ppm): 106.15, 107.28 (hydroxylated-C), 122.56 and 123.32 (Ar-C).

Collection and processing of plant

The rules governing plant collection and extraction were observed thereby guaranting the intergrity of the extract and fractions.[17-18] Two previous studies had reported that the crude extract of *A. wilkesiana var. lace-acalypha* contained saponins, tannins, flavonoids, terpenes and cardiac glycosides while alkaloids, anthraquinones and cyanogenic glycosides were absent. Furthermore, the antibacterial and antifungal activities resided in the butanol fraction.[9-10] In addition, the H_2O/BuOH partition extracted the largest amount of plant constituents, hence the choice of the BuOH fraction for column chromatography from where the isolates **1** and **2** were obtained.

Elucidation of structures of compounds 1 **and** 2

Some physical constants of compounds **1** and **2** such as the refractive index measured at the λ 589.3nm (Na-D light) and 20 ^{0}C and melting point were determined. The results highlighted (Experimental Section) show that compound **1** with a higher refractive index (1.4118) is denser than compound **2** (1.4079). This is not surprising because **1** (ethyl gallate) has a molecular weight of 198 while **2** (pyrogallol or fouramine brown) has a molecular weight of 126. The higher the molecular weight or the more the atomic species in a compound, the higher the refractive index.[19-21] The melting points of **1** and **2** are 149-151 ^{0}C and 131-133 ^{0}C respectively in literature. These values are consistent with those obtained in this study. The structures of **1** and **2** were established by a combination of spectroscopic techniques as highlighted above.

Table 1. Antimicrobial screening of crude extract, butanol fraction and isolates **1** and **2** at different concentrations on test microbes in 100 % MeOH.

Test microbe	LA 20 mg mL^{-1}	BU 10 mg mL^{-1}	1 2 mg mL^{-1}	2 2 mg mL^{-1}	Streptomycin 10 µg mL^{-1}	Nystatin 1 mg mL^{-1}	100 % MeOH
B. subtilis (NCTC 8853)	14	15	13	21	22	5	5
S. aureus (NCTC 6872)	13	21	20	31	37	5	5
E. coli (NCTC 10764)	5	5	14	18	18	5	5
Ps.aeriginosa (ATCC 2654)	7	18	12	18	5	5	5
S. typhi (NCTC 5438)	12	8	14	19	19	5	5
C. albicans (NCYC 436)	11	5	5	5	5	28	5

Key: The zone diameter recorded is zone of inhibition + size of cup (zone of inhibition +5) **in** mm; **LA** = crude ethanolic extract; **BU** = butanol fraction; **1** = Ethyl 3,4,5-trihydroxybenzoate (ethyl gallate); **2** = 1,2,3-benzenetriol (pyrogallol); **NCTC** - National Collection of Type Cultures, Central Public Health Laboratory, Colindale Avenue, London NW9, UK; **NCYC** - National Collection of Yeast Cultures, UK; **NCYC** - National Collection of Yeast Cultures, UK; **ATCC** - American Type Culture Collection**,** Washington, DC.

The obtained MS data were matched with library data of organic compounds,[22] hence, **1** and **2** were identified to be ethyl 3,4,5-trihydroxybenzoate (ethyl gallate) and 1,2,3-benzenetriol (pyrogallol or fouramine brown) respectively. The ES$^+$-MS of **1** showed diagnostic peaks such as $[M]^+$ at m/z 198 (48.45 %) while 183 (5.24 %), 154 (20.49 %) and the base peak at 153 (100.00 %) represent the losses of -CH_3, -COO and -OC_2H_5 units respectively from the $[M]^+$. Due to the nature of the matrix, many fragmented ions also appeared in the MS of **2** but those that could readily be identified include: $[M]^+$ at m/z 126 (also base peak) (100.00 %) while 108 (62.82 %) indicates the loss of -OH_2. However, the peak at 52 (21.53 %) represents the disintegration of $[M]^+$ save for the 3 OH groups. The IR spectra of the two compounds show diagnostic Ar-CH=CH at 1641 and 1648 cm^{-1} and Ar-OH at 3528 and 3647 cm^{-1} respectively. In addition, the -C=O absorption at 1720 cm^{-1} observed in **1** was equally very diagnostic. Also, the obtained ^{1}H and ^{13}C NMR spectra of both compounds are consitent with those in literature.[10,22] **1** and **2** are polyhydroxyl benzenoid compounds. It is very probable that **2** could have arisen *in-situ* from biogenetic chemical transformations of **1** in the presence of enzymes in the plant. These possible transformations are provided in the Scheme.

Antimicrobial screening

The results of the antimicrobial tests presented in **Table 1** show that the two compounds were strongly bacteriostatic against against *B. subtilis*, *S. aureus*, *E. coli*, *Ps. aeriginosa* and *S. typhi*. Interestingly, the two compounds were remarkably active against gram negative strains such as *E. coli* and more especially *Ps. aeriginosa*. These bacteria are well known for their unique resistance to antimicrobial agents. This resistance is believed to be due to the nature of the cell envelope of these organisms which unlike gram positive organisms, posses a sophisticated three-layered envelope which does not allow permeation of external agents.[23] Furthermore, compound **2** was observed to be more suppressive of the bacterial strains than **1**. This observation was unexpected because both compounds are polyphenols with 3 OH groups each which confer hydrophilic character on them and as well as some level of antimicrobial activity. Polyphenols (tannins) obtained in previous studies have demonstrated antimicrobial activities.[10,24] However, the C_2H_5 group attached to the -COO link in **1** is expected to make it more lyphophilic and consequently more antimicrobial.[20]

However, the contrary was obtained in this study. It would be interesting to know the mechanisms of the antimicrobial activities demonstrated by these compounds. Also, both compounds demonstrated no antifungal activity against *C. albicans*. This particular observation was not surprising because fungal strains such as *Candida spp*. limit the permeation of substances because of their integral structures which are pleomorphic and facultative in nature hence, resembling those of higher plants.[23]

CONCLUSIONS

This study reports for the first time the isolation of ethyl gallate and pyrogallol from the butanol fraction of *A. wikesiana var. lace-acalypha*. These two compounds are expected to serve as chemotaxonomic markers for this species and variety in particular and the genus, *Acalypha* in general. Also, the observed antimicrobial activities of the isolated compounds have lent credence to the folkloric uses of the plant especially in the treatment of diseases of microbial origin.

ACKNOWLEDGEMENTS

We acknowledge the efforts of B. Odjobo, formerly of the National Research Institute for Chemical Technology (NARICT) Zaria, Nigeria but now of the Federal Institute of Industrial Research, Oshodi (FIIRO) Lagos in obtaining the spectra of the compounds. The contribution of E. Akpan, Principal Technologist, Pharmaceutical Microbiology Unit, Faculty of Pharmacy, University of Uyo, Uyo, Nigeria is equally appreciated.

REFERENCES

[1]Riley, H. P., *Families of Flowering Plants of Southern Africa*. University of Kentucky Press, **1963**, 73.

[2]Oliver, B., *Medicinal Plants in Nigeria*. Nigerian College of Arts, Science and Technology, **1959**, 58.

[3]Akinde, B. E., Odeyemi, O. O., *Nigerian Med. J.*, **1987**, *17*, 163-165.

[4]Alade, P. I., Irobi, O. N., *J. Ethnopharmacol*., **1993**, *39*, 171-174.

[5] Ikewuchi, J. C., Anyadiegwu, A., Ugono, E. Y., Okungbara, S. O., *Pak. J. Nutr.*, **2008**, *17(1)*, 130-132.

[6]Bussing, A., Stein, G. M., Herterich, A. L., Pfuller, M., *J. Ethnopharmacol.*, **1997**, *66*, 301-309.

[7]Al-Attar, A. M., *Am. J. Med.*, **2010,** *1(1)*, 51-58.

[8]Lim, S. W., Ting, K. N., Bradshaw, T. D., Zeemathul, N. A., Wiart, C., Khoo, T. J., Lolin, K. H., Loh, H. S., *J. Ethnopharmacol.*, **2011**, *130*, 97-101.

[9]Oladimeji, H. O., *Bioactivity-guided Fractionation of Acalypha wilkesiana*. M.Sc. Thesis, Obafemi Awolowo University, **1997**.

[10]Adesina, S. K., Idowu, O., Ogundaini, A. O., Oladimeji, H., Olugbade, T. A., Onawunmi, G. O., Pais, M., *Phytother. Res.*, **2000**, *14*, 371-374.

[11]Gibson, L., Khoury, J., *Lett. Appl. Microbiol.*, **1986**, *3*, 127-129.

[12]Murray, P., Baron, E., Pfaller, M., Tenover, F., Yolken, R., *Manual of Clinical Microbiology*. 4th edition, American Society of Microbiology Press, **1995**, 967-970.

[13]Washington, J., *The Agar Diffusion Method*. In: *Manual of Clinical Microbiology*, 4th edition, American Society of Microbiology Press, **1995**, 971-973.

[14]*NCCLS Performance Standard for Antimicrobial Susceptibility Test*. 8th edition, Approved Standard. The Committee, **2003**, 130.

[15]Nia, R., *Isolation and Characterization of Antibacterial Constituents from Calliandra haematocephala Hassk and Cissus quandrangularis L.*, Ph. D. Thesis, Obafemi Awolowo University, **1999**.

[16]Oladimeji, H. O., *Chemical and Bological Studies on Cyathula prostrata (L.)Blume*, Ph.D. Thesis, University of Uyo, **2012.**

[17]Odebiyi, O. O., Sofowora, A., *Lloydia*, **1978**, *41*, 234.

[18]Odebiyi, O. O., Sofowora, A., *Phytochemical Screening of Nigerian Medicinal Plants-Part II*. 2nd OAU/STRC Inter-Afr. Symp. Trad. Pharmac. Afr. Med. Plants, OAU/STRC Publishers No 115, **1979.**

[19]Oladimeji, H. O., Usifoh, C.O., *Int. J. Pharm. Sci. Res.*, **2013,** *4(2)*, 628-633.

[20]Olaniyi, A. A., *Essential Medicinal Chemistry*. 1st edition, Shaneson C. I. Limited, **1989**, 136-138.

[21]Olaniyi, A. A., *Principles of Quality Assurance and Pharmaceutical Analysis.* Mosuro Publishers, **2000**, 321-327.

[22]Lopez-Avila, V., *Org. Mass Spect.*, **1987**, *22*, 557.

[23] Brown, M. R., *Pharm. J.*, **1975**, *215*, 239-242.

[24]Lamikanra, A., Ogundaini, A. O., Ogungbamila, F. O., *Phytother. Res.*, **1990,** *4(5)*, 198-200.

Received: 06.06.2014.
Accepted: 19.07.2014.

SYNTHESIS AND ANTI-MICROBIAL ACTIVITIES OF SOME THIOUREA BASED METAL COMPLEXES

Vinayak S. Sonnekar,[a] Wamanrao N. Jadhav,[b] Satish A. Dake,[c] Swapanil G. Dhole,[c] Shankar S. Narwade[c]and Rajendra P. Pawar[c]*

Keywords: Antibacterial activity; antifungal activity; metal complex; Schiff bases; FT-IR and UV-VIS spectral data.

The transition metal (II) complexes were formed by the reaction of Co(II), Ni(II), Zn(II), Fe(II) and Cu(II) nitrates with the Schiff base ligands. The complexes were characterized using infrared (FT-IR), electronic spectral (UV), elemental analysis, melting points and XRD analysis etc. The transition metal(II) complexes were screened for antibacterial and antifungal activities. Antibacterial activity against four bacteria such as *Escherichia coli, Salmonella typhi, Staphylococcus aureus* and *Bacillus subtilis* bacterial strains by the agar-cup method. Antifungal activity was studied against four bacteria *Aspergillus Niger, Penicillium Chrysogenum, fusarium moneliforme and aspergillus flavus* bacterial strains by the poison plate method. The complexes were found to exhibit higher to moderate activity against some bacterial species.

*Corresponding Authors
E-Mail: rppawar@yahoo.com
[a] Department of Chemistry, Sant Tukaram College, Parbhani-431401, MS, India
[b] Organic Chemistry Synthesis Laboratory, Dnyanopasak College, Parbhani-431401, MS, India
[c] Department of Chemistry, Deogiri College, Aurangabad-431 005, MS, India

INTRODUCTION

The treatment of infectious diseases always remains a significant and serious problem in society, because of increasing number of multidrug resistant microbial pathogens and emerging infectious diseases. The increasing human resistance and antimicrobial agents are being well thought as essential sources in novel drug discoveries for treating a range of fungal and bacterial infections. In present study, we focus on synthesis of metal complexes, and their antibacterial and antifungal activities.

Schiff bases are important precursors in various organic syntheses.[1-4] The schiff base ligands are immense coordinating compounds. It forms stable complexes with different transition metal ions. The transition metal complexes have been always in the investigation due to their broad applications in wide ranging areas from natural sciences to material science.

Schiff bases have also been exhibits a broad range of biological activities, including antifungal, antibacterial, antimalarial, antiproliferative, anti-inflammatory, antiviral, and antipyretic properties.[5-6]

The mixed ligand complexes formation was an important aspect in inorganic and analytical chemistry.

The uses of mixed ligand complexes in various fields diverted us to develop novel methodologies with increased atom economy, selectivity and biological applications and environmental approach.[7] They are also used as catalyst, in medicine like antibiotics and anti-inflammatory agents and antibacterial agents[8-16] as well as in industry as anticorrosion agents.[17-23]

The present investigation reports the synthesis of some substituted novel bis-metal complexes. In this process, Schiff bases and metal nitrate were dissolved in ethanol separately. On addition, the mixture was refluxed for appropriate time (Scheme 1). The separated transition metal(II) complexes were screened for antibacterial and antifungal activities against different bacteria.

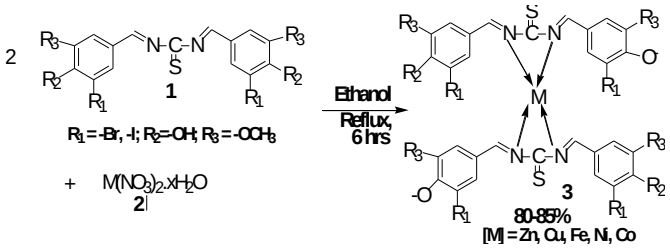

Scheme 1. General synthesis route of complexes

RESULTS AND DISCUSSION

Novel metal complexes are synthesized using Schiff bases of thiourea and urea with nitrates of metal Zn(II), Co(II), Fe(II), Cu(II), Ni(II) dissolved in ethanol. Physical parameters were discussed in detail with their colour and melting point and reported in Table 1. Spectral characterization FT-IR and UV-visible spectra of these complexes were scanned and reported.

FT-IR spectrum analysis

Infrared spectra were recorded on a spectrophotometer in wave number region 4000-400 cm^{-1}.The spectra bands of metal complexes at 410-497 cm^{-1} were characterized for metal which indicates that the nitrogen atom of the ligand was coordinated i.e., (M-N) bands frequency. The strong bands at 3200-3640 cm^{-1} assigned as *v* O-H group and 1648-1679 cm^{-1} band assigned for *v*C=N group. The stretching frequency at 3000-3150 cm^{-1} can be recognized to C-H bond.

 DOI: 10.17628/ecb.2014.3.792-797

Table 1. Synthesis of novel metal complexes

Codes	Complexes (3)	Colour	MP. (^{O}C)
W1	Bis[bis(4-hydroxy-3-methoxybenzylidene)thiourea-]zinc(II)	Yellowish	135 ^{0}C
W2	Bis[bis(4-hydroxy-3-methoxybenzylidene)thiourea-]cobalt(II)	Cream	162 ^{0}C
W3	Bis[bis(4-hydroxy-3-methoxybenzylidene)thiourea-]iron(II)(II)	Violet	141 ^{0}C
W4	Bis[bis(4-hydroxy-3-methoxybenzylidene)thiourea-]copper(II)	Brown	121 ^{0}C
W5	Bis[bis(4-hydroxy-3-methoxybenzylidene)thiourea-]nickel(II)	Gray	118 ^{0}C
T1	Bis[bis(4-hydroxy-3-iodo-5-methoxybenzylidene)thiourea-]zinc(II)	Pale Brown	160 ^{0}C
T2	Bis[bis(4-hydroxy-3-iodo-5-methoxybenzylidene)thiourea-]copper(II)	Gray	230 ^{0}C
T3	Bis[bis(4-hydroxy-3-iodo-5-methoxybenzylidene)thiourea-]iron(II)	Faint Brown	150 ^{0}C
T4	Bis[bis(4-hydroxy-3-iodo-5-methoxybenzylidene)thiourea-]nickel(II)	Cream	185 ^{0}C
T5	Bis[bis(4-hydroxy-3-iodo-5-methoxybenzylidene)thiourea-]cobalt(II)	Purple	159 ^{0}C
S1	Bis[bis(3-bromo-4-hydroxy-5-methoxybenzylidene)thiourea-]iron(II)	Gray	161 ^{0}C
S2	Bis[bis(3-bromo-4-hydroxy-5-methoxybenzylidene)thiourea-]cobalt(II)	Faint Brown	163 ^{0}C
S3	Bis[bis(3-bromo-4-hydroxy-5-methoxybenzylidene)thiourea-]nickel(II)	Brown	162 ^{0}C
S4	Bis[bis(3-bromo-4-hydroxy-5-methoxybenzylidene)thiourea-]copper(II)	Faint Brown	142 ^{0}C
S5	Bis[bis(3-bromo-4-hydroxy-5-methoxybenzylidene)thiourea-]zinc(II)	Brown	164 ^{0}C

The stretching frequencies appear for C-O functional group region are 1268-1385 cm^{-1}. IR stretching frequencies for C=S bond are found to be in the region 1143-1260 cm^{-1}. The medium intensity but relatively shaped (instead of very strong and diffuse) ν_{OH} bands may be the consequence of the fact that only the half of the phenolic hydroxyls are deprotonated to compensate the charges of the central metal cations, and the residual OH groups are located in well defined hydrogen bound network.

Electronic absorption spectrum

DMSO solvent is used for UV-visible spectrum of complexes. The peaks are observes at λ_{max} = 362 nm for bis[(4-hydroxy-3-methoxybenzylidene(4-oxy-3-methoxy-benzylidene)thiourea]zinc(II) (W1); λ_{max} = 363 nm for bis[(4-hydroxy-3-methoxybenzylidene)(4-oxy-3-methoxy-benzylidene)thiourea]cobalt(II) (W2); λ_{max} = 478 nm for bis[(4-hydroxy-3-methoxybenzylidene)(4-oxy-3-methoxy-benzylidene)thiourea]iron(II) (W3); λ_{max} = 324 nm for bis[(4-hydroxy-3-methoxybenzylidene(4-oxy-3-methoxy-benzylidene))thiourea]copper(II) (W4); λ_{max} = 362 nm for bis[(4-hydroxy-3-methoxybenzylidene)(4-oxy-3-methoxy-benzylidene)thiourea]nickel(II) (W5); λ_{max} = 325 nm for bis[(4-hydroxy-3-iodo-5-methoxybenzylidene)(4-oxy-3-io-do-5-methoxybenzylidene)thiourea]zinc(II) 8T1); λ_{max} = 326 nm for bis[(4-hydroxy-3-iodo-5-methoxybenzylidene)(4-oxy-3-iodo-5-methoxybenzylidene)thiourea]copper(II) (T2); λ_{max}=412 nm for bis[(4-hydroxy-3-iodo-5-methoxy-benzylidene)(4-oxy-3-iodo-5-methoxybenzylidene)thio-urea]Iron(II) (T3); λ_{max}=325 nm for bis[(4-hydroxy-3-iodo-5-methoxybenzylidene)(4-oxy-3-iodo-5-methoxybenzylide-ne)thiourea]nickel(II) (T4); λ_{max}=326 nm for bis[(4-hydroxy-3-iodo-5-methoxy benzylidene)(4-oxy-3-iodo-5-methoxybenzylidene)thiourea]copper(II) (T5); λ_{max}=326 nm for bis[(3-bromo-4-hydroxy-5-methoxybenzylidene)(3-bro-mo-4-oxy-5-methoxybenzylidene))thiourea]iron(II) (S1); λ_{max}=326 nm for bis[(3-bromo-4-hydroxy-5-methoxybenzylidene)(3-bromo-4-oxy-5-methoxybenzylide-ne)thiourea]cobalt(II) (S2); λ_{max}=325 nm for bis[(3-bromo-4-hydroxy-5-methoxybenzylidene)(3-bromo-4-oxy-5-meth-oxybenzylidene)thiourea]nickel(II) (S3); λ_{max}=325 nm for bis[(3-bromo-4-hydroxy-5-methoxybenzylidene)(3-bromo-4-oxy-5-methoxybenzylidene)thiourea]copper(II) (S4); λ_{max}=362 nm for bis[(3-bromo-4-hydroxy-5-methoxy benzylidene)(3-bromo-4-oxy-5-methoxybenzylidene)thio-urea]zinc(II) (S5) which were assignable to $\pi \rightarrow \pi^*$ transitions.

X-Ray diffraction studies

XRD study of bis[bis(4-hydroxy-3-methoxybenzylidene) thiourea-]nickel(II) were made on RIGAKU miniflex-II with Cu-Kα1 radiation (λ = 1.5406 Å). The powder XRD patterns were recorded in the 2θ range between 10^0 and 80^0 with a step size of 0.02. The X-ray powder diffractogram of nickel(II) complex exhibits crystalline in nature. The X-ray powder diffractogram of Ni(II) complex [$(C_{34}H_{30}N_4NiO_8S_2$] is given in (Figure 1). The diffractogram of Ni(II) complex showed eleven reflections with maxima at 2θ (12.88^0) corresponding to *d* value 6.8781 Å. [from Table 1 (W5)].

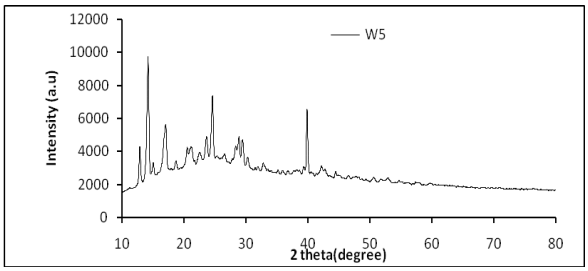

Figure 1. XRD pattern of Bis[bis(4-hydroxy-3-methoxybenzylidene) thiourea]nickel(II) complex (W5)

XRD study of the bis[bis(4-hydroxy-3-iodo-5-methoxybenzylidene)thiourea-]cobalt(II) were made on RIGAKU Miniflex-II with Cu-Kα1 radiation (λ = 1.5406 Å). The powder XRD patterns were recorded in the 2θ range between 10^0 and $80^0$with a step size of 0.02 The X-ray powder diffractogram of cobalt (II) complex exhibits crystalline in nature. The X-ray powder diffractogram of cobalt(II) complex [$C_{34}H_{26}CoI_4N_4O_8S_2$] is given in (Figure 2). The diffractogram of Co(II) complex showed twenty three reflections with maxima at 2θ (29.5^0) corresponding to *d* value 1.5706 Å. [from Table 1 (T5)].

 DOI: 10.17628/ecb.2014.3.792-797

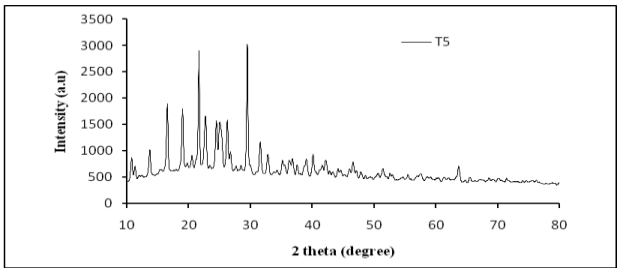

Figure 2. XRD pattern of bis[bis(4-hydroxy-3-iodo-5-methoxy benzylidene)thiourea-]cobalt(II) (T5)

XRD study of the bis[bis(3-bromo-4-hydroxy-5-methoxy-benzylidene)thiourea-]iron(II) were made on RIGAKU miniflex-II with Cu-Kα1 radiation (λ = 1.5406 Å). The powder XRD patterns were recorded in the 2θ range between 10^0 and 80^0 with a step size of 0.02 The X-ray powder diffractogram of iron(II) complex exhibits crystalline in nature. The X-ray powder diffractogram of Fe(II) complex [$C_{34}H_{26}Br_4FeN_4O_8S_2$] is given in (Figure 3). The diffractogram of Fe(II) complex showed twenty one reflections with maxima at 2θ (26.49^0) corresponding to d value 2.9292 Å.[Figure 3, Table 1 (S1)].

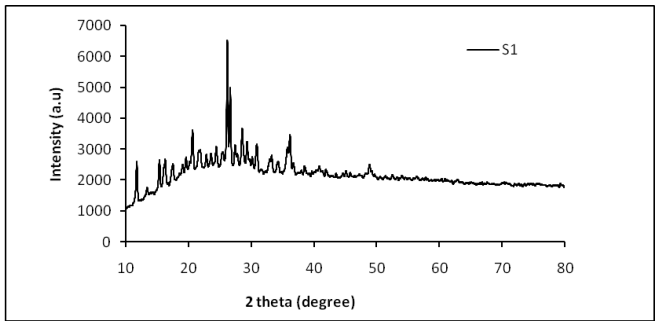

Figure 3. XRD pattern of Bis[bis(3-bromo-4-hydroxy-5-methoxy-benzylidene)thiourea-]iron(II) (S1)

The complexes are probably polymers with octahedral coordination with chelate structure involving the phenolate groups but the complete elucidation of theirs structure requires further spectroscopical and single crystal X-ray diffraction studies.

Biological screening

The biological screening of synthesized compounds was discussed in two sections i.e. antibacterial activity, antifungal Activity.

Antibacterial activity

In this research work the antibacterial activity was studied, but the standardization of all the parameters of ligands and calculation of MLD for individual organism is necessary. The antibacterial activities of 15 complexes with bacterium *E. coli* were studied using agar cup method and compared with standard antibiotic penicillin. It was found that 3 complexes (T3, S5 and W4) showed considerable antibacterial activity. But complexes S5 showed significant antibacterial activity because the zone of inhibition showed by standard antibiotic penicillin was 21 mm while the complexes S5 26 mm zone of inhibition.

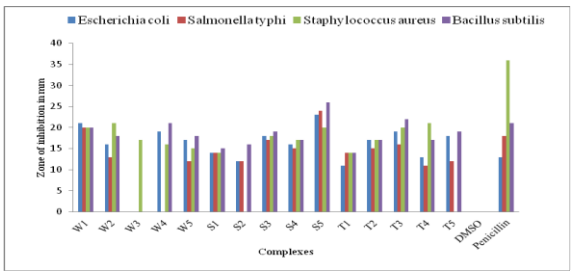

Figure 1. Antibacterial activity of novel metal complexes

Antibacterial activity of 15 complexes with bacterium *Salmonella typhi* were studied by agar cup method and compared with standard antibiotic penicillin. It was found that 2 complexes (W1 and S5) showed considerable antibacterial activity. But complexes S5 showed significant antibacterial activity. The zone of inhibition showed by standard antibiotic penicillin was 18mm while the complexes S5 24 mm zone of inhibition

The antibacterial activity of 15 complexes with bacterium *Staphylococcus aureus* were studied by agar cup method and compared with standard antibiotic penicillin. It was found that *staphylococcus aureus* was resistant to all the 15 complexes because the zone of inhibition obtained by standard penicillin was higher as compared to complexes.

Table 2. Antibacterial activity of novel metal complexes

Label	*Escherichia coli*	*Salmonella typhi*	*Staphylococcus aureus*	*Bacillus subtilis*
W1	21 mm	20 mm	20 mm	20 mm
W2	16 mm	13 mm	21 mm	18 mm
W3	0 mm	0 mm	17 mm	0 mm
W5	17 mm	12 mm	15 mm	18 mm
S1	14 mm	14 mm	14 mm	15 mm
S2	12 mm	12 mm	0 mm	16 mm
S3	18 mm	17 mm	18 mm	19 mm
S4	16 mm	15 mm	17 mm	17 mm
S5	23 mm	24 mm	20 mm	26 mm
T1	11 mm	14 mm	14 mm	14 mm
T2	17 mm	15 mm	17 mm	17 mm
T3	19 mm	16 mm	20 mm	22 mm
T4	13 mm	11 mm	21 mm	17 mm
T5	18 mm	12 mm	0 mm	19 mm
Dmso	0 mm	0 mm	0 mm	0 mm
Peni-cillin	13 mm	18 mm	36 mm	21 mm

The antibacterial activity of 15 complexes with bacterium *Bacillus subtilis* were studied by agar cup method and compared with standard antibiotic penicillin. It was found that 3 complexes (W4, T3 and S5) showed considerable antibacterial activity. But complexes S5 showed significant antibacterial because the zone of inhibition showed by standard antibiotic penicillin was 18 mm while the complexes S5 26 mm zone of inhibition.

In this study all the 15 complexes were tested. Complex S5 showed significant activity against three test cultures i.e. *E. coli*, *Salmonella typhi* and *Bacillus subtilis*, but no complex active against *Staphylococcus aureus* (Table 2).

Table 2. Antibacterial activity of novel metal complexes

Sr.No.	Label	*Escherichia coli*	*Salmonella typhi*	*Staphylococcus aureus*	*Bacillus subtilis*
1	W1	21 mm	20 mm	20 mm	20 mm
2	W2	16 mm	13 mm	21 mm	18 mm
3	W3	00 mm	00 mm	17 mm	00 mm
4	W4	19 mm	00 mm	16 mm	21 mm
5	W5	17 mm	12 mm	15 mm	18 mm
6	S1	14 mm	14 mm	14 mm	15 mm
7	S2	12 mm	12 mm	00 mm	16 mm
8	S3	18 mm	17 mm	18 mm	19 mm
9	S4	16 mm	15 mm	17 mm	17 mm
10	S5	23 mm	24 mm	20 mm	26 mm
11	T1	11 mm	14 mm	14 mm	14 mm
12	T2	17 mm	15 mm	17 mm	17 mm
13	T3	19 mm	16 mm	20 mm	22 mm
14	T4	13 mm	11 mm	21 mm	17 mm
15	T5	18 mm	12 mm	00 mm	19 mm
16	DMSO	00 mm	00 mm	00 mm	00 mm
17	Penicillin	13 mm	18 mm	36 mm	21 mm

Table 3. Antifungal activities of novel metal complex derivatives

Sr. No.	Compounds	*Aspergillus niger*	*Penicillium chrysogenum*	*Fusarium moneliforme*	*Aspergillus flavus*
1	W1	RG	-ve	-ve	-ve
2	W2	+ve	-ve	-ve	RG
3	W3	RG	-ve	-ve	RG
4	W4	RG	-ve	-ve	-ve
5	W5	RG	-ve	+ve	RG
6	S1	-ve	-ve	-ve	-ve
7	S2	-ve	-ve	-ve	RG
8	S3	-ve	-ve	-ve	-ve
9	S4	-ve	-ve	-ve	-ve
10	S5	-ve	-ve	-ve	-ve
11	T1	RG	-ve	-ve	RG
12	T2	RG	-ve	-ve	-ve
13	T3	-ve	-ve	-ve	-ve
14	T4	RG	-ve	-ve	RG
15	T5	RG	-ve	-ve	RG
16	Grysofulvin	-ve	-ve	-ve	-ve
17	Blank	+ve	+ve	+ve	+ve

+ve – Growth (no antifungal activity); ve – No growth (antifungal activity observed); RG – reduced growth

Antifungal Activity

Antifungal activity of 15 metal complexes was tested for antifungal activity of four test fungal cultures by using poison plate technique. Complexes (S1, S2, S3, S4 S5 and T3) showed antifungal activity, Eight complexes (W1, W3, W4 W5, T1, T2 T4 and T5) reduces the growth while remaining one complexes W2 support the growth of fungal culture that mean serve as nutrient *for Aspergillus flavus*.

Penicillium chrysogenum and *Fusarium moneliforme* are more susceptible than the other two test fungal culture *Aspergillus niger* and *Aspergillus flavus*. *Aspergillus flavus* was susceptible for complexes (W1, W4, S1, S3, S4, S5, T2 and T3) while reaming reduces the growth.

In this study found that complexes S1, S2, S3, S4 and S5 shows significant antifungal activity against all the four tested fungal culture (Table 3).

EXPERIMENTAL SECTION

Preparation of bis(bis(4-hydroxy-3-methoxybenzylidene)thiourea-H)cobalt(II) (W2)

A mixture of Schiff base (1E,3E)-1,3-bis(4-hydroxy-3-methoxybenzylidene)thiourea 6.88 g, 2 mmol) and cobalt nitrate (1.82 g, 1 mmol) dissolved in ethanol (5 ml) was refluxed for 6 hours. The pH of solution was adjusted to 7-8

using alcoholic ammonia solution. The progress of reaction mixture is monitored by thin layer chromatography (TLC) using petroleum ether: ethyl acetate (7:3 ml) elute. The coloured products were isolated after reduction of volume by evaporation. It was filtered of washed with ethanol, dried under vacuum and recrystallized in ethanol. Spectral data for synthesized complexes

Bis[(4-hydroxy-3-methoxybenzylidene)(4-oxy-3-methoxybenzylidenethiourea)zinc(II)] (W1): FTIR (KBr, cm^{-1}): 3640 (Ar-OH), 3150 (Ar-C-H), 2970 (C-H), 1649 (C=N), 1238 (C-O phenolic), 1165 (C=S), 434 (Zn-N) cm^{-1}, UV-Vis: λ_{max} = 362 nm.

Bis[(4-hydroxy-3-methoxybenzylidene)(4-oxy-3-methoxybenzylidene)thiourea)cobalt(II)] (W2): FTIR (KBr, cm^{-1}): 3216 (Ar-OH), 3050 (Ar-C-H), 2978 (C-H), 1648 (C=N), 1236(C-O phenolic), 1162 (C=S), 429(Co-N) cm^{-1} Anal. Calc. for $C_{34}H_{30}CoN_4O_8S_2$ C: 54.76, H: 4.06, N: 7.51, Found: C: 54.57, H: 3.74, N: 7.55; UV-Vis: λ_{max} = 363 nm.

Bis[(4-hydroxy-3-methoxybenzylidene)(4-oxy-3-methoxybenzylidene)thiourea)iron(II)] (W3): FTIR (KBr, cm^{-1}): 3206 (Ar-OH), 3010 (Ar-C-H), 2839 (C-H), 1672 (C=N), 1272(C-O phenolic), 1143 (C=S), 475(Fe-N) cm^{-1}; UV-Vis: λ_{max} = 478 nm.

Bis[(4-hydroxy-3-methoxybenzylidene)(4-oxy-3-methoxybenzylidene)thiourea)copper(II)] (W4): FTIR (KBr, cm^{-1}): 3233 (Ar-OH), 3140 (Ar-C-H), 2839 (C-H), 1679 (C=N), 1385(C-O, phenolic), 1207 (C=S), 411(Cu-N) cm^{-1}; UV-Vis: λ_{max} = 324 nm.

Bis[(4-hydroxy-3-methoxybenzylidene)(4-oxy-3-methoxybenzylidene)thiourea)nickel(II) (W5): FTIR (KBr, cm^{-1}): 3205 (Ar-OH), 3045 (Ar-C-H), 2940 (C-H), 1648 (C=N), 1343(C-O, phenolic), 1274 (C=S), 430 (Ni-N) cm^{-1} Anal. Calc. for $C_{34}H_{30}N_4NiO_8S_2$ C: 54.78, H: 4.06, N: 7.51, Found: C: 54.60, H: 4.54, N: 7.49; UV-Vis: λ_{max} = 362 nm.

Bis[(4-hydroxy-3-iodo-5-methoxybenzylidene(4-oxy-3-iodo-5-methoxybenzylidene))thiourea)zinc(II)] (T1): FTIR (KBr, cm^{-1}): 3200 (Ar-OH), 3050 (Ar-C-H), 2942 (C-H), 1665 (C=N), 1295(C-O, phenolic), 1257, (C=S), 670 (C-I), 435 (Zn-N) cm^{-1} Anal. Calc. for $C_{34}H_{26}ZnI_4O_8N_4S_2$ C: 32.52, H: 2.09, N: 4.46, Found: C: 32.57, H: 2.54, N: 4.35; UV-Vis: λ_{max} = 325 nm.

Bis[(4-hydroxy-3-iodo-5-methoxybenzylidene(4-oxy-3-iodo-5-methoxybenzylidene))thiourea)copper(II)] (T2): FTIR (KBr, cm^{-1}): 3499 (Ar-OH), 3105 (Ar-C-H), 2846 (C-H), 1666 (C=N), 1293(C-O, phenolic), 1258, (C=S), 672 (C-I), 410 (Cu-N) cm^{-1}; UV-Vis: λ_{max} = 326 nm.

Bis[(4-hydroxy-3-iodo-5-methoxybenzylidene(4-oxy-3-iodo-5-methoxybenzylidene))thiourea)iron(II)] (T3): FTIR (KBr, cm^{-1}): 3485 (Ar-OH), 3150 (Ar-C-H), 2915 (C-H), 1667 (C=N), 1268 (C-O, phenolic), 1237 (C=S), 672 (C-I), 497 (Fe-N) cm^{-1}; UV-Vis: λ_{max} = 412 nm.

Bis[(4-hydroxy-3-iodo-5-methoxybenzylidene(4-oxy-3-iodo-5-methoxybenzylidene))thiourea)nickel(II) (T4): FTIR (KBr, cm^{-1}): 3498 (Ar-OH), 3000 (Ar-C-H), 2845 (C-H), 1666 (C=N), 1295 (C-O, phenolic), 1257 (C=S), 670 (C-I), 434 (Ni-N) cm^{-1}; UV-Vis: λ_{max} = 325 nm.

Bis[(4-hydroxy-3-iodo-5-methoxybenzylidene(4-oxy-3-iodo-5-methoxybenzylidene))thiourea)copper(II) (T5): FTIR (KBr, cm^{-1}): 3207 (Ar-OH), 3050 (Ar-C-H), 2845 (C-H), 1665 (C=N), 1295 (C-O, phenolic), 1257 (C=S), 671 (C-I), 433 (Co-N) cm^{-1} Anal. Calc. for $C_{34}H_{26}CuI_4N_4O_8S_2$ C: 32.52, H: 2.09, N: 4.46, Found: C: 32.69, H: 2.24, N: 4.35; UV-Vis: λ_{max} = 326 nm.

Bis[(3-bromo-4-hydroxy-5-methoxybenzylidene)(3-bromo-4-oxy-5-methoxybenzylidene)thiourea)iron(II) (S1): FTIR (KBr, cm^{-1}): 3302 (Ar-OH), 3055 (Ar-C-H), 2852 (C-H), 1676 (C=N), 1292 (C-O, phenolic), 1200 (C=S), 680 (C-Br), 458 (Fe-N) cm^{-1} Anal. Calc. for $C_{34}H_{26}Br_4FeN_4O_8S_2$ C: 38.59; H: 2.48; N: 5.29; Found: C: 38.60, H: 2.54, N: 5.69; UV-Vis: λmax = 326 nm.

Bis[(3-bromo-4-hydroxy-5-methoxybenzylidene)(3-bromo-4-oxy-5-methoxybenzylidene)thiourea)cobalt(II) (S2): FTIR (KBr, cm^{-1}): 3323 (Ar-OH), 3060 (Ar-C-H), 2931 (C-H), 1674 (C=N), 1290 (C-O, phenolic), 1170 (C=S), 680 (C-Br), 412 (Co-N) cm^{-1} Anal. Calc. for $C_{34}H_{26}Br_4CoN_4O_8S_2$ C: 38.48, H: 2.47, N: 5.29, Found: C: 38.57, H: 2.54, N: 5.35; UV-Vis: λmax = 326 nm.

Bis[(3-bromo-4-hydroxy-5-methoxybenzylidene)(3-bromo-4-oxy-5-methoxybenzylidene)thiourea)nickel(II) (S3): FTIR (KBr, cm^{-1}): 3298 (Ar-OH), 3100 (Ar-C-H), 2850 (C-H), 1674 (C=N), 1290 (C-O, phenolic), 1155 (C=S), 678 (C-Br), 441 (Ni-N) cm^{-1}; UV-Vis: λ_{max} = 325 nm.

Bis[(3-bromo-4-hydroxy-5-methoxybenzylidene)(3-bromo-4-oxy-5-methoxybenzylidene)thiourea)copper(II) (S4): FTIR (KBr, cm^{-1}): 3274 (Ar-OH), 3102 (Ar-C-H), 2982 (C-H), 1675 (C=N), 1291 (C-O, phenolic), 1159 (C=S), 680 (C-Br), 436 (Cu-N) cm^{-1}; UV-Vis: λ_{max} = 325 nm.

Bis[(3-bromo-4-hydroxy-5-methoxybenzylidene)(3-bromo-4-oxy-5-methoxybenzylidene)thiourea)zinc(II) (S5): FTIR (KBr, cm^{-1}): 3410 (Ar-OH), 3140 (Ar-C-H), 2924 (C-H), 1676 (C=N), 1290 (C-O, phenolic), 1159 (C=S), 680 (C-Br), 418 (Zn-N) cm^{-1}; UV-Vis: λ_{max} = 362 nm.

CONCLUSION

In conclusion, series of novel metal complex derivatives using thiourea schiff bases has been synthesized and screened for antibacterial and antifungal activities. Some of them metal complexes exhibits moderate to excellent antibacterial and antifungal activities. Synthesized compounds are characterized using infrared (FT-IR), electronic spectral (UV), elemental analysis, melting points and XRD analysis etc.

ACKNOWLEDGEMENT

Authors are thankful to the Principal Dr. P. L. More, DSM, College, Parbhani and Dr. S. N. Thore, Deogiri College, Aurangabad for encouragement during the process of carrying out this research work.

REFERENCES

[1]Tupare, S. D., Bhagat, D. V., Dake, S A., Pawar, R. P., *Int. J. Chem. Sci.*, **2012,** *10(4)*, 1-7.

[2]Pawar, R. P., Andurkar, N. M., Vibhute, Y. B., *J. Indian Chem. Soc.*, **1999**, *76*, 271-272.

[3]More, S. V., Dongarkhadekar, D. V., Chavan, R. N., Jadhav, W. N., Bhusare, S. R., Pawar, R. P., *J. Indian Chem. Soc*., **2002,** *79*, 768-769.

[4]Kendrekar, P. S., Siddiqui, R. F., Patil, P. S., Bhusare, S. R., Pawar, R. P., *Indian J. Pharm. Sci.*, **2003,** *65*, 313-315.

[5]Dhar, D. N.; Taploo, C. L., *J. Sci. Ind. Res.*, **1982,** *41*, 501-506.

[6]Przybylski, P., Huczyński, A., Pyta, K., Brzezinski, B., Bartl, F., *Curr. Org. Chem.*, **2009,** *13*, 124-148.

[7]Casassas, E., Izquierdo-ridora, A., Tauler, R., *J. Chem. Soc., Dalton Trans.*, **1990,** 2341-2345.

[8]De, B., Marbaniang, E. M., Kalita, R., Debnath, M., Das, M. C., Kalita, U., Lalfukmawia, S., Gupta, J. K., *J. Inst. Chemists (India)*, **2005,** *77*, 20-22.

[9]Brousse, B. N., Massa, R., Monglioni, A. G., Alho, M. M., D' Accorso, N., Gutkind, G., Moltrasio, G. Y., *J. Chilean Chem. Soc.*, **2004,** *49*, 45-49.

[10]Raman, M., Muthural, V., Ravichandran, S., Kulandaisamy, A., *Proc. Indian Acad. Sci. (Chem. Sci.)*, **2003,** *115(3)*, 161–167.

[11]Mulwad, V. V., Shriodkar, J. M., *Indian J. Heterocycl. Chem.*, **2002,** *11*, 199-202.

[12]Chohan, Z. H., Farooq, M. A., Scoozzafava, A., Supuran, C. T., *J. Enzym Inhib. Med. Chem.*, 2002, *17*, 1-7.

[13]Shikkargol, R. K., Malikarjuna , N. N., Angadi, S. D., *Natl. Acad. Sci. Lett.*, **2001**, *24*, 39-43.

[14]More, P. G., Bhalvankar, R. B., Pattar, S. C., *J. Indian Chem. Soc.*, **2001,** *78*, 474-475.

[15]Bi, S., Li, G., *Synth. React. Inorg. Met.-Org. Chem.*, **1999,** *29*, 1829-1841.

[16]Desai, J. M., Desai, K. K., *Asian J. Chem.*, **1999,** *11*, 1071-1073.

[17]Sun, B., Chen. J., Hu, J. Y., Lix, J., *Chin. Chem. Lett.*, **2001,** *12*, 1043.

[18]Boghaei, D. M., Mohebi, S., *Tetrahedron*, **2002,** *58*, 5357.

[19]Liu, J., Wu, B., Zhang, B., Liu, Y., *Turk. J. Chem.*, **2006,** *30*, 41.

[20]Britovsek, G. J. P., Gibson, V. V., Mastroianni, S., Oakes, D. C. H., Red, S. C., Solan, G. A., White, A. J. P., Williams, D. J., *Eur. J. Inorg. Chem.*, **2000,** *2*, 431.

[21]Budakoti, A., Abid, M., Azam, A., *Eur. J. Med. Chem.*, **2006,** *41*, 63.

[22]Jin, V. X., Tan, S. I., Ranford, J. D., *Inorg. Chim. Acta.*, **2005,** *358*, 677-686.

[23]Mehta, N. K., Agarwala, V. S., *Int. Corros. Cong. Proc.*, **1996,** *13*, 1.

Received: 30.03.2014.
Accepted: 30.06.2014.

THE INFLUENCE OF HYDROGEN SULPHIDE AND CONFIGURATION OF A DBD REACTOR POWERED WITH NANOSECOND HIGH VOLTAGE PULSES ON HYDROGEN PRODUCTION FROM BIOGAS

Miroslaw Dors,[a]* Tomasz Izdebski,[a] Mateusz Tański,[a] Jerzy Mizeraczyk[b]

Keywords: hydrogen; biomethane; dielectric barrier discharge; plasma; hydrogen sulphide.

The production of hydrogen from CH_4:CO_2:H_2S (70 % : 30 % : 1000 ppm) mixture, simulating dry biogas in a DBD reactor, supplied with nanosecond negative pulses, is presented. We have found that sulphur produced from H_2S during the process changes the electrical parameters of the reactor with a RVC electrode. As a result, the production of syngas and the selectivity of methane conversion into hydrogen, decreases. Due to changed electrical parameters of the reactors, radicals formed from methane recombine into C_2 and C_3 hydrocarbons more efficiently, resulting in lower production of hydrogen. Major by-product of the methane processing is propane, concentration of which is comparable to hydrogen.

* Corresponding author
E-Mail: mdors@imp.gda.pl
[a] Centre for Plasma and Laser Engineering, The Szewalski Institute of Fluid Flow Machinery, Gdańsk, Poland
[b] Department of Marine Electronics, Gdynia Maritime University, Gdynia, Poland

Introduction

So far, most of the plasma methods of the hydrogen production use such substrates, as natural gas, gasoline, heavy oils, and kerosene. Many of them use a combination of plasma and catalysts, either as a single-stage or two-stage system. The single-stage type is composed of the packing catalyst pellets within the plasma zone, or a coating catalyst on the surface of the electrode(s). As for the two-stage type, the plasma zone is located either upstream or downstream the catalyst bed, which is termed as the plasma preprocessing and plasma post-processing, respectively.

Unfortunately, the plasma-catalytic systems are not useful when biogas containing sulphides (mainly H_2S) is going to be processed, due to the catalyst poisoning. There are several publications claiming to describe the production of hydrogen from the biogas, using plasma-catalyst systems.[1-4] However, the authors have used a mixture of methane and carbon dioxide simulating the biogas, without any additives which are present in the real biogas, such as water vapor, H_2S and NH_3. Such a simple simulation of the biogas is not adequate when the outlet gas is going to be used with fuel cells, which are very sensitive to H_2S traces. There are only 2 papers on using the real biogas and both of them were published by the same research group, in 2008 and 2010.[5-6] Sekine et al studied the application of the pulsed corona discharge (PCD) reactor and the dielectric barrier discharge (DBD) reactor without any catalyst and they found, that the PCD could convert the biomethane into the syngas and H_2S into the solid sulphur simultaneously.[5-6] This is due to the high electron energy of the PCD - the electron has enough energy to dissociate a C–C bond and a C–S bond. On the other hand, the DBD could convert H_2S into solid sulphur too, but methane and CO_2 in the biogas have not reacted at the lower input power. In this work, we present the results of an experiment in which both the DBD and the pulsed power supply, are used. These results show the influence of the plasma reactor configuration, the catalyst typical for steam hydrocarbon reforming, and hydrogen sulphide polluting the biogas on the process of hydrogen production, methane conversion and its by-products formation.

Experimental set-up

In this paper the results obtained in three specific DBD reactors are presented. The schemes of the reactors are shown in Figs. 1-3. The reactor No. 1 represents basic construction which was used for the next two. It is made of a quartz glass tube of inner diameter 15 mm, in which a high voltage RVC (Reticulated Vitreous Carbon) electrode is placed. The glass tube is covered with an aluminum foil, remaining a 4 mm wide slit along the reactor. The RVC electrode is formed as a tube of outer diameter 8 mm, inner diameter 3 mm and length of 150 mm. Through that RVC tube, a mixture of methane, carbon dioxide and hydrogen disulfide (70 %:30 %:1000 ppm, respectively), simulating a dry biogas, was introduced into the reactor. Due to the relatively low porosity of the RVC tube, which is 80 ppi (pores per inch), the gas flow was not disturbed and was kept at 200 cm^3 min^{-1} at the atmospheric pressure. An average residence time for the processed gas in the discharge space of the reactor No. 1 is about 5.7 s.

In the reactor No. 2, there is an additional dielectric barrier in the form of ceramic tube, covering tightly the RVC electrode (Fig. 2). Then, the gas gap in the reactor decreases from 3.5 mm to 2 mm, which results in the average residence time in the discharge space of about 1 s (at the flow rate of 200 cm3 min-1). This additional barrier is also used as a support for Ni catalyst, incorporated into the ceramic via an impregnation method. The shorter residence time is compensated to some extend by more uniform and distributed non-thermal plasma generated by the DBD (Fig. 3).

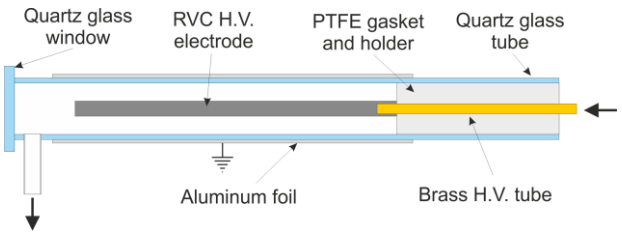

Figure 1. DBD reactor with RVC electrode (Reactor No. 1)

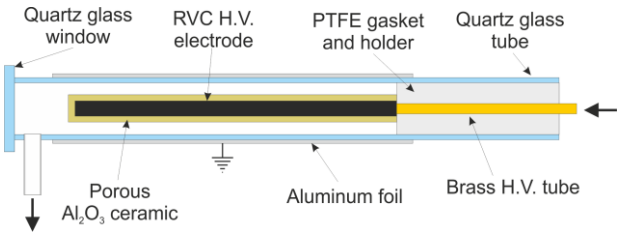

Figure 2. DBD reactor with RVC electrode and porous ceramic tube as the second dielectric barrier (Reactor No. 2)

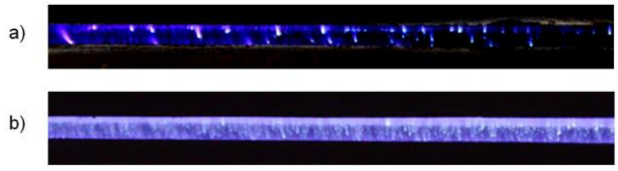

Figure 3. Images of DBD supplied by nanosecond pulses of 29 kV and 50 Hz in Reactor No.1 (a) and No.2 (b)

In the reactor No. 3 there is no additional dielectric barrier, but the gap between RVC electrode and the quartz glass tube is filled with glass beads (Fig. 4). This way, the DBD is transformed into the surface discharge developing on glass beads, instead of bridging the gas gap.

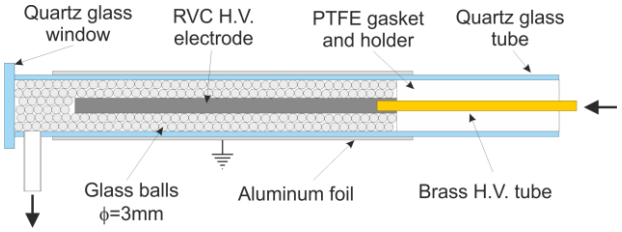

Figure 4. DBD reactor with RVC electrode and glass spheres

As a source of nanosecond pulses, we used the NPG-15/2000 pulse generator by Megaimpulse Ltd., producing negative voltage pulses of 29 kV with the repetition rate in the range of 50 Hz – 3.0 kHz. Typical voltage and current pulses are presented in Fig. 5. The voltage pulse is not influenced by the presence of H_2S in the gas, but the current pulse decreases significantly. Voltage pulses were measured using the Tektronix P6015A high voltage probe , whereas current pulses were measured using the Pearson 2877 coil. The discharge power was calculated by multiplying the repetition rate by a single discharge pulse energy (E_p), which was obtained after the experiment by the integration of the pulse voltage (U) times the current (I) over the pulse duration (t):

$$E_p = \int_{pulse} U(t)I(t)\mathrm{d}(t) \qquad (1)$$

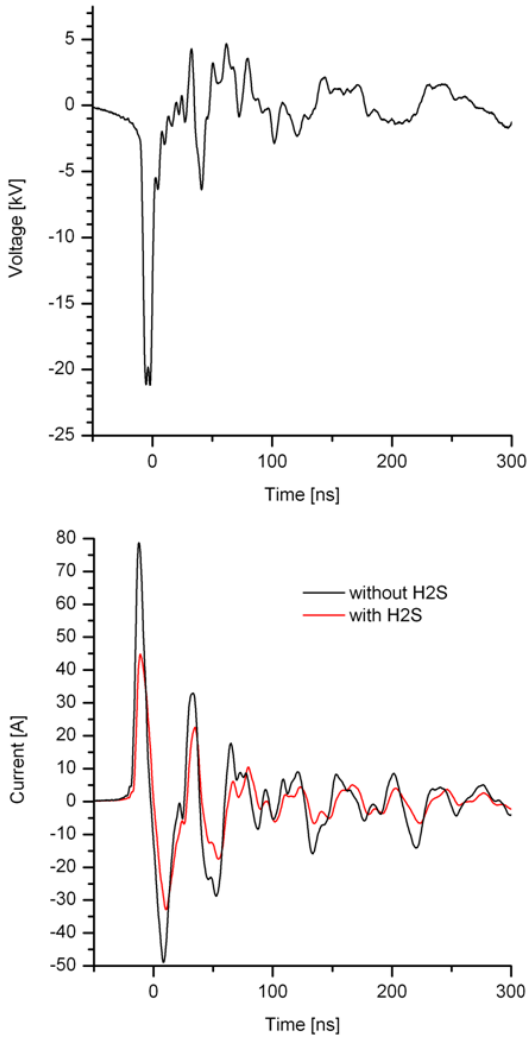

Figure 5. Typical voltage and current pulses in the Reactor No. 1 with and without H_2S in the processed gas

The gas composition before and after the processing in the DBD reactor was analyzed using FTIR spectrophotometer and gas chromatograph. For the measurements of CO_2, CO and CS_2, the FTIR Nicolet 380 spectrophotometer with gas cell of 10 cm optical path length and $CaCl_2$ windows was used. It was calibrated using certificated mixtures delivered by Linde Gaz Polska Ltd.: N_2:CO_2 (50 % : 50 %), N_2:CO (90 % : 10 %) and N_2:CS_2 (99 % : 1 %). Every single component was calibrated with a single mixture diluted in several proportions by nitrogen in a flowing regime, i.e. nitrogen stream was mixed with a stream of one compound and then introduced into the FTIR spectrophotometer. Mass flow controllers were used for accurate control of flow rates of each stream. The precision of the measurements of CO_2, CO and CS_2 was 90 ppm, 7 ppm, and 1.3 ppm, respectively.

The diagnostics of H_2 and CH_4 was carried out using the SRI 8610C gas chromatograph with the gas sampling valve, TCD, molecular sieve column and argon as a carrier gas. When the gas chromatograph was equipped with the FID and Hayesep Q column, then CH_4 and other hydrocarbons were detected. The gas chromatograph was calibrated towards H_2, CH_4, C_2H_2, C_2H_4, C_2H_6 and C_3H_8 with the same procedure as used for the FTIR spectrophotometer.

 DOI: 10.17628/ecb.2014.3.798-804

The calibration of hydrogen and methane was carried out with pure gases whereas C_2 and C_3 hydrocarbons were calibrated using certified mixtures composed of 5 % of each components and nitrogen. The precision of the measurements of H_2, C_2H_2, C_2H_4, C_2H_6 and C_3H_8 was 50 ppm, whereas for CH_4 it was only 450 ppm.

Unfortunately, hydrogen sulphide could not be measured neither with FTIR spectrophotometer (too low sensitivity when using 10 cm gas cell) nor GC (no detection available). For monitoring H_2S concentration we used colorimetric gas detection tubes by Dräger Safety AG, Germany.

Since the DBD formed in our reactor emits relatively strong light when applying high voltage, it was possible to apply optical emission spectroscopy. For that purpose, Mechelle 5000 spectrometer with ICCD i-Star camera by Andor Technology, equipped with UV transmitting optical fiber, was used.

The temperatures of the processed gas at the inlet and outlet of the DBD reactor was measured with thermocouples. Initial gas temperature was kept at 19 °C all the time during the experiment.

Results and discussion

A. Gas composition

The hydrogen production is exactly the same in the DBD reactor without and with the porous ceramic barrier when no catalyst and no H_2S is present (Fig. 6). It suggests the same mechanism of hydrogen formation from methane. In the presence of Ni, the highest H_2 concentration observed at the discharge power of 22 W, is also the same as in the other cases, but the shape of the curve describing the hydrogen production is different. After extrapolating all 4 curves obtained when using all of the reactors, and without H_2S, one can conclude that concentration of hydrogen is about to the highest value when no catalyst is used, i.e. the H_2 production is decreasing, whereas in the presence on Ni the production of hydrogen may still increase, with the potential of giving much more hydrogen. This leads to another conclusion, that the activity of Ni catalyst grows with the DBD power.

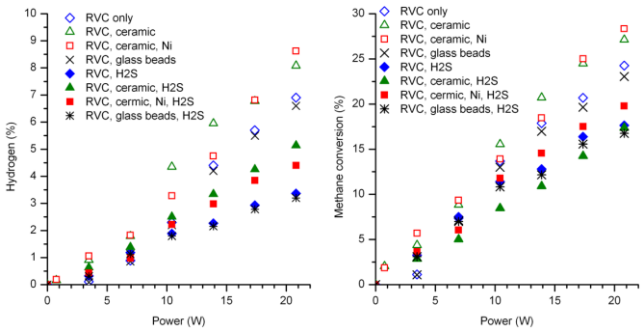

Figure 6. Concentrations of H_2 and methane conversion in the gas mixture processed by DBD with RVC electrode in Reactors No.1-3

Such a tendency is even better seen in the variations of the methane conversion degree (Fig. 6) and CO concentrations (Fig. 7). It is clear that at the highest discharge power of 22 W, in the experiment without the porous ceramic barrier, the CO concentration have reached the maximum, and with the ceramic free of the catalyst, it is close to a maximum, whereas in the presence of the catalyst in the porous ceramic the CO concentration still grows linearly. These differences in the shape of the curves may be explained by the different temperature of the gas in the plasma region. Simple modelling using a Thermodynamic Equilibrium Reactor (TER) shows a very similar tendencies at an assumption that the gas is heated up by the DBD to 300 K, 600 K and 800 K in the Reactor No. 2 with the catalyst, in the same reactor without the catalyst, and in the Reactor No. 1, respectively. This assumption is reasonable since, as seen in Fig. 3, the DBD in the reactor with the RVC electrode only forms a low number of filaments with plasma, which is more luminous and therefore hotter than uniform and less intensive plasma in the reactor with the additional ceramic barrier.

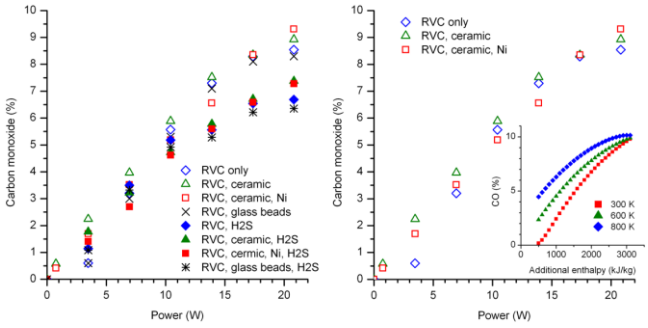

Figure 7. Concentrations of CO in the gas mixture processed by DBD with RVC electrode in Reactors No.1-3 and calculated using TER model.

It is clear from Figs. 6 and 7 that the addition of H_2S to the CH_4:CO_2 mixture inhibits the methane conversion and the production of hydrogen and CO in the DBD reactors. In the group of results obtained when H_2S was present in the gas mixture, the lowest production of hydrogen was observed in the reactor with RVC only (Reactor No. 1) and in the reactor packed with glass beads (Reactor No. 3), whereas the highest – in the reactor with ceramic tube but not saturated with Ni catalyst (Reactor No. 2). Hydrogen concentrations are 40-60 % lower comparing to the results for the mixture without H_2S. Such a high influence of H_2S on the hydrogen concentration cannot be explained by the gas phase reactions only, since the concentration of H_2S is almost 1000 times lower than methane. Hydrogen sulphide (Fig. 8) is decomposed in 90-96 % simply into hydrogen and solid sulphur. The contribution of H_2 from H_2S into the total balance of H_2 is small, i.e. below 1000 ppm, which and can be hardly distinguished. On the other hand, the formation of solid sulphur is clearly visible on the reactor wall (Fig. 9). The deposited sulphur forms a resistive layer which decreases the discharge current (Fig. 5). The only product of the H_2S reactions with CH_4, is CS_2 seen in the FTIR spectra (Fig. 10). Since CS_2 is well recognized in the spectra, it means that the reaction:

$$2H_2S + CH_4 \rightarrow CS_2 + 4H_2, \quad (2)$$

is the main one involving H_2S. This conclusion is supported by the results obtained experimentally and via modeling by Petherbridge et al.[7] They proposed a scheme of subsequent reactions:

$$CS_2 + H \rightarrow CS + HS, \quad (3)$$

$$H + SH \rightarrow S + H_2, \quad (4)$$

$$2HS \rightarrow S_2 + H_2. \quad (5)$$

Carbon disulfide is an intermediate by-product. It is decomposed in reaction (3), causing a drop of CS_2 concentration when H_2S concentration is too low to support high CS_2 production. This process is well seen in Fig. 8, showing a peak in CS_2 concentration at the DBD power of 10 W. It is interesting that Sekine et al. have obtained exactly the same CS_2 profile, when increasing the DBD current.[5] In their experiment, they were able to use much higher power and obtain the complete decomposition of carbon disulfide. They also found, that the final product of H_2S transformations is solid sulphur, depositing on the reactor wall.

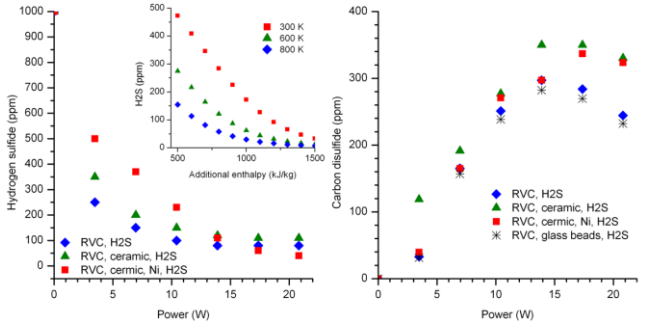

Figure 8. Concentrations of H_2S and CS_2 in the gas mixture processed by DBD with RVC electrode in Reactors No.1-3 and calculated using TER model (only H_2S)

Figure 9. Sulfur deposited on the reactor cylinder

It is interesting to note, that the decrease in H_2S concentration in all of the reactors (Fig. 8) is close to the results obtained from the TER model, similarly as in the case of CO. This may prove the conclusion on the different temperature of the gas in the plasma region in all studied reactors.

The concentrations of the hydrocarbon by-products detected in the gas mixture processed by the DBD in the different reactors are shown in Fig. 11. The formation of acetylene, as was observed in our previous experiments, is not related to the syngas production.[8] The biogas processing in the DBD reactor with the RVC electrode only resulted in the small concentrations of acetylene, not exceeding 0.126 % at the maximum discharge power of 22 W.

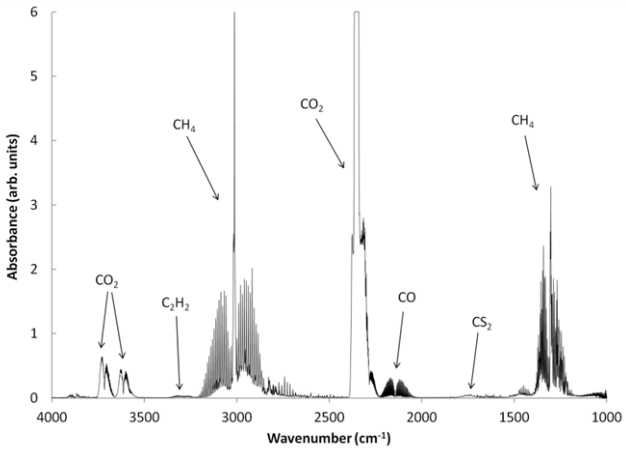

Figure 10. Typical FT-IR spectra of gas exiting DBD reactors with RVC electrode. Discharge power 22 W.

Adding the porous ceramic barrier caused the increased production of acetylene. Up to the level of 14 W of the discharge power, the concentrations of C_2H_2 are similar when the ceramic is free or impregnated with Ni. Further power increase reveals an activation of the Ni catalyst towards the decomposition of the acetylene, concentration of which drops dramatically down to 0.065 % at 22 W. In the presence of 1000 ppm H_2S in the processed gas, this drop is not observed. The most probable reason is poisoning of the Ni catalyst by sulphur, which suppresses the activation of the catalyst.

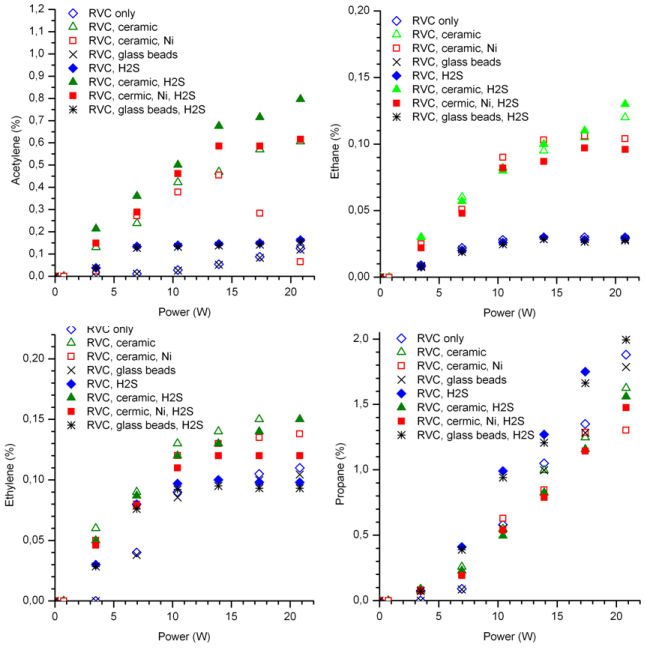

Figure 11. Concentrations of C_2H_2, C_2H_6, C_2H_4 and C_3H_8 in the gas mixture with H_2S processed by DBD with RVC electrode in Reactors No.1-3.

As seen from the linear growth of the ethane and ethylene concentrations, their production is constant up to 10 W of the DBD power. At the higher power levels the concentrations of those hydrocarbons reach plateau in the reactors with the RVC electrode only and in the reactor with the ceramic tube saturated with Ni catalyst.

In the reactor with the clean ceramic, the concentrations of C_2 hydrocarbons still grow. On the other hand, the production of propane is quite different. The concentration of C_3H_8 increases almost linearly till the last point of the DBD power.

Generally, the lower concentrations of all detected hydrocarbons in the reactor with the RVC electrode only (Reactor No. 1) result from the lower methane conversion (Fig. 6), which also explains the differences in the results obtained using each of the reactors. According to the results of the modelling performed by De Bie et al., the increase in the methane conversion degree up to 20 % is accompanied with the increase in concentrations of acetylene, ethylene and ethane and decrease in propane concentration, exactly as we observed.[9] Chemical reactions responsible for the production and the consumption of C_2H_2, C_2H_4, C_2H_6 and C_3H_8 are as follows. Acetylene and ethylene are produced mainly in one reaction:

$$C_2H_3 + C_2H_3 \rightarrow C_2H_2 + C_2H_4 \quad (6)$$

where C_2H_3 radicals results from the recombination of CH and CH_3 radicals produced directly from CH_4 in the electronic reaction:

$$CH + CH_3 \rightarrow C_2H_3 + H \quad (7)$$

In reactions of recombination and hydrogenation of C_2H_5 radicals ethane and propane molecules are formed:

$$C_2H_5 + C_2H_5 \rightarrow C_2H_6 + C_2H_4 \quad (8)$$

$$C_2H_5 + CH_3 \rightarrow C_3H_8 \quad (9)$$

As predicted by the calculations of De Bie et al C_2H_5 is formed mainly by hydrogen attachment to C_2H_4:[9]

$$C_2H_4 + H \rightarrow C_2H_5 \quad (10)$$

As can be seen in Fig. 11, hydrogen sulphide does not influence much higher hydrocarbons production, except acetylene. When comparing to the highly influenced methane conversion and hydrogen production, one can conclude that the formation of higher hydrocarbons is not controlled by the electronic reactions but by the gas temperature. Since in the experiment with H_2S we observed formation of the sulphur resistive layer causing the drop in the discharge current, it means that the rest of the power delivered to the reactor dissipated as the heat. The increased gas temperature is enough to influence C_2 and C_3 hydrocarbons production, but not enough to play a role in CH_4 dehydrogenation. Therefore, still the key reaction in the methane conversion and hydrogen production is the dissociation of methane molecules by the energetic electrons.

The selectivity of the hydrogen production (Fig. 12) shows that only up to 21 % of hydrogen atoms from the methane molecule leaves the DBD reactors as H_2. The rest forms higher hydrocarbons and water vapour. The highest selectivity was recorded in the experiment with H_2S in the gas processed in the reactor with the ceramic tube not saturated with Ni catalyst at the DBD power of 11 W. At the higher DBD power, the selectivity in this reactor drops slightly, whereas in the other cases H_2 selectivity grows up to the highest values at 22 W. The influence of the DBD reactor configuration and the presence of H_2S on the hydrogen selectivity is not so well seen as in the case of concentrations of all the measured products.

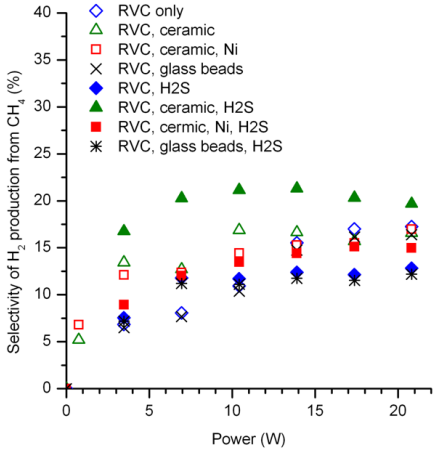

Figure 12. Selectivity of hydrogen production from methane in the gas mixture processed by DBD with RVC electrode in Reactors No.1-3.

B. Plasma diagnostics by OES

The typical spectra in the range of 250-450 nm recorded in this experiment are presented in Fig. 13. Increasing the DBD power results only in the increased intensity of each band. It means that more light from the increasing number of streamers generated during the discharge was emitted. At the same time the discharge energy transfer into the gas in the form of heat was very low. Temperature of the gas leaving the DBD reactors increased with the discharge power but only up to 38 °C (at 15 W delivered to the discharge).

In the recorded spectra most of the bands originated from N_2^+ second positive system except those marked as CH bands and C triplet. The highest CH band is from CH (A-X) transition. What is important when analyzing an influence of the hydrogen sulphide presence on the DBD plasma is that the CH (A-X) band (as well as other bands marked in Fig. 13) is less intensive comparing to the experiment without H_2S (Fig. 14). The lower intensity of the bands can be caused either by the lower discharge current in the gas with H_2S or by the reaction (2), in which a portion of methane is consumed without the formation of CH radicals.

When comparing the spectra recorded in the experiments with 3 different reactor configurations, it is seen that in all cases plasma composition is similar (Fig. 15). There are no significant differences in those spectra except the CH (A-X) and CH (B-X) bands, which are higher in the reactor with the ceramic tube but without the Ni catalyst.

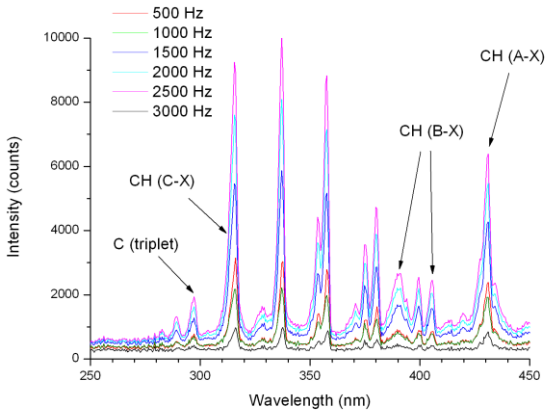

Figure 13. Optical emission spectra of the DBD in Reactor No. 1 for the repetition rate of nanosecond pulses 500-3000 Hz. Processed gas mixture CH_4:CO_2:H_2S

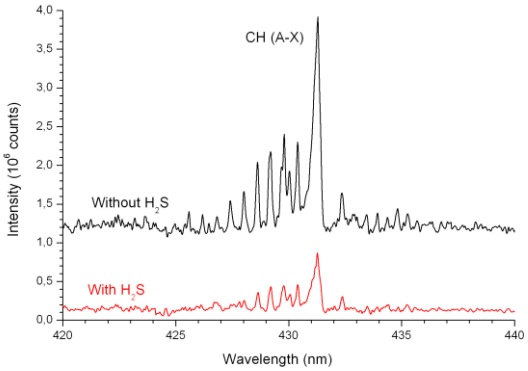

Figure 14. Comparison of optical emission spectra obtained in the DBD reactor No. 1 with and without H_2S in the CH_4:CO_2 mixture in the range of CH (A-X) band. Repetition rate of nanosecond pulses 1 MHz

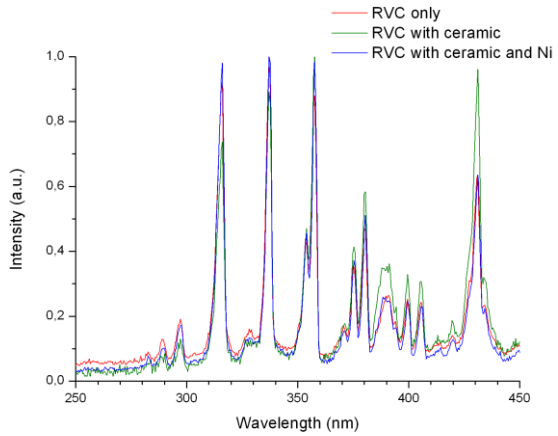

Figure 15. Optical emission spectra of DBD plasma generated in CH_4:CO_2:H_2S mixture processed in reactors No. 1-3. Repetition rate of nanosecond pulses 1 MHz.

Conclusions

Processing of the CH_4:CO_2: (70 % : 30 % : 1000 ppm) gas mixture simulating dry biogas, using different dielectric barrier discharge reactors with reticulated vitreous carbon high voltage electrode and nanosecond high voltage pulses showed, that:

- Presence of the additional ceramic barrier in the DBD reactor strongly influences plasma properties and consequently the production of syngas and higher hydrocarbons. The plasma is more uniform and colder, which results in different kinetics, comparing to the reactor without the additional barrier.

- Nickel catalyst incorporated in the additional ceramic barrier can by activated by the discharge at higher power. After being activated it supports acetylene decomposition.

- Sulphur produced from H_2S during the process changes the resistivity of the DBD reactor causing decrease in the discharge current. As a result, the production of syngas and methane conversion decreases.

- Electron impact dissociation of CH_4 resulting in the formation of CH_3 radical starts the conversion process. This radical initiates recombination reactions towards higher hydrocarbons such as C_2H_6 and C_3H_8. A further play of dissociation and recombination leads to the conversion towards C_2H_2 and C_2H_4. Finally, dissociation of CH_4 and the higher hydrocarbons also results in the formation of H_2. Production of CO is separated from the methane conversion.

This work was carried out using gas of room temperature and without water vapor normally present in the real biogas. Thus, in the real biogas we may expect much higher hydrogen production efficiency and methane conversion degree as observed by other researchers conducting the plasma assisted steam reforming of methane. Moreover, at such conditions the reactions involving hydrogen sulphide and its influence on by-products may be different than those described in this paper.

Acknowledgements

This work was supported by the National Science Centre under the project No. 2011/01/B/ST8/04131.

References

[1]Nozaki, T., Tsukijihara, H., Fukui, W., Okazaki, K., *Energy & Fuels*, **2007**, *21*, 2525.

[2]Goujard, V. Tatibouet, J.M., Batiot-Dupeyrat, C., *Appl. Catal. A*, **2009**, *353*, 228.

[3]Yang, Y.C., Lee, B.J., Chun, Y.N., *Energy*, **2009**, *34*, 172.

[4]Chun, Y.N., Yang, Y.N., Yoshikawa, K., *Catal. Today*, **2009**. *148*, 283.

[5]Sekine, Y, Yamadera, J., Matsukata, M., Kikuchi, E., *Energy & Fuels*, **2008**, *22*, 693.

[6]Sekine, Z., Yamadera, J., Matsukata, M., Kikuchi, E., *Chem. Eng. Sci.*, **2010**. *65*, 487.

[7]Petherbridge, J. R., May, P. W., Crichton, E. J., Rosser, K. N. and Ashfold, M. N. , *Physical Chemistry Chemical Physics*, **2002**, *4(*20), 5199.

[8]Dors, M., Izdebski, T., Berendt, A., and Mizeraczyk, J., *Int. J. Plasma Environ. Sci. Technol.*, **2012**, *6*(2), 93.

[9]De Bie, C., Verheyde, B., T. J. van Dijk, Paulussen, S., Bogaerts, A., *Plasma Process Polym*., **2011**, *8*, 1033.

Received: 10.07.2014.
Accepted: 25.07.2014.

IMPLICATIONS OF TEXTILE DYEING AND PRINTING EFFLUENTS ON GROUNDWATER QUALITY FOR IRRIGATION PURPOSE PALI, RAJASTHAN

Jaya S. Ratthore,[a]* Vimla Choudhary[a] and Shobha Sharma[a]

Keywords: Groundwater; electrical conductivity; sodium adsorption ratio; residual sodium carbonate; irrigation water quality.

The dyeing and printing of cotton and synthetic fabrics constitute highly specialized industries at Pali. Pollution of surface water stream has always implicit effect on groundwater quality and river Bandi is no more an exception. The primary and foremost cause is the release of untreated effluents in the river by the industries at Pali city. The sodium salts of chloride carbonate, bicarbonate and sulphate are the major pollutants which have increased significantly in polluted groundwaters besides dyes and organic substances. The application of polluted groundwater (salinity >8000 µS cm^{-1} and SAR >30) in agriculture fields has reduced the yields of crops considerably. The majority of well waters (67.92 %) are characterized (Group V classes) with very high to excessive salinity and sodium hazard (C5S3, C5S4 and C5S5).

* Corresponding Authors
E-Mail: : jayasratthore@gmail.com
[a] Department of Chemistry, Jai Narain Vyas University, Jodhpur-342005, Rajasthan, India

Introduction

During last two decades the problem of quality of groundwater has become more acute moreover it has become contaminated due to several anthropogenic activities. Dramatic increase in population, rapid growth in industrial sector, extensive use of fertilizers, and uncertainty in monsoon has further increased the exploitation of this precious natural resource all around the world.[1]

Groundwater is the promising source of irrigation in western Rajasthan where the surface water resources are scanty and often remains dry due to frequently occurring droughts. Generally the water levels are very deep and the occurrence is often restricted to certain geological formations. Not only the inherent groundwater in western Rajasthan is saline and alkaline but they also contain the constituents like fluoride, nitrate, sulphate, chlorides, and heavy metals etc which are considered as potential health hazards.[2] The use of such waters only adds to the sufferings of local agricultural based population by severely affecting crop productivity and quality of food product.

The burning question in such regions is not the availability of water but its chemical quality. Shortage of irrigation water especially in the arid regions necessitates use of even poor quality of water. The present paper embodies the results of study on the quality of groundwater for irrigation purposes and emphasizes the need for appropriate soil and water management for the utilization of waters even of poor quality.

Experimental

Study Area

The study area is part of Pali and Rohat blocks of Pali district located in the southwestern part of the Rajasthan state. Situated on the bank of river Bandi, Pali city lies between 25.77º N latitude to 73.33º E longitude.

Bandi river is a major tributary of Luni river and flows in almost east to west direction and passes through south of Pali city. The river lies between 25º 42’43” to 25º 55’ N latitude and 72º 50’ 45” to 73º 28’ 30” E longitude (Fig.1).

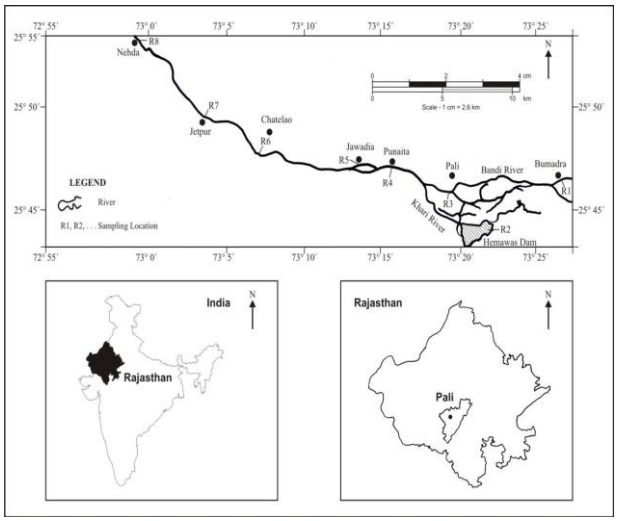

Figure 1. Study Area and sampling sites

 DOI: 10.17628/ecb.2014.3.805-808

Materials

Groundwater samples from 108 were collected from wells situated on both side of river bank from Bumadra (R1) village on upstream to Nehda (R8) village downstream along the river course during the year (Fig. 1). pH of wastewater was measured by potable pH meter (ELICO), electrical conductivity was also measured by potable EC meter (ELICO) in the field. Major ionic constituents were measured by standard methods.[3] The analytical results are given in (Table 1).

Table 1. Ionic constituents in groundwater

Chemical Constituents/Parameters	Range of Variation		
	Minimum	Maximum	Average
Electrical conductivity μS cm^{-1}	740	33000	9130
pH	6.7	9.1	-
Total dissolved solids, mg L^{-1}	437	23900	5820
Sodium, mg L^{-1}	220	8260	1710
Potassium, mg L^{-1}	2	375	24.8
Calcium, mg L^{-1}	6	1020	226
Magnesium, mg L^{-1}	9	630	146
Chloride, mg L^{-1}	71	8970	2390
Sulphate, mg L^{-1}	16	4460	910
Carbonate, mg L^{-1}	0	564	13.5
Bicarbonate, mg L^{-1}	146	2370	675
Nitrate, mg L^{-1}	1	380	64
Fluoride, mg L^{-1}	0	11.2	2.35
Total alkalinity, mg $CaCO_3$ L^{-1}	120	2270	580
Total hardness, mg $CaCO_3$ L^{-1}	52	5140	1170
Sodium absorption ratio (SAR)	2.63	95.85	22.85
Percent sodium	37.20	94.44	74.68
Residual sodium carbonate, meq L^{-1}	0	25.46	2.97

Results and discussion

Electrical Conductivity (EC)

Dissolved inorganic substances are present in the ionized form in groundwater and as such contribute to electrical conductance which is directly proportional to the concentration of ionized substances in water i.e. salinity. It is also a function of temperature and charge of ions present in water at 25 ^{0}C. It is seen that slightly saline well waters (24.7 %) have electrical conductivity less than 4000 μS/cm whereas 27.77 %, 16.67 % and 31.48 % waters fall in the salinity ranges of 4000-6000, 6000-8000 and above10000 μS cm^{-1} respectively. Fresh groundwater is not available in the study area. Well waters (8.33 %) having salinity less than 2000 μS/cm are observed around surface water bodies of Pali city or near river bed as localized patches (north, east) in the upstream areas. The groundwater in the rest of the region is brackish to saline.

Highly saline groundwater is seen in east of Hemawas dam, south and south west of Pali city covering textile industrial areas, west, south and northern parts excluding few patches in north-east and around Nehda-Dholeria section, localised patches at Jetpur, Jawadia, Mandia, Rupawas, Mandawas and Diwandi villages where salinity have exceeded 8000 μS cm^{-1}. In general, salinity increases from north-western region of Pali city to central part, east, south, north-west and west of the study area. The central parts covering Kerla-Chatelao and Rupawas-Mauliawas-Sukarlai sections have exceptionally high salinity extending up to Gadwara-Jetpur section. Similarly Sajji, Sonai Lakha and Sonai Lakha Dhani in north-west also have higher salinity. However, groundwater around Hemawas dam has lower salinity but the salinity increases with distance from dam in east and south-west. The increase in salinity is supported by the arid climate, a very prominent feature of the region, adds up to overall salinity in soils and groundwater of the study area. Moreover, the regular flow of untreated alkaline-saline textile effluents in the river further enhance the salinity in groundwater downstream from Pali city.

Total dissolved solids (TDS)

Theoretically dissolved solids are anhydrous residues of the soluble salts in water. Like electrical conductance, total dissolved solids in groundwater also show wide variations i.e. from 437 mg L^{-1} to 23880 mg L^{-1} with an average value of 5820 mg L^{-1}. The ground water in north-east is more or less fresh to slightly saline with respect to rest of the area. Sodium salts of chloride, sulphate and bicarbonate usually make up the bulk of dissolved solids up to the range of 2000 mg L^{-1}. While sulphate and chloride salts of calcium and magnesium also contribute significantly to the bulk of dissolved solids with the rise in salinity of groundwater.

A graph of electrical conductivity and total dissolved solids of well waters (Fig. 2) indicating the increase in conductance with the increase in dissolved solids in groundwater. The ratio of electrical conductivity to dissolved solids varies from 0.60 for waters of low dissolved solids to more than 0.65 for waters with dissolved solids more than 3000 mg L^{-1}. The total dissolved solids to electrical conductivity ratio increases with rise in salinity.

Much natural groundwater contains dissolved solids in concentrations exceeding 1000 mg L^{-1}, such water is classed as saline. According to salinity classification by Davis and De Wiest[4] 5.55 % of the samples fall under fresh water category, 28.70 % of the samples fall under slightly saline category, 50 % of the samples fall under saline category and 15.74 % under very saline category.

Total Hardness (TH)

According to Rao[5] water with hardness below 500 mg L^{-1} are recommended for drinking purpose. But for agricultural purpose, more than 1000 mg L^{-1} of hardness is also accepted. Based on the hardness classification of Ragunath[6] more than 67.59 % of samples fall under very hard category, 19.44 % fall under moderately hard category and 12.03 % fall under slightly hard category.

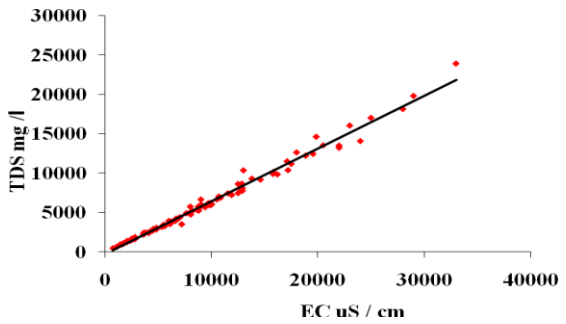

Figure 2. Variation of EC and TDS in groundwater. Relation of EC and TDS in groundwaters: TDS range: 0–1000, 1000–3000 and more than 3000 mg L^{-1} and TDS/EC ratio are 0.60, 0.62 and >0.64, respectively.

Suitability of groundwater for agriculture

The degree of salinity and alkalinity of groundwater is a key factor in water quality ratings for irrigation. Soil type, drainage and local conditions are other important parameters which affect the crop output. A brief discussion have been made on the quality of ground water that can be used safely for irrigation using different criteria's for rating irrigation water. Irrigation waters having dominant sodium ions are responsible for effecting the soil characteristics and crop productivity. Thus, the sodium adsorption ratio is considered to be the best indication of quality of ground water for irrigation purposes. Based on U.S. salinity diagram[7] ground water has been classified to know the suitability and groups of various classes (Table 2).

Table 2.Classes of groundwater for irrigation suitability based on U.S. S. L. diagram

Group	Classes	No. of samples in each		Type of crop to be grown on sandy soil w.r.t. each group.
		class	group	
I	C2 S1	1	9	Salt-sensitive
	C2 S2	-		
	C3 S1	-		
	C3 S2	8		
	C4 S1	-		
II	C3 S3	3	8	Semi-tolerant
	C4 S2	5		
III	C3 S4	1	13	Tolerant
	C4 S3	12		
IV	C4 S4	4	4	High salt-tolerant
V	C5 S3	2	74	Not even high salt - tolerant
	C5 S4	3		
	C5 S5	69		

It is found that 8.49 % well waters fall under group-1 classes are considered suitable for irrigation on various soils. Further 23.58 % samples covered under group II (7.55 %), III (12.26 %) and IV (3.77 %) can be used for growing most of the semi tolerant to tolerant crops on the sandy soils. The majority of the well waters (68.51 %) are characterized (Group V classes) with very high to excessive salinity and sodium hazard (C5 S3, C5 S4 and C5 S5).

The occurrence of these waters in major parts and could be attributed to pollution of groundwater along river course due to textile industrial effluent flowing regularly in river.[8-9] The crop production in this area has declined to a great extent and soils have become hard and even barren owing to use of polluted groundwater.

Residual sodium carbonate (RSC)

Alkalinity in irrigation water creates sodicity problems in soils. The excess alkalinity termed as residual sodium carbonate is a measure of sodium hazard. It adversely affects the soil texture and the soils become hard and compact due to reduction in permeability. The unfavourable condition so developed inhibits the intake of essential nutrients to the plants and affect the agricultural yield. The water analyses indicate that 31.13 % well waters have residual sodium carbonate above 2 meq L^{-1}. The villages located along the river course i.e. Jawdia, Mandia, Giradara ki Dhani, Kerla, Sukarlaie, Jetpur, Gadwara Dholeria jagir and Dholeria shasan have considerable residual sodium carbonate Some of the groundwater in north-east around Akeli-Nayagaon section also has considerable residual sodium alkalinity. The 64.15 % ground water has percent sodium above 70. Higher percent sodium (> 80) in ground water are encountered in north-east to south i.e. from Bumadra-Utwan to Mandia-Giradara-Dayalpura section and Sukarlai-Chatelao section to Dholeria Jagir-Sonaie Dhani also show higher sodium contents. It is clearly observed that ground waters all along the river course from Pali city to Dholeria Jagir are characterized by high sodicity.

Table 3. Tolerant and semi–tolerant crops with respect to salinity

Semi-tolerant crops **EC = 4000-8000** µS cm^{-1}	**Tolerant crops** **EC = 8000 – 16000** µS cm^{-1}
Jowar	Sugarbeet
Rice	Tobacco
Maize	Barley
Oat	Turnip
Wheat	Dhaincha
Senji	Spinach
Berseem	Datepalm
Tomato	Guava
Bajra	
Mango	
Pomegranate	

Thus, high alkalinity as well as soluble sodium contents is the main hindrances inspite of sandy soils available in the study area i.e. favourable for irrigation and good crop yields. Since, plants are relatively more sensitive at the germination stage and salt-tolerances also differ with the stage of growth as such farmers can go for various crops with relative salt tolerances Table 3. The agriculture can be enhanced by giving due consideration to soil-water-plant relationship and adequate leaching of salts through soils.

Conclusion

The application of polluted groundwater (salinity >8000 µS cm^{-1} and SAR >30) in agriculture fields has reduced the yields of crops considerably. The suspended and colloidal

matter have clogged the pores of the soil and reduced its permeability due to use of river water for irrigation. The high alkalinity and sodicity of polluted waters have been detrimental to several crops and impaired their growth due to hard and barren soils [9]. Thus, there is an economical loss for riverain population of more than forty villages from Pali to Nehda village. Since these soils are located in arid environment where good quality of groundwater is not available, the reclamation of such type of affected soils is a big problem. Considering the above problem and limitation, the alternate remains is to utilize rainwater by proper collection in the field through construction of strong earthen bunds on field boundary. Deep ploughing should be done before onset of monsoon to increase the infiltration and percolation rate process as this will help in leaching of the soluble salts from upper horizons thus improving the physical condition of soil. The application of gypsum with organic manure to the soil is also beneficial.

References

[1]Fakayode, S. O., *Ajeam-Ragee*, **2005**, *10*, 1-13.

[2]Kumar, D., Jain, M., Dhindsa, S. S., Devanda, H. S., Singh, R. V., *Indian J. Environ. Sci.*, **2005**, *9(1)*, 71-74.

[3]APHA-AWWA-WPCF, *Standards methods of the examination of water and wastewaters*, **2004**.

[4]Davis, S. N., De Wiest, R. J. M. *Hydrogeology*, John Wiley & Sons, New York, **1996**, 463.

[5]Rao, K. L., *Assessment of Flow and Quality of Water Health- its Assessment Uses and projection*, Orient Longman Ltd, New Delhi, **1975**, 49-53.

[6]Ragunath, H. M., *Groundwater*, Wiley Eastern Limited, New Delhi, **1987**, 343-347.

[7]Richards, L. A., *Diagnosis and Improvement of Saline and Alkali Soils*, Agricultural Handbook 60, US Department of Agriculture, Washington, DC, **1954**, 160.

[8]Richards, L. A., *Diagnosis and Improvement of Saline and Alkali Soils, Agricultural Handbook 60*, US Department of Agriculture, Washington, DC, **1954**, 160.

[9]Kannan, V., Ramesh, R. Sasikumar, C., *J. Environ. Biol.*, **2005**, *26(2)*, 269-272.

[10]Kovda, V. A., *Chemistry of saline and alkaline soils of arid zone*, FAO/UNESCO, Rome, **1973**.

Received: 09.06.2014.
Accepted: 28.07.2014.

COMBINING APTAMERS AND *IN SILICO* INTERACTION STUDIES TO DECIPHER THE FUNCTION OF HYPOTHETICAL PROTEINS

Prashanth Suravajhala,[a,b]* Harsha Vardhan Reddy Burri[c] and Arto Heiskanen[c]

Keywords: Aptamers, hypothetical proteins, pull down assay, in silico studies.

We present the potential role of aptamers in elucidating the function of hypothetical proteins, as well as the possibilities provided by bioinformatics for establishing a benchmark for aptamer-protein prediction methods. With these future perspectives, the role of hypothetical proteins as target molecules for diagnostics and therapies could prove to be very useful in development of medical technology.

*Corresponding author:
E-mail: prash@bioclues.org.
[a] Bioclues.org, India and Denmark
[b] Bioinformatics.Org, 28 Pope Street, Hudson, MA 01749, USA
[c] Department of Micro- and Nanotechnology, Technical University of Denmark, Produktionstorvet 423, 2800 Kgs. Lyngby, Denmark

Introduction

Aptamers are single stranded DNA or RNA or small peptide molecules designed to bind target molecules with high affinity and selectivity. Aptamers have been developed to specifically bind small organic molecules and cellular toxins, viruses, ligands to important proteins enabling biomarker discovery and early treatment of diseases, with the latter subjected to using developed cell lines with defined genetic elements.[1] In the recent past, DNA/RNA aptamers have been widely employed as a novel tool for elucidation of protein and/or nucleic acid interactions,[2,3] detection applications, regulation of gene expression, as well as purification of target molecules for diagnostics and therapies.[4-6] The global market for aptamers is expected to make a turnover in excess of $1200 million showing a vast growth of the market from the $10 million. An overall 120 % Compound Annual Growth Rate (CAGR) suggests that aptamers are emerging and will play a major role in all biotechnological, pharmaceutical and diagnostic applications.[7]

Discussion

On the technical side, when a protein or other target of interest is presented to an aptamer library, any unbound aptamers are washed away and aptamers that survive multiple bind/wash cycles are enriched. While aptamers undergo in vitro selection process, production of antibodies requires biological systems. In comparison with aptamers, the limitations of antibodies include inadequate supply, high costs and heterogeneity. To produce antibodies, the induction of an immune response is necessary. This procedure may discriminate target proteins that have a similar structure in comparison with endogenous proteins. Moreover, toxic compounds used as antigens or epitopes in a bioconjugated construct may lead to severe systemic effects and be ultimately lethal to the host organism. By isolating aptamers in vitro using chemical modification, they can be easily produced for any target molecule. Moreover, they are known to be stable at elevated temperatures and can be regenerated easily. Due to this, the structural features determined by the functional mers can be retained despite temporary denaturation during experimental procedures. Theoretically, as for antibodies, all proteins are targets for aptamers, making it difficult to predict which aptamers would be better than others. However, several researchers are working on generation of aptamers with high specificity for chosen target proteins.[8]

While aptamers are inexpensive compared to antibodies, the fundamental science of aptamers needs to mature to identify conditions/applications where they would be most suitable. To find more specific aptamers for a target protein, machine learning methods can help increase the likelihood in determining whether or not an aptamer can recognize the protein with high specificity. A recent report suggests that an improved understanding of the interactions between nucleic acid aptamers and their targets – the molecular recognition properties help improving design of aptamers.[9]

A pull-down assay uses a small-scale affinity tag to an antibody similar to immunoprecipitation. The affinity system consists of a glutathione S-transferase (GST)-, polyHis- or streptavidin bead which is then immobilized and can be cleaved only by thrombin. In the recent years, single-molecule pull-down (SiMPull) assay was introduced, facilitating probing of single macromolecular complexes directly in cell or tissue extracts.[10] In the case of proteins, whose existence, function and even interacting partner have been theoretically (hypothetically) predicted but never experimentally demonstrated, pull-down assays can have a significant role. The use of biological data along with Gene Ontology functional dependencies specific to organelles could be of immense interest for deducing functions of uncharacterized proteins. However, based on the

conventional usage of antibodies, such pull-down assays would be highly expensive, counteracting the feasibility of the required experimentation. Hence, such hypothetical proteins (HP) and their interacting partners remain uncharacterized due to lack of feasible screening methods. Although the methods to identify the functional contexts of activity of the interacting protein have been presented, the necessary experimental boundary to characterize them does not exist.[11] Therefore, we envisage the use of aptamers for pull-down assays or label-free detection to ascertain function of some classes of proteins such as HPs. Application of aptamers in this research area would have immense potentials as only few analytical techniques are known to be capable of detecting minute changes with a sensitivity matching that of antibodies. Targeting whole proteins and selection of specific residual sequences as epitopes is needed for functional characterization of HPs, such as Twinkle helicase, also known as Progressive External Opthalmoplegia (PEO) in humans, encoded by the gene C10orf2 which is similar to the GP4 helicase structure and an interacting partner of the DNA mismatch repair protein, MLH1.

The ability to predict aptamer binding sites for known proteins, aided by bioinformatics predictions, could allow researchers to develop new diagnostic markers and procedures beyond the traditional medical diagnostics, as well as design new vaccines. Development of such bioinformatics prediction tools could also provide the fundamental basis and standard applicable for elucidation of functions and interacting partners of hypothetical proteins, lessening the scale of needed experimentation. Existing experimental data could be utilized as input for computational methods, to establish a benchmark for aptamer-protein prediction methods. We anticipate that aptamers can make good candidates for use in diagnostics and therefore can be tailored to address the role of hypothetical proteins in therapeutics, drug discovery and clinical applications in the future.

Acknowledgments

Prashanth Suravajhala would like to thank Dr. Pawan Dhar for his constructive comments.

References

[1]Fang, X., Tan, W., *Acc. Chem. Res*., **2010**, *43(1)*, 48-57.

[2]Ritzefeld, M., Walhorn, V., Anselmetti, D., Sewald N. *Amino Acids*, **2013**, *44(6*), 1457-75.

[3]Schou, C., Heegaard, N. H., *Electrophoresis*, **2006;** *27(1)*, 44-59.

[4]Liu, K., Lin, B., Lan X., *J. Cell Biochem.*, **2013**, *114(2)*, 250-5.

[5]Keefe, A. D., Pai, S., Ellington, A., *Nat. Rev. Drug Discov*., **2010,** *9*, 537–550.

[6]Lim, D. V., Simpson, J. M., Kearns, E. A., Kramer, M. F., *Clin. Microbiol. Rev*., **2005**, *18(4)*, 583-607.

[7]BCC report: URL: http://www.bccresearch.com/report/nucleic-acid-aptamers-global-markets-bio071b.html

[8]Thiel, K. W., Giangrande, P. H., *Oligonucleotides*, **2009**, *19*, 209–222.

[9]Zichel, R., Chearwae, W., Pandey, G. S., Golding, B., Sauna, Z. E., *PLos One*, **2012**, *7(2)*, e31948.

[10]Jain, A., Liu, R., Xiang, Y. K., Ha, T., *Nat. Protoc*., **2012**, *97(3)*, 445-52.

[11]Benso, A., Di Carlo, S., Ur Rehman, H., Politano, G., Savino, A., Suravajhala, P., *Proteome Sci.*, **2013**, *11*(Suppl 1), S1.

Received: 14.07.2014.
Accepted: 28.07.2014.

ENERGY EMISSIONS OF SPARK DISCHARGE UNDER WATER

Tomasz Izdebski[a]*, Miroslaw Dors[a], Jerzy Mizeraczyk[a,b]

Presented at Fifth Central European Symposium on Plasma Chemistry (Budapest, 2013. augusztus 25-29.)

Keywords: spark discharge, electrohydraulic discharge, energy emission.

The recent focus of research with electrohydraulic discharges is on bacteria and microorganism inactivation. The processes and main biocidal effects in which this occurs are not fully understood. In this paper a study of energy emission from electrohydraulic spark discharge is presented. The spark discharge was generated in a cylindrical reactor 25 mm in diameter made of PTFE between a stainless steel hollow needle electrode and a steel rod electrode. Distilled water was used and the flow was 30 ml/min. The gap between the electrodes was 3 mm. Spark discharge energy was measured to be 1.2-1.4 J. Measurements show that over 50% of this energy is used for heating of the reactor and electrodes, and about 2% for acoustic waves. The rest of the discharge energy, i.e. ~0.54 J, is distributed among UV/Vis radiation, production of primary active species and ultrasonic.

* Corresponding author
E-Mail: tizdebski@imp.gda.pl
[a] Centre for Plasma and Laser Engineering, The Szewalski Institute of Fluid Flow Machinery, Gdańsk, Poland
[b] Department of Marine Electronics, Gdynia Maritime University, Gdynia, Poland

Introduction

Generation of plasmas in liquids has been studied extensively in the past for various applications, e.g. insulation and high power switching[1], removal of organic contaminants[1-5] and water sterilization.[2-3] A lot of research in physics and chemistry of such discharges was made and still we don't know much about them. There is no consensus over plasma formation mechanism and all the more on biocidal effects leading to sterilization. It is generally accepted that the main energy emissions from spark discharges are heat emission, UV/Vis radiation, shock wave formation, and energy used for chemical reactions and formation of active species.[2,6] The primary chemical reactions inside water originated from plasma result in the formation of chemically active species (e.g. OH•, H•, O•, HO_2•) which either recombine to form stable by-products such as H_2O_2 and H_2, or they return to a lower energetic state and emit UV light.[7-10]

However, in the presence of impurities (organic and inorganic compounds), primary and secondary molecular, ionic, or radical species produced by the discharge can attack these molecules and cause their degradation. Alternatively, these impurities can be degraded indirectly through pyrolysis in the vicinity of high voltage electrode or photolysis.

In the electrohydraulic discharge like spark, the generation of active species follows the formation and propagation of the plasma channel. Researchers have shown that as the plasma channel expands throughout the surrounding liquid it forms shock wave, induces cavitations and emits UV light.[2,10]

While studies on chemical effects of the shock wave-induced cavitations and UV light are scarce, the biological effects of shockwaves on the soft animal tissue are currently under full investigation.[11-12] Establishing the effects of chemical species, shock wave and UV light on the degradation of molecules in the bulk phase is extremely important to understand their role in the sterilization of water. To fully understand which of these effects of spark discharge has the main influence on bacteria and microorganism inactivation, first we need to understand the distribution in so called electrohydraulic discharge.

Experimental set-up

Cylindrical reactor made of PTFE was 6 cm in height and had a diameter of 25 mm. The material was chosen to be the least chemically active and capable of withstanding high pressure waves from the spark discharge. A quartz window was inserted in the side of the reactor for UV/Vis emission spectra analysis.

A pulsed positive discharge was generated between a high voltage stainless steel hollow needle electrode and a grounded steel rod electrode (5 mm in diameter), both immersed in the water. The inner and outer diameter of the hollow needle were 1.4 mm and 1.6 mm, respectively. The discharge was generated at the edge of the hollow needle, whereas the rest of the needle was covered with an insulator. Spark discharge was generated when the needle-rod spacing was 3 mm. A technical scheme of reactor configuration and power supply is presented in figure 1. A voltage of 16 kV was applied to the needle electrode with a frequency of 50 Hz. Positive high voltage pulses were applied to the hollow needle electrode from a discharge capacitor C1 (2 nF). The capacitor was charged from a DC power supply through a resistor R (10 kΩ) and a capacitor C2 (22 nF). The pulse repetition rate of 50 Hz was fixed by the rotation velocity of a rotating spark gap switch. The amplitudes of the voltage and current corona pulses were measured using a TEKTRONIX P6015A high voltage probe and a PEARSON 2878 current monitor (Rogowski coil), respectively.

The waveforms were observed and recorded on a TEKTRONIX TDS 3052B oscilloscope. Pulse discharge energy was between 1.2 and 1.4 J. Typical voltage and current pulses are presented in Figure 2.

The acoustic energy measurements were carried out in a 30 cm distance from the source with a certified acoustic meter SVAN 945 which measures the sound intensity in a frequency range from 1 Hz to 20 kHz. Temperature and relative humidity of the ambient air were 22 °C and 20%.

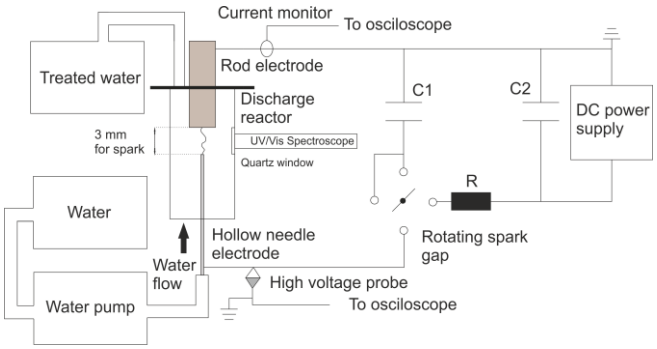

Figure 1. Experimental set-up scheme of spark discharge reactor and power supply. C1 = 2 nF, C2 = 22 nF, R = 10 kΩ

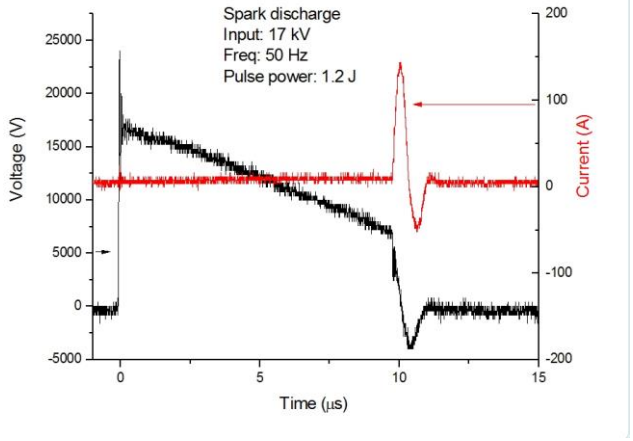

Figure 2. Typical voltage and current pulse of the spark electrohydraulic discharge

The UV radiation emission spectroscopy was performed using Maya2000 spectrometer equipped with a UV/Vis transmittable optical fibre with optical resolution (FWHM) of 0.5 nm. Acquisition was done 5 cm from the discharge through a quartz window.

Water volume in the reactor was 26 ml. The water was flowing once through the reactor chamber with a flow rate of 30 ml/min. Conductivity was adjusted with NaCl to 300 μS in order to be the similar to river water which was the subject of our previous studies.

Temperature of the water was measured using thermocouple placed inside the reactor immediately after the discharge was turned off.

Results

The distribution of energy emitted during the spark discharge in water can be described by the balance:

Energy delivered to the spark discharge = Energy emitted from the plasma.

Since we are not able to measure each and every form of the energy emitted by the plasma separately such as ultrasound and UV/Vis radiation we assume that equation (1) has a form:

$$E_p = E_{aq} + E_{us} + E_{UV} + E_{th} + E_{th} \quad (1)$$

where

E_p – input energy,
E_{aq} – acoustic energy,
E_{us} – ultrasonic energy,
E_{UV} – UV/Vis emission energy,
E_{th} – thermal Energy,
E_{ch}- energy spent on chemical reactions (ionization, dissociation and excitation).

The energy E_p delivered by the spark discharge to the water was calculated from the current and voltage pulses presented in Figure 2 using standard equation:

$$E_p = \int U(t)I(t)dt \quad (2)$$

The E_p value varies in our reactor in the range of 1.2 to 1.4 J.

As for the forms of energy emitted from the spark discharge they are described below. It is worthy of noting that in some works theoretical computations of several energies associated with spark discharges are given.[13-14] However, it seems that in these computations several parameters can be set rather arbitrarily to obtain the desired result.

UV/Vis light emission

Emission spectra observed in the range of 200-1100 nm during the spark discharge is shown in figure 3. The spectra includes a strong continuous band from 200 to 1000 nm which is typical for highly heated solids (black body radiation). This is an evidence that local temperature in the plasma region is very high. Unfortunately, because of the continuous spectra it was not possible to determine the temperature of the plasma. It is also seen that OH, O and H species are formed but other peaks that appear in the emission spectra could not be identified. The spectra observed was similar to that of Sun et al.[15]

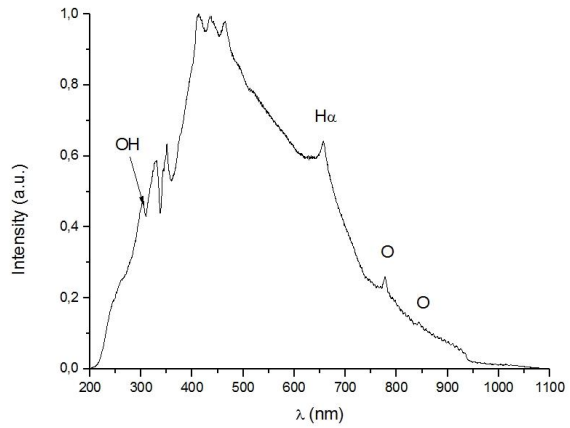

Figure 3. UV/Vis emission spectra of spark discharge in water

It must be pointed out that UV light recorded by the spectrometer is not the same as produced by the plasma. Part of it is absorbed by the water and transformed into heat and consumed in chemical reactions. Determination of exact amount of UV energy produced by the spark discharge is difficult. Many researchers use emission spectroscopy as a tool for the characterization of underwater discharges but they present only evolution of active species produced in the plasma and estimation of rotational/vibrational temperatures and electron densities in the plasma region. To our knowledge there is no literature showing that spectra emitted by the underwater discharge can be used to estimate quantity of discharge energy transferred into UV/Vis light. Therefore, we can only estimate UV energy in conjunction with other forms of energy which we cannot measure separately.

Acoustic energy emission

The frequency distribution of sound intensity generated by the electrohydraulic discharge reactor at 30 cm distance is presented in table 1. For this close proximity from the source we can omit the ambient air attenuation. We assume the spherical emission of the source. For the power calculations the sound intensities were integrated over the frequency spectra. The power of acoustic source is:

$$P = \frac{I}{e^{-mr}} 4\pi r^2 = 1.43\,\mathrm{W} \qquad (3)$$

where:

r – distance from the discharge,
I – sound intensity,
m – sound absorption coefficient of air.

Acoustic power converted to a one pulse energy is E_{ac} = 0.028 J. The ratio of estimated energy absorbed by the water to the electrical energy delivered to the spark discharge is then 2.0-2.3 %. This value is reasonable when comparing to results obtained by Buogo et al.[16] They also studied the underwater spark discharge and found that 1.4-5.6 % of available energy was transferred into the acoustic energy.

Table 1. Frequency distribution of sound intensity levels

Frequency, Hz	Sound intensity level, dB	Sound intensity, W m^{-2}
1	25.9	$3.89.10^{-10}$
2	38.5	$7.07.10^{-9}$
4	49.8	$9.55.10^{-8}$
8	52.2	$1.66.10^{-7}$
16	51.0	$1.25.10^{-7}$
31.5	51.0	$1.25.10^{-7}$
63	48.0	$6.31.10^{-8}$
125	50.4	$1.09.10^{-7}$
250	48.0	$6.31.10^{-8}$
500	50.9	$1.23.10^{-7}$
1000	57.1	$5.12.10^{-7}$
2000	74.8	$3.02.10^{-5}$
4000	79.5	$8.91.10^{-5}$
8000	80.4	$1.09.10^{-4}$
16000	78.2	$66.0.10^{-5}$

It is known from literature that the underwater spark discharges produces strong ultrasounds.[17] Unfortunately, we are not able to measure this form of energy and we can only assume that it is a part of unaccountable energy together with UV radiation and energy spent on ionization, dissociation and excitation of molecules in the plasma region.

Thermal energy emission

Measuring the water temperature just after switching off the power supply shows that during 30 s of pulsed spark operation the temperature increases from 13.5 °C to 21.5 °C. As was shown by Foster et al. during the underwater plasma generation the temperature rise is rapid and essentially linear.[18] Therefore, in our experiment measuring initial and final temperatures without intermediate points is justified. The calculation should yield a reasonable estimate of power deposited into the water. The energy absorbed by the water is simply calculated from the Joule's law:

$$Q = c \cdot m \cdot (T_k - T_p) \qquad (4)$$

where

c – specific heat of the medium,
m – mass of the medium,
T_p – initial temperature,
T_k – final temperature.

For the thermal energy emission measurement data was as follows: water mass: 26 mL = 26 g, specific heat of water: 4187 J kg K^{-1} = 1 kcal kg K^{-1}, specific heat of steel electrode: 300 J kg K^{-1}, mass of the electrodes: 4.2 g, time: 30 s.

Amount of thermal energy emission from equation (3) is Q = 1097 J. It means that during one spark discharge pulse about E_{th} = 0.73 J was emitted as thermal energy. The ratio

of estimated energy absorbed by the water to the electrical energy delivered to the spark discharge is then 52-61 %. This value is reasonable when comparing to 63 % obtained by Foster et al.[18]

Conclusions

Spark discharge pulse was measured to be 1.2 to 1.4 J. Results of measurements show that 0.73 J, which is more than 50% of energy delivered to the spark discharge, is spent for water heating. Acoustic energy emission is 0.028 J which is comparable to loud speaking. Therefore, the rest of the discharge energy, i.e. ~0.54 J, is distributed among UV/Vis radiation and chemical reactions and ultrasonic waves in the reactor.

Acknowledgement

This research work was supported by the European Social Fund, the State Budget and the Pomorskie Voivodeship Budget according to the Operational Programme Human Capital, Priority VIII, Action 8.2, Under-action 8.2.2: 'Regional Innovation Strategy' within the system project of the Pomorskie Voivodeship "InnoDoktorant – Scholarships for PhD students, Vth edition" and by the National Center of Science according to decision number DEC-2011/01/N/ST8/05300.

References

[1]Malik, M. A., Ghaffar, A., Malik, S. A., *Plasma Sources Sci. Technol.*, **2011**, *10*, 82.

[2]Sunka, P., *Phys. Plasmas*, **2001**, *8*, 2587.

[3]Yang, Y., Fridman, A., Cho, Y., *Adv. Heat Transfer*, **2010**, *42*, 179.

[4]Locke, B. R., Sato, M., Sunka, P., Hoffmann, M. R., Chang, J. S., *Ind. Eng. Chem. Res*., **2006**, *45*, 882.

[5]Bruggeman, P., Leys, C., *J. Phys. D: Appl. Phys.*, **2009**, *42*, 053001.

[6]Locke, B. R., Thagard, S. M., *Plasma Chem. Plasma Process*, **2012**, *32*, 875.

[7]Kirkpatrick, M. J., Locke, B. R., *Ind. Eng Chem. Res*, **2005**, *44*, 4243.

[8]Sahni, M., Locke, B. R., *Ind. Eng Chem. Res*, **2006**, *45*, 5819.

[9]Lukes, P., *PhD dissertation*, *Institute of Chemical Technology*, Prague, Czech Republic, **2001**.

[10]Anpilov, A. M., Barkhudarov, E. M., Bark, Y. B., Zadiraka, Y. V., Christofi, M., Kozlov, Y. N., Kossyi, I. A., Kop'ev, V. A., Silakov, V. P., Taktakishvili, M. I., Temchin, S. M., *J, Phys. D. Appl. Phys.*, **2001**, *34*, 993.

[11]Sunka, P., Benes, J., Lukes, P., Zadinova, M., Hoffer, P., Pouckova, P., *IEEE Int. Conf. Plasma Sci.*, **2009**, 1.

[12]Sunka, P., Babicky, V., Clupek, M., Benes, J., Pouckova, P., *IEEE Trans. Plasma Sci*., **2004**, *32*, 1609.

[13]Roberts, R. M., Cook, J. A., Rogers, R. L., Gleeson, A. M., Griffy, T. A., *J. Acoust. Soc. Am.*, **1996**, *99*, 3465.

[14]Lu, X., Pan, Y., Liu, K., Liu, M., *J. Appl. Phys*., **2002**, *91*, 24.

[15]Sun, B., Sato, M., Harano, A., Clements, J. S., *J. Electrostatics*, **1998**, *43*, 115.

[16]Buogo, S., Plocek, J., Vokurka, K., *Acta Acoustica*, **2009**, *5*, 46.

[17]Martinson E., Delsing, J., *Flow Measurement Instrum.*, **2010**, *21*, 394.

[18]Foster, J. E., Weatherford, B., Gillman, E., Yee, B., *Plasma Sources Sci. Technol.*, **2010,** *19*, 025001.

Received: 14.07.2014.
Accepted: 28.07.2014.

NON-EXISTENCE OF SECONDARY COORDINATES OF INTERSECTS

V. I. Krupyanko

Keywords: noncompetitive enzyme inhibition; corrected coordinates for calculation of enzyme inhibition and enzyme activation constants; secondary coordinates of intersects

The analysis of algebraic forms of corrected equations for the calculation of constants of enzyme inhibition (K_i) and activation (K_a) have shown that the secondary intersects coordinates (1/ V'; i) may be use for calculation only K_{IIIi} constants of noncompetitive enzyme inhibition. A few examples of application of corrected coordinates are given in the present research article.

* Corresponding Authors
Fax: :(495) 956-3370
E-Mail: krupyanko@ibpm.pushchino.ru; pH76@mail.ru
[a] G. K. Skryabin Institute of Biochemistry and Physiology of Microorganisms, Russian Academy of Sciences, Pushchino, Prospect Nauki 5, Moscow region, 142290 Russia

Introduction

In the already available reports[1-4] the possibilities of plotting the ($\mathbf{L}_i$) vectors of inhibited enzymatic reactions and ($\mathbf{L}_a$) vectors of activated enzymatic reactions in the three-dimensional $K'_mV'I$ coordinate system[1] and also of using the properties of such vectors for plotting the parametric classification of types of enzymatic reactions[2] and the deduction of equations for calculation of initial rates of activated (v_a) and inhibited (v_i) enzymatic reactions and also of equations for calculation of (K_a) constants of enzyme activation and (K_i) constants of non-trivial types of enzyme inhibition unavailable in usual practice are considered.

The present paper is dedicated to the possibility of using the secondary coordinates of slopes that take into account the orthogonal projections of $\mathbf{L}_i$ and $\mathbf{L}_a$ vectors of inhibited and activated enzymatic reactions on the basic (σ_0) plane of the $K'_mV'I$ coordinate system (Figure 1) for calculation of K_i and K_a constants.

Correction of the coordinates of slopes and intersects for calculation of constants of enzyme inhibition and activation

Deduction of equations for calculation of K_i constants of enzyme inhibition and K_a constants of enzyme activation[4] that take into account the position of orthogonal projections of $\mathbf{L}_i$ vectors of enzyme inhibition and $\mathbf{L}_a$ vectors of activated enzymatic reactions on the basic (σ_0) plane (Figures 1 and 2) opens up the possibility of plotting the secondary (corrected) coordinates of slopes for more accurate estimation of such constants.

Example 1

Calculation of the K_{Ii} constant of enzyme inhibition. Let us consider the inhibitory effect of increasing concentrations of sodium molybdate ($Na_2MoO_4{\cdot}2H_2O$) on initial rates of pNPP cleavage catalyzed by calf alkaline phosphatase (EC 3.1.3.1).

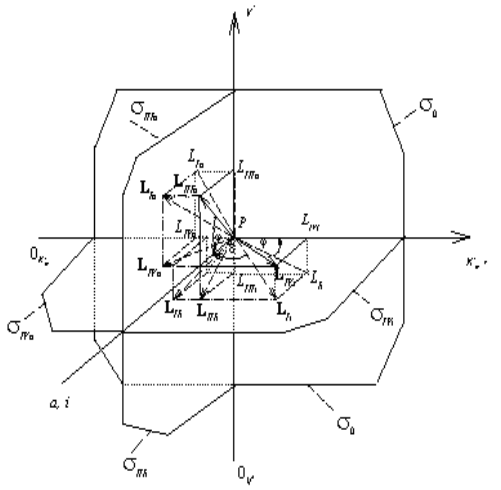

Figure 1. Three-dimensional (folded) $K'_mV'I$ coordinate system with coincident Pa,i semi-axis. The description of kinetic parameters: K'_m, K^0_m …; vectors $\mathbf{L}_{IVi}$ … $\mathbf{L}_{Ii}$ and their scalar projections L_{IVi} … L_{Ii} on the basic σ_0 plane and also of planes σ_{IVi}, σ_{IIIi}, $\sigma_{IV\alpha}$ is given in more detail in.[1,6]

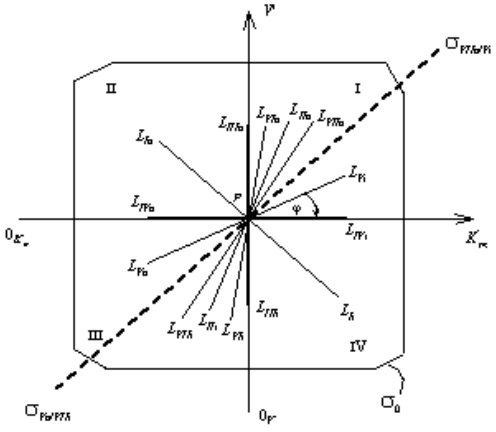

Figure 2. Two-dimensional (scalar) K'_mV' coordinate system. The description of kinetic parameters: K'_m, K^0_m, V' … and vector projections L_{IVi}, L_{Ii} … on the basic σ_0 plane. The projections of planes $\sigma_{VIIa/Vi}$ and $\sigma_{V\alpha/VIIi}$ of transient state between the $VII_a \Leftrightarrow V_i$ and $V_a \Leftrightarrow VII_i$ types of activated and inhibited enzymatic reactions on the σ_0 plane are marked with a dotted line.

 DOI: 10.17628/ecb.2014.3.815-822

Enzyme Activity Assay

Reactions were performed in 0.05 M Tris-HCl buffer (pH 9.0) at ionic strength 0.1 by NaCl of high purity under constant mixing[5] in a thermostat at 37 ^{0}C. The final concentrations of pNPP were varied within $2.94\cdot10^{-5}$ - $9.8\cdot10^{-5}$ M, the concentration of enzyme was constant 1.13 μg mL^{-1} and that of (10^{-4} M) $Na_2MoO_4\cdot2H_2O$ was varied within 0.0625 – 0.25·(Figure 3A). The course of pNPP cleavage by calf alkaline phosphatase was recorded by a CF-4 DR double-beam spectrophotometer (Optica Milano, Italy). Reactions were registered at the wave length ($+\Delta D_{400}$) of solution containing substrate, enzyme and inhibitor against the solution of the same composition, but without the enzyme.

Initial reaction rates ν_0 of pNPP cleavage were determined by the slope angles of tangents to initial segments of curves representing a course of reaction change in not less than five sets of parallel experiments.

The kinetic V and K_m parameters of calf alkaline phosphatase inhibition were calculated by plots in the (ν^{-1}, S^{-1}) coordinates of Lineweaver-Burk by using the program SigmaPlot, version 2000 (USA). Root-mean-square deviations at five-fold determination were as follows: ν=±2.5 %; K_m and V = ± 7.5 %, K_i (and K_a) = ± 10 %.

Results

As clearly observed from the results given in Figure 3A and Table 1 the increasing concentrations of MoO_4^{2-} exhibit all the features of the biparametrically coordinated I_i type ($K'_m>K^0_m$, $V'<V^0$, $i>0$) of enzyme inhibition and hence, we shall use (Eq. 1 of Table 2):

$$K_{Ii}=\frac{i}{\left(\left(\frac{K'_m-K^0_m}{K^0_m}\right)^2+\left(\frac{V^0-V'}{V'}\right)^2\right)^{0.5}} \quad (1)$$

for calculation of the K_{Ii} constant of enzyme inhibition.

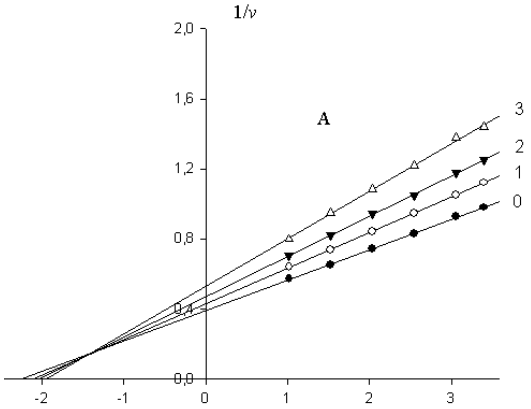

Figure 3A. Plots of inhibitory effect of anions MoO_4^{2-} on initial rates of pNPP cleavage by calf alkaline phosphatase. Designation, the concentration of MoO_4^{2-} (10^{-4} M) is: 0.0625 – line 1; 0.125 – line 2 and 0.25 – line 3. Line 0 – the inhibitor is absent; V μmol·min^{-1} μg protein^{-1}.

Table 1. Inhibitory effect of increasing concentrations of anions MoO_4^{2-} on calf alkaline phosphatase

Inhibitor, 10^{-4} M	**K'_m, 10^{-5} M**	**V' μmol·min^{-1} μg protein^{-1}**	**K_{Ii}, 10^{-4} M**	***A****
0	4.45	2.56		
0.0625	4.75	2.33	0.523	0.1195
0.125	4.91	2.13	0.551	0.2268
0.250	5.14	1.89	0.646	0.3869

*A – according to Eq. (1), it is a dimensionless value.

Substitution of appropriate parameters in this equation yields the following values of the constant of enzyme inhibition: K_{Ii} (10^{-4} M): 0.523, 0.551 and 0.646 – by the first, second and third concentration of MoO_4^{2-}.

However, Eq. (1) provides for another more preferable option for calculation of such constants: plotting of dependencies of change in the values of denominators of this equation in the coordinates (A;i), where K_{Ii} of enzyme inhibition can be calculated by the slope angle (tg a) of the experimental line (Figure 3B):

$$A=\frac{1}{K_{Ii}}i+0 \quad (2)$$

to the abscissa axis:

$$K_{Ii}=\frac{1}{tga} \quad (3)$$

where

A – a course of change of the denominator of Eq. (1) on increasing concentrations of MoO_4^{2-}.

Data analysis of Figure 3A by using the program Sigma Plot, version 2000 (USA) shows:

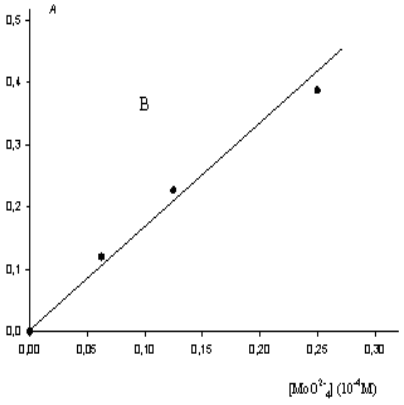

Figure 3B. Dependence of A parameters of Eq. (2) (Figure 3A) on increasing concentration of anions MoO_4^{2-} in the coordinates (A;i).

that the line of Eq. (2) goes via the origin of the coordinates at the slope angle to the abscissa axis (tg a) = [b(1) = $1.575\cdot10^4$ M^{-1}]: where: b(1) – a parameter of the program SigmaPlot 2000 (USA).

 DOI: 10.17628/ecb.2014.3.815-822

This gives the following (average) value of the K_{Ii} constant of calf alkaline phosphate: $K_{Ii}=1/(1.575\cdot10^4\ M^{-1})=0.635\cdot10^{-4}$ M.

At analogous data analysis (Figure 3A) a technique of plotting the dependencies of change in the ratio K'_m/V' of inhibited enzymatic reactions on molar concentrations of inhibitor i_{Ii} in the secondary coordinates of slopes (K'_m/V'; i) and the coordinates of intersects ($1/V'$; i) used for calculation of the K_{is} - slope constant and K_{ii} - intersects constant in enzyme inhibition is widely employed.[7-11]

Plotting the dependencies of change in the ratio K'_m/V' (Figure 3A) on the molar concentrations of I_{Ii} in the coordinates of slopes (K'_m/V'; i) (see Figure 3C, line 2) for calculation of K_{is} - slope-constant and the coordinates of intersects ($1/V'$; i) (Figure 3C, line 1) for calculation of K_{ii} - intersect-constant of enzyme inhibition.

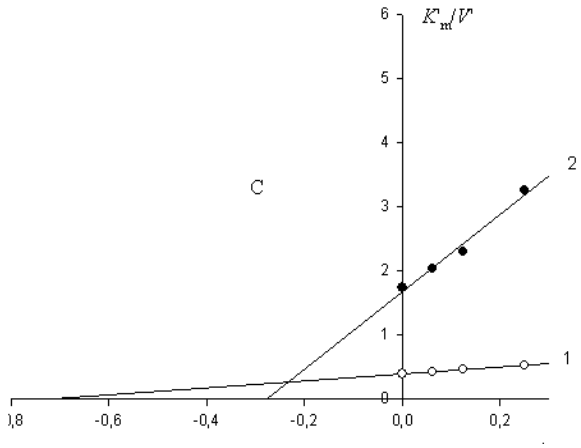

Figure 3C. Dependence of change in the ratio K'_m/V' (Figure 3A) on the concentration of MoO_4^{2-} in the coordinates of slopes (K'_m/K^0_m; i) – line 2 and the coordinates of intersects ($1/V'$; i) – line 1.

This gives the following values: $K_{is}= 0.275\cdot10^{-4}$ M in the first case and $K_{ii} = 0.715\cdot10^{-4}$ M – in the second case (Figure 3C), which neither in the second case nor in the first one would correspond the actual value: $K_{Ii} = 0.635\cdot10^{-4}$ M calculated by Eqn. 3.

Deviation between the values of constants K_{Ii} and K_{is}, K_{ii} can be explained as: at calculation of the latter, the lengths of orthogonal projections of $\mathbf{L}_{Ii}$ vectors on the basic σ_0 plane in the $K'_mV'I$ coordinate system (Figures 1 and 2) were not taken into account, and besides this, as shown below (Example 3), the coordinates of intersects ($1/V'$; i) are a simplified form (K'_m/V'; i) of the coordinates of slopes (Table 3), and plotting the dependencies in these coordinates does not take into account changes K'_m parameters of the biparametrical reactions, to which the data of Figure 3A are referred.

Examples of using the coordinates *(K'_m/V'; i) and ($1/V'$;i)* to data analysis of such type (Figure 3A) of enzyme inhibition are numerous in literature.[7-11]

The K^0_m and V^0 parameters of initial reaction (i= 0, or a =0) are present in all the equations of Table 2 used for calculation of K_i and K_a constants of enzyme inhibition and activation. This may lead to difficulties, for example, in search of a response to a query as to how shall we use these equations, if the values K^0_m and V^0 parameters of initial reaction have not been determined ? Such data are often available in experimental part of the reports in literature.[7,12,14,16]

The best possible answer here follows from analysis of plots of Figures 3A and 3B. Thus, as clearly observed from Figure 3B, the slope angles (tg a) of rectilinear segments of dependencies A = f(i) well coincide by tested intervals (Δi) of the concentrations of inhibitor: for $\Delta(i_1 - 0)$ = (0.0625 – 0) 10^{-4} M, where: $K_{Ii(0)} = 0.523\cdot10^{-4}$ M, for $\Delta(i_2 - i_1)$ = (0.125 – 0.0625) 10^{-4} M, whereе $K_{Ii(2)} = 0.551\cdot10^{-4}$ M, for $\Delta(i_3 - i_2)$ = (0.25 – 0.125) 10^{-4} M where $K_{Ii(3)} = 0.646\cdot10^{-4}$ M (see Table 1). Such coincidence of the results is evident.

Example 2

Calculation of the K_{VIa} constant of enzyme activation. Earlier, the activating effect of arginine-containing activator (ArgA), on initial rates of P_9 polyphosphate cleavage by vacuolar Mg^{2+} - independent polyphosphate hydrolase from the fungus, *Neurospora crassa* (E.C. 3.6.11) which exhibits the maximum activity at pH 6.4. The conditions of enzyme isolation and study of its activity are given in the reference.[12]

Results

The results of this experiment presented in Figure 4A show that in the presence of 1.1 μM activator the activity of P_9 polyphosphate cleavage by vacuolar polyphosphate hydrolase under study had the following parameters: $K'_m=3.810\cdot10^{-4}$ M, $V'=2.110\cdot\mu E\cdot min^{-1}$; in the presence of 2.20 μM – by $K'_m= 4.359\cdot10^{-4}$ M, $V'=2.773\cdot\mu E\cdot min^{-1}$; in the presence of 3.3 μM – parameters: $K'_m = 4.836\cdot10^{-4}$ M, $V'= 3.494\cdot\mu E\cdot min^{-1}$.

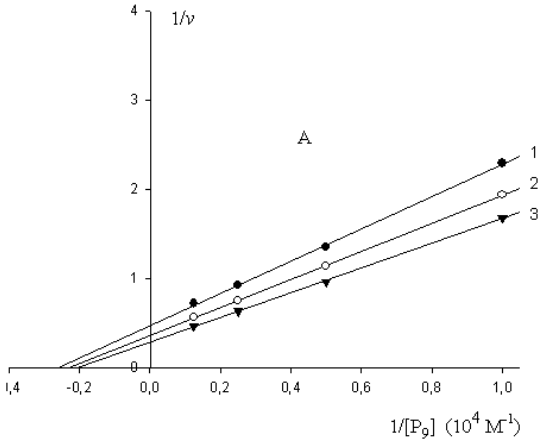

Figure 4A. Activating effect of ArgA on initial rates v_{VIa} of P_9 polyphosphate cleavage catalyzed by vacuolar polyphosphatase from *N. crassa*: the concentration of ArgA; line 1 – 1.1 μM, line 2 – 2.2 μM, and line 3 – 3.3 μM. Designation: v $\mu E\cdot min^{-1}$.

 DOI: 10.17628/ecb.2014.3.815-822

Table 2. Equations for calculation of the K_i and K_a constants

Type of effect	New name of the types of enzymic reactions	Traditional name	Equation for calculation of the K_i and K_a constants
I_i	biparametrically coordinated inhibition	mixed inhibition	$K_{Ii}=\frac{i}{\left(\left(\frac{K_m^{'}-K_m^0}{K_m^0}\right)^2+\left(\frac{V^0-V^{'}}{V^{'}}\right)^2\right)^{0.5}}$
II_i	unassociative inhibition	uncompetitive inhibition	$K_{IIi}=\frac{i}{\left(\left(\frac{K_m^0-K_m^{'}}{K_m^{'}}\right)^2+\left(\frac{V^0-V^{'}}{V^{'}}\right)^2\right)^{0.5}}$
III_i	catalytic inhibition	noncompetitive inhibition	$K_{IIIi}=\frac{i}{V^0/V^{'}-1}$
IV_i	associative inhibition	competitive inhibition	$K_{IVi}=\frac{i}{K_m^{'}/K_m^0-1}$
V_i	pseudoinhibition		$K_{Vi}=\frac{i}{\left(\left(\frac{K_m^{'}-K_m^0}{K_m^0}\right)^2+\left(\frac{V^{'}-V^0}{V^0}\right)^2\right)^{0.5}}$
VI_i	discoordinated inhibition		$K_{VIi}=\frac{i}{\left(\left(\frac{K_m^0-K_m^{'}}{K_m^{'}}\right)^2+\left(\frac{V^0-V^{'}}{V^{'}}\right)^2\right)^{0.5}}$
VII_i	transient inhibition		$K_{VIIi}=\frac{i}{\left(\left(\frac{K_m^0-K_m^{'}}{K_m^{'}}\right)^2+\left(\frac{V^0-V^{'}}{V^{'}}\right)^2\right)^{0.5}}$
I_0	initial (uninhibited i = 0 and nonactivated) enzymatic reaction		
VII_a	transient activation		$K_{VIIa}=\frac{a}{\left(\left(\frac{K_m^{'}-K_m^0}{K_m^0}\right)^2+\left(\frac{V^{'}-V^0}{V^0}\right)^2\right)^{0.5}}$
VI_a	discoordinated activation		$K_{VIa}=\frac{a}{\left(\left(\frac{K_m^{'}-K_m^0}{K_m^0}\right)^2+\left(\frac{V^{'}-V^0}{V^0}\right)^2\right)^{0.5}}$
V_a	pseudoactivation		$K_{Va}=\frac{a}{\left(\left(\frac{K_m^0-K_m^{'}}{K_m^{'}}\right)^2+\left(\frac{V^0-V^{'}}{V^{'}}\right)^2\right)^{0.5}}$
IV_a	associative activation	competitive activation	$K_{IVa}=\frac{a}{K_m^0/K_m^{'}-1}$
III_a	catalytic activation	noncompetitive activation	$K_{IIIa}=\frac{a}{V^{'}/V^0-1}$
II_a	unassociative activation	uncompetitive activation	$K_{IIa}=\frac{a}{\left(\left(\frac{K_m^{'}-K_m^0}{K_m^0}\right)^2+\left(\frac{V^{'}-V^0}{V^0}\right)^2\right)^{0.5}}$
I_a	biparametrically coordinated activation *	mixed activation	$K_{Ia}=\frac{a}{\left(\left(\frac{K_m^0-K_m^{'}}{K_m^{'}}\right)^2+\left(\frac{V^{'}-V^0}{V^0}\right)^2\right)^{0.5}}$

Table 3. The coordinates of slopes for calculation of K_i and K_a constants of enzyme inhibition and activation

No	Effect	Type	Plots in (v^{-1}; S^{-1}) coordinates	Coordinates of slopes for calculation of K_i and K_a constants
1	Inhibition ($i > 0$)	I_i	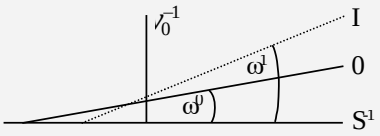	(A; i) (see Figure 3B in the text)
2		II_i	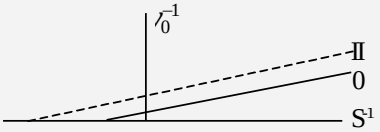	(A; i)
3		III_i	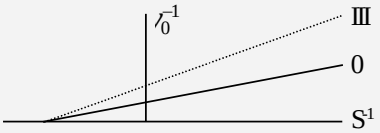	$\left(\frac{K_m^{'}}{V^{'}};i\right);\left(\frac{1}{V^{'}};i\right)$ or $\left(\frac{tg\omega^{'}}{tg\omega^{0}};i\right)$ and $\left(tg\omega^{'};i\right)$ (see Figure 5B in the text)
4		IV_i	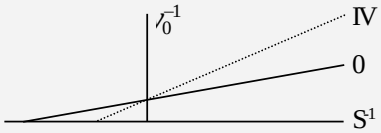	$\left(\frac{K_m^{'}}{V^{'}};i\right)$ and $\left(K_m^{'};i\right)$
5		V_i	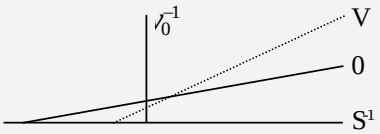	(A; i)
6		VI_i	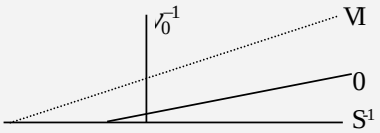	(A; i)
7		VII_i	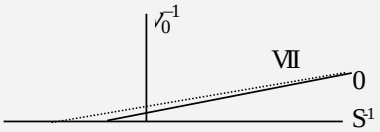	(A; i)
8	None	I_0	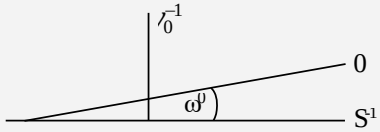	None
9	Activation ($a > 0$)	VII_a	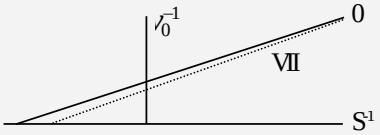	(A; a)
10		VI_a	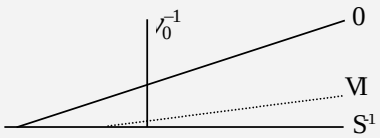	(A; a) (see Figure 4B in the text)

 DOI: 10.17628/ecb.2014.3.815-822

Cont. Table 3.

11	V_a	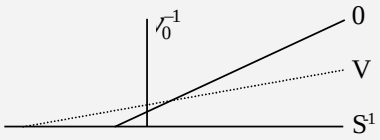	(*A*; *a*)
12	IV_a	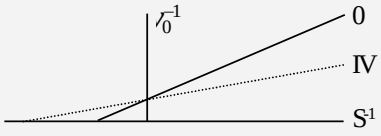	$\left(\frac{V}{K_m};a\right);\left(\frac{1}{K_m};a\right);\left(\frac{tg\omega}{tg\omega'};a\right)$ and $\left(\frac{1}{tg\omega'};a\right)$
13	III_a	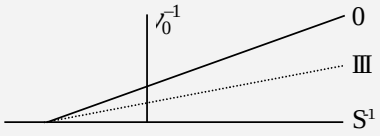	$\left(\frac{V}{K_m};a\right);(V;a);\left(\frac{tg\omega}{tg\omega'};a\right)$ and $\left(\frac{1}{tg\omega'};a\right)$
14	II_a	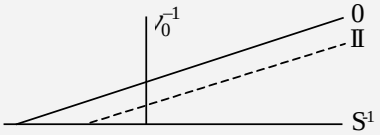	(*A*; *a*)
15	I_a	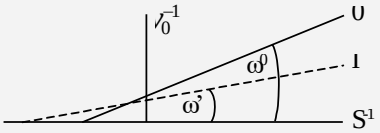	(*A*; *a*)

It satisfies type VI_a of enzyme activation (line 10, Table 3) and hence. Eqn. 10 of Table 2, is applicable here for calculation of K_{VIa} constant of enzyme activation), as the parameters of initial reaction (K^0_m and V^0) in this case were not determined, because of weak enzyme activity in the absence of activator.

Use of this equation gives the following values of constants of polyphosphatase hydrolase activation: K_{VIa}=3.182 μM – in the interval ArgA (2.2-1.1=1.1) μM and K_{VIa} = 3.103 μM – in the interval ArgA (3.3–1.1 = 2.2) μM, where $K_{m(2.2)}=K'_m$, $K_{m(1.1)}=K^0_m$ and so on.

By having marked according to the equation:

$$K_{Ia}=\frac{1}{tg\alpha}=\frac{1}{A/a}=\frac{a}{A} \qquad (4)$$

the numerical values of *A* denominators by intervals of tested concentrations of ArgA. One shall obtain that the values of *A* parameters are in the following functional dependence on the intervals of tested concentrations of activator (Figure 4B):

Hence, the average value of this constant (by intervals of ArgA concentrations as activator) shall be the value:

$$K_{VIa}= 1/b(1) = 1/3.2227\ (\mu M)^{-1} = 0.3103\ \mu M, \qquad (5)$$

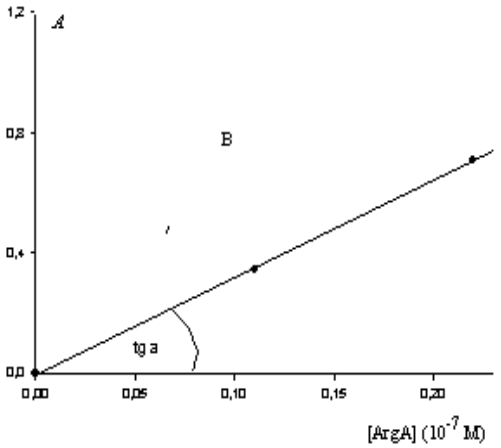

Figure 4B. Dependence of *A* parameters of Eqn. 5 (Figure 4A) on increasing concentrations of ArgA in the coordinates (*A*; [ArgA]). Designation: the intervals of tested concentrations ArgA were 1.1 and 2.2 μM.

where, *b*(1) = 3.2227 – a parameter of the subprogram statistics of the computer program SigmaPlot, version 2000.

Probably, this technique may also be used in the case of single intervals of Δ*a* and Δ*i* parameters of both the biparametrical and monoparametrical K_a and K_i constants of enzyme inhibition and activation (Table 2).

At data analysis of the VI_a type of enzyme activation (the positions of plots are typical of Figure 4A).

The many authors[7,13-16] used to plot such dependences of a course of change of the slope angles (tg ω′) and the intersection points (1/*V'*) of the ordinate axis as a function of reverse concentrations of activator 1/*a* in the coordinates of : (tg ω′;1/*a*) slopes and (1/*V*';1/*a*) intersects. It is incorrect. Plotting the dependencies of change of K'_m/V' on 1/*a* in the coordinates of slopes (K'_m/V'; 1/*a*) and coordinates of intersects (*1/V'*; 1/*a*) does not take into account symmetric counter-directivity of effects of enzyme activation to → enzyme inhibition, which is so evident at the comparison of the positions of one-type $\mathbf{L}_a$ and $\mathbf{L}_i$ and their L_a and L_i projections in the three-dimensional (Figure 1) and two-dimensional (Figure 2) systems of coordinates. It is taken into account by reversion of V'/K'_m parameters relative to non-reversed concentrations of activator (*a*) in the corrected coordinates of slopes (Table 3, lines 12 and 13). So, one must use either (V'/K'_m; *a*) or (*V'*; *a*) coordinates of slopes instead of (K'_m/V'; *a*) coordinates for calculation of only monoparametrical K_{IIIa} constants of enzyme activation. The coordinates of slopes for calculation of biparametrical K_a constants of enzyme activation are given in Table 3 and their application is established in Examples 1 and 2.

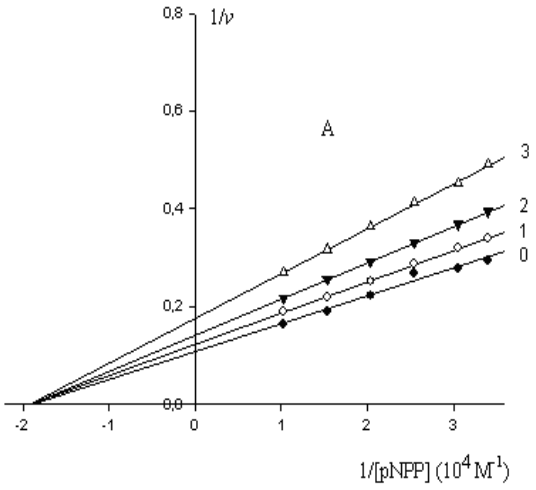

Figure 5A. Inhibitory effect of $K_3Fe(CN)_6$· on initial rates of pNPP cleavage catalyzed by porcine alkaline phosphatase. Designation: line 1 –$0.25\cdot10^{-3}$ M, line 2 – $0.5\cdot10^{-3}$ M, line 3 - $1.0\cdot10^{-3}$ M. Line 0 – the inhibitor is absent, ν μmol·min^{-1} μg protein^{-1}.

Example 3

Calculation of K_{IIIi} constant of enzyme inhibition. Let us use the data obtained at study of the inhibitory effect of potassium ferrocyanide $K_3Fe(CN)_6$ on initial rates of pNPP cleavage catalyzed by porcine alkaline phosphatase (EC 3.1.3.1) for calculation of K_{IIIi} constants of enzyme inhibition. The enzyme is produce of Sigma (USA).

The concentration of pNPP in the experiment was varied within $0.294\cdot10^{-4}$ – $0.98\cdot10^{-4}$ M, the concentration of enzyme was kept constant 1.13 μg mL^{-1}. The other conditions are same as in Example 1.

Results

The results of study showed that the kinetic parameters of initial reaction (K^0_m= $5.31\cdot10^{-5}$ M, V^0= 9.321 μmol·min^{-1} μg protein^{-1}) in the presence of 0.25 10^{-3} M $K_3Fe(CN)_6$ change as follows: K'_m=$5.23\cdot10^{-5}$ M, V'= 8.158 μmol·min^{-1} μg protein^{-1}, in the presence of 0.5 $\cdot10^{-3}$ M $K_3Fe(CN)_6$: K'_m=$5.25\cdot10^{-5}$ M, V'= 5.70 μmol·min^{-1} μg protein^{-1} and in the presence of (1 10^{-3} M) $K_3Fe(CN)_6$ –K'_m= $5.27\cdot10^{-5}$ M, V'= 7.085 μmol·min^{-1} μg protein^{-1} (Figure 5A).

It satisfies all the features ($K'_m=K^0_m$, $V'<V^0$, $i>0$) of the catalytic *III*$_i$ type of enzyme inhibition. As seen from Figure 5A, lines 1, 2 and 3 of inhibited reactions go above line 0 of initial reaction in the first quadrant of the (v^{-1}, S^{-1}) coordinates in the point (-1/K'_m; 0) located on the continuation of the abscissa axis. The positions of lines 1, 2 and 3 (Figure 5A) are typical to such of lines III and 0 (Figure 3 in Table 3); hence, for calculation of K_{IIIi} constant of enzyme inhibition we shall use the equation:

$$K_{IIIi} = \frac{i}{V^0/V' - 1} \qquad (6)$$

of (Table 2, line 3).[4]

To calculate the value of the constant of enzyme inhibition independently of deviations due to sue of separate (individual) concentrations of $K_3Fe(CN)_6$, it is also desirable to employ already above-descript techniques (Examples 1 and 2) – it is study of effect of increasing concentrations of inhibitor on initial rates of substrate cleavage by plotting dependencies in one (or several) variants of the secondary coordinates of slopes, which proceed from transformation of Eq. (6). It is easy to see that in the (V^0/V; *i*) coordinates of slopes the experimental line:

$$\frac{V^0}{V} = \frac{1}{K_{IIIi}} \cdot i + 1 \qquad (7)$$

,

explained by this equation (Figure 5B, line 2) or in the (1/*V*; *i*) variant of the same coordinates of slopes the line:

$$\frac{1}{V} = \frac{1}{V^0} \cdot \frac{1}{K_{IIIi}} \cdot i + \frac{1}{V^0} \qquad (8)$$

(Figure 5B, line 1) shall intersect the continuation of the abscissa axis of molar concentrations of inhibitor in the point: $-i_{IIIi} = K_{IIIi}$.

Analysis of the positions of the intersection points of the abscissa of Figure 5A using the subprogram Statistics of the computer program SigmaPlot, version 2000 (USA) gives the following of K_{IIIi} = $1.550\cdot10^{-3}$ M in the first case (line 2) and K_{IIIi} = $1.552\cdot10^{-3}$ M in the second case (line 1).

Experimental data of catalytic type of enzyme inhibition in literature there are.[7, 8,19,20] Now it becomes necessary to discuss the question of using the secondary (1/*V'*; *i*) coordinates of intersects for experimental data analysis on enzyme inhibition, which follows from transformation of Eq. (6) to Eq. (8) due to the equality $K'_m=K^0_m$ of parameters characteristic of only this *III*$_i$ type of enzyme inhibition (Table 3, line 3).

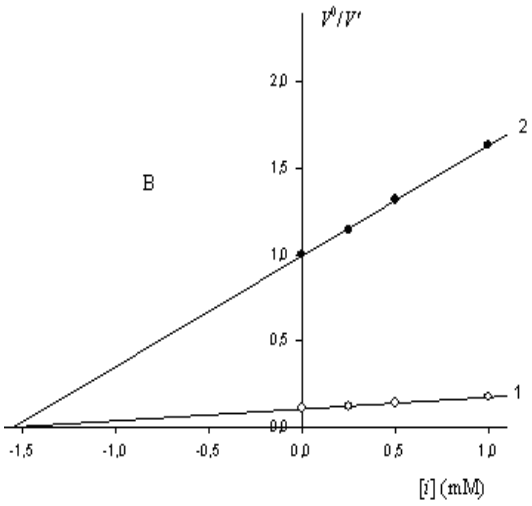

Figure 5B. Data representation of Figure 5A in the coordinates (V^0/V'; i) of slopes – line 2 and in the ($1/V'$; i) variant of the same coordinates – line 1,

It becomes evident from analysis of the Eqns. 6, 7 and 8 of the text that ($1/V'$; i) coordinates can be used for data analysis of only III_i type of enzyme inhibition characterized by change of only one $V'<V^0$ reaction parameter, and as the coordinates of slopes for calculation of K_{is} slope constants of this type of enzyme inhibition, but not K_{ii} intersects coordinates that actually do not exist (Table 3).

Apparently, using the ($1/V'$; i) coordinates of intersects for data analysis of types I_i and other biparametrically II_i, V_i, VI_i and VII_i types of enzyme inhibition that exhibit themselves by change of two (K'_m and V') reaction parameters seems incorrect, as the course of change of K'_m parameters of such reactions shall not be taken into account.

Examples of simultaneous use of the coordinates of slopes and intersects for calculation of K_{is} slope constants and K_{ii} intersect constants of biparametrical types of enzyme inhibition are numerous in literature.[6-11,17,18]

Besides, the authors do not discuss the question that, what does the value of K_{ii} constant of enzyme inhibition characterize, if K_{is} constant is attached the sense of constant of dissociation of the enzyme-inhibitor complex, especially in those cases, when their values do not coincide ? This question can be put in another way that, could one and the same inhibitor exhibit different binding to enzyme under the same experimental conditions?

Probably, not. The situation gets simplified at refusal of calculation and using symbols of K_{ii} intersect constants of enzyme inhibition, because they are the K_{is} constants of enzyme inhibition, But then, the necessity of using symbols of K_{is} slope constants of enzyme inhibition is also of no use, and only one symbol remains – it is the K_i constant of enzyme inhibition (for the convenience, it is preferable to indicate the type of inhibited reaction). It is analogous in enzyme activation (Tables 3 and 2).

References

[1]Krupyanko, V. I., *J. Biochem. Mol. Toxicol.*, **2009**; *23(2)*, 97.

[2]Krupyanko, V. I., *J. Biochem. Mol. Toxicol.*, **2009**; *23(2)*, *101*.

[3]Krupyanko, V.I.. *J. Biochem. Mol. Toxicol.*, **2009**; *23(2)*, 108.

[4]Krupyanko, V. I.,. *J. Biochem. Mol. Toxicol.*, **2010**; *24(3)*, *145*.

[5]Krupyanko, V.I., *A Vector Method Representation of Enzymic Reactions*. Moscow, Nauka, **1990**, 146 (in Russian).

[6]Krupyanko, V. I., *Eur. Chem. Bull.*, **2014**; *3(6)*, *582*.

[7]Seubert, P.A,, Renosto, F., Knudson, P. and Segel, I. H., *Arch. Biochem. Biophys*., **1985**; *240(2)*, *509*.

[8]Li, B. H., Ma, X-F., Wang, Y. and Tian, W-X., *J. Biochem*., **2005**, *138(6)*, 679.

[9]Sanz-Rodriguez, C. E., Concepcion, J. L., Pekerar, S., Oldfield, E. and Urbina, J. A., *J. Biol. Chem*., **2007**, *282(17)*,12377.

[10]Krath, B. N, and Hove-Jensen, B., *Protein Sci.*, **2001,** *10(11)*, 2317.

[11]Wilson, J. E. and Chung, W., *Arch. Biochem. Biophys*., **1989**, *269(2)*, 517.

[12]Vagabov, V. M., Knyazeva, I. N., Lupashin, V. V., Krupyanko, V. I. and Kulaev, I. S., *Biochemistry* (Moscow), **1987**, *52(4)*, 534 (in Russian).

[13]Kearns, A. E., Campbell, S. C., Westley, J. and Schwartz. N. B.,. *Biochemistry*, **1991**, *39(30)*, 7477.

[14]Vincenzini, M. T., Vanni, R., Giachetti, E., Hanozet, G. M. and Pinzauti. G., *J. Biochem*., **1986**, *99(2)*, 375.

[15]Edelberg, J. M,, Weissler, M. and Pizzo, S. V., *Biochem. J*., **1991**, *76(3)*, 785.

[16]Falany, C. N., Green, M. D. and Tephly, T. R., *J. Biol. Chem*., **1987**, *262(3)*,1218.

[17]Hara, A., Nakayama, T., Nakagawa, M.,, Inoue, Y., Tanabe, H. and Sawada, H., *J. Biochem*., **1987**, *102(6)*, 1585.

[18]Cacciapouti, G., Moretti, M. A., Forte, S., Brio, A., Camardella, L., Zappia, V., Porcelli, M., *Eur. J. Biochem*., **2004**, *271(23-24)*, 4834.

[19]Vetrano, A. M., Heck, D. E., Mariano, T. M., Mishi, V., Laskin, D. L. and Laskin, J. D., *J. Biol. Chem*., **2005**, *280(42)*, 35372.

[20]Papp, E., Tse, J. K. Y., Ho, H., Wang, S., Shaw, D., Lee, S., Barnett. J., Swinney, D. C. and Bradshaw, J. M., *Biochem.*, **2007**, *46(51)*, 15103.

Received: 11.06.2014.
Accepted: 30.07.2014.

KINETIC AND MECHANISTIC STUDIES IN THE OXIDATIVE REGENERATION OF CARBONYL COMPOUNDS FROM OXIMES BY BIS[DIPYRIDINESILVER(I)] DICHROMATE

Lokesh Mathur,[a] Vasudha Ranga,[a] Garima Goswami, [a] Saraswati Agarwal[b] and Pradeep K. Sharma*[a]

Keywords: carbonyl compounds; bis[dipyridinesilver(I)] dichromate, kinetics; mechanism; oxidation; oximes.

The oxidative deoximination of several aldo- and keto-oximes by bis[dipyridinesilver(I)] dichromate (BDSD), in dimethylsulphoxide (DMSO), exhibited a first order dependence on BDSD. A Michaelis-Menten type kinetics was observed with respect to oximes. The oxidation of ketoximes is slower than that of aldoximes. The rates of oxidation of aldoximes correlated well in terms of Pavelich-Taft dual substituent-parameter equation. The low positive value of polar reaction constant indicated a nucleophilic attack by a chromate-oxygen on the carbon. The reaction is subject to steric hindrance by the alkyl groups. The reaction of acetaldoxime has been studied in nineteen different organic solvents. The solvent effect has been analysed by multiparametric equations. A mechanism involving the formation of a cyclic intermediate, in the rate-determining step is suggested.

Corresponding Authors
E-mail: drpkvs27@yahoo.com
[a] Chemical Kinetics Laboratory, Department of Chemistry, J.N.V. University, Jodhpur, India
[b] Department of Chemistry, Govt. JDB College, Kota (Rajasthan) India

INTRODUCTION

Regeneration of carbonyl compounds from its derivatives under mild conditions is an important process in synthetic organic chemistry. Several oxidative methods are available for deoximation.[1] Salts of Cr(VI) have long been used as oxidizing reagents in synthetic organic chemistry. However, these salts are drastic and non-selective oxidants in nature. Further, they are insoluble in most of the organic solvents also. Thus miscibility is a problem. To overcome these limitations, a large number of organic derivatives of Cr(VI) have been prepared and used in synthetic organic syntheses as mild and selective oxidants in non-aqueous solvents.[2] One such compound is bis[dipyridinesilver(I)] dichromate (BDSD) reported by Firouzabadi and co-workers.[3] Only a few reports are available in literature regarding oxidation aspects of BDSD.[4-6] It is known that the mode of oxidation depends on the nature of the counter-ion attached to the chromium anion. Therefore, in continuation of our earlier work,[7] we report here the kinetics of the oxidative deoximation of several aldo- and keto-oximes by BDSD in several organic solvents but mainly in dimethylsulphoxide (DMSO). Mechanistic aspects have also been discussed.

EXPERIMENTAL

Materials

Oximes were prepared by the reported standard methods[8] and their mp were checked with the literature values. BDSD also was prepared by the reported method.[3] Solvents were purified by the usual procedure.[9]

Product Analysis

The oxidation of the oximes results in the regeneration of corresponding carbonyl compounds, as confirmed by TLC (eluent: CCl_4/Et_2O). Isolation of the product was attempted in the oxidation of oximes of benzaldehyde and acetophenone.

In a typical experiment, the oxime (0.2 mol) and BDSD (0.02 mol) were dissolved in 50 ml of DMSO and allowed to stand for *ca*. 10 h for the completion of the reaction. Silica gel (5 g) was then added to the reaction mixture and the mixture was stirred for 15 min.[10] It was then filtered and the solid residue was washed with the solvent (2 % 15 ml). The solvent was removed on a rotary evaporator and the residue was purified on a silica-gel column (eluent: CCl_4/Et_2O). Evaporation of the solvent afforded the pure carbonyl compound. Yields of benzaldehyde and acetophenone were 1.85 g (87.0 %) and 2.13 g (89.0 %) respectively. The presence of HNO_2 in completely reduced reaction mixtures was confirmed by a positive starch-iodide test.[11] The oxidation state of chromium in a completely reduced reaction mixture, as determined by an iodometric method, is 3.90±0.10.

Kinetics Measurements

The reactions were studied under pseudo-first-order conditions by keeping a large excess (× 10 or greater) of the oxime over BDSD. The solvent was DMSO, unless mentioned otherwise. The reactions were studied at constant temperature (±0.1 K). The reactions were followed by monitoring the decrease in the concentration of BDSD at 370 nm spectrophotometrically. The pseudo-first-order rate constant, k_{obs}, was evaluated from the linear least-squares plots of log [BDSD] *versus* time. Duplicate kinetic runs showed the rate constants to be reproducible to within ±4 %. The second order rate constants were evaluated from the relation $k_2 = k_{obs}/[\text{reductant}]$.

RESULTS AND DISCUSSION

Stoichiometry

The analysis of products indicated the following overall reaction.

$$R_2C = N{-}OH + Cr_2O_7^{2-} + 10H^+ \longrightarrow R_2C{=}O + HNO_2 + 5H_2O + 2Cr^{+3} \quad (1)$$

Rate Laws

The reactions are of first order with respect to BDSD. Further, the pseudo-first order rate constant, k_{obs} is independent of the initial concentration of BDSD. The reaction rate increases with increase in the concentration of the oximes but not linearly (Table 1). The Fig. 1 depicts a typical kinetic run. A plot of $1/k_{obs}$ against 1/[Oxime] is linear ($r > 0.995$) with an intercept on the rate-ordinate. Thus, Michaelis-Menten type kinetics is observed with respect to oximes. This leads to the postulation of following overall mechanism (2) and (3) and rate law (4).

$$\text{Oxime} + \text{BDSD} \overset{K}{\rightleftharpoons} [\text{Complex}] \quad (2)$$

$$[\text{Complex}] \xrightarrow{k_2} \text{Products} \quad (3)$$

$$\text{Rate} = \frac{k_2 K[\text{Oxime}][\text{BDSD}]}{1 + K[\text{Oxime}]} \quad (4)$$

The dependence of k_{obs} on the concentration of oxime was studied at different temperatures and the values of K and k_2 were evaluated from the double reciprocal plots (Fig. 2). The thermodynamic parameters for the complex formation and activation parameters of the disproportionation of the complexes, at 298 K, were calculated from the values of K and k_2 respectively at different temperatures (Tables 2 and 3).

Table 1. Rate constants for the oxidation of acetaldoxime by BDSD at 288 K

10^3[BDSD], mol dm^{-3}	[Oxime], mol dm^{-3}	10^4 k_{obs}, s^{-1}
1.00	0.10	12.9
1.00	0.20	18.9
1.00	0.40	24.6
1.00	0.60	27.3
1.00	0.80	28.9
1.00	1.00	30.0
1.00	1.50	31.5
1.00	3.00	33.2
2.00	0.20	25.2
4.00	0.20	23.4
6.00	0.20	25.0
8.00	0.20	24.3
1.00	0.40	24.0

*contained 0.001 mol dm^{-3} acrylonitrile

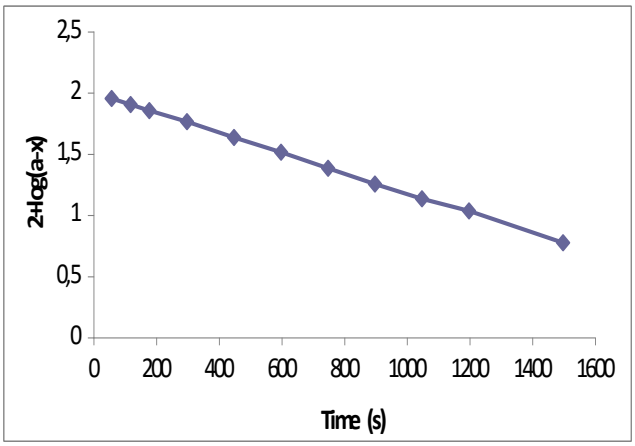

Figure 1. Oxidation of acetaldoxime by BDSD: A typical Kinetic Run

Effect of Solvents

The oxidation of acetaldoxime was studied in nineteen different solvents. The choice of solvents was limited due to the solubility of the reactants and the reaction of BDSD with primary and secondary alcohols. There was no reaction with chosen solvents. The kinetics were similar in all the solvents. The values of k_2 are recorded in Table 4.

There is no significant isokinetic relationship between activation entropy and enthalpy of the oxidation of oximes ($r^2 = 0.4329$). A correlation between the calculated values of enthalpies and entropies of activation is often vitiated by the experimental errors associated with them. Exner[12] has suggested an alternative method of testing the validity of the isokinetic relationship. An Exner's plot between log k_2 at 288 and 318 K was linear ($r^2 = 0.9985$; slope = 0.7198 ± 0.0199) (Fig. 3). The value of isokinetic temperature evaluated from this plot is 435±15 K. The linear isokinetic correlation suggests that all the oximes are oxidized by the same mechanism and are governed by the changes in both the enthalpy and entropy of the activation.

A perusal of the data shows that the formation constants do not vary much with the nature of the solvents. However, the rate constants, k_2 varied considerably with the solvents. The rate constants for oxidation, k_2, in eighteen solvents (CS_2 was not considered, as the complete range of solvent parameters was not available) were correlated in terms of the linear solvation energy relationship (Eq.5) of Kamlet et al.[13]

$$\log k_2 = A_0 + p\pi^* + b\beta + a\alpha \quad (5)$$

In this equation, π^* represents the solvent polarity, β the hydrogen bond acceptor basicities and α is the hydrogen bond donor acidity. A_0 is the intercept term. It may be mentioned here that out of the 18 solvents, 12 have a value of zero for α. The results of correlation analyses in terms of Eq. (5), a biparametric equation involving π^* and β, and separately with π^* and β are given below [Eqs. (6) - (9)].

 DOI: 10.17628/ecb.2014.3.823-828

Table 2. Rate constants and activation parameters for the oxidation of BDSD-oximes (R^1R^2C=N–OH) complexes

Substituents, R	$10^4 k_2$, dm^3 mol^{-1} s^{-1}				ΔH^*, (kJ mol^{-1})	$-\Delta S^*$, J mol^{-1} K^{-1}	ΔG^*, kJ mol^{-1}
	288	298	308	318			
H – H	1710	1850	2010	2120	30.0±0.7	249±1	77.2±0.1
H – Me	35.1	54.0	83.7	126	30.0±0.3	188±1	85.9±0.2
H – Et	25.2	39.6	63.9	98.1	32.2±0.4	183±1	86.7±0.8
H – Pr	11.7	20.7	34.2	56.7	37.4±0.2	172±1	88.4±0.7
H – Pr^i	7.92	14.4	24.3	42.3	39.7±0.4	167±1	89.3±0.7
H – $ClCH_2$	108	144	189	234	17.2±0.4	223±1	93.5±0.6
H – Ph	72.9	108	162	243	28.0±0.5	189±2	94.2±0.6
Me – Me	3.60	5.67	8.73	13.5	31.0±0.3	204±1	91.5±0.3
Me – Et	2.88	4.50	6.93	10.8	30.9±0.4	206±1	92.1±0.4
Et – Et	2.34	3.69	5.67	8.73	30.8±0.3	208±1	92.6±0.2
Me – Ph	6.30	10.8	17.1	27.0	34.2±0.3	188±1	89.9±0.2

$$\log k_2 = -3.78 + 1.47(\pm0.18)\pi^* + 0.19(\pm0.18)\beta + 0.03(\pm0.14)\alpha \quad (6)$$

$R^2 = 0.8517$; $sd = 0.17$; $n = 18$; $\psi = 0.42$

$$\log k_2 = -3.79 + 1.48(\pm0.17)\pi^* + 0.18(\pm0.14)\beta \quad (7)$$

$R^2 = 0.8511$; $sd = 0.21$; $n = 18$; $\psi = 0.41$

$$\log k_2 = -3.75 + 1.53(\pm0.17)\pi^* \quad (8)$$

$r^2 = 0.8351$; $sd = 0.17$; $n = 18$; $\psi = 0.25$

$$\log k_2 = -2.92 + 0.44(\pm0.32)\beta \quad (9)$$

$r^2 = 0.1043$; $sd = 0.39$; $n = 18$; $\psi = 0.97$

Here n is the number of data points and ψ is Exner's statistical parameter.[14]

Kamlet's[13] triparametric equation explains *ca.* 85.2 % of the effect of solvent on the oxidation. However, by Exner's criterion[14] the correlation is not even satisfactory (cf. Eq. 6). The major contribution is of solvent polarity. It alone accounted for *ca.* 83.5 % of the data. Both β and α play relatively minor roles.

The data on the solvent effect were analysed in terms of Swain's equation[15] of cation- and anion-solvating concept of the solvents also [Eq. (10)].

$$\log k_2 = aA + bB + C \quad (10)$$

Here A represents the anion-solvating power of the solvent and B the cation-solvating power.

C is the intercept term. (A + B) is postulated to represent the solvent polarity. The rates in different solvents were analysed in terms of Eq. (7), separately with A and B and with (A + B).

$$\log k_2 = 0.72(\pm0.06)A + 1.54(\pm0.04)B - 3.92 \quad (11)$$

$R^2 = 0.9890$; $sd = 0.05$; $n = 19$; $\psi = 0.11$

$$\log k_2 = 0.50(\pm0.51)A - 2.93 \quad (12)$$

$r^2 = 0.0530$; $sd = 0.41$; $n = 19$; $\psi = 1.00$

$$\log k_2 = 1.49(\pm0.13)B - 3.75 \quad (13)$$

$r^2 = 0.8802$; $sd = 0.15$; $n = 19$; $\psi = 0.36$

$$\log k_2 = 1.27\pm0.11(A+B) - 3.94 \quad (14)$$

$r^2 = 0.8853$; $sd = 0.14$; $n = 19$; $\psi = 0.35$

The rates of oxidation of acetaldehyde in different solvents showed an excellent correlation in Swain's equation [cf. Eq.(11)] with both the anion- and cation-solvating powers playing almost equal role. However, individually A and B are able to account for only 5.3 % and 88.0 % of the data only. The solvent polarity, represented by (A+B), also exhibited an excellent correlation. In view of the fact that solvent polarity is able to account for *ca.* 98.9 % of the data, an attempt was made to correlate the rate with the relative permittivity of the solvent. However, a plot of $\log k_2$ against the inverse of the relative permittivity is not very significant ($r^2 = 0.5515$; $sd = 0.28$; $\psi = 0.69$). The analysis of solvent effect indicated the formation of an activated complex which is more polar than the reactants. The rate is affected by the solvent polarity.

Table 3. Formation constants and thermodynamic parameters of the oxidation of BDSD-oximes (R^1R^2C=N–OH) complexes

Substituent, R	K, dm^3 mol^{-1}				$-\Delta H^*$, kJ mol^{-1}	$-\Delta S^*$, J mol^{-1} K^{-1}	ΔG^*, kJ mol^{-1}
	288	298	308	318			
H – H	6.45	5.65	4.82	4.05	14.3±0.5	26±2	6.74±0.4
H – Me	5.36	5.07	4.32	3.42	16.1±0.7	33±2	6.46±0.6
H – Et	5.72	4.90	4.12	3.24	16.7±0.9	35±3	6.38±0.7
H – Pr	6.51	5.72	4.90	4.05	14.5±0.7	26±2	6.77±0.5
H – Pr^i	6.08	5.22	4.41	3.69	15.2±0.4	29±1	6.56±0.3
H – $ClCH_2$	5.85	5.06	4.23	3.45	15.9±0.7	32±2	6.46±0.5
H – Ph	5.30	4.50	3.69	2.95	17.3±0.7	38±2	6.17±0.5
Me – Me	5.77	4.95	4.14	3.35	16.2±0.7	33±2	6.41±0.5
Me – Et	6.21	5.42	4.60	3.80	14.9±0.6	28±2	6.44±0.5
Et – Et	5.52	4.70	3.92	3.12	16.9±0.7	36±2	6.28±0.6
Me – Ph	5.34	4.52	3.75	2.95	17.0±0.6	37±2	6.19±0.5

Correlation Analysis of Reactivity

We could not find any report about the mechanism of the reaction between a C=N bond and a halochromate derivative. However, the reaction of alkenes with chromium (VI) has been well studied.[16] Since, olefinic bonds are not usually subject to a nucleophilic attack, it has been suggested that in the alkene-chromate reaction, an organometallic derivative is formed initially.[16] The organometallic derivative then changes to a chromium (IV) diester in the rate-determining step. However, carbon-nitrogen double bonds, being dipolar in nature, can be easily attacked by a nucleophile. The data in Table 2 showed that the rate of oxidation of ketoximes is much less as compared to that of the aldoximes. The reason for the slower reaction of ketoximes must be steric. As the central carbon changes from a trigonal to a tetragonal state, the crowding around it increases. This increase in the steric crowding will be more in the case of ketoximes as compared to that in aldoximes. This observation is supported by the correlation analysis of the reactivity of the aldoximes also. The rate of oxidation of the aliphatic oximes did not yield significant correlation separately with Tafts's σ^* and E_S values [Eqs. (15) and (16)]. The rates were, therefore, correlated with Pavelich-Taft's[17] dual substituent-parameter Eq. (17).

$$\log k_2 = 1.02\pm0.60\sigma^* - 2.32 \quad (15)$$

$r^2 = 0.4204$, $sd = 0.65$, $n = 6$, $\psi = 0.86$, $T = 298$ K

$$\log k_2 = 1.14\pm0.23E_S - 2.15 \quad (16)$$

$r^2 = 0.8566$, $sd = 0.32$, $n = 6$, $\psi = 0.38$, $T = 298$ K

$$\log k_2 = \rho^*\sigma^* + \delta E_S + \log k_0 \quad (17)$$

The rates exhibited excellent correlations in terms of the Pavelich-Taft equation (Table 5); the reaction constants are being positive.

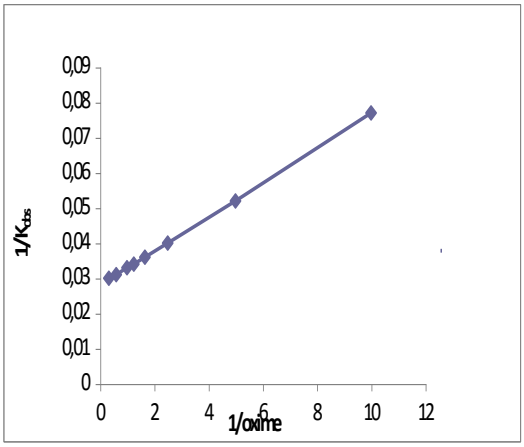

Figure 2. Oxidation of acetaldoxime by BDSD: A double reciprocal plot

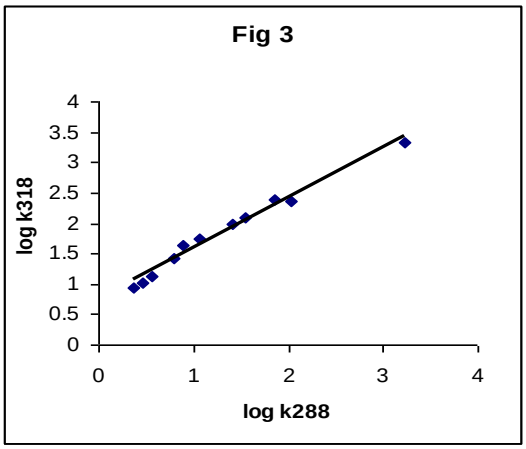

Figure 3. Exner's isokinetic relationship in the oxidation of oximes by BDSD

 DOI: 10.17628/ecb.2014.3.823-828

Table 4. Effect of solvents on the oxidation of acetaldoxime by BDSD at 298 K

Solvents	K, dm^{-3} mol^{-1}	k_{obs}, s^{-1}	Solvents	K, dm^{-3} mol^{-1}	k_{obs}, s^{-1}
Chloroform	4.55	30.9	Toluene	4.33	7.94
1,2-Dichloroethane	5.63	33.9	Acetophenone	5.62	38.9
Dichloromethane	5.90	25.5	THF	5.50	13.5
DMSO	4.23	83.7	t-Butylalcohol	4.67	14.5
Acetone	4.55	25.1	1,4-Dioxane	5.50	13.8
DMF	5.35	51.3	1,2-Dimethoxyethane	4.38	13.8
Butanone	5.92	19.1	CS_2	5.61	4.37
Nitrobenzene	4.32	38.9	Acetic Acid	4.55	6.08
Benzene	5.60	10.2	Ethyl Acetate	5.32	12.9
Cyclohexane	5.35	1.48			

Table 5. Reaction constants for the oxidative deoximination of aliphatic aldoximes by BDSD[a]

Temperature, K	ρ^*	δ	r^2	sd	ψ
288	0.71±0.01	1.08±0.02	0.9999	0.004	0.02
298	0.63±0.02	0.98±0.01	0.9998	0.006	0.01
308	0.55±0.01	0.90±0.02	0.9989	0.005	0.01
318	0.45±0.01	0.82±0.02	0.9989	0.003	0.02

[a] Number of compounds is 6

Mechanism

The low positive polar reaction constant points to an almost cyclic transition state in which the formation of the bond between chromate-oxygen and the carbon is somewhat ahead of the formation of N – O bond. This supports a nucleophilic attack by a chromate-oxygen on the carbon. The positive steric reaction constant points to a steric hindrance by the substituents. Therefore, the following mechanism (Scheme 1) is proposed for the reaction. The mechanism is supported by the values of activation parameters also. The low values of enthalpy of activation indicate that the bond-cleavage and bond-formation are almost synchronous. The large negative entropies of activation support the formation of a rigid cyclic activated complex from two acyclic molecules. The faster oxidation of benzaldoxime may be attributed to the resonance stablization of the cyclic activated complex. The oxidation of benzphenoxime is much slower. This may well be due to steric hindrance by the bulky phenyl and methyl groups. Hydroxynitrene (N-OH) has been recently reported as a very reactive intermediate.[18]

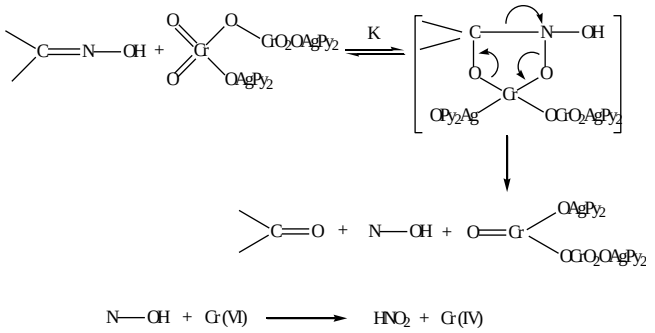

Scheme 1. The mechanism of the oxidation.

CONCLUSION

Oxidation of oximes by BDSD is a reaction subject to the steric hindrance by the alkyl group. Oxidation of ketoximes is slower than acetaldoximes. The reaction proceeds through a cyclic intermediate in the rate-determining step.

ACKNOWLEDGEMENTS

Thanks are due to University Grants Commission, New Delhi for financial support in the form of BSR-One Time Grant (PKS), No. F. 4–10/2010 (BSR) dated 07.03.2012, Minor Research Project to (LM) to Professor KK Banerji, Dean, Sciences, NLU, Jodhpur for his critical suggestions and helpful discussions.

REFERENCES

[1]Firouzabadi, H., Sadarian, A. *Synth. Commun.*, **1983**, *13*, 863; Drabowicz, J., *Synthesis*, **1980**, 125; Hopkins, P.B., Kim, S., Yoo, S., Nambiar, K.P., Flack, J.R. *J. Am. Chem. Soc.*, **1979**, *101*, 7131; Sankhla, R., Kothari, S., Kótai, L., Banerji, K.K. *J. Chem. Res. S*, **2001**(4), 127-12; Kumar, A., Mishra, P., Kotai, L., Banerji K. K., *Ind. J. Chem. Sect. A. Inorg. Bio-Inorg. Phys. Theor. Anal. Chem.*, **2003**. *42*(1), 72-74; Garnovskii, D. A., Kukushkin, V. Y., *Usp. Khim.*, **2006**, *75(2)*, 125-140;

[2]Mahanti , M.K., Banerji, K.K. *J. Indian Chem. Soc.*, **2002**, *79*, 31.

[3]Firouzabadi, H., Sardarian, A., Giaribi, H. *Synth. Comm.*, **1984**, *14*, 89.

[4]Meena, A. K., Daiya, A., Banerji, J., Sajo, I., Kotai, L., and Sharma, V., *J. Indian Chem. Soc.*, **2011**, *88*, 1887.

[5]Meena, A. K., Daiya, A., Sharma, A., Choudhary, A., Banerji, J., Kotai, L., Sajo, I., and Sharma, V., *Int. J. Chem.*, **2012**, *1(1)*, 55.

[6]Daiya, A., Sharma, D., Baghmar, M., Mishra, P., Sharma, S. and Sharma, V., *Eur. Chem. Bull.*, **2012**, *1(3-4)*, 75.

[7]Sharma, P. K., *Int. J. Chem.*, **2013**, *2(3)*, 294.

[8]Vogel, A.I. "A Text Book of Practical Organic Chemistry", ELBS, London, **1973**, 343.

[9]Perrin, D. D., Armarego, L., Perrin, D. R., "*Purification of Organic Compounds*," **1966** (Pergamon, Oxford).

[10]Baltrok, I. M., Sadegi, M. M., Mahmoodi, N., Kharamesh, B. *Indian J. Chem.*, **1997**, *36B*, 438.

[11] Feigl, F., Anger, V. "*Spot Tests in Organic Analysis*", Elsevier Publ., **1966**.

[12] Exner, O. *Prog. Phys. Org. Chem.*, **1973**, *10*, 411.

[13]Kamlet, M. J., Abboud, J. L. M., Abraham, M. H., Taft, R. W., *J. Org. Chem.*, **1983**, *48*, 2877.

[14]Exner, O. *Collect. Chem. Czech. Commun.*, **1966**, *31*, 3222.

[15]Swain, C. G., Swain, M. S., Powell, A. L., Alumni, S., *J. Am. Chem. Soc.*, **1973**, *105*, 502.

[16]Freeman, F., Fuselier, C. O., Armstead, C. R., Dalton, C. E., Davidson, P. A., Karchefski, E., Krochman, D. F., Johnson, M. N., Jones, N. K., *J. Am. Chem. Soc.*, **1983**, *103*, 1154.

[17]Pavelich, W.A., Taft, R. W., *J. Am. Chem. Soc.*, **1957**, *79*, 4935.

[18]Maier, G., Reisenauer, H. P., Marco, M. D., *Angew. Chem. Int. Ed*., **1999**, *38*, 108.

Received: 03.07.2014.
Accepted: 31.07.2014.

CRYSTAL STRUCTURE OF 2,7-DIBENZYLOXY-1,8-BIS(4-FLUOROBENZOYL)NAPHTHALENE AND THE COMPARISON WITH THE HOMOLOGUES: CONTRIBUTION OF $_{(Ar)}$C–H…O=C AND $_{(sp3)}$C–H…π INTERACTIONS TO THE MOLECULAR PACKING

Akiko Okamoto[a], Sayaka Yoshiwaka[a], Saki Mohri,[a] Daichi Hijikata[a], and Noriyuki Yonezawa[a]

Keywords: Non-coplanarly aromatic-rings-accumulating molecules, Crystal structure, Spatial organization, Non-bonding molecular interactions, C–H…O=C interaction, C–H…π interaction

As a part of our structural studies of 1,8-dibenzoylnaphthalene compounds, one of the highly congested aromatic-rings-accumulated molecules, 2,7-dibenzyloxy-1,8-bis(4-fluorobenzoyl)naphthalene is designed and determined the crystal structure by X-ray crystallography. Through comparison of the single molecular structure and the molecular packing structure with the homologues bearing alkoxy/aryloxy groups (methoxy, ethoxy, butoxy, and phenoxy groups) at the 2,7-positions, the contribution of the non-bonding molecular interactions to stabilization of the molecular packing is estimated. As a common feature of single molecular structure in the series of the compounds, two aroyl groups are attached to the naphthalene ring in a nearly perpendicular fashion. In the crystal packing of these compounds, aromatic hydrogen interacts with carbonyl oxygen to stabilize the spatial organization of non-coplanarly accumulated aromatic rings replacing π…π stacking interaction of benzene rings. Especially, intermolecular $_{(Ar)}$C–H…O=C interactions between the benzene rings of the aroyl groups and the carbonyl groups of the neighbouring molecules are influential. The pile superposing the naphthalene ring planes constructed mainly by this intermolecular interaction probably plays the most important role for stabilizing the crystal structure of these compounds. In addition to the $_{(Ar)}$C–H…O=C interactions, butoxy-, phenoxy- and benzyloxy-bearing compounds have intermolecular $_{(sp3)}$C–H…π interactions between the methylene moieties (benzene rings for phenoxy-bearing homologue) of the 2,7-substituents and the aromatic rings of the neighbouring molecules (aromatic ring: the naphthalene ring for butoxy-bearing homologue; the benzene rings for phenoxy-bearing homologue; the benzene ring of the benzyloxy group for benzyloxy-bearing homologue). Furthermore, the effective contribution of $_{(Ar)}$C–H…O=C interaction depends on the kind of the 2,7-substituents. The existence of intermolecular $_{(sp3)}$C–H…π interactions by 2,7-substituents is plausible to weaken the contribution of intermolecular $_{(Ar)}$C–H…O=C interactions to the molecular packing. The stability of the molecular accumulation in the crystal is rationally interpreted from the viewpoint of the complementary combination of $_{(Ar)}$C–H…O=C and $_{(sp3)}$C–H…π interactions. The order of the total stability of the crystals of these compounds estimated on the basis of melting point and density is in good agreement of the number of these superior interactions, $_{(Ar)}$C–H…O=C and $_{(sp3)}$C–H…π interactions.

*Corresponding Authors
Fax:+81-42-388-7601
E-Mail:aokamoto@cc.tuat.ac.jp
[a] Department of Organic and Polymer Materials Chemistry, Tokyo University of Agriculture and Technology, 2-24-16 Naka-machi, Koganei, Tokyo 184–8588, Japan

Introduction

Molecules of congested non-coplanarly-accumulated aromatic rings structure such as binaphthyl[1-4] and biphenyl[5-8] have attracted the interests of the chemists in organic chemistry and material chemistry fields as unique building blocks affording characteristic optic and electronic properties in addition to construction of chiral molecular scaffold[9-13] for organic synthesis.

To integrate information about stabilization factors of crystalline accumulation state of organic molecules is significantly important as fundamental study for development of such functional organic materials.

Recently, the authors have reported *peri*(1,8)-selective diaroylation of naphthalene derivatives.[14,15] According to the X-ray crystal structure analyses of the resulting 1,8-diaroylnaphthalene compounds, they have been proved to have characteristic structure of non-coplanarly aromatic-rings-accumulated structures.[16-18] As single molecular structure, two aroyl groups are attached to the naphthalene ring in an almost perpendicular fashion and oriented in an opposite direction. The highly congested circumstance leading non-coplanar spatial organization of aromatic rings accumulation of these molecules means the reduced development of conjugation inevitably resulting in relatively lower contribution of interaction originated from conjugated planes. Instead, it affords the opportunity to reveal the normally hidden interactions.[19,20]

The authors have intended to disclose the stabilization factors of non-coplanarly aromatic-rings-accumulated compounds through investigation of the spatial organization of single molecule, the molecular accumulation structure, and the non-bonding molecular interactions in 1,8-diaroylnaphthalene homologues. In the course of these

studies,[21-23] the authors have designed and synthesized 1,8-bis(4-fluorobenzoyl)-2,7-dialkoxynaphthalene compounds followed by determination of the crystal structures, e.g., 1,8-bis(4-fluorobenzoyl)-2,7-di*methoxy*naphthalene,[24] 2,7-di-*ethoxy*-1,8-bis(4-fluorobenzoyl)naphthalene,[25] 2,7-di*butoxy*-1,8-bis(4-fluorobenzoyl)naphthalene,[26] and 1,8-bis(4-fluorobenzoyl)-2,7-di*phenoxy*naphthalene.[27] Herein, the authors will report crystal structure of 2,7-di*benzyloxy*-1,8-bis(4-fluorobenzoyl)naphthalene and discuss the contribution of the non-bonding molecular interactions to stabilization of the molecular packing through comparison of the crystal structures of the methoxy-, ethoxy-, butoxy-, and phenoxy-bearing homologues in detail.

Results and Discussion

The synthetic routes of the benzyloxy-bearing compound (**2f**) and the homologues **2a**(OMe), **2b**(OEt), **2c**(OBu), and **2e**(OPh) are summarized in the Scheme. The benzyloxy-bearing compound (**2f**) was synthesized via nucleophilic substitution reaction of 1,8-bis(4-fluorobenzoyl)-2,7-dihydroxynaphthalene (**2d**) with bromomethylbenzene. The homologous 1,8-bis(4-fluorobenzoyl)naphthalene compounds bearing methoxy (**2a**), ethoxy (**2b**), butoxy (**2c**), and phenoxy-bearing (**2e**) groups at the 2,7-positions, were synthesized on the basis of literatures.[24-27]

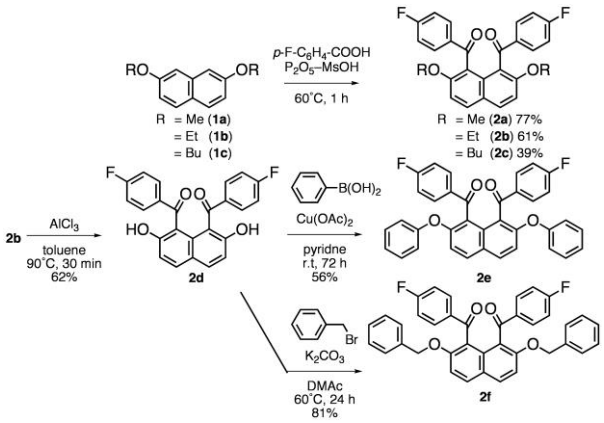

Scheme 1. Synthesis of 2,7-dibenzyloxy-1,8-bis(4-fluorobenzoyl)naphthalene and the homologous compounds.

Figure 1 gives ORTEP representation of the molecular structure of the benzyloxy-bearing compound (**2f**), as determined by the structured X-ray analysis.[28] In the benzyloxy-bearing compound (**2f**), two benzoyl groups at the 1,8-positions of the naphthalene ring system are aligned almost antiparallel, the naphthalene ring system makes dihedral angles of 71.25(9)˚ and 70.09(8)˚ with the benzene rings of the aroyl groups. The benzene rings of the benzyloxy groups are oriented in a perpendicular fashion to the benzene ring of the neighbouring aroyl groups [dihedral angles = 88.46(13)˚ and 87.06(12)˚]. The benzene rings of the benzyloxy groups are connected with the benzene rings of the neighbouring aroyl groups by *intra*molecular C–H…π interactions [2.89 Å and 2.97 Å]. Consequently, the dihedral angle between the benzene ring of the benzyloxy group and the benzene ring of the aroyl group is closer to 90˚ than that between the benzene ring of the aroyl group and the naphthalene ring.

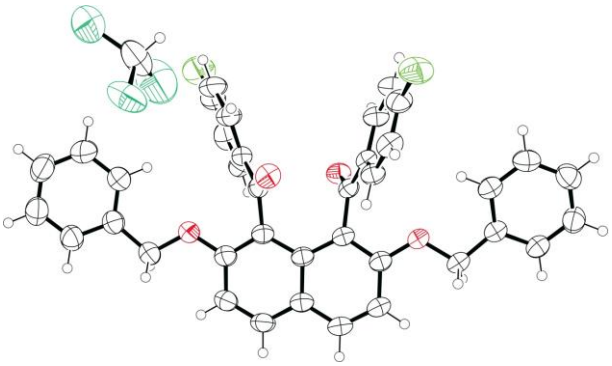

Figure 1. Molecular structure of 2,7-dibenzyloxy-1,8-bis(4-fluorobenzoyl)naphthalene, showing 50% probability displacement ellipsoids.

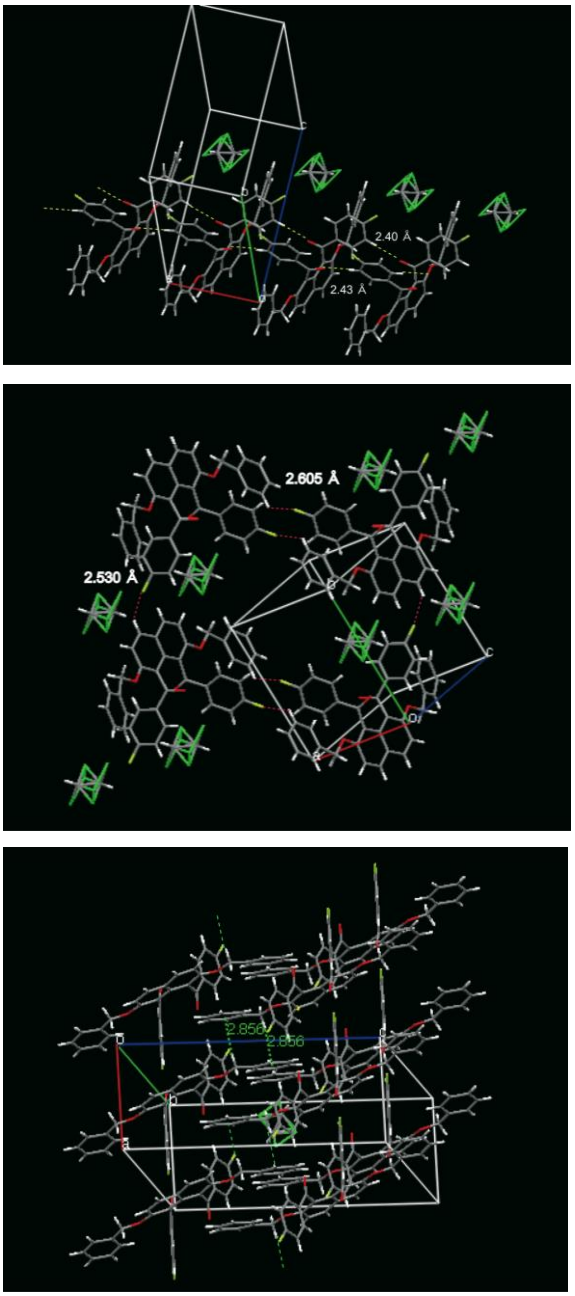

Figure 2. Observed molecular interactions of 2,7-dibenzyloxy-1,8-bis(4-fluorobenzoyl)naphthalene: C–H…O=C interactions between aromatic C–Hs and carbonyl groups (top), two types of C–H…F interactions (middle), and C–H…π interactions between methylene C–Hs and benzene rings of benzyloxy groups (bottom).

 DOI: 10.17628/ecb.2014.3.829-834

The chloroform molecule is disordered over two positions with site occupancies of 0.50 and 0.50.

In the crystal, three kinds of intermolecular interactions are observed, i.e., C–H…O=C interaction, C–H…F interaction, and C–H…π interaction. The duplicate C–H…O=C interactions between the benzene rings of the aroyl groups and the carbonyl groups arrange the molecules along *a*-axis (**Figure 2**, top).

The C–H…F interactions make molecular alignments along *bc*-diagonal (**Figure 2**, middle). The C–H…F interactions between the naphthalene rings and fluoro groups (2.530 Å) are formed between same enantiomeric isomers, whereas the duplicate C–H…F interactions between the benzene rings and the fluoro groups (2.605 Å) are connected with the counterpart isomers.

Furthermore, the C–H…π interactions between the methylene moieties and the benzene rings of the benzyloxy groups stack the benzyloxy groups into columnar structure along *a*-axis [C–H…*Cg* distance = 2.856 Å] (**Figure 2**, bottom).

These structural features of the benzyloxy-bearing compound (**2f**) are compared with the homologues. **Figure 3** displays ORTEP representation structures of homologues **2a**(OMe), **2b**(OEt), **2c**(OBu), and **2e**(OPh). **Table 1** shows the selected dihedral angles in the benzyloxy-bearing molecule and the homologues. The spatial structures of all compounds are apparently similar. The benzene rings of the aroyl groups are non-coplanarly situated to the naphthalene rings. However, these molecules are different each other from the viewpoint of the spatial symmetry. The difference in the dihedral angles between the benzene rings of the aroyl groups and the naphthalene ring in the molecule is smaller in the order of molecules **2a**(OMe), **2b**(OEt), **2f**(OBn), **2e**(OPh), and **2c**(OBu). On the other hand, the dihedral angles between the benzene rings are larger with decreasing of the difference, i.e., **2b**(OEt) < **2a**(OMe) < **2f**(OBn) < **2c**(OBu) < **2e**(OPh).

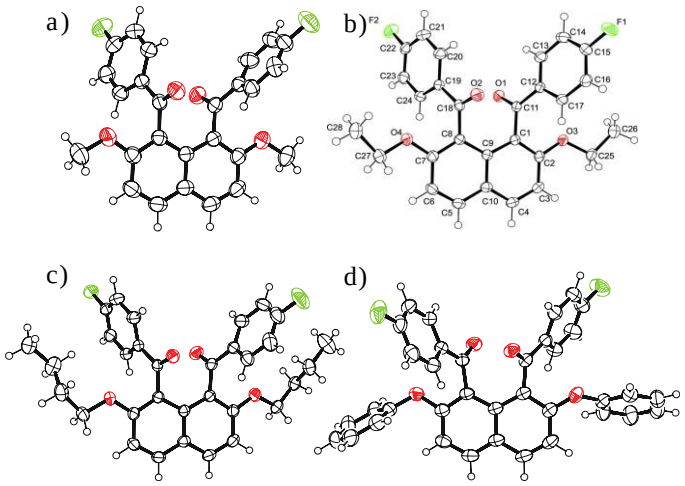

Figure 3. Molecular structures of 1,8-bis(4-fluorobenzoyl)naphthalene homologues bearing alkoxy/aryloxy groups at the 2,7-positions, showing 50% probability displacement ellipsoids: a) molecule **2a** (OMe), b) molecule **2b** (OEt), c) molecule **2c** (OBu), d) molecule **2e** (OPh).

Table 1. Selected dihedral angles of molecules **2a**, **2b**, **2c**, **2e**, and **2f**

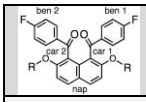	**2a** (OMe)	**2b** (OEt)	**2f** (OBn)	**2e** (OPh)	**2c** (OBu)
nap–ben1	66.87	70.24	71.23	72.07	74.54
nap–ben2	88.09	67.28	70.10	73.24	74.40
nap–ben3	-	-	20.33	62.49	-
nap–ben4	-	-	13.90	77.96	-
ben1–ben2	32.34	14.12	36.66	49.01	44.60
ben1–ben3	-	-	88.46	54.78	-
ben1–ben4	-	-	75.16	48.25	-
ben2–ben3	-	-	87.06	80.54	-
ben2–ben4	-	-	81.38	86.72	-
ben3–ben4	-	-	20.54	44.35	-
car1-nap	72.02	69.33	60.67	62.87	65.70
car2-nap	64.90	67.16	62.56	65.79	63.20
ben1-car1	14.55	2.89	14.96	17.58	12.42
ben2-car2	16.39	2.441	9.35	16.70	19.30

The abbreviations displayed in the left column are designated as aromatic ring moieties in molecules **2a**, **2b**, **2c**, **2e**, and **2f**, which are indicated on the molecular figure at the upper left of this Table.

Benzyloxy-bearing molecule **2f** and the homologue **2e**(OPh) have benzene rings in the 2,7-substituents. In the case of the benzyloxy-bearing molecule (**2f**), the benzene rings of the benzyloxy group are symmetrically situated against the benzene rings of the aroyl groups. Homologues **2a**(OMe) and **2e**(OPh) have apparently distinguishable structural feature from the others in view of the symmetry of the spatial property. Single molecular structure of compounds **2c**(OBu) and **2f**(OBn) can be regarded as a rather simple extension for homologue **2b**(OEt). Moreover, compound **2f**(OBn) seems to be more similar to compound **2c**(OBu) than compound **2b**(OEt) from the viewpoint of the spatial organization of single molecule.

Figure 4 and **Figure 5** show the crystal packing structures of the benzyloxy-bearing compound (**2f**) and the homologues when the naphthalene rings are placed in parallel fashion against the paper. Molecules are color-coded according to symmetry operation. There are two different types of atrope isomeric situations of the aroyl groups against the naphthalene ring, i.e., *R*,*R*-isomer and *S*,*S*-one. Pink-colored molecules and yellow-colored ones express *R*,*R*-isomers, whereas white-colored molecules and green-colored ones display *S*,*S*-isomers. The overlapping of *R*,*R*-isomers and *S*,*S*-ones seems to become smaller in the order of compounds **2a**(OMe), **2e**(OPh), **2b**(OEt), **2f**(OBn), and **2c** (OBu). In the cases of compounds **2b**(OEt), **2c**(OBu), and **2f**(OBn), column structure composed of same enantiomeric isomers seems to interpenetrate with the neighbouring columns composed of the counterpart isomers. These results are supposed the authors that molecules **2a**(OMe) and **2e**(OPh) form intermolecular interactions between *R*,*R*-isomer and *S*,*S*-isomer, whereas molecules **2b**(OEt), **2c**(OBu), and **2f**(OBn) have interactions between same enantiomeric isomers and those between the counterpart isomers in the crystals.

 DOI: 10.17628/ecb.2014.3.829-834

The observed non-bonding interactions in the molecular packing of the compounds are summarized in **Table 2**. The underlined C–H…X designates the highlighted interactions elucidated on the basis of shorter distance of two atoms less than the sum of the van der Waals radii. In the case of C–H…π interactions, the distances less than 3.0 Å are regarded as effective interactions. As the common features in these molecular packings, two kinds of non-bonding molecular interactions are observed, i.e., intermolecular $_{(Ar)}$C–H…O=C interactions between the carbonyl groups and the benzene rings of the aroyl groups (or the naphthalene ring) and intermolecular $_{(sp^3)}$C–H…π interactions between the methylene moieties of the 2,7-substituents and the naphthalene rings (or $_{(Ar)}$C–H…π interactions between the benzene rings of phenoxy groups). The former interactions are observed in all compounds. The latter interactions are observed in compounds **2c**(OBu), **2e**(OPh), and **2f**(OBn). The intermolecular $_{(Ar)}$C–H…O=C interactions are observed between *R,R*-isomers and *S,S*-isomers in compounds **2a** (OMe) and **2e**(OPh), whereas the interactions are formed between same enantiomeric isomers giving columnar structures for compounds **2b**(OEt), **2c**(OBu), and **2f**(OBn). The intermolecular C–H…π interactions are observed as the interpenetration of columns in compounds **2c**(OBu), **2e**(OPh) and **2f**(OBn). The intermolecular $_{(Ar)}$C–H…O=C interactions are weakened in the order of compounds **2b** (OEt) > **2e**(OPh), **2f**(OBn) > **2a**(OMe) >> **2c**(OBu) on the basis of distance between H and O atoms. On the other hand, the intermolecular $_{(sp3)}$C–H…π distances in compound are strengthened in the order of compounds **2c**(OBu) > **2f** (OBn) > **2e**(OPh). Therefore, the $_{(Ar)}$C–H…O=C interactions and $_{(sp3)}$C–H…π ones are regarded in complementary relationship for compounds **2c** (OBu), **2e**(OPh), and **2f**(OBn). Moreover, *intra*molecular C–H…π interactions between the benzene rings of the aroyl groups and the 2,7-substituents are formed in molecules **2c**(OBu) and **2f**(OBn).

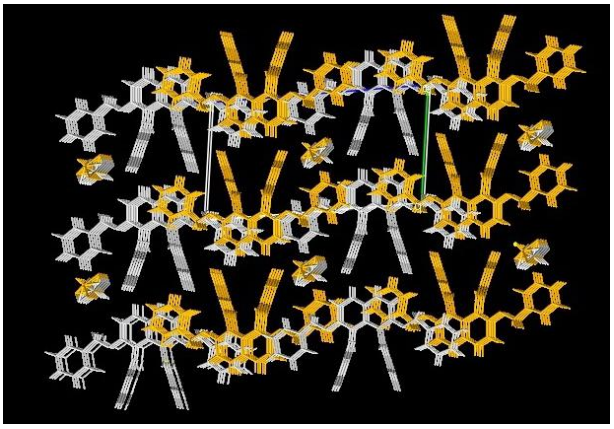

Figure 4. Molecular packing of 2,7-dibenzyloxy-1,8-bis(4-fluorobenzoyl) naphthalene compounds, viewed down *a*-axis.

The melting points lowers in the order of compounds **2b** (OEt) > **2a**(OMe)>> **2e**(OPh) >> **2f**(OBn) >> **2c**(OBu). The melting points of compounds **2b**(OEt) and **2a**(OMe) are nearly equal, however, there are three drastic droppings in the melting points between compounds **2a**(OMe) and **2e** (OPh), between compounds **2e**(OPh) and **2f**(OBn), and between compounds **2f**(OBn) and **2c**(OBu). The first dropping between compounds **2a**(OMe) and **2e**(OPh) indicates that existence of C–H…π interaction weakens the contribution of intermolecular C–H…O=C interaction to stabilize the molecular packing.

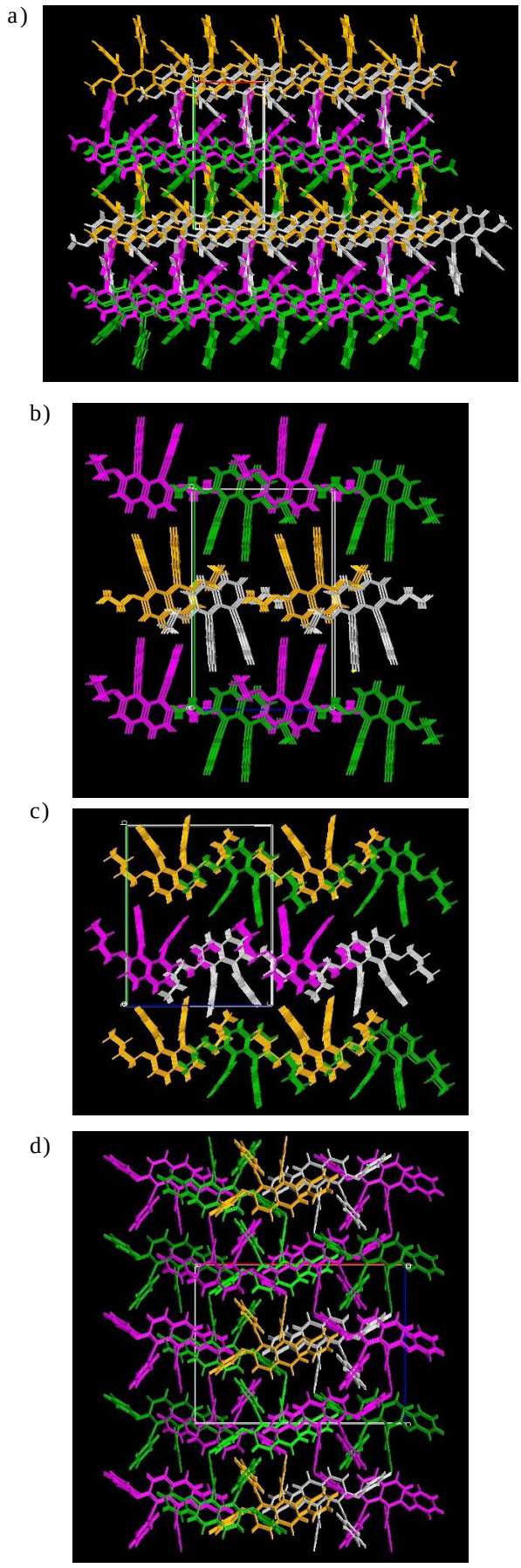

Figure 5. Molecular packing of 1,8-bis(4-fluorobenzoyl)naphthalene compounds bearing alkoxy groups at 2,7-positions: a) compound **2a** (OMe), b) compound **2b** (OEt), c) compound **2c** (OBu), d) compound **2e** (OPh).

 DOI: 10.17628/ecb.2014.3.829-834

Table 2. Non-bonding distances in molecules **2a**, **2b**, **2c**, **2e**, and **2f** with the melting point and the density

C–H...X	**2b** (OEt)	**2a** (OMe)	**2e** (OPh)	**2f** (OBn)	**2c** (OBu)
between same isomers					
$C–H_{Ar}…O=C_{car1}$	2.30	-	-	2.40	-
$C–H_{Ar}…O=C_{car2}$	2.37	-	-	2.43	2.70
$C–H_{nap}…F_1$	2.44	-	-	2.53	2.66
$C–H_{nap}…F_2$	-	-	-	-	2.50
between the counterpart isomers					
$C–H_{Ar}…O=C_{car1}$	-	2.54, 2.69	-	-	-
$C–H_{nao}…O=C_{car1}$			2.40	-	-
$C–H_{sp3}…O=C_{car1}$	-	-	-	-	2.64
$C–H_{Ar}…\pi_{2,7\text{-}Ar}$	none	none	2.80	-	none
$C–H_{sp3}…\pi_{2,7\text{-}Ar}$	none	none	-	2.86	none
$C–H_{sp3}…\pi_{nap}$	-	-	-	-	2.54
$C–H_{Ar}…F_2$	-	-	-	2.60	-
intramolecular					
$C–H_{sp3}…\pi_{1,8\text{-}Ar}$	-	-	-	-	2.79
$C–H_{2,7\text{-}Ar}…\pi_{1,8\text{-}Ar}$	none	none	-	2.89	none
$C–H_{2,7\text{-}Ar}…\pi_{1,8\text{-}Ar}$	none	none	-	2.97	none
M.p (˚C)	210	195	168	127	92
Density (g cm^3)	1.361	1.427	1.348	1.36	1.261

The second dropping between compounds **2e**(OPh) and **2f**(OBn) suggests that the contribution of the $_{(sp3)}$C–H…π interactions to the molecular packing competes with that of the $_{(Ar)}$C–H…O=C interactions. The third dropping between compounds **2f**(OBn) and **2c**(OBu) is essentially regarded as a continuation of the second dropping between compounds **2e**(OPh) and **2f**(OBn). In consequence of this, the *intra*molecular interaction character shown as *intra*molecular $_{(sp3)}$C–H…π interaction or $_{(2,7\text{-}Ar)}$C–H…π interaction seems to be more strengthened relatively to the intermolecular interaction character in the molecular packing of compounds **2f**(OBn) and **2c**(OBu). The number of C–H…F interactions seems to increase with emphasizing of the *intra*molecular interaction character. The relationship between melting point and molecular interactions is also in agreement with the density.

In 1,8-bis(4-fluorobenzoyl)naphthalene homologues, two aroyl groups are situated essentially perpendicularly against the naphthalene ring. The non-coplanarly accumulated-aromatic-rings structure indicates that 1,8-bis(4-fluorobenzoyl)naphthalene homologues avoid the internal steric repulsions *intra*molecularly in the first place. Furthermore, intermolecular $_{(Ar)}$C–H…O=C interactions are observed in the crystal packing of all of the compounds. The difference in the dihedral angles of two aroyl groups with the naphthalene ring is larger in the order of homologues **2a**(OMe) < **2b**(OEt) < **2f**(OBn) < **2e**(OPh) < **2c**(OBu). The order apparently correlates with the $_{(Ar)}$C–H…O=C distances. The relationship between the dihedral angle of the benzene rings and the $_{(Ar)}$C–H…O=C distance makes the authors naturally envision that formation of intermolecular $_{(Ar)}$C–H…O=C interactions is disturbed with increasing the *intra*molecular repulsion by replacing the 2,7-substituents. When the 2,7-substituents form effective interactions such as intermolecular $_{(sp3)}$C–H…π interactions, their contribution to the molecular packing precedes that of intermolecular $_{(Ar)}$C–H…O=C interactions. In the case of methoxy-bearing compound (**2a**), the melting point is high as same as ethoxy-bearing compound (**2b)**, whereas the $_{(Ar)}$C–H…O=C interactions is for weaker than ethoxy-bearing compound (**2b**). Small size of the methoxy groups at the 2,7-positions presumably allows the molecule to be in close proximity to the adjacent molecules. Under these circumstances, weak van der Waals interactions cooperatively contribute to stabilize the molecular packing. In consequence of this, alternative arrangement of *R*,*R*-isomer and *S*,*S*-one in compound **2a**(OMe) thus obtained might be sticky packed as suggested in density in Table 2.

Conclusively, the crystal structure of 2,7-dibenzyloxy-1,8-bis(4-fluorobenzoyl) naphthalene is determined. Through the comparison of the methoxy-, ethoxy-, butoxy-, and phenoxy group bearing homologues, 1,8-bis(4-fluorobenzoyl)naphthalene compounds bearing 2,7-dialkoxy/diaryloxy groups are analyzed to elucidate the governing factors that determine the structural feature in crystal. For these non-coplanarly aromatic-rings-accumulated compounds, the single molecular structure and the molecular packing feature are well interpreted that the whole stability is governed by intermolecular $_{(Ar)}$C–H…O=C and $_{(sp3)}$C–H…π interactions instead of π…π stacking interaction. The *intra*molecular avoidance of the steric hindrance at the first place presumably determines the single molecular structure. The *intra*molecular $_{(sp3)}$C–H…π interaction or $_{(2,7\text{-}Ar)}$C–H…π interaction contributes single molecular structure more stable. In other words, absence of *intra*molecular $_{(sp3)}$C–H…π interaction or $_{(2,7\text{-}Ar)}$C–H…π interaction in single molecular structure directly means larger contribution or emphasis of the intermolecular interaction character in the molecular accumulation structure. The mode of overlapping feature to give columnar structure is also determined at the same manner. Under the allowance of above requisites, the $_{(Ar)}$C–H…O=C interactions are placed to the maximum number in the crystalline molecular accumulation. This explanation is in good agreement with the melting point and the density of these crystals.

Experimentals

All reagents were of commercial quality and were used as received. Solvents were dried and purified using standard techniques.[29] 2,7-dimethoxynaphthalene (**1a**) and 2,7-diethoxynaphthalene (**1b**) were prepared according to literatures.[30, 31]

Measurements

^{1}H NMR spectra were recorded on a JEOL JNM-AL300 spectrometer (300 MHz) and a JEOL ECX400 spectrometer (400 MHz). Chemical shifts are expressed in ppm relative to internal standard of Me_4Si (δ 0.00). ^{13}C NMR spectra were recorded on a JEOL JNM-AL300 spectrometer (75 MHz). Chemical shifts are expressed in ppm relative to internal standard of $CDCl_3$ (δ 77.0). IR spectra were recorded on a JASCO FT/IR-4100 spectrometer. Elemental analyses were performed on a Yanaco CHN CORDER MT-5 analyzer.

High-resolution FAB mass spectra were recorded on a JEOL MStation (MS700) ion trap mass spectrometer in positive ion mode.

X-ray Crystallography

For the crystal structure determination, the single-crystal of the compound **2e** was used for data collection on a four-circle Rigaku RAXIS RAPID diffractometer (equipped with a two-dimensional area IP detector). The graphite-monochromated Cu Kα radiation (λ = 1.54187 Å) was used for data collection. The lattice parameters were determined by the least-squares methods on the basis of all reflections with $F^2>2\sigma(F^2)$. The data collection and cell refinement were performed using *PROCESS-AUTO* software. The data reduction was performed using *CrystalStructure*. The structures were solved by direct methods using *SIR2004* and refined by a full-matrix least-squares procedure using the program *SHELXL97*. All H atoms were found in a difference map and were subsequently refined as riding atoms, with the aromatic C–H = 0.95 Å and methyl C–H = 0.98 Å, and with $U_{iso}(H) = 1.2U_{eq}(C)$.

Synthesis of 2,7-dibenzyloxy-1,8-bis(4-fluorobenzoyl) naphthalene (2f)

To a 10 mL flask, 1,8-bis(4-fluorobenzoyl)-2,7-dihydroxynaphthalene (**2d**, 1.0 mmol, 404 mg), benzylbromide (5.0 mmol, 855 mg), potassium carbonate (5.0 mmol, 691 mg), DMAc (2.0 mL) were placed. The reaction mixture was stirred at 60 °C for 24 h. After the reaction, the mixture was extracted with AcOEt. The combined extracts were washed with brine. The organic layers thus obtained were dried over anhydrous $MgSO_4$. The solvent was removed under reduced pressure to give cake. The crude product was purified recrystallization from $CHCl_3$–MeOH (81% isolated yield). Furthermore, the isolated product was crystallized from methanol to give single-crystal.

^{1}H NMR δ (300 MHz, $CDCl_3$) : 5.00 (4H, s), 6.89-6.92 (4H, m), 7.01 (4H, t, *J*= 8.2 Hz) 7.16-7.20 (6H, m), 7.22 (2H, d, *J*= 8.9 Hz), 7.76 (4H, dd, *J*= 8.2, 5.4 Hz), 7.91 (2H, d, *J*= 8.9 Hz) ppm; ^{13}C NMR δ (75 MHz, $CDCl_3$) :70.81, 112.32, 115.13 (d, $^2J_{C\text{-}F}$= 22.4 Hz), 121.60, 125.70, 126.59, 127.71, 128.26, 130.24, 131.70 (d, $^3J_{C\text{-}F}$= 9.3 Hz), 132.25, 135.47 (d, $^4J_{C\text{-}F}$= 2.8 Hz), 136.10, 155.45, 165.56 (d, $^1J_{C\text{-}F}$= 253.6 Hz), 195.71 ppm; IR (KBr) : 1656 (C=O), 1595, 1505, 1454 (Ar, naphthalene), 1236 (=C — O — C) cm^{-1}; HRMS (m/z): $[M+H]^+$ calcd for $C_{38}H_{27}F_2O_4$, 585.1877 found, 585.1854. m.p.=127˚C

Acknowledgement

The authors express their gratitude to Professor Keiichi Noguchi, Instrumentation Analysis Center, Tokyo University of Agriculture & Technology, for his technical advice. This work was partially supported by Ogasawara Research Promotion Grant, Tokyo, Japan.

References

[1]Capici, C., Gattuso, G., Notti, A., Parisi, M. F., Bruno, G., Nicolo, F., Pappalardo, S., *Tetrahedron Lett.*, **2011**, 52, 1351.

[2]Deria, P., Von Bargen, C. D., Olivier, J-H., Kumbhar, A. S., Saven, J. G., Therien, M. J., *J. Am. Chem. Soc.*, **2013**, *135*, 16220.

[3]Hatano, S., Horino, T., Tokita, A., Oshima, T., Abe, J., *J. Am. Chem. Soc.*, **2013**, *135*, 3164.

[4]Yu, S., Plunkett, W., Kim, M., Pu, L., *J. Am. Chem. Soc.*, **2012**, *134*, 20282.

[5]Homs, A., Escofet, I., Echavarren, A. M., *Org. Lett.*, **2013**, *15*, 5782.

[6]Mata, G., Luedtke, N. W., *Org. Lett.*, **2013**, *15*, 2462.

[7]Fernandez-Blazquez, J. P., Bello, A., Perez, E., *Macromolecules*, **2007**, *40*, 703.

[8]Yamaguchi, I., Choi, B-J., Koizumi, T., Kubota. K., Yamamoto, T., *Macromolecules*, **2007**, *40*, 438.

[9]Wang, L., Dong, H., Li, Y., Xue, C., Sun, L-D., Yan, C-H., Li, Q., *J. Am. Chem. Soc.*, **2014**, *136*, 4480.

[10]Kano, T., Shirozu, F., Maruoka, K., *J. Am. Chem. Soc.*, **2013**, *135*, 18036.

[11]Akai, Y., Yamamoto, T., Nagata, Y., Ohmura, T., Suginome, M., *J. Am. Chem. Soc.*, **2012**, *134*, 11092.

[12]Trost, B., Bringley, D. A., Silverman, S. M., *J. Am. Chem. Soc.*, **2011**, *133*, 7664.

[13]Morisue, M., Fukui, H., Shimizu, M., Inoshita, K., Morisaki, Y., Chujo, Y., *Tetrahedron Lett.*, **2014**, *55*, 271.

[14]Okamoto, A., Yonezawa, N., *Chem. Lett.*, **2009**, *38*, 914.

[15]Okamoto, A., Mitsui, R., Yonezawa, N., *Chem. Lett.*, **2011**, *40*, 1283.

[16]Nakaema, K., Noguchi, K., Okamoto, A., Yonezawa, N., *Acta Cryst.*, **2008**, *E64*, o2497.

[17]Isogai, A., Tsumuki, T., Murohashi, S., Okamoto, A., Yonezawa, N., *Acta Cryst.*, **2013**, *E69*, o71.

[18]Sasagawa, K., Sakamoto, R., Hijikata, D., Yonezawa, N., Okamoto, A., *Acta Cryst.*, **2013**, *E69*, o651.

[19]Mohri, S., Yoshiwaka, S., Isozaki, K., Yonezawa, N., Okamoto, A., *Acta Cryst.*, **2013**, *C69*, 1541.

[20]Okamoto, A., Nagasawa, A., Yonezawa, N., *Eur. Chem. Bull.*, **2014**, *3*, 263.

[21]Okamoto, A., Nagasawa, A., Siqingaowa, Yonezawa, N., *Cryst. Struct. Theor. Appl.*, **2012**, *1*, 121.

[22]Okamoto, A., Nagasawa, A., Yonezawa, N., *Eur. Chem. Bull.*, **2014**, *3*, 13.

[23]Okamoto, A., Watanabe. S., Nakaema, K., Yonezawa, N., *Cryst. Struct. Theor. Appl.*, **2013**, *2*, 141.

[24]Watanabe, S., Nagasawa, A., Okamoto, A., Noguchi, K., Yonezawa, N., *Acta Cryst.*, **2010**, *E66*, o329.

[25]Mouri, S., Hijikata, D., Isozaki, K., Yonezawa, N., Okamoto, A., *Acta Cryst.*, **2013**, *E69*, o637.

[26]Hijikata, D., Sasagawa, K., Yoshiwaka, S., Okamoto, A., Yonezawa, N., *Acta Cryst.*, **2012**, *E68*, o3287.

[27]Hijikata, D., Sasagawa, K., Yoshiwaka, S., Okamoto, A., Yonezawa, N., *Acta Cryst.*, **2012**, *E68*, o3246.

[28]CCDC-1016938 contains the supplementary crystallographic data for this paper. These data can be obtained free of charge from The Cambridge Crystallographic Data Centre via www.ccdc.cam.ac.uk/data_request/cif.

[29]Armarego, W.L. F., Perrin, D. D., "*Purification of Laboratory Chemicals",* Fourth edition, Reed Educational and Professional Publishing Ltd, Oxford, **1996**.

[30]Domasevitch, K. V., Solnsev, P. V., Krautscheid, H., Zhylenko, I. S., Rusanov, E. B., Chernega, A. N., *Chem. Commun.*, **2012**, *48*, 5847.

[31]Kuwano, R.,Morioka, R., Kashiwabara, M., Kameyama, N., *Angew. Chem., Int. Ed*., **2012**, *51*, 4136.

Received: 14.06.2014.
Accepted: 03.08.2014.

IN–VITRO INHIBITION OF MINERALIZATION OF URINARY STONE FORMING MINERALS BY GLYCOLIC ACID

Ashish Kumar[a] and Basabi Mahapatra[b]

Keywords: urinary stone; urolithiasis; flow static and dynamic models; in vitro inhibition; glycolic acid

The inhibition of mineralisation of urinary stone forming minerals by glycolic acid has been investigated. The inhibition efficiency of different concentration was studied. Increased intake of glycolic acid would be helpful in urinary stone prophylaxis. Glycolic acid acts as 'protecting agent'. It has been suggested that 'proteceting agents' perhaps withdraw the metal cation from solution, and thus increase the degree of 'supersaturation and it is to be expected that their addition to solution containing such ions would cause a reduction in the rate of crystal growth. Crystal growth is a very complex process since both the surface and the super saturation varies continuously throughout the period of the growth.

* Corresponding Authors
E-Mail: ashpwc2008@rediffmail.com; basabi2011@gmail.com
[a] Dept. of Chemistry, Patna Women's College, atna University, Patna, India
[b] Dept. of Chemistry, Magadh Mahila College, Patna University, Patna, India

Introduction

A number of people suffer from problems due to urinary stones (calculi). In India 12 % of the population is expected to have urinary stones, out of which 50 % may end up with loss of kidneys or renal damage. Also nearly 15% of the population of northern India suffers from kidney stones. Urinary stone contains both crystalloid and colloid components. The crystalloid components are mainly calcium oxalate, calcium phosphate, calcium carbonate, magnesium ammonium phosphate, uric acid and cystine. Stone formation is apparently related to the level of urinary inhibitors of calculogenesis in urine. Human urine is known to contain some protective compounds called inhibitors. These compounds sequestrate the stone and prevent the supersaturation of urine. In present work we have estimated the inhibition efficiency of glycolic acid on the mineralisation of calcium oxalate, calcium carbonate and calcium phosphate. Glycolic acid is easily available, non-toxic and does not have any side effects.

Experimental

Materials and Methods

All the chemicals used were of AR Grade. Crystalloid forming solutions viz. solution of disodium oxalate, sodium carbonate and trisodium phosphate were prepared in distilled water. Solution of 0.01 M and 0.001 M glycolic acid were also prepared in distilled water. Four experimental model namely 'Simultaneously flow static model (s.s.m), Simultaneously flow dynamic model (s.d.m), reservoir static model (r.s.m) and reservoir dynamic model (r.d.m) were designed.[1] Simultaneously blank experiments were also carried out for evaluating the inhibition efficiency of inhibitor. All the experiments were conducted at room temperature. Percentage efficiency of inhibitor was calculated.[4]

Results and Discussion

The inhibition efficiency of 0.01 M and 0.001 M glycolic acid had been investigated in different models. The results were recorded in table and Figs. 1 and 2.

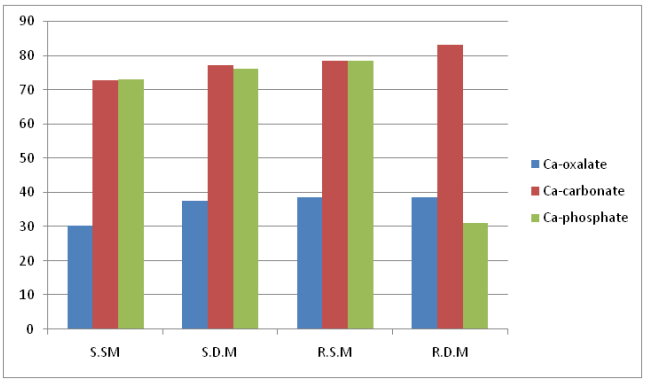

Figure 1. The inhibition efficiency of 0.01 M glycolic acid

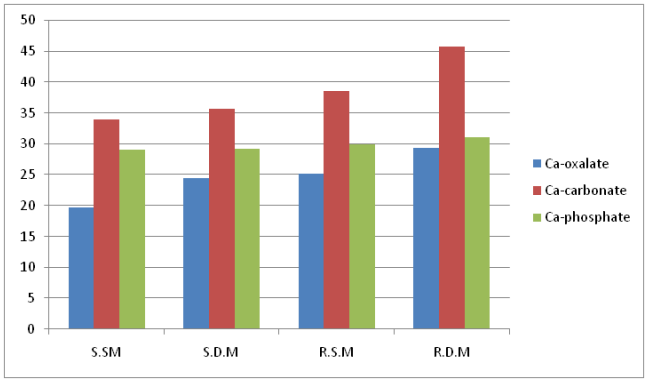

Figure 2. The inhibition efficiency of 0.001 M glycolic acid

Suspension of known weight of calcium phosphate, calcium oxalate and calcium carbonate in 100 ml deionized conductivity water were titrated conductometrically against the aqueous solution of glycolic acid. Specific conductivity for each set of titration was plotted against the volume of titrant added and the breaks in the curves were located.

Table 1. Inhibition efficiency (%) of 0.01 M and 0.001 M gylcolic acid on in vitro mineralization of urinary stone components in simultaneously flow static model (s.s.m), simultaneously flow dynamic model (s.d.m), reservoir static model (r.s.m) and reservoir dynamic model (r.d.m

Stone forming minerals	Simultaneously flow static model		Simultaneously flow dynamic model		Reservoir static model		Reservoir dynamic model	
	0.01 M	0.001 M	0.01 M	0.001 M	0.01 M	0.001 M	0.01 M	0.001 M
Calcium oxalate	30.3	19.7	37.6	25.5	38.6	25.2	38.6	29.4
Calcium carbonate	72.8	34.0	77.3	35.7	78.7	38.6	83.3	45.8
Calcium phosphate	73.1	29.1	76.3	29.2	78.5	29.9	81.8	31.1

In all the titrations specific conductivity continued to increase with the addition of titrant, however, the rate of increase of specific conductivity decreased at the break point (Figure 3a-c).

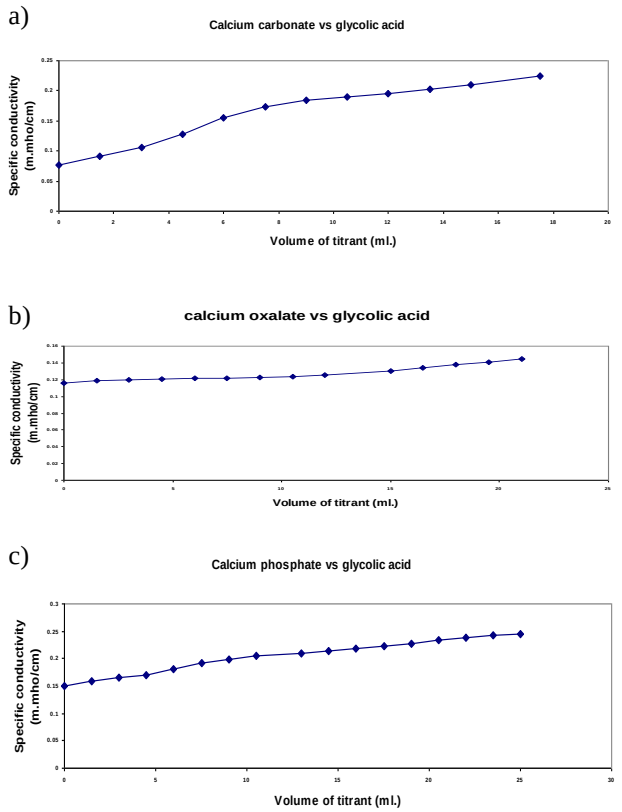

Figure 3. Titration curves of calcium salts a) calcium carbonate; b) calcium oxalate; c) calcium phosphate

Suspension of known weight of calcium phosphate, calcium oxalate and calcium carbonate in 100 ml deionized conductivity water were titrated conductometrically against the aqueous solution of glycolic acid (titation curves can be sene in the Supplementary Material). Specific conductivity for each set of titration was plotted against the volume of titrant added and the breaks in the curves were located. In all the titrations specific conductivity continued to increase with the addition of titrant, however, the rate of increase of specific conductivity decreased at the break point .

Study of the Table 1 and Figs. 1 and 2 suggests that glycolic acid is moderate to good inhibitor of calcium oxalate, calcium carbonate and calcium phosphate mineralisation. Sequestering of this insoluble calcium salts by glycolic acid might be due to effective single or mixed ligands chelation[5-6] by the hydroxyl acid present in them.

The hydroxyl acids are expected to form metal ion complexes with calcium. The presence of hydroxyl acids in urine may decrease the amount of ionised calcium available for calcium oxalate precipitate. Relatively poor inhibition of mineralisation of calcium oxalate, calcium carbonate and calcium phosphate precipitate by glycolic acid might be due to higher pka value of carbonic acid leading to replacement and precipitation of calcium salts of inhibitors rather than soluble mixed chelation.[7-8] Calcium oxalate is a stubborn constituents of urinary calculi being highly insoluble. The inhibition efficiency of oxalate is less than as compared to carbonate and phosphate.

A comparative study of different model indicates that the r.s.m model is the most effective one in the inhibition of calcium oxalate, calcium carbonate and calcium phosphate mineralisation. This might be due to mass effect.[9-10] An ab-initio presence of large concentration of inhibition (in the reservoir) coupled with continuous stirring might be effectively chelating the calcium ion and screening from precipitating anions like oxalate, carbonate and phosphate.

A comparative study also suggests that the inhibition efficiency decreases with a decrease in the strength of inhibitor solution. As the concentration of inhibitor decreases, the equilibrium might be favouring the precipitate of insoluble salts. lesser the inhibitor present less calcium ion be trapped as calcium-inhibitor complex and more calcium ions will be free for precipitate as insoluble salt. Our present study suggests that the regular intake of glycolic acid would be helpful in urinary stone prophylaxis.

References

[1]Kumar, A., Mahapatra (Choudhary), B., *Acta Ciencia Indica*, **2011,** *37C(4)*, 321.

[2]Kumar, A., Mahapatra (Choudhary), B., *Bull. Pure Appl. Sci.*, **2011**, *30C(1-2)*, 31-38.

[3]Curhan, C. C., Willett, W. C., Speizer, P. D. Stampfer, M. J., *Ann. Int. Med.*, **1998**, *128*, 534.

[4]Parman, M. S., *Brit. Med. J.*, **2004**, *328*, 1420.

[5]Das, I., Gupta, S. K., Pandey, V. N. and Shoeb, A. A., J. Cryst. Growth, **2004**, *267*, 654.

[6]Smith, L. H., Meyer J. L. and McCall, J. T., *Int. Symp. Renal Stone Res., Karger, Basel*, **1973**, 318.

[7]Stamatelou, K. K., Francis, M. E., Jones, C. A., Nyberg, L. M. Jr., and Curhan, G. C., *Kidney Int.*, **2003**, *63*, 1817.

[8]Seltzer, M. A. Low, R. K. Mc Donald, M., Shami, G.S. and Stolter, M. L., *J. Urol.*, 1996, 1156, 907.

[9]Mayer, J. L. and Smith, L. H., *Invest. Urol.*, **1975**, *13*, 36.

[10]Selvam, R., Kalaiselvi, P., Govindaraj, A., Murugan, V. B. and Sathish Kumar, A. S., *Pharmacol. Res*., **2001**, *43*, 89.

[10]http:// www.newbeingnutrition.com/

[11]Munoz, J. A. and Valiente, M., *Urol. Res*., **2005**, *33(4)*, 267.

[12]Joshi, V. S., Parekh, B. B., Joshi, M. J. and Vaidya, A. B., *J. Cryst. Growth*, **2005**, *275*,1403.

Received: 11.05.2014.
Accepted: 08.08.2014.

ADSORPTION BEHAVIOUR OF *REACTIVE RED 2* (RR2) TEXTILE DYE ONTO CLAYS: EQUILIBRIUM AND KINETIC STUDIES

Manpreet Kaur[a] and Monika Datta[b]*

Keywords: adsorption; adsorption kinetics; cation exchange; montmorillonite; organophilic clays; zeta potential

Batch adsorption studies were carried out to investigate the adsorption behaviour of textile dye- *Reactive red 2* (RR2) from aqueous solution onto montmorillonite (Mt) clay and organophilic Mt clays. The monovalent organic cations- cetyltrimethylammonium (CTA^+) and cetylpyridinium (CP^+) were exchanged for the metal cations in montmorillonite clay to prepare the organophilic Mt clays- CTA–Mt and CP-Mt. The synthesis of these organophilic clays was confirmed by X-Ray diffraction (XRD), Fourier Transformed Infra Red (FTIR), specific surface area (BET) and zeta potential techniques. The adsorption affinity of Mt, CTA-Mt and CP-Mt for RR2 was investigated as a function of pH of the aqueous dye solution, contact time, initial dye concentration and adsorbent dosage. The adsorption data obtained was fitted to the Langmuir, Freundlich and Temkin adsorption models and it was found that Langmuir adsorption isotherm yielded the most favourable representation of the adsorption behaviour of RR2. The adsorption kinetics of RR2 has been studied in terms of pseudo-first-order, pseudo-second-order and intraparticle diffusion processes. It was found that the pseudo-second-order mechanism is predominant in the present adsorption system suggesting chemisorption of the dye.

*Corresponding Authors
E-Mail: monikadatta_chem@yahoo.co.in
[a] Department of Chemistry, University of Delhi, Delhi-110007, India. E-mail:manpreetkaur.chem@gmail.com
[b] Department of Chemistry, University of Delhi, Delhi-110007, India

INTRODUCTION

Treatment of a highly colored aqueous effluent from textile dye house industries has attracted the attention of environmentalists, technologists as more than 60 % of the world dyes production is consumed by textiles industries.[1] The classes of dyes mostly used by the textile industry are azo dyes containing reactive group.[2] Fibre reactive dyes are colored organic compounds capable of forming covalent bonds between reactive group of the dye molecule and nucleophilic groups on the polymer chain within the fibre. Reactive dyeing of cotton is currently the most widespread textile dyeing process in the world. Approximately 80% of the reactive dyes are based on the azo chromogen.[3]

Reactive dyes react with cellulosic fibres (cotton) under alkaline conditions. However, because of the competition between the Cell-O^- from the cellulose fibres and hydroxide (OH^-) ions present in the dye bath at elevated pH values, a portion of the dye reacts with OH^- ions instead of the Cell-O^- ions. Under typical dyeing conditions, approximately 50 % of the dye remains in the dyebath in its hydrolyzed form which has no further affinity for the fiber.[4] Thus reactive dyes have a low utilization degree compared to other types of dyestuff because of undesirable hydrolysis reaction.

Reactive dye wastewater is characterized by poor biodegradability, thus conventional wastewater treatment is not suitable.[5] Thus both biological and physical/chemical methods have been employed for dye removal, the former have not been very successful, due to the essential non-biodegradable nature of most of these dyes.[6,7] The physical/chemical methods that have been proven to be successful are adsorption, coagulation/ flocculation, membrane filtration, chemical oxidation and electrochemical treatment.[8]

Currently the adsorption technique is proved to be an effective and attractive process for the treatment of these dye bearing wastewaters.[9,10] The use of activated carbon as an adsorbent is still very popular because of its extended surface area, micro porous structure, high adsorption capacity and high degree of surface reactivity. However, regeneration or reuse of carbon results in a steep reduction in performance, and efficiency becomes unpredictable.[11]

Because of the abundance in most continents of the world, low cost, high specific surface area, potential for ion exchange, high sorption capability etc., clays such as montmorillonite, bentonite, and sepiolite are being considered as low cost alternative adsorbents.[12,13] Among many kinds of clay minerals, montmorillonite (Mt) clays have often been used in the remove of organic pigments and dyes due to their high surface area and high cation exchange capacity. Montmorillonite is a 2:1 smectite clay having chemical composition-$M^+_{x+y}(Al_{2-x})(OH)_2(Si_{4-y}Al_y)O_{10}$. The isomorphous substitution of Al^{3+} for Si^{4+} in the tetrahedral layer and Mg^{2+} for Al^{3+} in the octahedral layer results in a net negative surface charge which is balanced by inorganic exchangeable cations (Na^+, Ca^{2+}, etc.). These highly hydrated ions are responsible for the hydrophilic nature of the clay.[14-16]

However, Mt adsorbs the anionic dyes only onto the external broken-bonds surface in very small amounts. Therefore, in order to improve their adsorption capacities for anionic dyes, the surface of Mt needs to be modified by a suitable approach. The exchange of inorganic ions (Na^+, Ca^{2+}, etc.) by the intercalation of organic cations through ion exchange phenomenon makes the clay organophilic in nature[17,18] as well as renders the clay surface positively charged when treated in excess of cation exchange capacity of clay. The intercalation of the organic cation in the clay layers results in an increase in the interlamellar spacing which results in exposure of new sorption sites in the clay. The characteristics of these so-called organophilic clays can be changed

by variation of surfactant properties,[19] such as alkyl chain length, number and branches.[20,21] Although the modification of clays with surfactants increases their cost significantly, the resultant increase in adsorption capacity may still make surfactant-modified clays cost effective. So clay and modified clay based derivatives may prove to be promising adsorbents.

The present work is aimed to study the adsorption capacity and mechanism of removal of anionic dye *Reactive red 2* (RR2) by Mt and organophilic Mt clays from aqueous solution. The reason behind selecting C.I. *Reactive red 2* dye in the present work, is its extensive use in textile industry for dyeing cellulose fiber, its high solubility and its persistent nature once it is discharged into the water bodies. Moreover, only 60-70% of this dye reacts with the fiber during dyeing, the remaining gets hydrolyzed and is released into the water bodies. Also, *reactive red 2* is a non biodegradable dye because of the recalcitrant nature of the azo group.

The removal of RR2 from aqueous solutions by the clays was investigated with respect to pH of the aqueous dye solution, contact time, initial dye concentration and adsorbent dosage. The experimental data were evaluated by applying different kinetic models to understand the dye adsorption behaviour.

EXPERIMENTAL

Materials

All the reagents used in the present work were of analytical grade and were used without any further purification. The clay montmorillonite used in the present work was obtained from Sigma Aldrich, St. Louis, U.S.A. The cation exchange capacity (CEC) of the clay was determined by ion exchange method[22] and was found to be 47.83 mEqv./100 g. The textile dye - *Reactive red 2* (C.I. 18200) (empirical formula - $C_{19}H_{10}Cl_2N_6Na_2O_7S_2$, mol. wt. 615.33 g mol^{-1}, dye content – 40 % and absorbance maxima - 537 nm was obtained from Sigma Aldrich, St. Louis, U.S.A. The surfactant N-cetylpyridiniumchloride monohydrate ($C_{21}H_{38}ClN.H_2O$, mol.wt. 358.01 g mol^{-1}) was obtained from E. Merck, Germany and cetyltrimethylammonium bromide, ($[CH_3(CH_2)_{15}](CH_3)_3$ NBr, mol. wt. 364.47 g mol^{-1}) was obtained from BDH, England. For the entire experimental process, double distilled water was used.

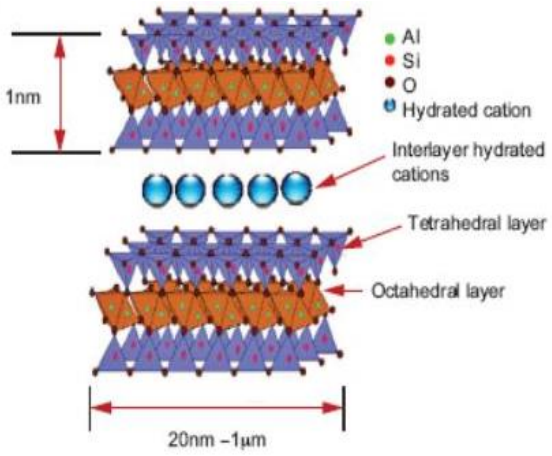

Structure of montmorillonite (Mt) clay

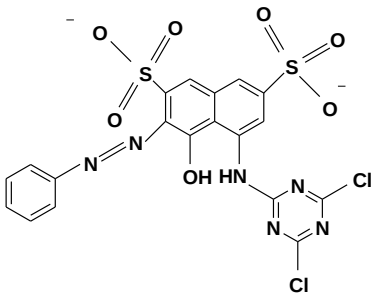

Chemical structure of C.I. *reactive red 2*

Synthesis of organophilic clays

Organophilic clays were prepared via a cation-exchange process employing a modification of the reported procedure.[23] To a known amount of Mt in 100 ml of double distilled water 1% aqueous solution of organic cation was gradually added with continuous stirring over a period of 5-6 hours. The resultant clay was centrifuged at 8000 rpm using REMI R24 centrifuge and washed with double distilled water till complete removal of halide ions and then dried in an oven at 80 °C. The organophilic clays thus prepared are designated as CP-Mt and CTA-Mt.

Characterization of the synthesized organophilic clays

X-Ray diffraction (XRD) patterns of Mt, CP-Mt and CTA-Mt were recorded using Cu Kα radiation (n =1.54056 Å) on a Philips X′ Pert-PRO MRD system operating at 2θ values between 2–50°. The system was operated at 50 kV and 100 mA in continuous scan mode with a scanning speed of 0.008 ° sec^{-1}. The FT-IR spectra were recorded using a Perkin-Elmer FT-IR spectrophotometer. The spectra of the samples contained in a KBr matrix were recorded at room temperature over the wavenumber range 4000–400 cm^{-1} employing a total of 64 scans at a resolution of 4 cm^{-1}. The specific surface areas of the clay and the organophilic clays calculated by the BET method were determined using an ASAP - Micromeritics 2420 instrument employing nitrogen as the adsorbate at −196 ºC. The zeta potential measurements were performed using Malvern zetasizer. All the measurements were done with samples dispersed in double distilled water for zeta potential measurements.

pH stability study of the aqueous RR2 dye solution

To investigate the pH stability of the aqueous RR2 dye solution, the aqueous dye solutions (20 $mgdm^{-3}$ concentration) in the pH range 2 to 10 were prepared. The pH of the solutions was maintained using 0.1N and 0.01N HCl/NaOH solutions using pH 510 cyberscan pH meter (Eutech instruments). The solutions thus prepared were analysed spectrophotometrically at 537 nm.

Adsorption equilibrium studies of RR2 dye on clay and organophilic clays

Employing the batch method, the adsorption behaviour of the dye on Mt, CP-Mt and CTA-Mt was investigated as a function of

- ✓ pH of the aqueous dye solution
- ✓ contact time for batch adsorption
- ✓ concentration of the dye solution
- ✓ adsorbent dosage

All adsorption experiments were performed using 0.1 g of each adsorbent at 30 °C. To investigate the effect of pH on the adsorption efficiency, the aqueous dye solutions (50 mg dm^{-3}concentration) having pH values 2, 4, 6, 8 and 10 were prepared. Each one of these solutions (50 ml) was treated with the adsorbents for a fixed period of 25 minutes. To study the effect of contact time on the adsorption efficiency, 50 ml of 50 mg $dm^{-3}$of the aqueous dye solution maintained at pH 6.0 were treated with the adsorbents over a period of 5 to 120 minutes. To investigate the effect of initial dye concentration on adsorption efficiency, aqueous dye solutions having 40 mg dm^{-3} to 280 mg/dm^3 concentration range were prepared. Each one of these solutions (50 ml) maintained at pH 6.0 was treated with the adsorbents for a fixed time period of 25 minutes. To study the effect of adsorbent dosage on adsorption efficiency, 50 ml of 300 mg $dm^{-3}$of the aqueous dye solution maintained at pH 6.0 were treated with 0.1 to 0.3 g of the adsorbent dosage for a period of 25 minutes. After each set of experiment, the adsorbent was recovered by centrifugation at 10 000 rpm for 20 min using an REMI R24 centrifuge and the supernatant thus obtained was used for the estimation of the unadsorbed dye in the solution by spectrophotometric method. The absorbance was measured at 537 nm and the concentration of the unadsorbed dye was determined from the Beer's Lamberts plot at 537 nm with the percentage of the dye adsorbed, β and the amount of dye adsorbed q_e (mg g^{-1}) being calculated using equation (1) and (2) respectively.

$$\beta = \frac{(C_i - C_e)}{C_i} \times 100 \quad (1)$$

where,

C_i is the initial concentration (mg dm^{-3}) of the dye solution and

C_e is the concentration of the dye (mg dm^{-3}) in the supernatant at the equilibrium stage.

$$q_e = \frac{(C_i - C_e)V}{m} \quad (2)$$

where,

V is the volume of the dye solution (dm^3) and

m is the mass of adsorbent employed (g).

Kinetic modelling

The kinetic studies of the dye adsorption were carried out with respect to the initial concentration of the dye solution at 30 °C. Three different concentrations of the dye – 50, 100 and 160 mg dm^{-3} were prepared and 50 dm^3 of each of these solution maintained at pH 6.0 was treated with 0.1g of the adsorbents for a time period of 5 to 60 minutes.

RESULTS AND DISCUSSION

Characterization of the synthesized organophilic clays

X-Ray diffraction (XRD) studies

To confirm the intercalation of CP^+ and CTA^+ in the interlayer region of Mt, XRD studies were performed. The diffractogram of Mt, CP-Mt and CTA-Mt (Fig.1) indicated a shift in the peak in the lower angle region in the 001 plane from 2θ= 6.8° in the pristine Mt to 4.8° in CP-Mt and 4.9° in CTA-Mt resulting in an increase in the corresponding d spacing from 13.4 Å in pristine Mt to 18.2 Å in both the cases. This relative increase in the d spacing confirms the intercalation of the surfactants into the interlayer region of Mt.[24]

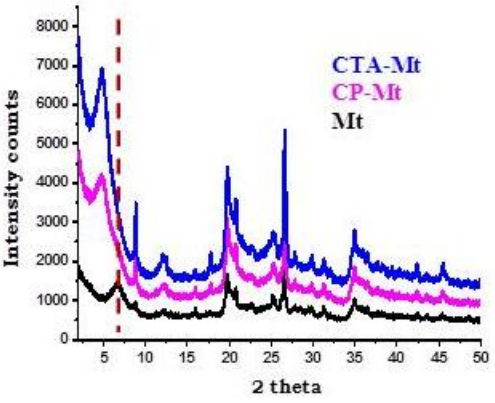

Figur

Fouri

The Mt are shown in Fig.2. In the FTIR spectrum of Mt, the vibrational band at 1049 cm^{-1} has been assigned to Si-O stretching and is the characteristic band of Mt. The vibrational band at 1639 cm^{-1} corresponds to the H-O-H bending mode from sorbed water. The broad band from 3000 to 3700 cm^{-1} in Mt has been assigned to H-O-H stretching vibrations from sorbed water and O-H stretching vibrations of the structural OH groups merged together. The band is broad because of hydrogen bonding between the interlayer water and structural OH groups. The vibrational bands at 527 cm^{-1} and 466 cm^{-1} are strong bending vibrations corresponding to Al-O-Si and Si-O-Si respectively.[25]

Pair of strong vibrational bands at 2925, 2852 cm^{-1} and 2925, 2853 cm^{-1} observed in the case of CP-Mt and CTA-Mt correspond to the C-H antisymmetric and C-H symmetric vibrations respectively from the methylene group of surfactants.[26] In case of CP-Mt and CTA-Mt, the vibrational bands at 3449 cm^{-1} and 3451 cm^{-1} respectively have been assigned to the H-O-H stretching vibrations of the sorbed water but the intensity of these peaks is low as compared to Mt as the intercalation of the surfactant (confirmed by XRD) in the clay layers displaces the water molecules. The displacement of the water molecules is also evident from the presence of relatively distinct and sharp peaks at 3631cm^{-1} and 3632 cm^{-1} observed in case of CP-Mt and CTA-Mt respectively as the extent of hydrogen bonding is lesser. The presence of these bands in the synthesized organophilic clays indicate the presence of surfactant in the clay.[27,28]

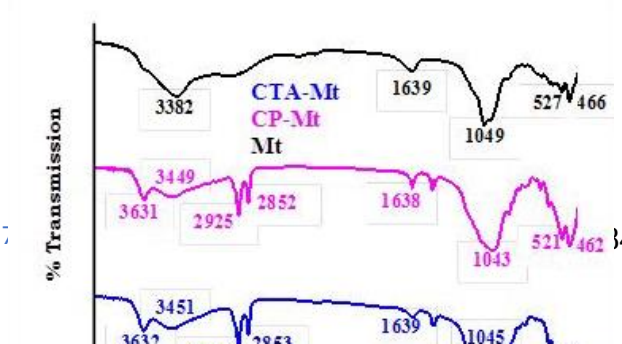

Figure 2. FTIR spectra of clay and organophilic clays

Surface charge analysis using zeta potential measurements

The adsorption of the surfactant (organic cations) on Mt was also evident from the zeta potential measurements. The Mt particles were found to carry a net positive charge, +6.23 mV. However, after treatment with the surfactant, the clay particles exhibited an increased positive charge from +6.23 mV in Mt to +22.6 mV and +17.2 mV in case of CTA-Mt and CP-Mt respectively. The results obtained indicates that the organic cations after complete interlayer exchange with the hydrated metal ions covers the surface of Mt as the surfactant loading was found to be in excess of the cation exchange capacity (CEC) of clay (1.3 times of CEC). The organic cations are probably oriented in a bilayer arrangement on the surface of Mt, thus making the surface of the organophilic clays more positive.

Specific surface area measurement by BET method

Application of BET analysis to the respective nitrogen isotherms measured at -196 ^{o}C showed that the specific surface areas of Mt, CP-Mt and CTA-Mt were 2.87 $m^2 g^{-1}$, 8.2 $m^2 g^{-1}$ and 9.82 $m^2 g^{-1}$, respectively. This increase in surface area may be attributed to an increase in the basal spacing (d), and to the creation of micro porosity due to intercalation of the organic cations in the clay interlayers.

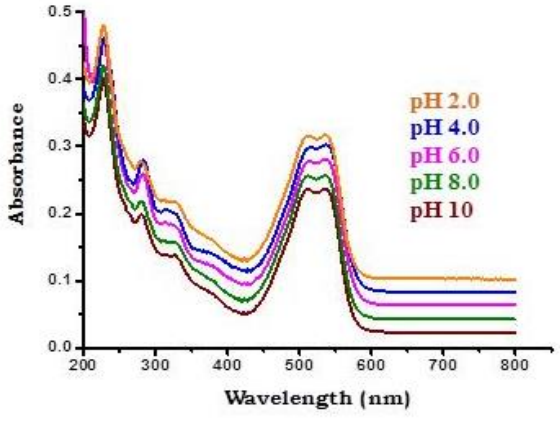

Figure 3. Absorption spectra of aqueous dye solution as a function of pH

pH stability study of the aqueous RR2 dye solution

The behaviour of the aqueous dye solution in the pH range 2 - 10 was investigated spectrophotometrically (Fig. 3). The absorption band at 537 nm corresponds to the π–π* transition of electrons in the azo-group connecting phenyl and naphtyl ring.[29] Within near ultraviolet region (280–380 nm), absorption bands result from the unsaturated system of benzene and naphthalene ring. However, no shift in the absorption maxima of the dye was found indicating that the dye remains stable in the entire pH range studied.

Adsorption equilibrium studies of RR2 dye on clay and organophilic clays

Influence of pH of the aqueous dye solution on adsorption efficiency

There was no pronounced effect of pH of the aqueous dye solution on the adsorption efficiency of CP-Mt and CTA-Mt as more than 95 % of the dye was removed in the entire pH range studied except at pH 6.0 at which almost 100 % of the dye was absorbed by the organophilic clays (Fig. 4). On the other hand, the dye uptake by Mt was low, showing a maximum of 24 % uptake at pH 6.0. Under strong alkaline conditions (pH 10.0), the dye adsorption by Mt fell sharply which may be because of de-protonation of the silanol/aluminol groups on the clay giving rise to negatively charged surface which resists the adsorption of the anionic dye.[30]

$$AlOH + OH^- \rightleftharpoons AlO^- + H_2O$$

Since pristine Mt is hydrophilic in nature owing to the presence of greater amount of surface and interlayer water hence it is more susceptible to change in pH values.

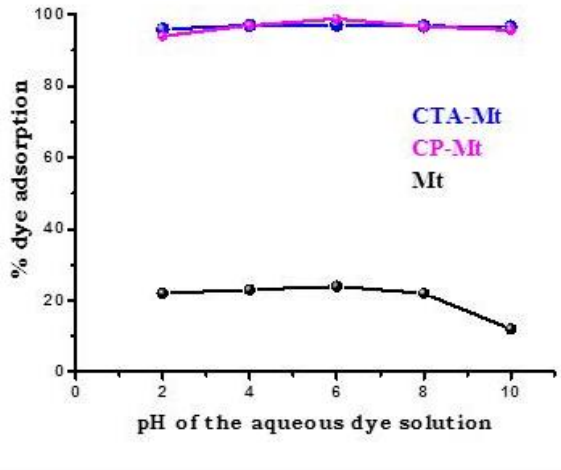

Figure 4. Effect of pH of aqueous dye solution on adsorption efficiency. Adsorbent dose = 0.1 g; conc. of dye = 50 mg dm^{-3}; contact time = 25 min; T = 30° C

Influence of contact time on adsorption efficiency

An increase in % adsorption was found with an increase in the contact time for batch adsorption studies (Fig. 5). The equilibrium was attained within 25 minutes with Mt, CTA-Mt and within 10 minutes with CP-Mt showing 15.2 %, 100 % and 98.9 % adsorption respectively. The adsorption process was found to be extremely rapid in case of organophilic clays with ~ 99 % of the dye (initial

concentration of 50 mg dm^{-3}) being removed in the first 10 minutes of the contact time. This initial rapid uptake can be attributed to the concentration gradient created at the start of the adsorption process between dye concentration in solution and that at the adsorbent surface. As the dye loading increases on the adsorbent, this gradient reduces and gives way to a slower uptake.

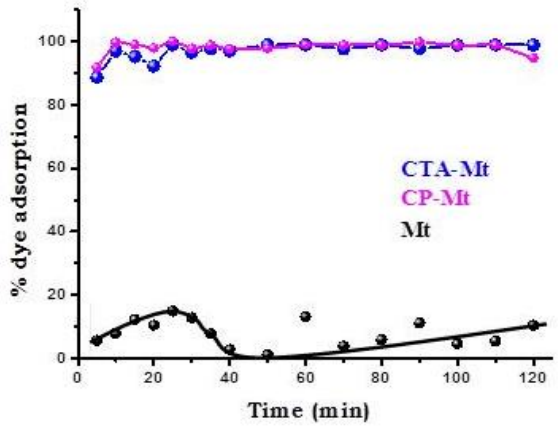

Figure 5. Effect of contact time on adsorption efficiency. Adsorbent dose = 0.1 g; conc. of dye = 50 mg dm^{-3}; pH = 6.0; *T* = 30° C

Influence of the initial dye concentration on adsorption efficiency

It was observed that with an increase in the initial dye concentration, the % adsorption decreased after reaching saturation at a particular initial dye concentration for all the three adsorbents studied (Fig. 6). Almost 100 % adsorption was observed in case of CP-Mt and CTA-Mt up to 220 mg dm^{-3} dye concentration after which a decrease was seen. A similar trend was also observed in case of Mt but the % adsorption decreased rapidly with increase in the initial dye concentration, showing a maximum of 25 % adsorption.

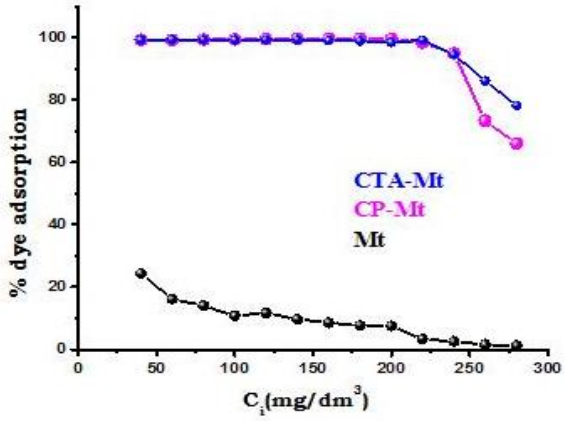

Figure 6. Effect of initial dye concentration on adsorption efficiency. Adsorbent dose = 0.1 g; pH = 6.0; contact time = 25 min; *T* = 30° C

For all the three adsorbents studied, the % dye adsorption was higher for low initial dye concentration because of the availability of the unoccupied sorption sites on the adsorbents. At higher concentrations, the number of available adsorption sites becomes lower, and subsequently the removal of dye depends on the initial concentration.

Influence of the adsorbent dose on adsorption efficiency

It was observed that as the mass of the adsorbent dosage increased from 0.1 g to 0.3 g, the percentage dye adsorption also increased (Fig. 7). This increase in % adsorption observed with all the three adsorbents is due to increase in the number of adsorption sites associated with higher adsorbent dosage.

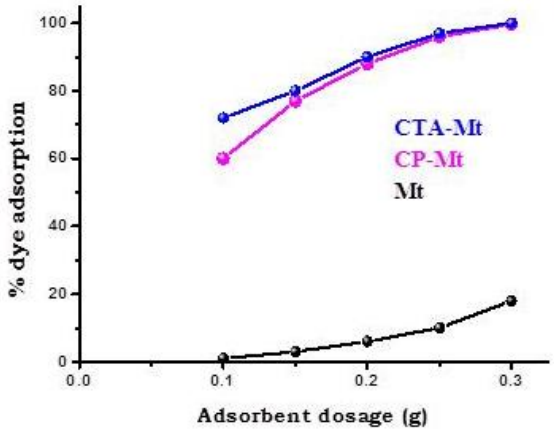

Figure 7. Effect of adsorbent dosage on adsorption efficiency. Contact time = 25 min; conc. of dye = 300 mg dm^{-3}; pH = 6.0; *T* = 30° C

Adsorption equilibrium models

The adsorption capacity of Mt, CP-Mt and CTA-Mt for the dye was determined by studying the equilibrium adsorption isotherm. The adsorption isotherms of *reactive red 2* dye on CP-Mt and CTA-Mt as shown in Fig. 8 were of L-type according to the Giles classification.[31] In this type of isotherm, the initial curvature indicates that a large amount of dye gets adsorbed at lower dye concentrations; however with increase in the dye concentration monolayer formation occurs, signified by the plateau as near the monolayer capacity all sorption sites are occupied. Three common isotherms equations were tested in the present study: Langmuir, Freundlich and Temkin models. Applicability of the adsorption isotherm equations was compared by judging the correlation coefficients.

Langmuir adsorption isotherm

The Langmuir adsorption isotherm is based on the assumption of a structurally homogeneous adsorbent, where all the sorption sites are identical and energetically equivalent.[17] Therefore the sorbent has a finite capacity for the sorbate. The Langmuir isotherm equation may be expressed in a linearized form as shown in Eqn. (3).

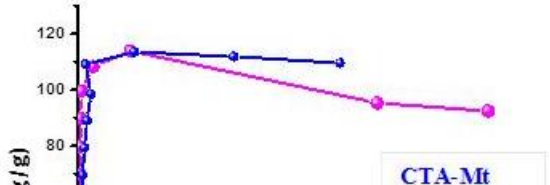

Figure 8. Adsorption isotherm, q_e as a function of C_e

$$\frac{C_e}{q_e} = \frac{1}{q_{max}K_L} + \frac{C_e}{q_{max}} \quad (3)$$

where

C_e (mg dm^{-3}) is the liquid phase concentrationof the adsorbate at equilibrium

q_e (mg g^{-1}) is the solid phase concentration of an adsorbate at equilibrium

q_{max} = monolayer capacity of the adsorbent (mg g^{-1}), a constant related to the area occupied by a monolayer of adsorbate, reflecting the limiting adsorption capacity,

K_L = Langmuir adsorption constant (dm^3 mg^{-1}) which measures the enthalpy of adsorption process.

The plot of C_e/q_e vs. C_e gives a straight line (Fig. 9), with slope equal to $1/q_{max}$ and intercept equal to $1/(q_{max}K_L)$.

The essential characteristics of the Langmuir equation can be expressed in terms of a dimensionless constant which is defined as

$$R_L = \frac{1}{1+K_L C_i} \quad (4)$$

where,

C_i = highest initial dye concentration

The value of R_L indicates the type of the isotherm to be either unfavourable (R_L >1), linear (R_L =1) or favourable (R_L <1).[32,33]

Figure 9. Langmuir adsorption isotherm

Freundlich adsorption isotherm

The Freundlich adsorption isotherm is applicable to multilayer and heterogeneous surface and is expressed by the following equation.

$$\log q_e = \log K_F + \frac{1}{n}\log C_e \quad (5)$$

where,

K_F is a constant for the system, related to the bonding energy.

The slope 1/n, ranging between 0 and 1, is a measure for the adsorption intensity or surface heterogeneity.[34]

1/n values indicate the type of isotherm to be irreversible (1/n = 0), favourable (0 < 1/n < 1), and unfavourable (1/n > 1).[35] A plot of log q_e vs log C_e (Fig. 10) enables the empirical constants K_F and 1/n to be determined from the intercept and slope of the linear regression.

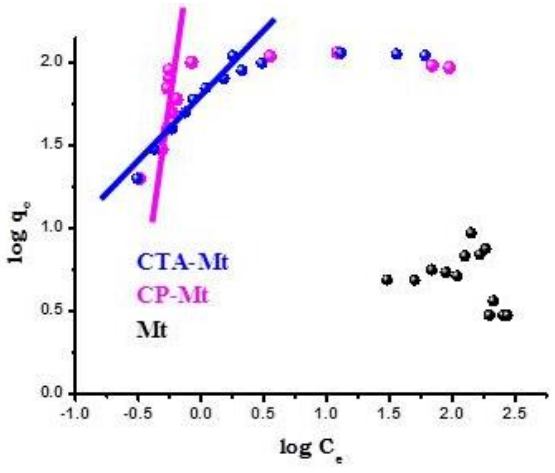

Figure 10. Freundlich adsorption isotherm

Temkin adsorption isotherm

The Temkin isotherm equation assumes that the heat of adsorption of all the molecules in layer decreases linearly with coverage due to adsorbent-adsorbate interactions, and that the adsorption is characterized by a uniform distribution of the bonding energies, up to some maximum binding energy.[36]

The Temkin isotherm is given as:

$$q_e = B\ln A + B\ln C_e \qquad (6)$$

where

A (dm^3 g^{-1}) is the equilibrium binding constant, corresponding to the maximum binding energy and

constant B is related to the heat of adsorption.

A plot of q_e versus ln C_e (Fig. 11) enables the determination of the isotherm constants B and A from the slope and intercept of the straight line plot.

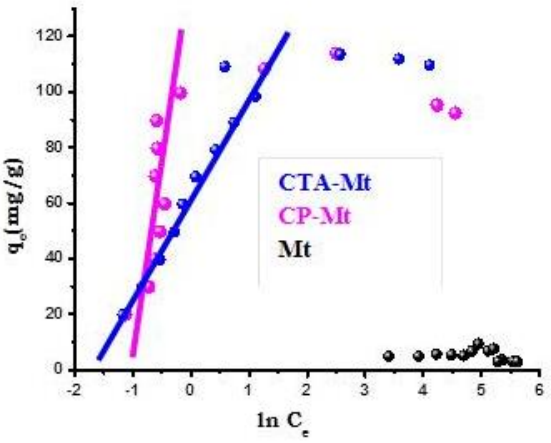

Figure 11. Temkin adsorption isotherm

The model parameters for all the isotherms studied at 30 °C are presented in table 1. The linear plot of specific sorption (C_e/q_e) against the equilibrium concentration (C_e) (Fig. 9) shows that the adsorption of the dye on CP-Mt and CTA-Mt obeys the Langmuir model. The high regression coefficient values R^2 obtained for this model for CP-Mt and CTA-Mt as compared to the Freundlich and Temkin adsorption isotherm support this fact. Also, the value of R_L obtained for the adsorption of the dye on CP-Mt and CTA-Mt falls in the range $0 < R_L < 1$, indicating that the adsorption process is favourable. For Mt, the experimental adsorption data follows Langmuir adsorption model only upto 120 mg dm^{-3} dye concentration and does not fit beyond this concentration. Till this concentration, the adsorption is favorable as indicated by the R^2 and R_L values.

The Freundlich and Temkin adsorption isotherms do not fit well to the experimental adsorption data in the higher concentration region. The magnitude of K_L quantifies the relative affinity between an adsorbate and the adsorbent surface. The higher value of K_L observed in the case of CP-Mt as compared to CTA-Mt demonstrates the higher ability of this adsorbent to adsorb dye molecules and form stable complexes. The high value of K_F obtained in case of CP-Mt as compared to CTA-Mt indicates that CP-Mt has a strong affinity for the dye. However, at higher concentration of the dye, CTA-Mt was found to be a more suitable adsorbent. The high value of the constant B obtained from the Temkin model in case of CP-Mt and CTA-Mt suggest that there is a strong interaction between the adsorbate and the adsorbent surface. The confirmation of the experimental adsorption data with the Langmuir model in the entire concentration range studied indicates the monolayer coverage of dye on the surface of CP-Mt and CTA-Mt which suggests that the adsorption of the dye on CP-Mt and CTA-Mt involves chemisorption. This is because chemisorption involves a more specific binding of the adsorbate to the adsorbent hence chemisorption ceases once a mono layer is formed.

Table 1. Parameters for the fitted isotherm models for RR2 dye adsorption

Isotherm	Parameters	Adsorbents		
		CP-Mt	CTA-Mt	Mt
Langmuir	K_L, dm^3 mg^{-1}	7.7883	1.8628	-0.02099
	q_{max}, mg g^{-1}	93.721	111.61	2.853
	R_L	0.00046	0.0019	-0.2049
	R^2	0.9995	0.9994	0.9010
Freund-lich	K_F, mg g^{-1} (dm^{3}mg$^{-1/n}$)	59.73	54.11	11.324
	$1/n$	0.1557	0.2648	-0.1702
	R^2	0.5662	0.7829	0.2997
Temkin	A,dm^3 mg^{-1}	1162	39.35	3.76×10^{-7}
	B	9.5778	16.8905	-0.5326
	R^2	0.6126	0.8463	0.1804

The q_{max} values for the adsorption of *Reactive red 2* dye on the adsorbents used in the present study listed in table 1 are compared in table 2 with the corresponding values for other adsorbents reported in the literature for this dye. As can be seen, the adsorption efficiency of organophilic clays towards *Reactive red 2* dye is found to be relatively high in comparison to most of the adsorbents reported in the literature recently except few. Mg-Fe layered double hydroxide shows higher monolayer adsorption capacity but this efficiency was attained at relatively longer equilibration time (90 minutes) and the synthesis of the adsorbent is comparatively tedious in comparison to the present adsorption system.

Calcium alginate immobilized fungal biomass shows slightly more monolayer adsorption efficiency but the processing of the adsorbent is time consuming as is the case with biological treatment processes. Moreover, the equilibration is achieved in 2 days and effective adsorption takes place under highly acidic conditions.

Table 2. q_{max} values reported in the literature for the adsorption of RR2 dye

 DOI: 10.17628/ecb.2014.3.838-849

Adsorbent	q_{max} mg g^{-1}	Limitations
$Al(OH)_3$ sludge	14.9	Long equilibration time of 2 d. Low adsorption efficiency.[37]
Soybean meal	16.4	Long equilibration time (> 60 min). Effective adsorption only under strong acidic conditions (pH 2.0). Low adsorption efficiency.[38]
Calcined Zn-Al layered double hydroxide	116.3	Long equilibration time of 210 min. Effective adsorption between pH= 4-8 only. Maximum adsorption was obtained at 20°C.[39]
Tannery sludge based activated carbon	52.4	Long equilibration time of 4 h. Effective adsorption only under strong acidic conditions (pH 2.0). Low adsorption efficiency.[40]
Mg-Fe layered double hydroxide	161.3	Long equilibration time of 90 min. Comparatively tedious synthesis of the adsorbent.[41]
Calcium alginate immobilized fungal biomass	120.5	Long equilibration time of 48 h. Effective adsorption under only highly acidic conditions (pH 2.0). Process is time consuming.[42]
Surfactant modified macro fungus	133.5	Effective adsorption only under strong acidic conditions (pH 2.0).[43]
Nymphaea rubra stem	66.7	Long equilibration time of 180 min. Efficient uptake under highly acidic conditions (pH 2.0) only. Low adsorption efficiency.[44]
Soybean meal	76.9	Long equilibration time of 125 min. Effective adsorption under only highly acidic conditions (pH 2.0). Low adsorption efficiency.[45]
Tamarindus indica	102.0	Long equilibration time of 90 min. Effective adsorption only under highly acidic conditions (pH 2.0).[46]
Carbon nanotubes	44.6	Long equilibration time of 24 h. Adsorption studies performed only at pH 6.5 and pH 10. Low adsorption efficiency.[47]
Coir pith activated carbon	30.0	Long equilibration time of 4 h. Efficient adsorption only under acidic conditions (pH – 3.0). Low adsorption efficiency.48
Metal hydroxide sludge	66.7	Long equilibration time of 1 h. Low adsorption efficiency.[49]

Zn-Al calcined layered double hydroxide as adsorbent showed slightly higher uptake but it was achieved at a longer equilibration time (210 min) and the process was found to be pH and temperature dependent. Surfactant modified macro fungus as an adsorbent is highly pH dependent as it is found to be efficient only under highly acidic conditions (pH=2.0). This is in comparison to the present adsorption system wherein the process was found to be nearly pH independent for organophilic clays in the entire experimental pH range (pH=2-10) studied and the equilibrium was attained within 10 minutes of the contact time.

Kinetic modelling

The kinetics of RR2 dye removal was carried out to understand the dye adsorption behaviour on the three adsorbents with respect to concentration. Since Mt did not show appreciable dye removal, therefore the kinetic studies were performed with the organophilic clays. To evaluate the mechanism of the adsorption process, pseudo first order, second order and intraparticle diffusion models were applied to the experimental data.

Pseudo-first-order kinetic model

The pseudo-first-order kinetic model known as the Lagergern equation can be represented in the linear form[50,51] as:

$$\log(q_e - q_t) = \frac{\log(q_e - k_1)}{2.303} t \qquad (7)$$

where,

q_e and q_t relate to the amounts of dye (mg g^{-1}) adsorbed at equilibrium and at a time t (min), respectively and

k_1 (min^{-1}) is the equilibrium rate constant of the pseudo-first-order adsorption process.

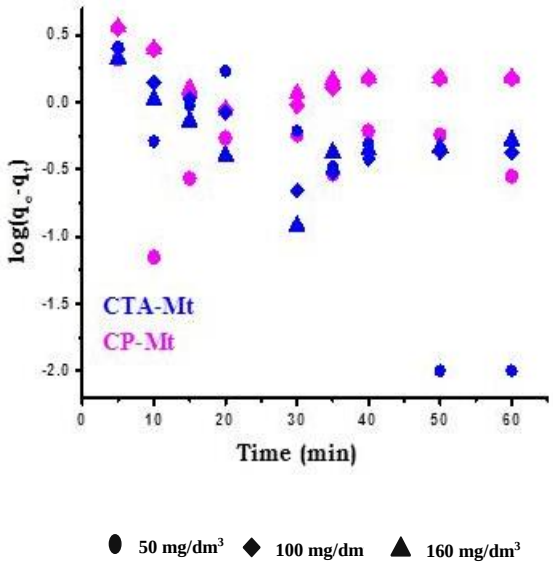

Figure 12. Pseudo-first order kinetic plot for dye adsorption

The pseudo first order rate constants and correlation coefficients were calculated from the plot of $\log(q_e - q_t)$ versus t (Fig. 12) and are given in Table 3.

The correlation coefficients, R^2 obtained for pseudo first order kinetic model were found to be very low. The calculated q_e values for all dye concentrations obtained from the first-order kinetic model do not give reasonable values, which are low compared with experimental q_e values. Thus pseudo first-order kinetic model of Lagergren does not fit well to the adsorption data.

Table 3. Pseudo first order kinetic parameters for dye adsorption

Adsor-bent	Dye conc. mg dm^{-3}	q_e(exp) mg g^{-1}	Parameters		
			k_1, min^{-1}	q_e, cal mg g^{-1}	R^2
CP-Mt	50	25.0000	0.0016	0.4313	0.0318
	100	49.7071	0.0083	1.9098	0.3445
	160	79.7191	0.0084	2.0202	0.3791
CTA-Mt	50	24.7300	0.0950	4.9499	0.8697
	100	49.6244	0.0325	1.6196	0.7565
	160	79.2378	0.0203	0.9663	0.4851

Pseudo-second-order kinetic model

The pseudo-second-order model is based on the assumption that the rate-limiting step is chemical adsorption involving valance force through sharing or exchange of electrons between adsorbent and adsorbate.[52,53]

The linear form of the pseudo-second-order kinetic model can be represented as:

$$\frac{t}{q_t} = \frac{1}{k_2 q_e^2} + \frac{1}{q_e} t \qquad (8)$$

where,

k_2 is the equilibrium rate constant [g (mg^{-1} min^{-1})] for the pseudo-second-order adsorption process.

If the initial adsorption rate is $h = k_2 qe^2$, then the above equation becomes

$$\frac{t}{q_t} = \frac{1}{h} + \frac{1}{q_e} t \qquad (9)$$

Employing this equation and plotting t/q_t versus t gives a straight line of slope $1/q_e$ and intercept $1/k_2 qe^2$.[54]

Fig.13 shows the applicability of the pseudo-second-order kinetic model to the experimental data generated for the adsorptive removal of dye from aqueous solution.

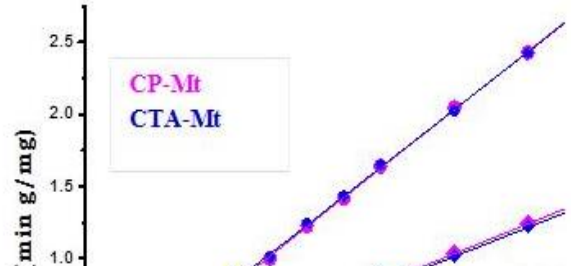

Figure 13. Pseudo-second order kinetic plot for dye adsorption

The pseudo-second-order rate constant k_2, initial adsorption rate h, amount of the dye adsorbed at equilibrium q_e and the corresponding linear regression coefficients R^2 are given in Table 4. It was observed that an increase in the initial dye concentration caused an increase in the equilibrium adsorption capacity, q_e with both the adsorbents but reduced the sorption rate, k_2 in case of CP-Mt. However, in case of CTA-Mt, an increase in the sorption rate, k_2 and a decrease in the initial adsorption rate, h was observed with an increase in the initial dye concentration. The calculated q_e values agreed well with the experimental q_e values. The values of R^2 obtained were all greater than 0.999, which is much higher than the R^2 values obtained for pseudo first order kinetic model. The results show that the adsorption system studied fit with the pseudo-second-order kinetic model for the entire adsorption period. The higher values of R^2 and the calculated values of equilibrium sorption capacity, q_e, which is very much in agreement with experimental data for all initial dye concentrations, confirms that the adsorption process follows a pseudo-second order mechanism suggesting that chemisorption might be the rate limiting step that controlled the adsorption process.[13]

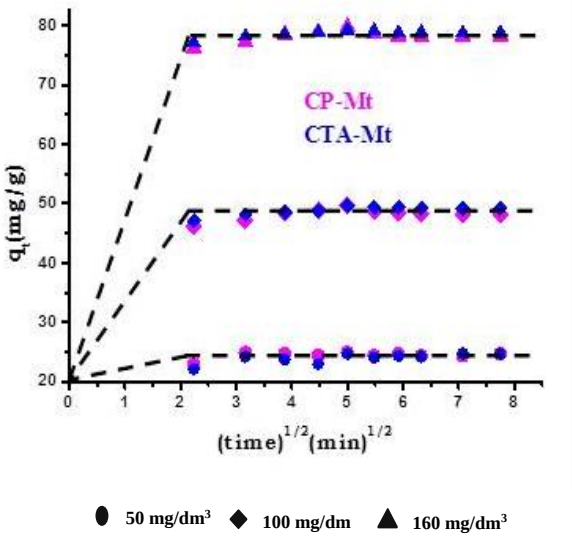

Figure 14. Intraparticle diffusion plot for dye adsorption

Table 4. Pseudo second order kinetic parameters for dye adsorption

Adsorbent	Dye conc., mg dm^{-3}	q_e (exp) mg g^{-1}	Parameters			
			k_2, g mg^{-1} min^{-1}	h, mg g^{-1}min^{-1}	q_e, cal mg g^{-1}	R^2
CP-Mt	50	25.0000	0.6060	1.6502	24.6310	0.9999
	100	49.7071	0.2556	3.9129	48.2625	0.9999
	160	79.7191	0.3353	2.9819	78.2473	0.9995
CTA-Mt	50	24.7300	0.0521	19.213	24.9626	0.9997
	100	49.6244	0.1146	8.7227	49.4315	0.9999
	160	79.2378	0.3536	2.8284	78.9266	0.9999

Intraparticle diffusion model

According to the intraparticle diffusion model proposed by Weber and Morris,[55] the initial rate of intraparticle diffusion is given by the equation:

$$q_t = k_i t^{1/2} + C \quad (10)$$

where,

k_i is the intraparticle diffusion rate constant, mg g^{-1} min$^{-1/2}$,

t is the time (min) and

C is the intercept.

According to this model, a plot of q_t versus $t^{1/2}$ should be linear if intraparticle diffusion is involved in the adsorption process and if the plot passes through the origin then intraparticle diffusion is the sole rate-limiting step.[56] It has also been suggested that in instances when q_t versus $t^{1/2}$ is multilinear two or more steps govern the adsorption process.[57] As the plots of q_t versus $t^{1/2}$ in the present case are linear (Fig. 14), it suggests that intraparticle diffusion is involved in adsorption but since the plots did not pass through the origin, it is indicative of the fact that intraparticle diffusion was not the rate-limiting step in the present adsorption process. The values of constant C and k_i along with regression coefficient are listed in Table 5.

Table 5. Intraparticle diffusion kinetic parameters for dye adsorption

Ad-sor-bent	Dye conc. mg dm^{-3}	Parameters		
		k_i, mg g^{-1} min$^{-1/2}$	C, mg g^{-1}	R^2
CP-Mt	50	0.1422	23.7428	0.4206
	100	0.2696	46.8426	0.4812
	160	0.2649	76.8194	0.4827
CTA-Mt	50	0.3557	22.1889	0.7419
	100	0.3393	47.1263	0.7899
	160	0.2345	77.4198	0.6772

Mechanism of RR2 dye adsorption on organophilic clays

Since the organic cations loading was found to be in excess of the cation exchange capacity of the clay (~1.3 times the CEC of the clay), therefore after complete exchange with the interlayer ions, the excess of the organic cation gets adsorbed on the clay surface in a bilayer arrangement making the clay surface positively charged. The *reactive red 2* dye on being dissolved in aqueous medium becomes negatively charged because of the presence of two sulphonic acid groups. When the organophilic clay is added to this aqueous dye solution, the negatively charged dye ions are electrostatically attracted to the positively charged head groups of the organic cations adsorbed on the surface of the clay thereby removing the dye from the aqueous solution (Fig.15). Thus the clay is acting as a host material for localizing the organic cations on its surface.

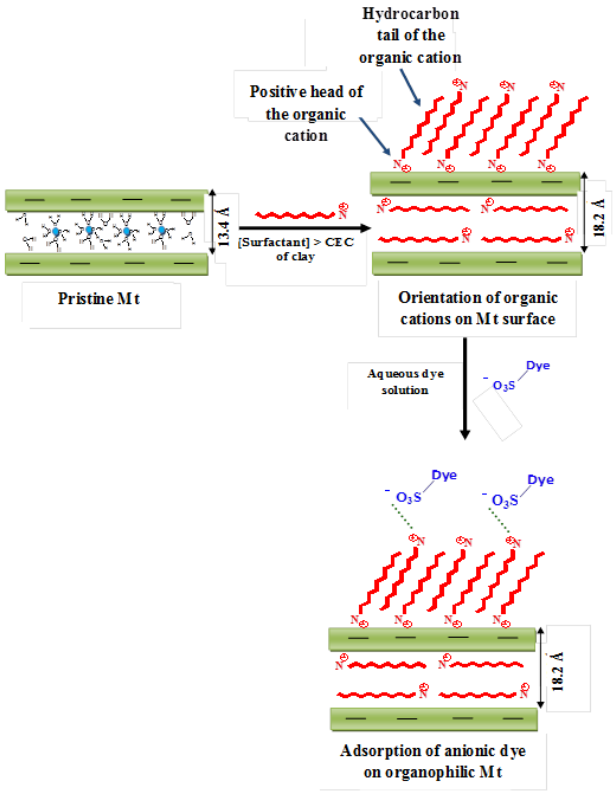

Figure 15. Diagrammatic representation of adsorption of anionic dye on organophilic Mt clay

CONCLUSION

The adsorptive removal of *Reactive red 2* dye was studied using Mt, CP-Mt and CTA-Mt. The results of the present investigation show that the dye adsorption by organophilic clays remains almost independent of the pH of the aqueous dye solution in comparison to Mt. The equilibrium was established within 10 minutes of the contact time in case of organophilic clays. The adsorption process was found to be extremely rapid in case of organophilic clays with over 99% of the dye (initial concentration of 50 mg/dm^3) being removed in the first 10 minutes of the contact time suggesting very active surface phenomenon of these adsorbents. On the other hand, the dye adsorption efficiency of Mt was found to be very low as compared to the organophilic clays. The experimental adsorption equilibrium data obtained for all the adsorbate-adsorbent systems were tested for Langmuir, Freundlich and Temkin adsorption isotherm models. The Langmuir model provided a better fit than the others suggesting monolayer coverage of the dye on the surface of the adsorbents. The Langmuir monolayer adsorption capacity of Mt, CP-Mt and CTA-Mt for the dye was found to be 2.85, 93.72 and 111.61 mg g^{-1}, respectively.

Three adsorption kinetic models pseudo first, pseudo second order and intraparticle diffusion models were applied to investigate the mechanism of adsorption. It was found that the intercept of the pseudo first order plot did not equal q_e and the magnitude of the correlation coefficient were quite low indicating that the reaction is not likely to be first order. The intraparticle diffusion kinetic model demonstrated linear plots but did not pass through origin suggesting that intraparticle diffusion is not the only rate controlling step, but also other kinetic processes may control the rate of adsorption, all of which may be operating simultaneously. However, low correlation coefficients were obtained suggesting the inapplicability of this model to the present adsorption system. Application of the pseudo second order kinetic model to the experimental data within the time range of adsorption showed high correlation coefficient all nearing 1.0 and the q_e values obtained were close to the experimental q_e values. These findings suggest that the pseudo second order mechanism is predominant and chemisorption may be the rate limiting step that controls the adsorption process.

ACKNOWLEDGEMENT

The authors are grateful to the Head of the Department of Chemistry and the Director of the University Science Instrumentation Centre of the University of Delhi for providing the necessary laboratory facilities and financial support.

REFERENCES

[1]Chatterjee, D., Patnam, V. R., Sikdar, A., Misra, P. R., Rao, N. N., *J. Hazard. Mater.*, **2008**, *156*, 435-441.

[2]Akkaya, G., Uzun, I., Güzel, F., *Dyes Pigm.*, **2007**, *73*, 168-177.

[3]Zollinger, H., *Color Chemistry: Synthesis, Properties and Applications of Organic Dyes and Pigments.* 2nd Ed., VCH Publishers, New York, **1991**.

[4]Rys, P., Zollinger, H., *The Theory of Coloration of Textiles.* Johnston, A., ed., Society of Textile Dyers and Colorists, West Yorkshire, England, **1989**.

[5]Xu, Z. Y., Zhang, Q. X., Fang, H. H. P., *Crit. Rev. Environ. Sci. Technol.*, **2003**, *33*, 363-389.

[6]Mahlok, J. L., Shindala, A. M., Griff, E. C., Barnett, W. A., *Am. Dye Stuff Report*, **1975**, *64*, 24–46.

[7]Horning, R. H., *Tex. Chem. Colourists*, **1977**, *9*, 24–27.

[8]Konduru, R., Ramakrishna, K. R., Viraraghavan, T., *Water Sci. Technol.*, **1997**, *36*, 189–196.

[9]El Guendi, M. S., *Adsorpt. Sci. Technol.*, **1995**, *13*, 295–303.

[10]Mc Kay, G., Allen, S. J., *Can. Chem. Eng.*, **1980**, *J58*, 521–525.

[11]Raghavacharya, C., *Chem. Eng. World*, **1997**, *32*, 53–58.

[12]Orthman, J., Zhu, H. Y., Lu, G. Q., *Sep. Purif. Technol.*, **2003**, *31*, 53.

[13]Ozacar, M., Sengil, I. A., *J. Hazard. Mater.*, **2003**, *B98*, 211.

[14]Shen, Y. H., *Chemosphere*, **2001**, *44*, 989.

[15]Kim, J. H., Shin, W. S., Kim, Y. H., Choi, S. J., Jeon, Y. W., Song, D. I., *Water Sci. Technol.*, **2003**, *47*, 59.

[16]Prost, R., Yaron, B., *Soil Sci.*, **2001**, *166*, 880.

[17]Ozacan, A. S., Ozcan, A., *J. Colloid Interface Sci.*, **2004**, *276*, 39.

[18]Juang, R. S., Lin, S. H., Tsao, K. H., *J. Colloid Interface Sci.*, **2002**, *254*, 234.

[19]Wolfe, T. A., Demirel, T., Baumann, E. R., *Clays Clay Miner.*, **1985**, *33*, 301–307.

[20]Smith, J. A., Galan, A., *Environ. Sci. Technol.*, **1995**, *29*, 685–692.

[21]Klumpp, E., Contreras-Ortega, C., Klahre, P., Tino, F. J., Yapar, S., Portillo, C., Stegen, S., Queirolo, F., Schwuger, M. J., *Colloids Surf. A: Physicochem. Eng. Aspects*, **2003**, *230*, 111–116.

[22]Kahr, G., Madsen, F. T., *Appl. Clay Sci.*, **1995**, *9*, 327-336.

[23]He, H., Zhou, Q., Frost, R. L., Wood, B. J., Duong, L. V., Kloprogge, J. T., *Spectrochim. Acta*, **2007**, *66*, 1180.

[24]Xiao, J., Hu, Y., Wang, Z., Tang, Y., Chen, Z., Fan, W., *Eur. Polym.*, **2005**, *J41*, 1030.

[25]Bukka, K., Miller, J. D., *Clays Clay Miner.*, **1992**, *40*, 92-102.

[26]Kaur, M., Datta, M., *Adsorpt. Sci. Technol.*, **2011**, *29*, 306-307.

[27]Guangming, C., Suhuai, L., Shijuan, C., Zongneng, Q., *Macromol. Chem. Phys.*, **2001**, *202*, 1189–1193.

[28]Kungt, K. S., Hayes, K. F., *Langmuir*, **1993**, *9*, 263-267.

[29]Kusmierek, E., Chrzescijanska, E., Szadkowska-Nicze, M., Kaluzna-Czaplinska, J., *J. Appl. Electrochem.*, **2011**, *41*, 51-62.

[30]Nagy, N. M., Kónya, J., *Appl. Clay Sci.*, **2004**, *25*, 57– 69.

[31]Giles, C. H., MacEwan, T. H., Nakhwa, S. N., Smith, D., *J. Chem. Soc.*, **1960**, *11*, 3973.

[32]Baskaralingam, P., Pulikesi, M., Ramamurthi, V., Sivanesan, S., *J. Hazard. Mater.*, **2006**, *B136*, 989.

[33]Zheng, H., Wang, Y., Zheng, Y., Zhang, H., Liang, S., Long, M., *Chem. Eng. J.*, **2008**, *143*, 117–123.

[34]Treybal, R. E., *Mass transfer operations.* 2nd ed., McGraw Hill, New York, **1968**.

[35]Hameed, B. H., Mahmoud, D. K., Ahmad, A. L., *J. Hazard. Mater.*, **2008**, *158*, 65–72.

[36]Temkin, M. J., Pyzhev, V., *Acta Physiochim USSR*, **1940**, *12*, 217–222.

[37]Uçar, B., Güvenç, A., Mehmetoğlu, U., *Hydrol. Current Res.*, **2011**, *2*, 1-8.

[38]Peng, N., Wang, K., *Proc.Int. Conf. Computer Distributed Control Intelligent Environ. Monitoring, CDCIEM*, **2011**, 2193-2196.

[39]Zhang, L., Chen, Y., *Adv. Mat. Res.*, **2011**, *287*, 390-393.

[40]Geethakarthi, A., Phanikumar, B. R., *Int. J. Environ. Sci. Tech.*, **2011**, *3*, 561-570.

[41]Zhang, L., Chen, Y., *IEEE* 978-1-61284-459-6/11, **2011**.

[42]Zhang, L., Wang, M., *Adv. Mat. Res.*, **2011**, *213*, 432-436.

[43]Akar, T., Divriklioglu, M., *Bioresource Technol.*, **2010**, *101*, 7271–7277.

[44]Sahadevan, R., Kalpana, J., Kumar, M. D., Velan, M., *Clean*, **2009,** *11*, 901– 907.

[45]Sahadevan, R., Seenuvasan, M.**,** Selvaraj, S., Gautam, P., Velan, M., *Chem. Prod. Process Model*, **2008,** *3*, 1-18.

[46]Sahadevan, R., Kumar, D., Mahendradas, Shanmugasundaram, V., Shanmugam, K., Velan, M., *Int. J. Chem. Reactor Eng.*, **2009**, *A33*, 1-23.

[47]Wu, C-H., *J. Hazard. Mater.*, **2007**, *144*, 93–100.

[48]Santhy, K., Selvapathy, P., *Bioresource Technol.*, **2006**, *97*, 1329–1336.

[49]Netpradit, S., Thiravetyan, P., Towprayoon, S., *J. Colloid Interface Sci.*, **2004**, *270*, 255-261.

[50]Feng-Chin, W., Ru-Ling, T., Ruey-Shin, J., *J. Hazard. Mater.*, **2001**, *B81*, 167–177.

[51]Ho, Y. S., McKay, G., *J. Environ. Sci. Health A*, **1999a**, *34*, 1179–1204.

[52]Ho, Y. S., McKay, G., *Process Biochem.*, **1999**, *34*, 451–465.

[53]Ho, Y. S., McKay, G., *Process Safety Environ. Prot.*, **1998**, *76*, 332–340.

[54]Ho, Y. S., McKay, G., *Water Res.*, **2004**, *34*, 735–742.

[55]Banat, F., Al-Ashed, S., Al-Makhadmeh, L., *Process Biochem.*, **2003A**, *39*, 193.

[56]Senthilkumaar, S., Kalaamani, P., Porkodi, K., Varadarajan, P. R., Subburaam, C. V., *Bioresour. Technol.*, **2006**, *14*, 1618–1625.

[57]McKay, G., Poots, V.J.P., *J. Chem. Technol. Biotechnol.*, **1980**, *30*, 279–292.

Received: 04.04.2014.
Accepted: 11.08.2014.

C-BENZOTRAZOLATED NITRONES AS USEFUL SYNTHONS FOR THE SYNTHESIS OF 2,3-DISUBSTITUTED ISOXAZOL-5-ONES

Khalid Widyan[a]*

Keywords: Synthesis, Diaryl(heteroaryl) nitrones, *C*-benzotriazolated nitrones, isoxazol-5-ones, Reformatsky reagent.

A new and general method for preparation of C-benzotriazolated nitrones is reported. The reactivity of C-benzotriazolated nitrones is applied for reaction with Reformatsky reagent in the absence of Lewis acid to produce 2,3-Disubstituted isoxazol-5-ones in good yields.

*Corresponding Author
Fax: 0096232250431
E-Mail: k.widyan@ttu.edu.jo
[a] Department of Chemistry, Tafila Technical University, P.O. Box 179, Tafila, Jordan

Introduction

The chemistry and properties of nitrones **I** have been investigated for more than one century, and their reactivity as electrophiles towards organometallic reagents and as 1,3-dipolar reagents have been long investigated. Nowadays, these reactions are employed abundantly and nitrones have become useful intermediates in synthetic applications.

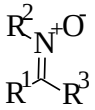

Figure 1. Structure of nitrones

The most convenient approach for the generation of nitrones is condensation between hydroxylamines and an aldehyde or a ketone,[1,2] other methods also exist such as oxidation of tertiary hydroxylamines, alkylation of oximes with alkyl halides or oxidation of imine.[3]

There are several reports on nucleophilic additions to nitrones.[4,5] The presence of the C=N moiety in nitrones gives the functionality an iminium character, which is responsible for its reactivity as electrophile with organometallic reagents. Many of these reactions are catalyzed by Lewis acids but strong binding of nitrones to the catalyst is a serious problem as the dipoles have a tendency to form inactive dipole/Lewis acid complexes.[6-16]

Isoxazol-5-ones are useful synthetic intermediates for the preparation of heterocyclic compounds, and important framework in biological systems exhibiting pharmacological activity.[17,18] The preparation of tri-,[19-22] 2,4-di-,[23-26] and 3,4-disubstituted[27-29] isoxazol-5-ones is well documented. By contrast limited literature is available for the preparation of 2,3-disubstituted isoxazol-5-ones although these are important synthetic precursors for pyridines and pyrroles,[30,31] oxazoles,[32] and thiazoles.[33] 2,3-Disubstituted isoxazol-5-ones were previously prepared (i) by reactions of hydroxylamine with β-keto esters,[34-36] but unsymmetrical β-keto esters can form two isomeric isoxazoles, often not easily separable or (ii) by reactions of diketene with hydroxylamines or sulfonylhydroxamic acids, but the starting materials are not easily available[37,38] or (iii) by acylation of 3-substituted isoxazol-5-ones with aroyl chlorides; although acylation frequently gives a mixture of *N*-aroyl and *O*-aroyl derivatives.[39] Thus previous reports for the preparation of 2,3-disubstituted isoxazol-5-ones have drawbacks including lack of generality, unavailability of starting materials, low yields and selectivity.

Continuing the ongoing interest in the study of the reactivity of benzotiazolated derivatives and its application for the synthesis of heterocycles, an easy preparation of *C*-benzotriazolated nitrones **3** and the conversion of **3** into 2,3-disubstituted isoxazol-5-ones **6** in the absence of Lewis acid is now described.

Results and Discussion

Diaryl(heteroaryl) nitrones **1a-h** were prepared following literature procedures (i) from a hydroxylamine and an aldehyde or (ii) by imine oxidation.[40-42] Treatment of **1a-h** with *N*-chlorobenzotriazole (BtCl) and sodium benzotriazolate (BtNa) in THF furnished exclusively **3a-h** in 73-81 % overall yields. Initial formation of **3** was demonstrated by the reaction of *C,N*-di(4-methylphenyl)nitrone **1a** with chlorobenzotriazole and sodium benzotriazolate in THF for 4 hours which gave a mixture separated by column chromatography into **2a** (40 %) and **3a** (35 %). However, when the reaction mixture was heated at reflux temerature for 3 hours, only isomer **3a** was obtained in 73 % yield; presumably due to the conversion of the kinetic product **2a** to the more stable thermodynamic product **3a** (Scheme 1).

The Reformatsky reagent **5** was prepared from ethylbromoacetate (**4**) and zinc after its activation with trimethylsilylchloride.

Table 1. Synthesis of **3**.

Starting materials				**Products**				
1	m.p. (°C)	Lit. m.p. (°C)	Reference	**3**	R^1	R^2	Yield (%)[a]	m.p. (°C)
a	129-130	129-130	43	**a**	4-$CH_3C_6H_4$	4-$CH_3C_6H_4$	77	140-141
b	111-113	114	44	**b**	C_6H_5	C_6H_5	81	131-133
c	116-117	116-117	44	**c**	4-$CH_3OC_6H_4$	C_6H_5	81	154-156
d	169-170	-[b]	45	**d**	4-$CH_3OC_6H_4$	4-ClC_6H_4	79	131-133
e	141-143	-[b]	46	**e**	4-$CH_3OC_6H_4$	$CH_3OC_6H_4$	80	165-167
f	108-109	109	47	**f**	2-Furyl	C_6H_5	75	128-129
g	87-89	-[b]	48	**g**	2-Thienyl	C_6H_5	76	183-185
h	89-91	88-89	49	**h**	3-Pyridyl	C_6H_5	73	153-155

[a] Isolated yield. [b] Melting point not reported.

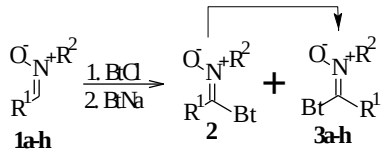

Scheme 1. C-benzotriazolated nitrones

Treatment of **3a-h** with Reformatsky reagent **5** at reflux temperature for 3 hours afforded exclusively the isoxazol-5-ones **6a-h** in 72-81 % overall yields after purification by column chromatography (Scheme 2, Table 2).

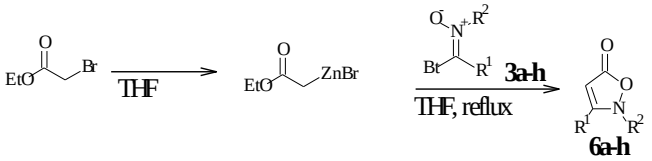

Scheme 2. Synthesis of isoxazol-5-ones

Table 2. Synthesis of isoxazol-5-ones **6**.

Entry	**R^1**	**R^2**	**Yield (%)**
6a	4-$CH_3C_6H_4$	4-$CH_3C_6H_4$	77
6b	C_6H_5	C_6H_5	81
6c	4-$CH_3OC_6H_4$	C_6H_5	79
6d	4-$CH_3OC_6H_4$	4-ClC_6H_4	72
6e	4-$CH_3OC_6H_4$	4-$CH_3OC_6H_4$	76
6f	2-Furyl	C_6H_5	78
6g	2-Thienyl	C_6H_5	73
6h	3-Pyridyl	C_6H_5	80

The structure of **3a-h** and **6a-h** were all supported by ^1H, ^{13}C NMR spectroscopy, elemental analysis and HRMS.

Experimental

Melting points were determined on a capillary point apparatus equipped with a digital thermometer. NMR spectra were recorded in $CDCl_3$ or DMSO-d_6 with TMS for ^1H (300 MHz) and ^{13}C (75 MHz) as the internal reference. Column chromatography was performed on silica gel 200–425 mesh. Nitrones **1a-h** were prepared according to literature procedure,[40-42] and the melting points are in accordance with literature data (Table 1).[43-49]

General procedure for preparation of 3

Chlorobenzotriazole (0.77 g, 5 mmol) was added to a stirred mixture of nitrone (4 mmol) and sodium benzotriazolate (0.74 g, 5 mmol) in THF (50 mL) at room temperature. The mixture was stirred at reflux temperature for 3 h. Diethyl ether was added and the mixture was filtered. The filtrate was evaporated and the residue was dissolved in diethyl ether, washed with saturated aqueous potassium carbonate, dried over magnesium sulfate and concentrated in vacuum. The residue was purified by flash chromatography on silica gel (eluent: *n*-hexane/ethyl acetate = 2/1).

***N*-[(1*H*-Benzotriazol-1-yl)-(4-methylphenyl)methylene]-4-methylbenzenamine oxide (3a)**

Yield 1.1 g (77 %); pale-yellow microcrystal; mp: 140-141 °C; ^1H NMR ($CDCl_3$) δ 2.16 (s, 3H), 2.39 (s, 3H), 6.89 (d, *J* = 8.1 Hz, 2H), 7.16 (d, *J* = 8.4 Hz, 2H), 7.21 (d, *J* = 8.1 Hz, 2H), 7.30 (d, *J* = 8.4 Hz, 1H), 7.37 (t, *J* = 7.2 Hz, 1H), 7.44-7.49 (m, 1H), 7.82 (d, *J* = 8.4 Hz, 2H), 8.01 (d, *J* = 8.4 Hz, 1H); ^{13}C NMR ($CDCl_3$) δ 21.0, 21.7, 109.4, 120.4, 122.2, 124.7, 126.5, 127.8, 129.2, 129.3, 129.4, 134.1, 137.2, 139.7, 142.5, 144.5, 144.9. Anal. Cald for $C_{21}H_{18}N_4O$: C, 73.67; H, 5.30; N, 16.36. Found: C, 73.91; H, 5.33; N, 16.18.

***N*-[(1*H*-Benzotriazol-1-yl) phenylmethylene]benzeneamine oxide (3b)**

Yield 1.0 g (81 %); pale-yellow microcrystal; mp: 131-133 °C; ^1H NMR ($CDCl_3$) δ 7.06-7.18 (m, 3H), 7.24-7.53 (m, 8H), 7.90-8.06 (m, 3H); ^{13}C NMR ($CDCl_3$) δ 109.3, 120.4, 122.4, 124.8, 127.8, 128.7, 128.8, 129.1, 129.2, 129.6, 131.8, 134.0, 137.3, 145.0, 146.7; HRMS Cald for $C_{19}H_{14}N_4O$ $[M+Na]^+$: 337.1060. Found: 337.1090.

***N*-[(1*H*-Benzotriazol-1-yl)-(4-methoxyphenyl)methylene]benzenamine oxide (3c)**

Yield 1.11 g (81%); pale-brown microcrystal; mp: 154-156 °C; ^1H NMR ($CDCl_3$) δ 3.86 (s, 3H), 6.87-6.97 (m, 2H), 7.07-7.15 (m, 3H), 7.28-7.42 (m, 4H), 7.48 (t, *J* = 7.7 Hz, 1H), 7.92-8.05 (m, 3H); ^{13}C NMR ($CDCl_3$) δ 55.5, 109.4, 114.1, 120.4, 121.8, 122.5, 124.8, 128.8, 129.2, 129.5, 130.1, 134.0, 144.9, 146.5, 162.1. Anal. Cald for $C_{20}H_{16}N_4O_2$: C, 69.75; H, 4.68; N, 16.27. Found: C, 69.41; H, 4.77; N, 16.02.

 DOI: 10.17628/ecb.2014.3.850-854

N-[(1*H*-Benzotriazol-1-yl)-(4-methoxyphenyl)methylene]-4-chlorobenzenamine oxide (3d)

Yield 1.19 g (79 %); pale-brown microcrystal; mp: 131-133 °C; ^{1}H NMR ($CDCl_3$) δ 3.86 (s, 3H), 6.92 (d, *J* = 9.0 Hz, 2H), 7.09 (d, *J* = 8.7 Hz, 2H), 7.22-7.32 (m, 3H), 7.40 (t, *J* = 7.7 Hz, 1H), 7.50 (t, *J* = 7.5 Hz, 1H), 7.93 (d, *J* = 9.0 Hz, 2H), 8.04 (d, *J* = 8.4 Hz, 1H); ^{13}C NMR ($CDCl_3$) δ 55.5, 109.2, 114.2, 120.6, 121.5, 124.0, 125.0, 129.0, 129.5, 130.1, 134.0, 135.3, 137.3, 144.9, 145.0, 162.2. Anal. Cald for $C_{20}H_{15}ClN_4O_2$: C, 63.41; H, 3.99; N, 14.79. Found: C, 63.24; H, 4.01; N, 14.62.

N-[(1*H*-Benzotriazol-1-yl)-(4-methoxyphenyl)methylene]-4-methoxybenzenamine oxide (3e)

Yield 1.20 g (80 %); pale-brown microcrystal; mp: 165-167 °C; ^{1}H NMR ($CDCl_3$) δ 3.64 (s, 3H), 3.85 (s, 3H), 6.58 (d, *J* = 9.0 Hz, 2H), 6.91 (d, *J* = 9.0 Hz, 2H), 7.22 (d, *J* = 9.0 Hz, 2H), 7.31 (d, *J* = 8.1 Hz, 1H), 7.37 (t, *J* = 7.5 Hz, 1H), 7.47 (t, *J* = 7.7 Hz, 1H), 7.93 (d, *J* = 9.3 Hz, 2H), 8.02 (d, *J* = 8.4 Hz, 1H); ^{13}C NMR ($CDCl_3$) δ 55.3, 55.4, 109.4, 113.8, 114.0, 120.4, 122.0, 123.9, 124.7, 129.2, 130.0, 134.0, 136.8, 139.8, 144.9, 159.8, 161.9. Anal. Cald for $C_{21}H_{18}N_4O_3$: C, 67.37; H, 4.85; N, 14.96. Found: C, 66.96; H, 4.90; N, 14.79.

N-[1*H*-Benzotriazol-1-yl)-(2-furyl)methylene]benzenamine oxide (3f)

Yield 0.912 g (75%); pale-brown microcrystal; mp: 128-129 °C; ^{1}H NMR ($CDCl_3$) δ 6.68-6.74 (m, 1H), 7.11-7.21(m, 3H), 7.25-7.44 (m, 5H), 7.50 (t, *J* = 7.2 Hz, 1H), 8.03 (d, *J* = 8.1 Hz, 1H), 8.28 (d, *J* = 3.9 Hz, 1H); ^{13}C NMR ($CDCl_3$) δ 109.2, 113.2, 118.3, 120.4, 122.9, 124.7, 128.9, 129.1, 129.2, 130.3, 134.1, 144.1, 144.9, 145.0, 145.3. Anal. Cald for $C_{17}H_{12}N_4O_2$: C, 67.10; H, 3.97; N, 18.41. Found: C, 67.35; H, 4.16; N, 17.95.

N-[(1*H*-Benzotriazol-1-yl)-(2-thienyl)methylene]benzenamine oxide (3g)

Yield 0.973 g (76%); pale-brown microcrystal; mp: 183-185 °C: ^{1}H NMR ($CDCl_3$) δ 6.77 (d, *J* = 3.6 Hz, 1H), 7.06-7.20 (m, 4H), 7.30-7.36 (m, 3H), 7.40 (d, *J* = 7.8 Hz, 1H), 7.49 (t, *J* = 7.5 Hz, 1H), 7.67 (d, *J* = 4.8 Hz, 1H), 8.05 (d, *J* = 8.4 Hz, 1H); ^{13}C NMR ($CDCl_3$) δ 109.2, 120.5, 123.0, 124.9, 127.2, 128.9, 129.5, 130.0, 130.7, 130.8, 131.5, 133.8, 144.2, 144.9. Anal. Cald for $C_{17}H_{12}N_4OS$: C, 63.73; H, 3.78; N, 17.49. Found: C, 63.48; H, 3.73; N, 17.33.

N-[(1*H*-Benzotriazol-1-yl)-(3-pyridyl)methylene]benzenamine oxide (3h)

Yield 0.792 g (73%); pale-brown microcrystal; mp: 153-155 °C; ^{1}H NMR ($CDCl_3$) δ 7.08-7.22 (m, 3H), 7.26-7.35 (m, 3H), 7.37-7.43 (m, 2H), 7.51 (t, *J* = 7.7 Hz, 1H), 8.03 (d, *J* = 8.4 Hz, 1H), 8.51-8.55 (m, 1H), 8.69 (d, *J* = 4.4 Hz, 1H), 8.91 (d, *J* = 1.8 Hz, 1H); ^{13}C NMR ($CDCl_3$) δ 109.0, 120.7, 122.4, 123.4, 125.1, 125.9, 128.9, 129.6, 130.0, 133.8, 134.6, 143.3, 145.0, 146.3, 148.6, 151.7; HRMS Cald for $C_{18}H_{13}N_5O$ $[M+Na]^+$: 338.1012. Found: 338.1036.

General procedure for preparation of 6

Trimethylsilyl chloride (0.04 mL) was added to a suspension of zinc (0.5 g, 7.7 mmol) in THF at room temperature and the mixture was stirred under reflux for 30 min. To the cooled reaction mixture was added ethyl bromoacetate (2.5 mmol) and the suspension was stirred for 1 h at room temperature followed by addition of **3** (1 mmol) dissolved in THF (1 mL). The reaction mixture was heated to reflux for 3 h and cooled to room temperature. The mixture was filtered, concentrated under reduced pressure and residue subjected to column chromatography on silica gel using ethyl acetate/hexane (1:3) to give **6**.

2,3-Di(4-methylphenyl)isoxazol-5-one (6a)

Yield 0.204 g (77%); pale yellow microcrystals; mp: 166.0-168.0 °C; ^{1}H NMR (DMSO-d_6) δ 2.28 (s, 3H), 2.38 (s, 3H), 7.15 (d, *J* = 8.1 Hz, 2H), 7.33 (d, *J* = 8.1 Hz, 2H), 7.67 (d, *J* = 8.1 Hz, 2H), 7.88 (d, *J* = 7.5 Hz, 2H), 10.09 (s, 1H); ^{13}C NMR (DMSO-d_6) δ 20.5, 21.0, 120.4, 127.7, 128.9, 129.0, 132.2, 132.5, 136.8, 141.4, 165.2. HRMS Cald for $C_{17}H_{15}NO_2$ $[M+H]^+$-H_2O: 248.1075. Found: $[M+H]^+$-H_2O: 248.1024.

2,3-Diphenylisoxazol-5-one (6b)

Yield 0.192 g (81%); pale yellow microcrystals; mp: 152.0-154.0 °C; ^{1}H NMR (DMSO-d_6) δ 7.10 (t, *J* = 7.4 Hz, 1H), 7.36 (t, *J* = 8.0 Hz, 2H), 7.49-7.64 (m, 3H), 7.78 (d, *J* = 7.5 Hz, 2H), 7.95 (d, *J* = 8.4 Hz, 2H), 10.26 (s, 1H); ^{13}C NMR (DMSO-d_6) δ 120.4, 123.7, 127.7, 128.4, 128.6, 131.6, 135.0, 139.2, 165.6. HRMS Cald for $C_{15}H_{11}NO_2$ $[M+H]^+$-H_2O: 220.0762. Found: $[M+H]^+$-H_2O 220.0711.

3-(4-Methoxyphenyl)-2-phenylisoxazol-5-one (6c)

Yield 0.211 g (79%); pale yellow microcrystals; mp: 160.0-162.0 °C; ^{1}H NMR (DMSO-d_6) δ 3.84 (s, 3H), 7.02-7.12 (m, 3H), 7.34 (t, *J* = 7.4 Hz, 2H), 7.77 (d, *J* = 7.8 Hz, 2H), 7.96 (d, *J* = 8.4 Hz, 2H), 10.09 (s, 1H); ^{13}C NMR (DMSO-d_6) δ 55.5, 113.6, 120.3, 123.4, 127.0, 128.6, 129.6, 139.4, 161.9, 164.9. HRMS Cald for $C_{16}H_{13}NO_3$ $[M+H]^+$-H_2O: 250.0868. Found: $[M+H]^+$-H_2O 250.0817.

2-(4-Chlorophenyl)-3-(4-methoxyphenyl)isoxazol-5-one (6d)

Yield 0.217 g (72%); yellow microcrystals; mp: 191.0 - 193.0 °C; ^{1}H NMR (DMSO-d_6) δ 3.84 (s, 3H), 7.07 (d, *J* = 9.0 Hz, 2H), 7.40 (d, *J* = 8.7 Hz, 2H), 7.81 (d, *J* = 8.7 Hz, 2H), 7.96 (d, *J* = 9.0 Hz, 2H), 10.21 (s, 1H); ^{13}C NMR (DMSO-d_6) δ 55.4, 113.6, 121.8, 126.7, 127.0, 128.5, 129.7, 138.4, 162.0, 165.0. HRMS Cald for $C_{16}H_{12}ClNO_3$ $[M+H]^+$-H_2O: 284.0478. Found: $[M+H]^+$-H_2O 284.0427.

2,3-Di(4-methoxyphenyl)isoxazol-5-one (6e)

Yield 0.226 g (76%); yellow microcrystals; mp: 188.0-190.0 °C; ^{1}H NMR (DMSO-d_6) δ 3.74 (s, 3H), 3.83 (s, 3H), 6.92 (d, *J* = 8.7 Hz, 2H), 7.05 (d, *J* = 8.7 Hz, 2H), 7.66 (d, *J* = 8.7 Hz, 2H), 7.95 (d, *J* = 8.4 Hz, 2H), 9.97 (s, 1H);

^{13}C NMR (DMSO-d_6) δ 55.2, 55.4, 113.6, 113.7, 122.0, 127.1, 129.5, 132.4, 155.4, 161.8, 164.5. HRMS Cald for $C_{17}H_{15}NO_4$ $[M+H]^+$-H_2O: 280.0973. Found: $[M+H]^+$-H_2O 280.0925.

3-(2-Furyl)-2-phenylisoxazol-5-one (6f)

Yield 0.177 g (78%); yellow microcrystals; mp: 148.0-150.0 °C; ^{1}H NMR (DMSO-d_6) δ 7.10-7.20 (m, 3H), 7.24-7.40 (m, 2H), 7.53 (t, J = 7.2 Hz, 1H), 8.00 (t, J = 8.1 Hz, 1H), 8.38 (d, J = 3.9 Hz, 1H), 10.12 (s, 1H); ^{13}C NMR (DMSO-d_6) δ 119.9, 122.3, 124.7, 134.4, 148.2, 149.5, 153.1, 165.5. Anal. Cald for $C_{13}H_9NO_3$: C, 68.72; H, 3.99; N, 6.16. Found: C, 68.65; H, 4.01; N, 6.22

2-Phenyl-3-(2-thienyl)isoxazol-5-one (6g)

Yield 0.178 g (73%); yellow microcrystals; mp: 143.0-145.0 °C; ^{1}H NMR (DMSO-d_6) δ 7.06-7.22 (m, 3H), 7.30-7.36 (m, 2H), 7.40 (d, J = 7.2 Hz, 1H), 7.49 (t, J = 7.4 Hz, 2H), 7.67 (d, J = 4.8 Hz, 1H), 10.16 (s, 1H); ^{13}C NMR (DMSO-d_6) δ 124.6, 136.5, 137.2, 137.4, 137.6, 138.5, 139.6, 143.5, 145.8, 148.2, 164.4. Anal. Cald for $C_{13}H_9NO_2S$: C, 64.18; H, 3.73; N, 5.76. Found: C, 64.24; H, 3.65; N, 5.92

2-Phenyl-3-(3-pyridyl)isoxazol-5-one (6h)

Yield 0.190 g (80%); yellow microcrystals; mp: 182.0-184.0 °C; ^{1}H NMR (DMSO-d_6) δ 7.08-7.22 (m, 3H), 7.37-7.43 (m, 1H), 7.51 (t, J = 7.7 Hz, 1H), 8.03 (d, J = 8.4 Hz, 1H), 8.51-8.55 (m, 1H), 8.69 (d, J = 4.4 Hz, 1H), 8.91 (d, J = 1.8 Hz, 2H), 10.21 (s, 1H); ^{13}C NMR (DMSO-d_6) δ 124.7, 134.3, 137.4, 137.6, 138.6, 143.6, 146.7, 148.3, 149.2, 149.5, 159.0, 163.3. Anal. Cald for $C_{14}H_{10}N_2O_2$: C, 70.58; H, 4.23; N, 11.76. Found: C, 70.41; H, 4.11; N, 11.65.

Conclusion

In summary novel *N*-substituted *C*-benzotriazolated nitrones were synthesized in good yields. The reactivity of nitrones was studied with Reformatsky reagent providing a new approach to 2,3-disubstituted isoxazol-5-ones without using Lewis acid.

References

[1]Merino, P., Franco, S., Merchan, F. L., Tejero, T., *Tetrahedron:Assymetry*, **1997**, *8*, 3489.

[2]Borch, R. F., Bernstein, M. D., Durst, H. D., *J. Am. Chem. Soc*., **1971**, 2897.

[3]Christenen, D., Jorgensen, K. A., *J. Org. Chem*. **1989**, 54, 126

[4]Merino, P., Franco, S., Merchan, F. L., Tejero, T., *Synlett*, **2000**, 442.

[5]Lombardo, M., Trombini, C. *Synthesis*, **2000**, 759.

[6]Cardona, F., Goti, A., *Angew. Chem. Int. Ed.*, **2005**, *44*, 7832.

[7]Palomo, C., Oiarbide, M., Areco, E., Garcia, J. M., Lopez, R., Gonzalez, A., Linden, A., *Angew. Chem. Int. Ed.*, **2005**, *44*, 6187.

[8]Gothelf, K. V., Jørgensen, K. A., *J. Org. Chem.*, **1994**, *59*, 5687.

[9]Hori, K., Kodama, H., Ohta, T., Furukawa, I. *Tetrahedron Lett.*, **1996**, *37*, 5947.

[10]Jensen, K., Gothelf, K. V., Hazell, R. G., Jørgensen, K. A. *J. Org. Chem.* **1997**, *62*, 2471.

[11]Kobayashi, S., Kawamura, M. *J. Am. Chem. Soc.*, **1998**, *120*, 5840.

[12]Hori, K., Kodama, H., Ohta, T., Furukawa, I. *J. Org. Chem.*, **1999**, *64*, 5017.

[13]Desimoni, G., Faita, G., Mortoni, A., Righetti, P., *Tetrahedron Lett.* **1999**, *40*, 2001.

[14]Iwasa, S., Tsushima, S., Shimada, T., Nishiyama, H., *Tetrahedron Lett.*, **2001**, *42*, 6715.

[15]Shirahase, M., Kanemasa, S., Oderaotoshi, Y. *Org. Lett.*, **2004**, *6*, 675.

[16]Dugovič, B., Fišera, L., Hametner, C., Prónayová, N., *ARKIVOC*, **2003**, *14*, 162.

[17]Laufhlin, S. K., Clark, M. P., Djungn J. F., Golebiowski, A., Brugel, T. A., Sabat, M., Bookland, R. G., Laufersweiler, M. J., VanRens, J. C., Townes, J. A., De, B., Hsieh, L. C., Xu, S. C., Walter, R. L., Mekel, M. J., Janusz, M. J., *Bioorg. Med. Chem. Lett*., **2005**, *15*, 2399.

[18]Ikegami, F., Yamamoto, A., Sekine, T., Ishikawa, T., Kusamae-Eguch, K., Kusama, T., Watanabe, K., *Chem. Pharm. Bull.*, **2000**, *48*, 278.

[19]Khalafy, J., Ebrahimlo, A. R. M., Eisavi, R., Dilmaghani, A., *ARKIVOC*, **2005**, (*xiv*), 59.

[20]Abbiati, G., Beccalli, E. M., Broggini, G., Zoni, C., *Tetrahedron*, **2003**, *59*, 9887.

[21]Prager, R. H., Smith, J. A., *J. Chem. Soc. Commun.*, **1994**, 1805.

[22]Chidichimo, G., Cum, G., Lelj, F., Sindona, G., Uccella, N., *J. Am. Chem. Soc.*, **1980**, *102*, 1372.

[23]Tamura, M., Ise, Y., Okajima, Y., Nishiwaki, N., Ariga, M., *Synthesis*, **2006**, 3453.

[24]Quesnelle, C. A., Gill, P., Roy, S., Dodier, M., Marinier, A., Martel, A., Snyder, L. B., D'Andrea, S. V., Bronson, J. J., Frosco, M., Beaulieu, D., Warr, G. A., DenBleyker, K. L., Stickle, T. M., Yang, H., Chaniewski, S. E., Ferraro, C. A., Taylor, D., Russell, J. W., Santone, K. S., Clarke, J., Drain, R. L., Knipe, J. O., Mosure, K., Barrett, J. F., *Bioorg. Med. Chem. Lett.*, **2005**, *15*, 2728,

[25]Beccalli, E. M., Marchesini, A., *Tetrahedron*, **1997**, *53*, 10433.

[26]Ang, K. H., Prager, R. H. *Tetrahedron* **1992**, *48*, 9073.

[27]Khalafy, J., Marjani, A. P., Ebrahimlo, A. R. N., *J. Braz. Chem. Soc***., 2006**, *17*, 570.

[28]Nenajdenko, V. G., Zakurdaev, E. P., Gololobov, A. M., Balenkova, E. S., *Russ. Chem. Bull., Int. Ed.*, **2005**, *54*, 220.

[29]Batra, S., Bhaduri, A. P., *J. Indian Inst. Sci.*, **1994**, *74*, 213.

[30]Cox, M., Dixon, M., Lister, T., Prager, R. H., *Aust. J. Chem.*, **2004**, *57*, 455.

[31]Cox, M., Prager, R. F., Riessen, D. M., *ARKIVOC*, **2001**, (*vii*), 88.

[32]Clark, A. D., Ha, U. T., Prager, R. H., Smith, J., *Aust. J. Chem.*, **1999**, *52*, 1029.

[33]Millan, D. S., Prager, R. H., *J. Chem. Soc., Perkin Trans. 1*, **1998**, 3245.

[35]Sasaki, T., Hayakawa, K., Nishida, S., *J. Chem. Soc. Commun.*, **1980**, 1054.

[35]Sarlo, F. D., Fabbrini, L., Renzi, G., *Tetrahedron*, **1996**, *22*, 2989.

[36]Saeki, S., Honda, H., Hamana, M., *Chem. Chem. Pharm. Bull.*, **1983**, *31*, 1474.

[37]Fujimoto, M., Sakai, M., *Chem. Pharm. Bull.*, **1965**, *13*, 248.

[38]Katritzky, A. R., Øksne, S., Boulton, A. J., *Tetrahedron*, **1962**, *18*, 777.

[39]Sato, K., Ueda, T., Sugai, S., *Chem. Pharm. Bull.* **1986**, *34*, 3153.

[40]Merino, P., Franco, S., Merchan, F. L., Tejero, T., *Tetrahedron:Asymmetry*, **1997**, *8*, 3489.

[41]Borch, R. F., Bernstein, M. D., Durst, H. D., *J. Am. Chem. Soc*., **1971**, *93*, 2897.

[42]Christenen, D., Jorgensen, K. A., *J. Org. Chem*., **1989**, *54*, 126.

[43]Rosenberg, H. M., Jorgensen, K. A., *J. Org. Chem*., **1972**, *37*, 1443.

[44]Tian, L., Xu, G. –Y., Liu, L.–Z., *Synthesis*, **2003**, 1329.

[45]Singh, N., Sethi, P. S., *Indian J. Chem.*, **1975**, *13*, 990.

[46]Dutta, D. K.; Boruah, R. C.; Sandhu, J. S. *Indian J. Chem., Sect. B.*, **1986**, *25B*, 350.

[47]Singh, J., Ishar, M. P. S., Girghar, N. K., Singh, L. *J. Heterocycl. Chem.*, **2005**, *42*, 1047.

[48]Liotta, D., Baker, A. D., Goldman, N. L., Weinstein-Lanse, F., Felsen-Reingold, D., Engel, R., *J. Org. Chem.*, **1974**, *39*, 1974.

[49]Lo, M. M. –C.; Fu, G. C., *J. Am. Chem. Soc*., **2002**, *124*, 45, 4572.

Received: 25.07.2014.
Accepted: 13.08.2014.